GEOPHYSICAL APPLICATIONS OF SURFACE WAVE IMPEDANCE MEASUREMENTS

Edited by:
L.S. COLLETT AND O.G. JENSEN

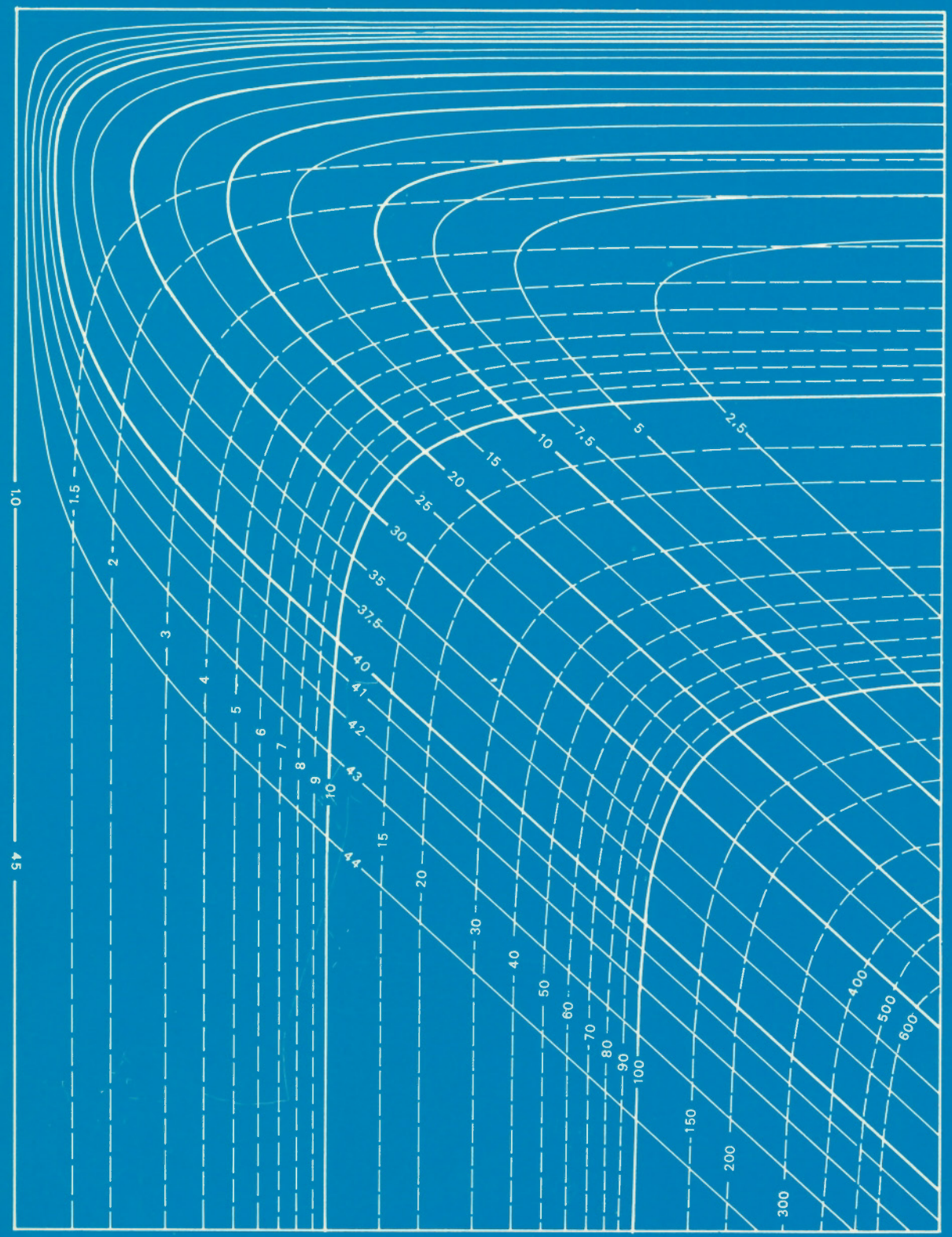

Canada

1982

PAPER 81-15

GEOPHYSICAL APPLICATIONS OF SURFACE WAVE IMPEDANCE MEASUREMENTS

Edited by:
L.S. COLLETT AND O.G. JENSEN

1982

Available in Canada through

authorized bookstore agents
and other bookstores

or by mail from

Canadian Government Publishing Centre
Supply and Services Canada
Hull, Québec, Canada K1A 0S9

and from

Geological Survey of Canada
601 Booth Street
Ottawa, Canada K1A 0E8

A deposit copy of this publication is also available
for reference in public libraries across Canada

Cat. No. M44-81/15E Canada: $7.00
ISBN 0-660-11113-6 Other countries: $8.40

Price subject to change without notice

Text prepared at McGill University, Montréal, Québec by:

Scientific and technical editing
Hazel DeNeeve
Elizabeth Baranyi

Draughting
Mark Bowman
Jose Bilodeau
Michel Vachon
Heather Frank

Word processing
Sandra Young

FORWARD

This volume of collected papers summarizes the results of three research projects which were conducted by the Laboratory in Applied Geophysics at McGill University during the years 1975 - 1981. The three projects entitled:

1. Wave-tilt EM applications to Permafrost Exploration,

2. VLF (Wave-tilt, Radiohm) and LF Applications to Near Horizontal Multilayer and Simple Discontinuous Geological Structures, and

3. Applications of Natural and Artificial EM-Wave Sources to Ground Impedance Measurement (ULF, VLF, LF)

were sponsored by the Geological Survey of Canada and supported under the Research Agreements Program administered by Energy, Mines and Resources, Canada. The volume is introduced by a comprehensive summary of the theory of wave-impedance measurements while the seven following articles presented here summarize the thesis research of a graduate student who, under the direction of the teaching staff of the Laboratory, undertook a particular aspect of a broadly conceived and evolutionary research plan. The focus of this body of work was directed towards an evaluation of the geophysical applications of the measurable physical characteristics of electromagnetic waves in the ultra-low-frequency (ULF, 300 Hz to 3 kHz) the very-low-frequency (VLF, 3 kHz to 30 kHz), and low-frequency (LF, 30 kHz to 300 kHz) bands of the radio frequency spectrum as they propagate over the ground surface. In particular, a delineation in terms of the geophysical parameters of the hidden, near-surface geological structure of the terrain was sought.

The earliest studies were directed towards the then-immediate problem of detecting and delineating permafrost through the measurement of the electromagnetic wave impedance at the ground surface. Subsequently, the research evolved towards the development of a more general methodology for the mapping of the characteristics of the terrain: overburden depth and conductivity, bedrock delineation, detection of ground water table, etc.. These studies themselves stimulated research on the theory of interpretation using inversion methods and led to the development of new instrumentation for the direct geophysical measurement of the surface wave impedance at frequencies both below and above the commonly used VLF band. This broadening of the frequency spectrum of measurements has allowed for the interpretation of more complex geological models and/or the inclusion of more geophysical parameters in geological modelling.

AVANT-PROPOS

On trouvera dans ce recueil de tirés à part le résumé des résultats de trois travaux de recherche menés au laboratoire de géophysique appliquée de l'université McGill de 1975 à 1981. Les études avaient pour titres:

1. *Applications EM de l'inclinaison du champ à l'étude du pergélisol.*

2. *Applications des très basses fréquences (TBF) (inclinaison du champ, Radiohm) et des basses fréquences (BF) à l'étude des structures géologiques à nombreuses multi-couches presque horizontales et aux structures géologiques simples discontinues.*

3. *Applications de sources naturelles et artificielles d'ondes EM à la mesure de l'impédance du sol (UBF, TBF, BF).*

Ces travaux ont été subventionnés par la Commission géologique du Canada conformèment au programme des accords sur la recherche administré par le ministère fédéral de l'Energie, des Mines et des Ressources. L'ouvrage débute par un résumé complet de la théorie de mesure des impédances; les sept articles présentés ici font le point sur les travaux de recherche d'un étudiant de cycle supérieur qui, sous la direction du personnel enseignant du laboratoire, a entrepris d'approfondir un aspect particulier d'un plan de recherche de conception globale et évolutive. Ce travail avait principlement pour but d'évaluer les applications géophysiques des caractéristiques physiques mesurables des ondes électromagnétiques à ultra-basses fréquences (UBF 300 Hz à 3 kHz), à très basses fréquences (TBF, 3 kHz à 30 kHz) et à basses fréquences (BF, 30 kHz à 300 kHz) du spectre de bandes radio lorsque ces ondes se propagent à la surface du sol. En particulier, on a tenté de délimiter en termes de paramètres géophysiques la structure géologique cachée à faible profondeur.

Les premières études visaient à résourdre un problème alors prioritaire: dépister et délimiter le pergélisol par la mesure de l'impédance de l'onde électromagnétique à la surface du sol. Par la suite, la recherche a évolué vers la mise au point d'une méthodologie générale de levés pour l'établissement des cartes des caractéristiques du terrain: profondeur et conductivite du mort-terrain, délimitation du socle, repèrage de la nappe d'eau souterraine, etc. Ces études ont elles-mêmes été à l'origine d'autres recherches sur la théorie de l'interprétation au moyen des méthodes d'inversion et permis la mise au point de nouveaux instruments de mesure directe de l'impédance caractéristique de l'onde de surface à des fréquences plus basses et plus élevées que la bande TBF habituellement utilisée. Cet élargissement de la gamme de fréquences de mesure a permis l'interprétation de modèles géologiques plus complexes et(ou) l'inclusion d'un plus grand nombre de paramètres géophysiques dans la conception de modèles géologiques.

This volume should provide a useful reference source for those geophysicists who employ wave-impedance measurements in mineral exploration, overburden delineation, permafrost studies, ground and slope stability evaluations, foundation studies, ground water and hydrological studies, and a host of other applications.

For convenience, the volume is referenced internally; references to each of the eight separate articles are designated by a Roman numeral, for example, I, indicating the internal article number.

The publication of this volume of collected papers on the Geophysical Applications of Surface-Wave Impedance Measurements has been supported by the Laboratory in Applied Geophysics, McGill University and the Geological Survey of Canada.

L.S. Collett
March, 1981 O.G. Jensen

L'ouvrage constituera sans doute une source de références utile pour les géophysiciens qui se servent de mesures de l'impédance caractéristique dans la recherche de minéraux, la délimitation du mort-terrain, les études sur le pergélisol, les évaluations de la stabilité du sol et de la pente, les études sur les fondations, sur les nappes d'eau souterraines et les études hydrologiques ainsi que de nombreuses autres applications.

Pour des raisons d'ordre pratique, les références du volume renvoient à d'autres passages du même ouvrage. Ainsi, les références de chacun des huit articles sont désignées par un chiffre romain, I, indiquant le numéro du chapitre du renvoi.

La publication de ce recueil d'études sur les applications géophysiques des mesures de l'impédance caractéristique de surface a reçu l'appui du Laboratoire de géophysique appliquée, de l'université McGill et de la Commission géologique du Canada.

L.S. Collett
Mars 1981 *O.G. Jensen*

Contents

THE THEORY OF EM SURFACE WAVE IMPEDANCE MEASUREMENTS

D.J. Crossley
Laboratory in Applied Geophysics, McGill University

Crossley, D.J., The theory of EM surface wave impedance measurements; in Geophysical Applications of Surface Wave Impedance Measurements, L.S. Collett and O.G. Jensen editors, Geological Survey of Canada, Paper 81-15, p. 1-17, 1981.

Abstract

Several powerful sources of EM radiation exist to probe the electrical properties of the Earth's crust. One natural source is the MT (magnetotelluric) field, generated either by thunderstorm activity (>1 Hz) or by micropulsations (<1 Hz), which can be considered as a distant generator of plane EM waves vertically incident on the Earth's surface. Other useful sources are the government-operated VLF (very low frequency) radio wave transmitters typically broadcasting at 20 kHz and strategically located to provide a worldwide network of marine navigation signals and, at slightly higher frequencies, the LF (low frequency) transmitters for providing world-wide time signals (e.g. 60 kHz, WWVB). The field far from these radio transmitters is well approximated by a plane wave polarized with the magnetic field horizontal to the Earth's surface.

Suitable receivers measure either a ratio of horizontal to vertical field components (wavetilt) or a ratio of electric to magnetic field components (wave impedance). Airborne sensors usually measure wavetilt, whereas ground systems can measure either wavetilt or wave impedance. At any frequency the amplitude and phase of either of these two quantities yields two pieces of information about the electrical structure of the ground. This paper reviews the necessary theory for interpreting wave impedance measurements at VLF and LF.

Particular attention is paid to the source fields for Canada, how the nature of these source fields affects the apparent resistivity and phase measurements and the possible dielectric effects created by a combination of (high frequency) × (high resistivity) × (high permittivity) on field measurements. The present state of interpretation for these methods is reviewed.

Résumé

On dispose de plusieurs sources puissantes d'émissions EM pour sonder les propriétés de l'écorce terrestre. L'une des sources naturelles qu'on peut utiliser est le champ MT (magnétotellurique) généré par l'activité électrique d'un orage (>1 Hz) ou par des micropulsations (<1 Hz) qu'on peut considérer comme un générateur éloigné d'ondes EM planes présentant une incidence verticale par rapport à la surface du globe. Il existe d'autres sources utiles, notamment les émetteurs-radio TBF (à très basses fréquences) exploités par le gouvernement; ces dernières émettent sur 20 kHz et sont situées de façon stratégique pour assurer un réseau mondial de signaux de navigation marine. A des fréquences plus élevées, on peut se servir des émetteurs BF (basses fréquences) qui diffusent mondialement des signaux horaires (par example, 60 kHz WWVB). A grande distance de ces émetteurs-radio on obtient une bonne approximation du champ par un modèle de type onde plane polarisée dont le champ magnétique est parallèle à la surface de la terre.

Tout récepteur adéquat mesure soit le rapport des composantes verticales aux composantes horizontales du champ (inclinaison du champ) ou le rapport des composantes électriques du champ sur ses composantes magnétiques (impédance caractéristique). Les capteurs aéroportés mesurent habituellement l'inclinaison du champ tandis que les systèmes au sol mesurent soit l'inclinaison du champ, soit l'impédance caractéristique. A n'importe quelle fréquence, l'amplitude et la phase de chacune de ces deux quantités nous apportent deux élements d'information sur la structure électrique du sol. Le présent article examine la théorie sur laquelle est fondée l'interprétation des mesures de l'impédance caractéristique aux très basses fréquences (TBF) et au basses fréquences (BF).

L'article s'intéresse particulièrement aux champs EM couvrant la territoire canadien. L'auteur y étudie comment la nature de ces champs influence la résistivité apparente et les mesures de phase ainsi que les effets diélectriques éventuels créés par une combinaison de haute fréquence, de haute résistivité et de haute constante diélectrique (haute fréquence) × (haute résistivité) × (haute constante diélectrique) sur les mesures faites sur le terrain. Enfin, l'article examine l'état actuel de l'interprétation de ces méthodes.

INTRODUCTION

The principles of magnetotelluric (MT) and very low frequency radio wave (VLF) propagation and the geophysical method based upon these fields can be found in a number of readily available sources. Two indispensable texts are due to Wait (1962) for the VLF method and Keller and Frischknecht (1966) for the MT method; both references contain detailed descriptions of the source fields and basic equations. In neither reference, however, is the question of interpretation pursued further than the use of type curves pre-calculated for certain ground resistivity models, a situation that was not unusual for exploration techniques in the 1960's. A recent review of the interpretation of MT data which covers the use of numerical methods for computer usage may be found in Patra and Mallick (1980).

Up to the present time the MT method has exemplified the 'record now-process later' philosophy, in which considerable manipulation of the recorded data is required to extract the quantities necessary for interpretation. An example of modern recording and interpretive techniques is given by Jones and Hutton (1979a,b) who use Monte Carlo inversion to satisfy the 'observed' variables which are the relative amplitude and phase of appropriate electric and magnetic field components.

Unlike apparent resistivity, which is related to the amplitude ratio of the horizontal electric and magnetic fields and hence not too difficult to derive electronically, a real time measurement of MT phase requires considerable instrumental ingenuity due to the rapidly varying polarization of the incident source fields. It would save both data storage space and processing time if the phase could be measured directly in the field by electronically following the polarization of the incident fields and then recording the appropriate phase difference only at times when the signal levels are relatively high and stable. Mathur and Telford (1981-VII) report some progress towards this goal and Nichols and Telford (1981-VIII) describe the present stage of construction of a field device to perform the phase measurement task. The design of sophisticated instrumentation to perform such data processing before recording is clearly a trend in geophysical exploration.

In VLF prospecting the interpretation aspect has not received a great deal of attention per se, with the (notable) exception of a few studies concerning permafrost (e.g. Hoekstra et al., 1975; Hoekstra, 1978). In fact, until recently, most of the data have been interpreted only in a qualitative fashion (e.g. Arcone, 1978) similar, for example, to the treatment of radiometric data. Considering the limitations of the data, this is not unduly surprising. Airborne VLF measures only one parameter, namely the quadrature component of wavetilt, although this is sometimes done at several frequencies e.g. the Barringer E-phase system (Barringer, 1972). By contrast, a typical ground system will usually measure both the magnitude and phase of the surface impedance, but only at a single frequency or within a narrow band, 15-23kHz (e.g. Geonics EM16R, Collett and Becker, 1967). Another factor which leads to a limited interpretative potential is that, in comparison to MT depth sounding which may yield structural information to depths of several hundred metres, the high frequencies of VLF transmissions limit penetration of the EM fields to relatively shallow depths. This can be however an advantage when resolution of near-surface structure is desired in which case two or three layer models are usually sufficient.

The VLF measurement is nonetheless both rapid and easy to make in the field and several recent papers deal with two and three layer models in detail (Jones and Telford, 1981-III; Powell and Jensen, 1981-II; Mathieson and Crossley, 1981-IV). Of particular interest from an interpretative point of view is the addition of a thin layer to a basic two-layer model. This situation frequently exists in the field due to seasonal effects, e.g. the formation of a surface water layer due either to a summer thaw in a permafrost layer or spring run-off. In this situation additional information about the structure can be achieved by the use of an extra transmitting station in the LF band. This requires a separate receiver such as the 60kHz instrument designed and described by LaFleche and Jensen (1981-V). The interpretive advantages in using data from both a VLF and a LF receiver have not been fully exploited at this time.

One of the main uses of the VLF method is in the detection of lateral changes in near-surface resistivity contrasts, such as dipping contacts, dikes, water-table layers etc. Often such structures are approximated by a one dimensional (vertical) model beneath each station location, but this is clearly inadequate where there are appreciable lateral changes in the resistivity or depth of geologic sections. A somewhat improved interpretation in this case is attempted by Teemull and Crossley (1981-VI), in which a spatially harmonic interface is fitted to single frequency VLF profiles. The extreme case of a vertical fault contact with overburden has been treated by Telford et al. (1977).

THE SOURCE FIELDS

Magnetotellurics

MT fields are described by Keller and Frischknecht (1966, Ch.IV), and we need review only their fundamental properties. The entire range of time-varying external current sources is about 10^{-4} to 10^{4} Hz. In the low frequency range, MT equipment generally records a wide band of signals, 10^{-3} to 10 Hz, whereas at higher frequencies a more common practise has been to monitor relatively few distinct frequencies e.g. 1, 8, 145 and 3000 Hz (Van Ngoc et al., 1976). Choice of frequencies is determined primarily by the nature of the survey. For example, high frequencies (>1Hz), generated by worldwide thunderstorm activity, are suitable for delineating near surface structure, whereas low frequencies (< 1Hz), generated by micropulsations, are appropriate for deep sounding.

One of the most important characteristics of such sources is that they are all more or less worldwide. This implies that both the low frequency magnetospheric waves (micropulsations) and the lightning activity (channelled by the Earth-ionosphere waveguide) can be taken to have infinite spatial extent, so MT sources can therefore be approximated as plane waves vertically incident at the Earth's surface. Both the polarization and intensity of such waves, however, change irregularly with time which makes it necessary to record simultaneously orthogonal electric and magnetic field components over many cycles of the lowest frequency. A continual shift in polarization complicates the interpretation of laterally varying resistivity structure because of the usual interpretative assumption that the incident wave should have a fixed orientation relative to the strike of local geological features. For this reason the MT method has been most widely used for deep resistivity sounding in horizontally stratified media.

Table 1. VLF and LF stations for surface-wave impedance measurements.

VLF Stations	Frequency (kHz)	Radian Wavelength (km)	Power (kw)	Lat.	Long.
FVO, Bordeaux, France	15.1	19.9	500	+44°50'	+0°34'
GBR, Rugby, England	16.0	18.8	750(a) 60(b)	+52°20'	+1°11'
JXZ, Heligoland, Norway	16.4	18.3	350		
JMS, Moscow, USSR	17.1	17.5	1000	+55°19'	-38°41'
NDT, Japan	17.4	17.2	50	+32°58'	-137° 1'
NAA, Cutler, Maine	17.8	16.9	2000(a) 1000(b)	+44°38'	+67°16'
NLK, Jim Creek, Washington	18.6	16.1	1200(a) 250(b)	+48°12'	+121°55'
NSS, Annapolis, Maryland	21.4	14.0	85(b)	+38°59'	+76°27'
NWC, Exmouth, Australia	22.3	13.4	1000	-21°48'	-114° 9'
NPM, Lualualei, Hawaii	23.4	12.8	1000(a)	+21°25'	+158° 9'

LF Stations	Frequency (kHz)	Radian Wavelength (km)	Power (kw)	Lat.	Long.
JG2AS, Chiba, Japan	40.0	7.5		+35°38'	-140° 4'
OMA, Podebrady, Czechoslovakia	50.0	6.0	5(a)	+50° 9'	- 15° 8'
RTZ, Irkutsk, USSR	50.0	6.0		+52°18'	-104°18'
MSF, Rugby, England	60.0	5.0	50(a)	+52°22'	+ 1°11'
WWVB, Fort Collins, Colorado	60.0	5.0	13(b)	+40°40'	+105° 3'
RBU, Moscow, USSR	66.67	4.5		+55°19'	-38°41'
HBG, Parangins, Switzerland	75.0	4.0		+46°24'	-6°15'
DCF77, Mainflingen, Germany, FDR	77.5	3.9	38(a)	+50° 1'	-9° 0'
NSS, Annapolis, Maryland	88.0	3.4		+38°59'	+76°27'
FTA91, St. Andre-de-Corcy, France	91.15	3.3		+45°55'	-4°55'

(a) Power to antenna
(b) Effective radiated power

From: Time and Frequency User's Manual, NBS Technical Note 695, US Department of Commerce, NBS Boulder, Colorado 80302, 1977.

and: BIH Annual Report 1974, 61, Avenue de l'Observatoire-75014 Paris.

VLF Radio Waves

The radio wave spectrum is divided into a number of bands with frequencies extending from 0.3×10^N Hz (included) to 3×10^N Hz (excluded). Band N=4 (3 to 30 kHz) is VLF and band N=5 (30 to 300 kHz) is LF.

The equations for a VLF radio wave can readily be derived for a vertical electric dipole antenna over a horizontally layered half space (Wait, 1962, p. 35). The field consists of three components with radial dependencies $1/r$, $1/r^2$ and $1/r^3$ representing radiation, induction and electrostatic contributions respectively. The $1/r^3$ term can be ignored for all geophysical purposes, whereas the $1/r^2$ term is predominant for EM induction methods at distances of the order of 10 km. The EM field associated with the $1/r$ term propagates very efficiently to great distances (thousands of km) and is used as a navigation system for ships and submarines.

The far-field components of a vertical electric dipole antenna radiating into free space are, at distance $r \gg \lambda$,

$$H_\varphi = -\frac{cp_0}{4\pi r\lambda^2} \sin\theta \, e^{i\omega t} \qquad (1)$$

and

$$E_\theta = -\frac{p_0}{4\pi \epsilon_0 r\lambda^2} \sin\theta \, e^{i\omega t} \qquad (2)$$

where p_0 is the dipole moment (= $I_0 s/i\omega$ if I_0 is the mean current and s the antenna length), λ is the radian wavelength of the wave (= c/ω), c is the velocity of light and ω is the angular frequency (Lorrain and Corson, 1970, Ch. 14). It is seen that there are only two orthogonal components, H_φ in an azimuthal direction and E_θ in the plane of the antenna (assumed to be at the origin of the spherical polar coordinate system) which are in phase at all

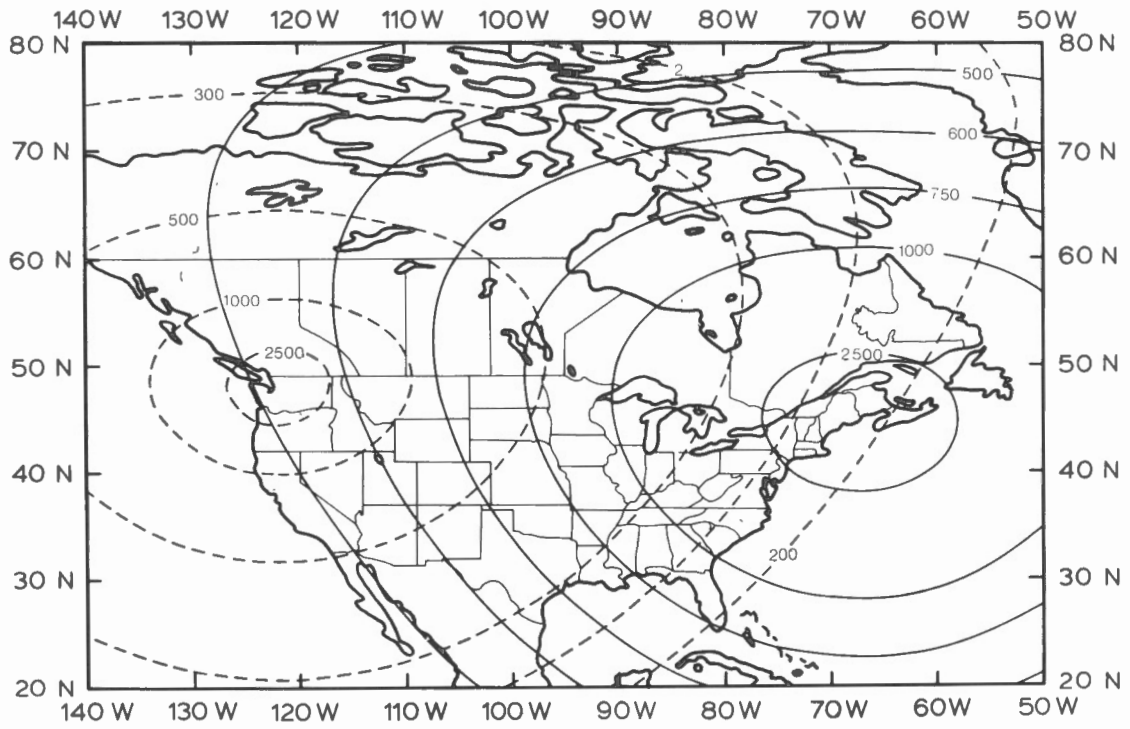

Figure 1. *Contours of free-space electric field strength for two VLF stations; Cutler, Maine (17.8 kHz, solid lines) and Jim Creek, Washington (18.6 kHz, dashed lines). At any location the local magnetic field is polarized parallel to these contours except in areas of low resistivity where significant distortion and attenuation of the field can take place.*

times. Their ratio, the wave impedance

$$Z = \frac{E_\theta}{H_\varphi} = \frac{1}{c\epsilon_0} = \sqrt{\frac{\mu_0}{\epsilon_0}} = 376.7\ \Omega \qquad (3)$$

is entirely real, and the Poynting vector giving the total outflow of energy per unit time per unit area is

$$\underline{S} = \underline{E} \times \underline{H} \qquad \text{or} \qquad \overline{\underline{S}} = \tfrac{1}{2} R_e(\underline{E} \times \underline{H}^*) \qquad (4)$$

averaged over a cycle. For the above wave in free space

$$\overline{\underline{S}} = \tfrac{1}{2} R_e(E_\theta H_\varphi^*)\ \underline{\hat{r}} \qquad (5)$$

which becomes

$$\overline{S} = \tfrac{1}{2}\sqrt{\frac{\epsilon_0}{\mu_0}}\ E_\theta^2 \qquad (6)$$

If we imagine an antenna with an effective radiating power P (watts), then for a hemisphere centered at the antenna,

$$P = \int_0^{2\pi}\int_0^{\pi/2} \overline{S}\, r^2 \sin\theta\ d\theta\, d\varphi \qquad (7)$$

so that the free-space electric field intensity is

$$E_\theta = \left(\frac{P \times 376.7}{\pi r^2}\right)^{\frac{1}{2}} \qquad (8)$$

We take r to be the great circle distance between an antenna at latitude and longitude (ℓ_0, L_0) and a field point (ℓ, L) ie.

$$r = R\cos^{-1}\left[\sin\ell\ \sin\ell_0 + \cos\ell\ \cos\ell_0\ \cos(L - L_0)\right] \qquad (9)$$

where R is the Earth's mean radius and the latitude or longitude is considered negative if south of the equator or east of Greenwich respectively.

Contours of E_θ are shown over Canada for two VLF stations (Cutler, Maine and Jim Creek, Washington) in Figure 1, with the pertinent transmitter data taken from Table 1. A similar set of contours for two LF stations (WWVB, Fort Collins, Colorado, and MSF, Rugby, England) is shown in Figure 2. The above expression (8) for E_θ fails to take into account dissipation of the wave energy into the ground which increases as the ground resistivity increases. Consequently, in Figures 1 and 2, the electric field strength has been multiplied by a factor 0.33 to give approximate agreement between the location of the 100 V/m contour for WWVB as computed theoretically and as measured on the ground (Kamas, 1977). Even though the field intensity is only approximate in Figures 1 and 2, the contours indicate fairly well the field orientation at any position.

It can be seen that the propagation directions are not nearly as convenient as one might desire from the requirement that geologic strike be parallel to the contours of at least one station. This is more troublesome with the EM16 tilt angle measurements when the local strike is N-S, but it also means that orthogonal (E_x, H_y) and (E_y, H_x) measurements with the EM16R are not often possible and these could be very useful for assessing resistivity anisotropy.

Once a suitable transmitter has been found, the VLF method requires only a passive receiver equipped with a pair of electrodes and a coil to measure the electric and magnetic fields respectively. Figure 3 shows the possible paths the EM wave may take between antenna and receiver. At distances of less than 50 km from the antenna the sky wave component can be ignored, whereas the space and space-reflected waves (with a π phase shift)

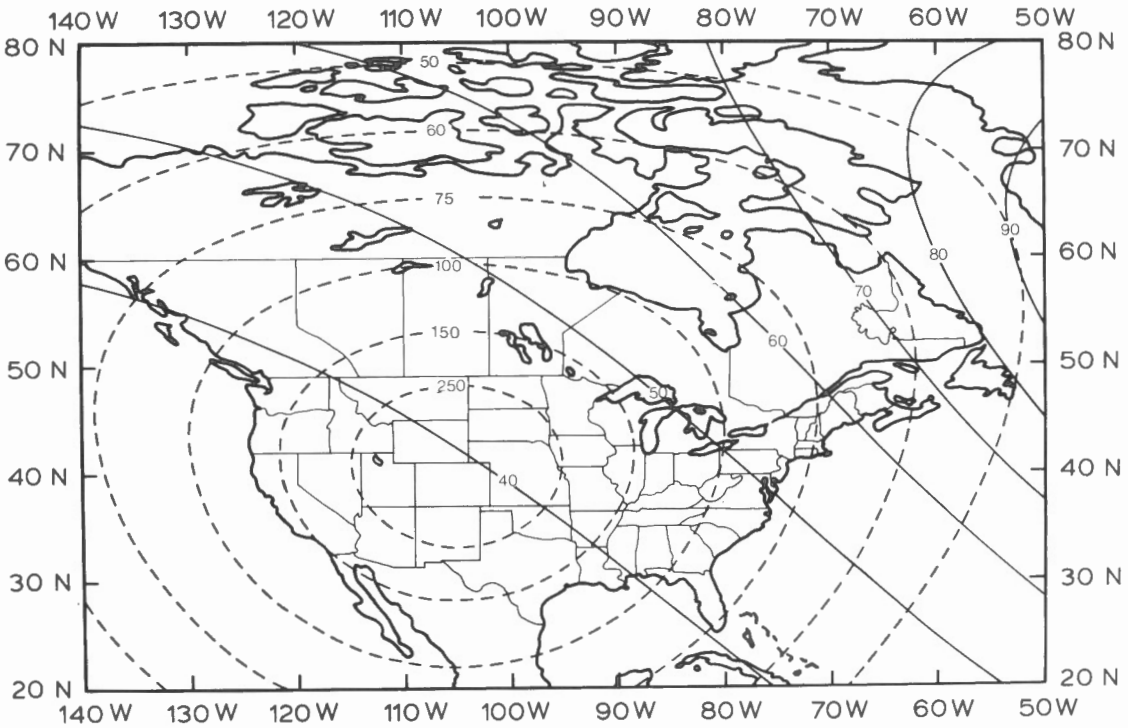

Figure 2. *As Figure 1 for two LF stations; Fort Collins, Colorado (60 kHz, dashed lines) and Rugby, England (60 kHz, solid lines).*

cancel for all distances greater than a few km. One then has to consider the ground wave and sky wave for most normal operating conditions in Canada. Arcone (1979) remarks that for distances over 800 km from the transmitter, the first sky 'hop' is most important for determining the VLF field strength.

A controversial aspect of VLF propagation has been the nature of the ground wave component; Wait (1971, p. 163) gives an interesting history of this. One might believe that a surface-trapped (Zenneck) wave is the ground wave, but, in fact, it does not appear explicitly as a solution of the radiating dipole antenna. It can be shown (e.g. Barlow and Brown, 1962, Ch. III) that a Zenneck wave, which is characterised by an exponential decay of amplitude above the air-ground interface, is equivalent to an inhomogeneous plane wave incident at the complex Brewster angle (Fig. 4(a)). There will not in this case be any reflected wave and the angles of incidence θ_0 and transmission θ_1 are related by

$$\cos \theta_0 = \frac{\mu_1 \gamma_0}{\mu_0 \gamma_1} \cos \theta_1 \quad , \tag{10}$$

where γ_0 and γ_1 are the propagation constants defined as in equations (40). Stratton (1941, pp. 516-522) shows that, as the ground conductivity increases, this condition leads to an incident and a transmitted wave which propagate increasingly parallel to and vertical to the interface respectively.

As Wait (1962, pp. 17-20) argues, however, such a wave is inconsistent with the idea of a source region (one can imagine a mixture of ground and sky waves) from which an incident plane wave appears at a fixed angle of incidence to the vertical (Fig. 4(b)). One then gets an increase in field amplitude with height above the ground instead of an exponential decay, as in the case of the Zenneck wave. In this second description, the plane wave is still inhomogeneous with a complex (but not necessarily critical) angle of incidence θ_0 , which should be interpreted as the real angle ψ_0 that the phase fronts in air make with the ground. When displacement currents in the ground are ignored this angle turns out to be

$$\tan \psi_0 = \frac{\mathrm{Im}(k)}{\mathrm{Im}(u_0)} = \frac{\mathrm{Im}(\gamma_0 \sin \theta_0)}{\mathrm{Im}(\gamma_0 \cos \theta_0)} = \tan \theta_0 \tag{11}$$

again borrowing results from later analysis. In the following discussion it will be assumed that the arbitrary angle θ is indeed real and to be interpreted as ψ_0 above.

It will be demonstrated later that the complex surface wave impedance measurements are independent of θ when displacement currents are ignored, but that θ must be specified if displacement currents are included. Sinha (1977) shows that for VLF airborne surveys, a change in wavetilt with height above the ground will also depend on θ, which in turn varies with the particular combination of ground and sky wave components at the measurement location. To be more precise one would have to solve the complex propagation problem in the spherical Earth-ionosphere waveguide as outlined by Wait (1978).

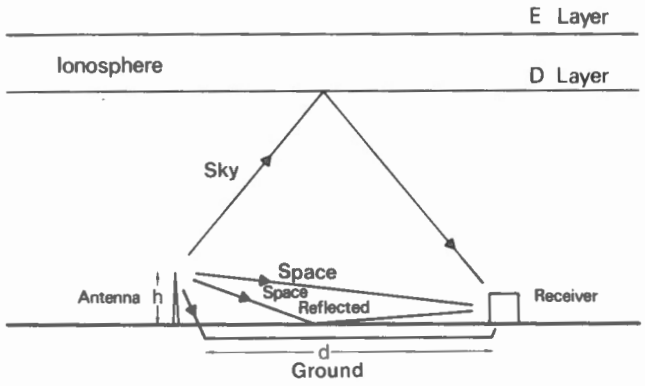

Figure 3. *Possible propagation paths for VLF radio waves between a vertical electric dipole antenna of height* h *and a receiver at distance* d . *The ionospheric D layer (~ 60 km) disappears at night and the sky wave is then reflected from the bottom of the E-layer (~ 90 km). The space and space reflected waves are* π *out of phase and of almost equal path lengths if* $h < 0.05d$. *The sky wave is only seen by the receiver if* $d > 50$ *km.*

PLANE EM WAVE INDUCTION

Basic Equations

We begin by stating the equations which will govern the propagation of EM waves in the present geophysical context. In most of the discussion to follow, the ground can be considered as divided into either vertical or horizontal strata of homogeneous isotropic material with constant electric and magnetic properties. We will therefore be dealing with standard EM analysis of the sort found in most textbooks on electricity and magnetism.

At any location in space, there are two fundamental Maxwell equations which relate five vector quantities: denoting $\partial/\partial t$ by ∂_t , these are

$$\nabla \times \underline{E} + \partial_t \underline{B} = 0 \tag{12}$$

and

$$\nabla \times \underline{H} - \partial_t \underline{D} = \underline{J} \quad , \tag{13}$$

(e.g. Stratton, 1941, p. 2). In SI units the field quantities are: $\underline{E}$, the electric field strength in volts per metre (V/m); $\underline{B}$, the magnetic induction in teslas (T); $\underline{H}$, the magnetic field strength in amperes per metre (A/m); $\underline{D}$, the electric displacement in coulombs per square metre (C/m^2) and $\underline{J}$, the surface current density in amperes per square metre (A/m^2). In the neighbourhood of any point, the divergence of the current density must equal the net outflow of the free charge density within a small region surrounding the point. This conservation of charge is expressed through the continuity equation

$$\nabla \cdot \underline{J} + \partial_t \rho_e = 0 \quad , \tag{14}$$

where ρ_e is the free charge density (C/m^2).

By taking the curl of (12) and (13) and noting the vector identity $\nabla \cdot (\nabla \times \underline{A}) = 0$ for any vector $\underline{A}$, the following two equations are obtained,

$$\nabla \cdot \underline{B} = 0 \tag{15}$$

and

$$\nabla \cdot \underline{D} = \rho_e \quad . \tag{16}$$

Because of their derivation these equations are not independent of (12) and (13) and we still need three additional equations relating the five vectors. These are provided by the following constitutive relations for a linear isotropic medium,

$$\underline{D} = \epsilon \underline{E} \quad , \tag{17}$$

$$\underline{B} = \mu \underline{H} \tag{18}$$

and

$$\underline{J} = \sigma \underline{E} \quad , \tag{19}$$

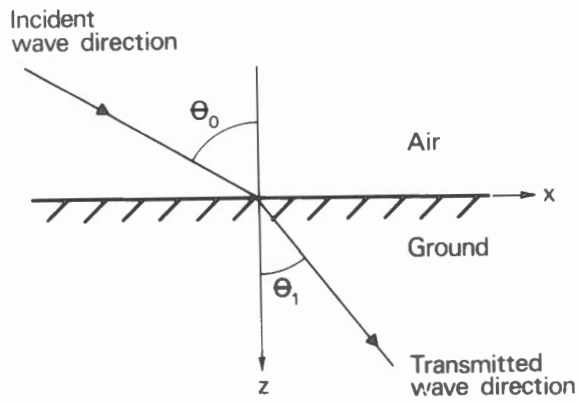

Figure 4a. *A Zenneck surface wave as a critically incident inhomogeneous plane wave. In air the incident wave varies as* $exp(+u_0 z)$, *where* u_0 *is the vertical wavenumber.*

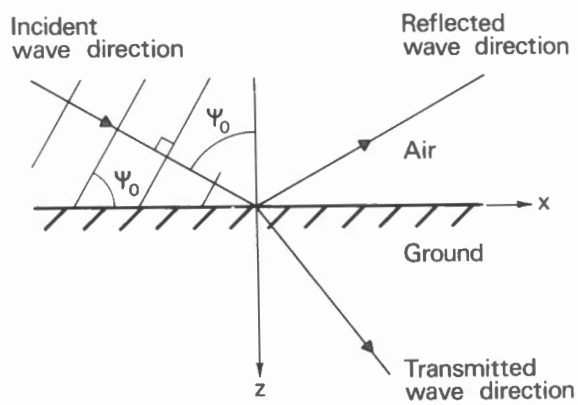

Figure 4b. *Inhomogeneous plane wave incident at the arbitrary angle* θ *which is taken to be the angle* ψ_0 *of the planes of constant phase. In air the incident wave varies as* $exp(-u_0 z)$.

in which ϵ is the absolute dielectric permittivity in farads per metre (F/m), μ is the absolute magnetic permeability in henries per metre (H/m) and σ is the electrical conductivity in siemens per metre (S/m). If the medium is anisotropic, then these material properties are tensors, and nonlinearities can be accounted for in some situations by allowing them to also be complex.

Within a conductor, there can be no free charges and so both $\underline{J}$ and $\underline{D}$ are solenoidal, i.e.

$$\nabla \cdot \underline{J} = 0 \tag{20}$$

and

$$\nabla \cdot \underline{D} = 0 \ . \tag{21}$$

Taking the curl of (12) and (13) yields

$$\nabla \times \nabla \times \underline{E} + \partial_t \ \nabla \times \underline{B} = 0$$

and

$$\nabla \times \nabla \times \underline{H} - \partial_t \ \nabla \times \underline{D} = \nabla \times \underline{J} \ .$$

We may now specify that ϵ, μ and σ are position independent within the particular volume of material considered, so that these two equations may be written as identical wave equations for the field intensities $\underline{E}$ and $\underline{H}$,

$$-\nabla \times \nabla \times \underline{E} + \nabla (\nabla \cdot \underline{E}) = \mu\sigma \ \partial_t \underline{E} + \epsilon\mu \ \partial_{tt} \underline{E} \tag{20a}$$

and

$$-\nabla \times \nabla \times \underline{H} + \nabla (\nabla \cdot \underline{H}) = \mu\sigma \ \partial_t \underline{H} + \epsilon\mu \ \partial_{tt} \underline{H} \tag{20b}$$

By virtue of (15) and (16), the second terms on the LHS are identically zero, but by introducing them we can use the following identity valid in rectangular Cartesian coordinates,

$$-\nabla \times \nabla \times \underline{A} + \nabla (\nabla \cdot \underline{A}) = \nabla^2 \underline{A} = \partial_{xx} A_x + \partial_{yy} A_y + \partial_{zz} A_z$$

where $\nabla^2 \underline{A}$ is the vector Laplacian of a vector $\underline{A}$ with components (A_x, A_y, A_z). A more compact form of the vector Helmholtz equations (20a) and (20b) is then

$$\nabla^2 \underline{E} = \gamma^2 \underline{E} \tag{21a}$$

and

$$\nabla^2 \underline{H} = \gamma^2 \underline{H} \ , \tag{21b}$$

in which

$$\gamma^2 = i\omega\mu\sigma - \omega^2\epsilon\mu \tag{22}$$

is the propagation constant of the medium (m^{-2}). It is assumed that all field vectors have a harmonic time dependence $e^{i\omega t}$, where ω is the angular frequency, and that $Re\ (\gamma) \geq 0$. This frequency domain representation is still appropriate for irregular MT fields by virtue of the Fourier integral theorem. For example, an arbitrary time domain electric field can be written

$$\underline{E}(\underline{r}, t) = \int_{-\infty}^{\infty} E(\underline{r}, \omega) \ e^{i\omega t} \ d\omega \tag{23}$$

where $\underline{r}$ is a position vector and $\underline{E}(\underline{r}, \omega)$ satisfies (21a).

With the above development, equations (12) and (13)

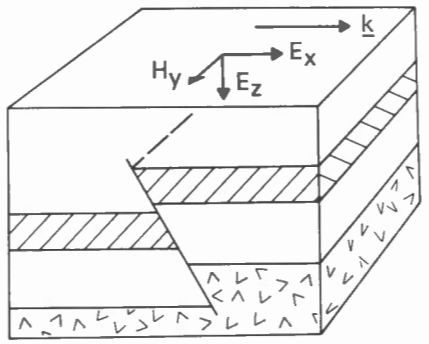

a) H - polarization

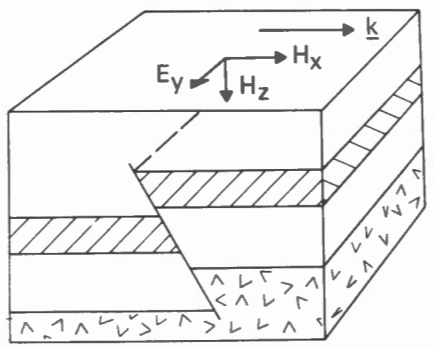

b) E - polarization

Figure 5. *EM field components where polarization is parallel to geological strike.*

can be simplified to

$$\underline{H} = -\frac{1}{i\omega\mu} \ \nabla \times \underline{E} \tag{24}$$

and

$$\underline{E} = \frac{1}{\sigma + i\omega\epsilon} \nabla \times \underline{H} \ . \tag{25}$$

The ratio of any component of electric field E_i to a component of magnetic field H_j (i,j = x , y , z) is a complex tensor quantity known as the wave impedance

$$Z_{ij} = \frac{E_i}{H_j} \ , \tag{26}$$

whose amplitude and phase are diagnostic of the electrical and magnetic properties of the medium. A related quantity of interest is the wavetilt, defined as the ratio of horizontal to vertical electric or magnetic components of the wave

$$W_{iz} = \frac{E_i}{E_z} \quad \text{or} \quad \frac{H_i}{H_z} \tag{27}$$

where (i = x , y).

Considerable simplification will ensue if the geophysical situation is assumed two dimensional such that we may ignore all spatial variations in one direction, e.g. $\partial_y(\ ) = \partial_{yy}(\ ) = 0$. For practical purposes, this direction should coincide with the strike direction of local geological features. A furthur assumption, which affects only the

orientation of the (right-handed) coordinate system, is that the electric field component is to be either normal to the strike direction (called H-polarization) or parallel to the strike direction (called E-polarization), as shown in Figure 5. As mentioned earlier, MT signals can be of either polarization, whereas the VLF-LF signals of a vertical electric dipole are H-polarized. This is contrary to the field of a long electrical wire source used in EM induction methods, which is E-polarized. The field components for these two cases are then for H-polarization,

$$\left.\begin{aligned} \underline{H} &= H_y \hat{j} \\ \underline{E} &= E_x \hat{i} + E_z \hat{k} \\ (\partial_{xx} + \partial_{zz})\, H_y &= \gamma^2 H_y \\ E_x &= -\frac{1}{\sigma + i\omega\epsilon}\, \partial_z H_y \\ E_z &= \frac{1}{\sigma + i\omega\epsilon}\, \partial_x H_y \end{aligned}\right\} \qquad (28)$$

and E-polarization,

$$\left.\begin{aligned} \underline{E} &= E_y \hat{j} \\ \underline{H} &= H_x \hat{i} + H_z \hat{k} \\ (\partial_{xx} + \partial_{zz})\, E_y &= \gamma^2 E_y \\ H_x &= \frac{1}{i\omega\mu}\, \partial_z E_y \\ H_z &= \frac{1}{i\omega\mu}\, \partial_x E_y \end{aligned}\right\} \qquad (29)$$

The next step is to seek a solution for the single field components H_y or E_y. In rectangular Cartesian coordinates, the most general solution of the scalar Helmholtz equation

$$(\nabla^2 - \gamma^2)\, \Psi = 0$$

is the function

$$\Psi = (c_1 e^{-uz} + c_2 e^{uz})(c_3 e^{-kx} + c_4 e^{kx})$$

where $\partial_y (\ ) = 0$ and the vertical and horizontal wavenumbers, u and k respectively, satisfy

$$u^2 + k^2 = \gamma^2$$

Again we assume $\mathrm{Re}\,(u) \geq 0$, $\mathrm{Re}\,(k) \geq 0$. There is no loss of generality by taking the direction of propagation of the polarized wave Ψ to be in the +ve x direction, so that c_4 must be set to zero to prevent an exponentially divergent solution. From (28) and (29) we therefore can write

$$H_y = (A e^{-uz} + B e^{uz})\, e^{-kx} \qquad (30a)$$

or

$$E_y = (A e^{-uz} + B e^{uz})\, e^{-kx} \qquad (30b)$$

as the most general solutions of the H- and E-polarization cases respectively.

Boundary Conditions

The constants A and B have to be determined by examining the boundary conditions for the fields. These can in general be expressed as two equations of continuity in tangential $\underline{E}$ and normal $\underline{B}$,

$$\hat{\underline{n}} \times (\underline{E}_2 - \underline{E}_1) = 0 \qquad (31)$$

and

$$\hat{\underline{n}} \cdot (\underline{B}_2 - \underline{B}_1) = 0 \qquad (32)$$

and two conditions on tangential $\underline{H}$ and normal $\underline{D}$, which introduce a possible current density $\underline{J}_s$ or surface charge density ρ_s,

$$\hat{\underline{n}} \times (\underline{H}_2 - \underline{H}_1) = \underline{J}_s \qquad (33)$$

and

$$\hat{\underline{n}} \cdot (\underline{D}_2 - \underline{D}_1) = \rho_s \qquad (34)$$

The suscripts 1 and 2 indicate different media and $\hat{\underline{n}}$ is a unit vector normal to the surface.

Should both media have finite conductivity, then $\underline{J}_s$ unequivocally vanishes as Stratton (1941, p. 37) shows. On the other hand, when both media are dielectrics, the free surface charge density ρ_s vanishes (e.g. Lorrain and Corson, 1970, p. 140). It follows that at the air-ground interface and at boundaries between conducting regions in the Earth, we cannot guarantee ρ_s is zero. An alternative general boundary condition can be derived from the equation for continuity of flow of charge across any surface, i.e. from (14),

$$\hat{\underline{n}} \cdot (\underline{J}_2 - \underline{J}_1) = -\partial_t \rho_s \qquad (35)$$

It is now possible to avoid consideration of ρ_s by eliminating it from (34) and (35). We have

$$\hat{\underline{n}} \cdot (\epsilon_2 \underline{E}_2 - \epsilon_1 \underline{E}_1) = \rho_s$$

and

$$\hat{\underline{n}} \cdot (\sigma_2 \underline{E}_2 - \sigma_1 \underline{E}_1) = -i\omega\rho_s \ .$$

Stratton (1941, p. 483) shows that these equations imply either the unlikely condition $\rho_s = 0$ and

$$\sigma_1\epsilon_2 - \sigma_2\epsilon_1 = 0$$

or, more reasonably, that $\rho_s \neq 0$ and

$$\hat{\underline{n}} \cdot \left[(\sigma_2 + i\omega\epsilon_2)\underline{E}_2 - (\sigma_1 + i\omega\epsilon_1)\underline{E}_1\right] = 0 \ . \qquad (36)$$

We may therefore summarize the boundary conditions as requiring continuity of normal $(\mu H\ ,\ (\sigma + i\omega\epsilon\ )\underline{E})$ and transverse $(\underline{E}, \underline{H})$. When applied to the two possible polarisations of the wavefield, these conditions become for H-polarization:

continuity of H_y, E_x and $(\sigma + i\omega\epsilon)E_z$ (37)

and E-polarization:

continuity of E_y, H_x and μH_z (38)

across any boundary.

HORIZONTALLY STRATIFIED MEDIA; H-POLARIZATION

We now follow the general formulation of Wait (1962) in considering an M-layered, horizontally stratified Earth model, in which the incident wave is H-polarized and at an angle θ to the normal (Fig. 6). In a typical m'th layer, the electrical and magnetic properties given by ϵ_m, μ_m and σ_m are assumed isotropic and homogeneous. The layer is bounded by the depths z_{m-1} and z_m and so has a thickness h_m of material in which the magnetic field component satisfies

$$(\nabla^2 - \gamma_m^2) H_{my} = 0 \quad , m = 0,1 \ldots M \tag{39}$$

where

$$\gamma_m^2 = i\omega\mu_m\sigma_m - \omega^2\epsilon_m\mu_m \quad , \tag{40a}$$

$$\gamma_0^2 = -\omega^2\epsilon_0\mu_0 \tag{40b}$$

and $Re(\gamma_m) \geq 0$ as before. We first consider the implication of the boundary condition (37) which, using (28) and (30a), leads to continuity of

$$(\sigma + i\omega\epsilon) E_z = \partial_x H_y = -k H_y \quad .$$

It is clear that because H_y is continuous across a boundary, k must be the same for all layers. The magnetic field component can then be written

$$H_{my} = (A_m e^{-u_m z} + B_m e^{u_m z}) e^{-kx} \tag{41}$$

where

$$u_m^2 = \gamma_m^2 - k_m^2 \quad . \tag{42}$$

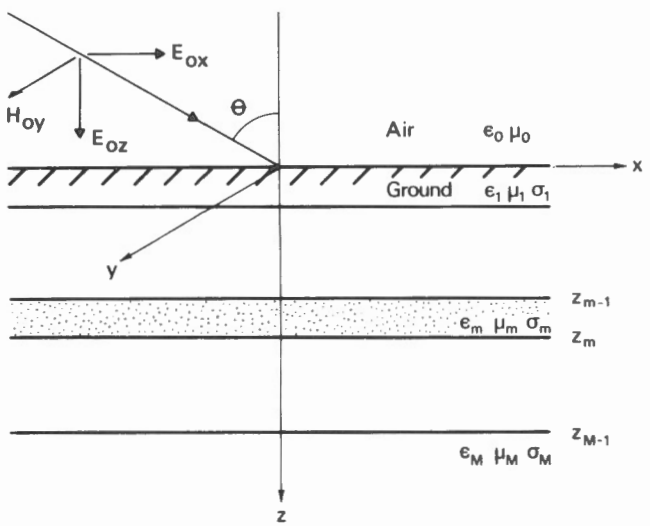

Figure 6. *Horizontally stratified Earth model.*

Using (27), it follows that

$$E_{mx} = \frac{u_m}{\sigma_m + i\omega\epsilon_m} (A_m e^{-u_m z} - B_m e^{u_m z}) e^{-kx} \tag{43}$$

and

$$E_{mz} = \frac{-k}{\sigma_m + i\omega\epsilon_m} (A_m e^{-u_m z} + B_m e^{u_m z}) e^{-kx} \quad . \tag{44}$$

The surface wave impedance at the top of the m'th layer is then

$$Z_m = \frac{E_{mx}}{H_{my}}\bigg|_{z_{m-1}} = \frac{E_{m-1,x}}{H_{m-1,y}}\bigg|_{z_{m-1}}$$

which is continuous across the interface (relation (37)). Using (41) and (43), we find

$$Z_m = K_m \frac{A_m e^{-u_m z_{m-1}} - B_m e^{u_m z_{m-1}}}{A_m e^{-u_m z_{m-1}} + B_m e^{u_m z_{m-1}}} \quad , \tag{45}$$

where

$$K_m = \frac{u_m}{\sigma_m + i\omega\epsilon_m} \tag{46}$$

is a modified propagation constant for the m'th layer. At the bottom of the m'th layer we can write in a similar fashion

$$Z_{m+1} = \frac{E_{mx}}{H_{my}}\bigg|_{z_m} = K_m \frac{A_m e^{-u_m z_m} - B_m e^{u_m z_m}}{A_m e^{-u_m z_m} + B_m e^{u_m z_m}} \tag{47}$$

which enables A_m/B_m to be eliminated from (45). The result is

$$Z_m = K_m \frac{Z_{m+1} + K_m \tanh(u_m h_m)}{K_m + Z_{m+1} \tanh(u_m h_m)} \quad , m = 1,2,\ldots M-1 \tag{48}$$

where in addition, for $m = M$,

$$Z_M = K_M \quad . \tag{49}$$

This last relation arises from the condition that H_{my} must be finite as $z \to \infty$ in the last layer, so that $B_M = 0$. The constancy of the horizontal wavenumber k then requires the M equations

$$\gamma_m^2 - u_m^2 = \gamma_{m+1}^2 - u_{m+1}^2 \quad ; \quad m = 0,1,\ldots M-1 \, . \tag{50}$$

There are (2M+1) relations in (48)-(50) which are sufficient to solve for the (2M+1) unknowns $u_0, u_1, \ldots u_m$, $Z_0, Z_1, \ldots Z_M$, and, except in the special case $M = 1$, these relations are independent. As can be imagined, an analytic solution is virtually impossible to obtain due to the non-linearity of the $\tanh(u_m h_m)$ and $\gamma_m^2 - u_m^2$ functions unless certain simplifications are made. It can be shown (e.g. Keller and Frischknecht, 1966, p. 304) that in all cases of interest, the vertical and horizontal wavenumbers in air are given by the expressions

$$u_0 = \gamma_0 \cos\theta \tag{51}$$

and

$$k = \gamma_0 \sin\theta \quad , \tag{52}$$

where θ is interpreted as a real angle (equation (11)). Therefore by specifying θ, u_0 and k are known. This immediately simplifies (50) and allows u_m to be computed independently of $Z_1, Z_2, \ldots Z_M$.

At this point we evaluate the wavetilt for H-polarization. From (27), we deduce the wavetilt in the mth layer to be

$$W_m(z) = \frac{E_{mx}}{E_{mz}} \quad , \quad m = 0,1,\ldots M-1 \tag{53}$$

which at the top of an interface can be evaluated as

$$W_m = \left(\frac{\sigma_m + i\omega\epsilon_m}{\sigma_{m+1} + i\omega\epsilon_{m+1}}\right) \left.\frac{E_{m+1,x}}{E_{m+1,z}}\right|_{z_m}$$

using (37). The wavetilt in air at the air-ground interface is then

$$W_0 = \frac{i\omega\epsilon_0}{\sigma_1 + i\omega\epsilon_1} \left.\frac{E_{1x}}{E_{1z}}\right|_{z=0} \tag{54}$$

which reduces to

$$W_0 = -\frac{i\omega\epsilon_0}{\gamma_0 \sin\theta} Z_1 \tag{55}$$

using (43), (44), (45) and (52).

NEGLECT OF DISPLACEMENT CURRENTS

General Expressions

Generally an approximation is now made whereby the displacement currents are ignored in comparison with the conduction currents. This is a valid assumption provided the parameter

$$\nu_m = \frac{\omega\epsilon_m}{\sigma_m} \ll 1 \quad , \quad m = 1,2,\ldots M \tag{56}$$

in which case

$$\gamma_m^2 \approx i\omega\mu_m\sigma_m \tag{57}$$

and $K_m \approx u_m/\sigma_m$. This simplification immediately enables a solution to be found regardless of the value of θ because

$$u_m^2 \approx i\omega\mu_m\sigma_m + \omega^2\epsilon_0\mu_0 \sin^2\theta$$

using (42) and (52), which further reduces to

$$u_m^2 \approx i\omega\mu_m\sigma_m \tag{58}$$

by a slight extension of (56).

Proceeding in a standard fashion, we can define a stratification or correction factor

$$Q_m = \frac{Z_m}{K_m} = \left(i\omega\mu_m\rho_m\right)^{-\frac{1}{2}} Z_m \quad , \tag{59}$$

where ρ_m is the resistivity (Ω . m) defined as $1/\sigma_m$. The complete M-layer solution can now be written

$$Z_1 = \left(i\omega\mu_1\rho_1\right)^{\frac{1}{2}} Q_1 \tag{60a}$$

in which

$$Q_m = \frac{\beta_m Q_{m+1} + \tanh\left(\alpha_m\sqrt{i}\right)}{1 + \beta_m Q_{m+1} \tanh\left(\alpha_m\sqrt{i}\right)} \quad , \tag{60b}$$

$$m = 1,2\ldots M-1$$

and

$$Q_M = 1 \quad . \tag{60c}$$

We have defined

$$\alpha_m = |u_m| h_m = \left(\omega\mu_m\sigma_m\right)^{\frac{1}{2}} h_m \tag{61}$$

and

$$\beta_m = \sqrt{\frac{\rho_{m+1}}{\rho_m}} \quad . \tag{62}$$

Homogeneous Ground

For homogeneous ground M=1 and the second and third equations of (60) are identical. We can then introduce an apparent resistivity

$$\rho_a = \frac{1}{\omega\mu_1} |Z_1|^2 = \rho_1 \tag{63}$$

and phase

$$\varphi = \arg Z_1 = \pi/4 \quad , \tag{64}$$

which determines the amount by which H_y lags E_x in a cycle. Even when the ground is not homogeneous, the quantities ρ_a and φ can continue to be defined by

$$\rho_a = \frac{1}{\omega\mu_1} |Z_1|^2 = \rho_1 |Q_1|^2 \tag{65}$$

and

$$\varphi = \arg Z_1 = \pi/4 + \arg Q_1 \quad . \tag{66}$$

In fact the Geonics EM16R is calibrated to read out ρ_a and φ directly, under the assumption that $\mu_1 = \mu_0$.

In any layer of the ground with reasonably high conductivity such that (56) holds, the electromagnetic skin depth is defined as

$$\delta_m = \sqrt{\frac{2}{\omega\mu_m\sigma_m}} = \sqrt{2}\ \frac{h_m}{\alpha_m} \tag{67}$$

If, for example, in the upper layer $\delta_1 > h_1$ ($\alpha_1 < \sqrt{2}$), then the surface impedance Z_1 is significantly perturbed by the properties of the lower layers. However, if $\delta_1 < h_1$ ($\alpha_1 > \sqrt{2}$), then the lower layers will be largely hidden by the first layer.

Using (56), the tilt angle for homogeneous ground is

$$W_0 = \frac{-1}{\sin\theta} \left(\frac{i\omega\mu_1\epsilon_0\rho_1}{\mu_0}\right)^{\frac{1}{2}} \tag{68}$$

which has a magnitude

$$|W_0| = \frac{1}{\sin\theta} \left(\frac{\omega\mu_1\epsilon_0\rho_1}{\mu_0}\right)^{\frac{1}{2}} \tag{69}$$

and phase angle -

$$\arg W_0 = 5\pi/4 \quad . \tag{70}$$

It can be seen that for any horizontally-layered model,

$$\rho_a = \frac{\mu_0 \sin^2\theta\, |W_0|^2}{\omega \mu_1 \epsilon_0} \tag{71}$$

implying that θ has to be assumed known, whereas

$$\varphi = \arg W_0 - \pi \tag{72}$$

is independent of θ. The tilt angle at any height ($-|z|$) above the air-ground interface can be expressed in terms of W_0 through the expression

$$W_0(z) = \frac{W_0 + \cot\theta \tanh(u_0 z)}{1 + W_0 \tan\theta \tanh(u_0 z)} \tag{73}$$

where $u_0 = i\omega\sqrt{\mu_0\epsilon_0}\cos\theta$ as before. Far above the ground, it can be assumed $\tanh(u_0 z) \to 1$ (provided $\theta \neq 90°$) and so

$$W_0(z) \approx \cot\theta \tag{74}$$

Two-Layer Model

A very common simplification of actual field conditions is to assume a single layer resting on an infinite half space. In this case M = 2 and equations (60) reduce to

$$\left.\begin{aligned} Z_1 &= (i\omega\mu_1\rho_1)^{\frac{1}{2}}\, Q_1 \\ \text{and} \\ Q_1 &= \frac{\beta_1 + \tanh(\alpha_1\sqrt{i})}{1 + \beta_1 \tanh(\alpha_1\sqrt{i})} \\ \text{in which} \\ \alpha_1 &= (\omega\mu_1\sigma_1)^{\frac{1}{2}}\, h_1 \\ \text{and} \\ \beta_1 &= \sqrt{\frac{\rho_2}{\rho_1}} \end{aligned}\right\} \tag{75}$$

Equivalent expressions for Q_1 found in the literature are

$$Q_1 = \tanh\left(\alpha_1\sqrt{i} + \tanh^{-1}\beta_1\right) ,$$

(Wait, 1962, p. 15) and

$$Q_1 = \coth\left(\alpha_1\sqrt{i} + \coth^{-1}\beta_1\right) ,$$

(Keller and Frischknecht, 1966, p. 218). Resolving Q_1 into its magnitude and phase components:

$$|Q_1|^2 = \frac{e^{2p} + 2q\, e^p \cos p + q^2}{e^{2p} - 2q\, e^p \cos p + q^2} \tag{76}$$

and

$$\arg Q_1 = \tan^{-1}\left(\frac{2q\, e^p \sin p}{q^2 - e^{2p}}\right) \tag{77}$$

where

$$p = \sqrt{2}\,\alpha_1 \tag{78}$$

and

$$q = \frac{\beta_1 - 1}{\beta_1 + 1} . \tag{79}$$

From (61) and (62), we find

$$\rho_a = \rho_1\left(\frac{e^{2p} + 2q\, e^p \cos p + q^2}{e^{2p} - 2q\, e^p \cos p + q^2}\right) \tag{80}$$

and

$$\varphi = \tan^{-1}\left(\frac{e^{2p} - 2q\, e^p \sin p - q^2}{e^{2p} + 2q\, e^p \sin p - q^2}\right) . \tag{81}$$

THE DIELECTRIC EFFECT

Dielectric Hysteresis

Certainly at MT frequencies the approximation (56) is sufficiently good that the expressions derived in the last section can be applied to the data without error. At VLF-LF frequencies, however, the impedance Z_1 may have to be corrected for dielectric effects if the ground is very resistive.

In a dielectric medium at high frequency, there may be appreciable energy loss due to a hysteresis effect similar to that in permeable media which results in an added contribution to the ohmic conductivity. To see this, we introduce the device of a complex dielectric constant

$$\epsilon = \epsilon' - i\epsilon'' , \tag{82}$$

where, for the Debye model,

$$\epsilon' = \epsilon_0\left(1 + \frac{a(\omega_0^2 - \omega^2)}{(\omega^2 - \omega_0^2)^2 + b^2\omega^2}\right) \tag{83}$$

and

$$\epsilon'' = \epsilon_0\left(\frac{ab\omega}{(\omega^2 - \omega_0^2)^2 + b^2\omega^2}\right) \tag{84}$$

are real quantities (Kraus and Carver, 1973, p. 334). The parameters a and b are equal to ($Nq^2/\epsilon_0 m$) and ξ/m respectively (N = number of polarized atoms per unit volume, q = dipole charge, m = atomic mass, ξ = damping coefficient and ω_0 is the dipole resonant frequency). The constitutive relations (17) and (19), when substituted into (13), yield

$$\nabla \times \underline{H} = (\sigma + i\omega\epsilon)\,\underline{E} \tag{85a}$$

or

$$\nabla \times \underline{H} = (\sigma' + i\omega\epsilon')\,\underline{E} , \tag{85b}$$

so that the total current density is due to both displacement and conductive currents. In (85b) the equivalent or effective conductivity of the medium is

$$\sigma' = \sigma + \omega\epsilon'' \tag{86}$$

combining true ohmic conductivity with the dielectric hysteresis which masquerades as a conduction term. From (84) and (86), we may therefore express the resistivity as

a function of frequency:

$$\rho = \left(\sigma + \frac{a\,b\,\epsilon_0\,\omega^2}{(\omega^2-\omega_0^2)^2+b^2\omega^2}\right)^{-1} \qquad (87)$$

which reduces to

$$\rho \approx \frac{1}{\sigma}\left(1-\frac{a\,b\,\epsilon_0\,\omega^2}{\sigma\omega_0^4}\right) \qquad (88)$$

for low frequencies.

The loss tangent of the medium is often quoted as

$$\ell.t. = \frac{\sigma}{\omega\epsilon} \quad , \qquad (89a)$$

which is just $1/\nu$ from (56). However, the ratio of conduction current density to displacement current density in equation (86) leads to a preferred definition

$$\ell.t. = \frac{\sigma'}{\omega\epsilon'} \quad , \qquad (89b)$$

because σ' and ϵ' are then real quantities at all frequencies. In practise σ' cannot be distinguished from σ, and, provided a measurement of ϵ yields its real part ϵ', the above distinction is academic. The frequency dependence of the loss tangent follows from the particular model chosen, e.g. from (83) and (84), the limits are

$$\left.\begin{array}{l} \omega \to 0 \;\; ; \;\; \epsilon' \to \epsilon_0\left(1+\frac{a}{\omega_0^4}\right); \epsilon'' \to 0 \;\; ; \;\; \ell.t. \to \infty \\ \omega \to \infty \;\; ; \;\; \epsilon' \to \epsilon_0 \qquad\quad ; \epsilon'' \to 0 \;\; ; \;\; \ell.t. \to 0 \end{array}\right\} (90)$$

Measured loss tangents generally decrease with frequency (e.g. Olhoeft, 1975).

Skin Depth

Another consequence of retaining the displacement current is a modification of the electromagnetic skin depth δ in (67). The propagation constant

$$\gamma_m^2 = i\omega\mu_m(\sigma_m + i\omega\epsilon_m)$$

is assumed to have real and imaginary parts

$$\gamma_m = \gamma_r + i\gamma_i \qquad (91)$$

where, from elementary analysis of a wave which propagates as $e^{i\omega t}$, it is clear that the skin depth is just

$$\delta_m = \frac{1}{\gamma_r} \quad . \qquad (92)$$

It can be easily shown that

$$\gamma_r = \omega\sqrt{\frac{\mu_m\epsilon_m}{2}}\left[\left(1+\frac{1}{\nu_m^2}\right)^{\frac{1}{2}}-1\right]^{\frac{1}{2}} \qquad (93)$$

and

$$\gamma_i = \omega\sqrt{\frac{\mu_m\epsilon_m}{2}}\left[\left(1+\frac{1}{\nu_m^2}\right)^{\frac{1}{2}}+1\right]^{\frac{1}{2}} \quad , \qquad (94)$$

from which δ_m can be deduced to be

$$\delta_m = \sqrt{\frac{2}{\mu_m\sigma_m\omega}}\left[(1+\nu_m^2)^{\frac{1}{2}}-\nu_m\right]^{\frac{1}{2}} \quad . \qquad (95)$$

At low frequencies, $\nu_m \ll 1$, the loss tangent is large and the approximations of the previous section are derived. At high frequencies, however, equations (93) and (94) are not phenomenologically correct unless we replace ϵ_m and σ_m by ϵ_m' and σ_m' as in (82) and (86). The true variation of δ_m with frequency must therefore include equations (83) and (84) or equivalent for the dielectric model used. We will not pursue these subtleties further at this stage but rather will go on to indicate how ρ_a and φ might be affected to first approximation by displacement currents.

Variation of ρ_a , φ

For homogeneous ground

$$Z_1 = K_1 = \frac{u_1}{\sigma_1 + i\omega\epsilon_1} \quad ,$$

from (46) and (49), so that we need to find u_1. From (50) and (51),

$$u_1^2 = \gamma_1^2 - \gamma_0^2\sin^2\theta \quad ,$$

indicating u_1 will now depend on θ and thus the mode of propagation. We find without approximation that

$$\rho_a = \rho_1\,\frac{1}{1+\nu_1^2}\left[1+\nu_1^2(1-e)^2\right]^{1/2} \qquad (96)$$

and

$$\varphi = \tan^{-1}\left\{\frac{\left[1+\nu_1^2(1-e)^2\right]^{1/2}-\nu_1 e}{1+\nu_1\left(\left[1+\nu_1^2(1-e)^2\right]^{1/2}+\nu_1(1-e)\right)}\right\} \qquad (97)$$

in which

$$e = \frac{\mu_0\epsilon_0}{\mu_1\epsilon_1}\sin^2\theta. \qquad (98)$$

There are two limiting conditions, the first of which occurs when $e \approx 0$ as a result of vertical incidence ($\theta = 0°$) or when either μ_0/μ_1 or ϵ_0/ϵ_1 is small. Equations (9) and (9) reduce to

$$\rho_a = \frac{\rho_1}{(1+\nu_1^2)^{1/2}} \qquad (99)$$

and

$$\varphi = \tan^{-1}\left\{(1+\nu_1^2)^{\frac{1}{2}} - \nu_1\right\} \qquad (100)$$

i.e.

$$\rho_a \approx \rho_1\left(1-\frac{\nu_1^2}{2}\right)$$

and

$$\varphi \approx \pi/4 - \nu_1/2 \quad ,$$

for small ν_1.

On the other hand, if $e \approx 1$ e.g. as a result of parallel incidence ($\theta = 90°$) over a half space with no dielectric or permeability inhomogeneities ($\epsilon_1 = \epsilon_0$, $\mu_1 = \mu_0$), then

$$\rho_a = \frac{\rho_1}{1+\nu_1^2} \qquad (101)$$

and

$$\varphi = \tan^{-1}\left\{\frac{1-\nu_1}{1+\nu_1}\right\} \quad , \qquad (102)$$

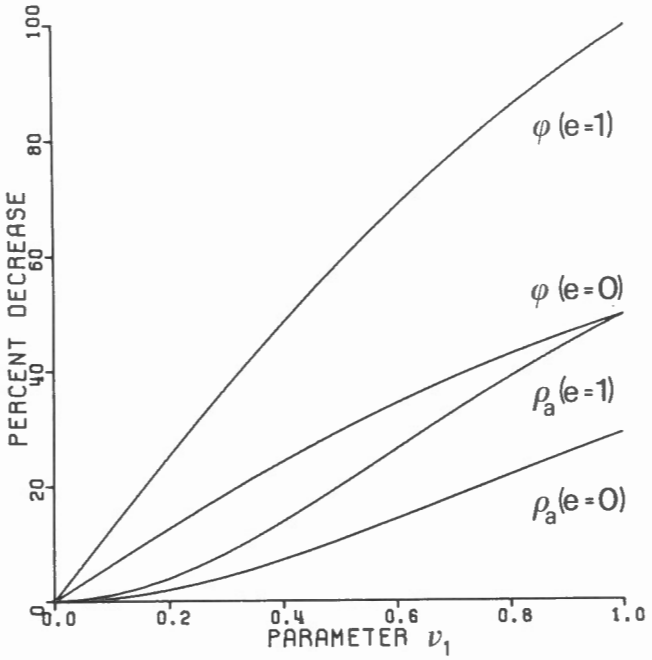

Figure 7. *Decrease in* ρ_a *and* φ *as a function of the parameter* $\nu_1 = \omega\epsilon_1\rho_1$ *for two values of* e = *0, 1.*

i.e.

$$\rho_a \approx \rho_1 \ (1 - \nu_1^2)$$

and

$$\varphi \approx \pi/4 - \nu_1 \ ,$$

for small ν_1 . We see that, in general, the phase angle is much more sensitive than ρ_a to dielectric properties of the half space.

Just how large can ν_1 become in reality? For a typical VLF station at 20 kHz, a surface resistivity of $\rho_1 = 10^5$ Ω.m will yield $\nu_1 = 0.1$ for a relative dielectric constant of ~10. At this level, the percentage decrease in either ρ_a or φ can be quite significant, as shown in Figure 7. Most rocks capable of resistivities of 10^5 Ω.m show dielectric constants less than 10 (Telford et al., 1976, Ch. 5), and, even though this may be increased by adding water, the conductivity would then also increase considerably. At high frequencies the reduction in resistivity due to a complex dielectric constant, equation (76), must also be taken into account. For a layered ground the original equations (48) and (49) should be solved iteratively for Z_M , Z_{M-1} ,... Z_1 , with

$$u_m^2 = \gamma_m^2 - \gamma_0^2 \sin^2\theta \qquad (103)$$

replacing (50). Further details are discussed by Sinha (1977).

E-POLARIZATION

For the MT method, E-polarization is just as likely as H-polarization, and we therefore replace (41) with

$$E_{my} = \left(A_m e^{-u_m z} + B_m e^{u_m z}\right) e^{-kx} \ , \qquad (104)$$

and thus, from (29)

$$H_{mx} = -\frac{u_m}{i\omega\mu_m}\left(A_m e^{-u_m z} - B_m e^{u_m z}\right) e^{-kx} \qquad (105)$$

and

$$H_{mz} = \frac{k}{i\omega\mu_m}\left(A_m e^{-u_m z} + B_m e^{u_m z}\right) e^{-kx} \ . \qquad (106)$$

Again the equality of k in all layers is guaranteed through (38) and we may define a new surface impedance

$$Z_m = \left.\frac{E_{my}}{H_{mx}}\right|_{z_{m-1}} = J_m \frac{A_m e^{-u_m z} - B_m e^{u_m z}}{A_m e^{-u_m z} + B_m e^{u_m z}} \ ,$$

where

$$J_m = -\frac{i\omega\mu_m}{u_m} \ .$$

Proceeding as before, we find

$$Z_m = J_m \frac{Z_{m+1} + J_m \tanh(u_m h_m)}{J_m + Z_{m+1}\tanh(u_m h_m)} \ , \qquad (107)$$

$$m = 1, 2, \ldots M-1$$

and

$$Z_M = J_M \ , \qquad (108)$$

where u_m is given by (50). At MT frequencies we may immediately assume the condition (56) and so it follows that instead of (59) we have

$$Q_m = \frac{Z_m}{J_m} \approx (i\omega\mu_m\rho_m)^{\frac{1}{2}} Z_m \ , \qquad (109)$$

exactly as before. Thereafter the rest of the equations (60)-(81) all apply to the E-polarization case. Numerical computations of the amplitude and phase of the wavetilt for the E-polarization case were presented by Singh and Lal (1981).

VLF INTERPRETATION

Measurements

The measurement of complex wavetilt at any aircraft altitude via equations (71)-(73) can in principle be used to deduce the apparent resistivity and phase angle between the E_x and H_y surface fields. In instruments such as the Barringer E-phase system, for practical reasons, only the quadrature phase component of the wavetilt is determined by measuring the E_x and E_z fields using dipole antennas (Hoekstra et al., 1975). Only one independent parameter of the model can then be determined for each frequency at which transmission can be received. As implied before, the VLF frequencies are so closely spaced that the only practical advantage in using more than one transmitter is to investigate anisotropy in the ground resistivity. Usually, it is the apparent resistivity, computed via (71), which serves as the parameter interpreted from these instruments, and this averages in some sense the actual ground resistivity both laterally and also vertically to a depth equivalent to several electromagnetic skin depths (at the VLF transmitted frequency). Contour plots of ρ_a can then be correlated with geological structure (e.g. Hoekstra et al., 1975), but they do not readily lead to a quantitative interpretation.

Modified ground instruments such as the Geonics EM16R have a pair of current electrodes 10 m apart which, through contact with the ground, are capable of reliably determining E_x in addition to H_y determined by a coil. Then (ρ_a , φ) are obtained at one frequency, which allows two independent parameters of the model to be found at any location. Usually ρ_a is measurable to within ±10% accuracy and φ to within ±1°, or maybe ±0.5° under very favourable conditions. For homogeneous ground the phase angle equals 45° and therefore any departure from this value in the field is generally taken as an indication of resistivity inhomogeneity. This need not be the case if there is structure at or greater than the skin depth, i.e. when $\alpha_1 > \sqrt{2}$, as can be seen in Figures 8 and 9 which show the magnitude and phase of Q_1 plotted as functions of α_1 for a range of values for β_1 . Even if ρ_1 is constant, there may be departures of ϵ_1 and μ_1 from their free-space values, which could lead to phase angles of less than 45°, as discussed above. The curves for three-layer models (e.g. Mathieson and Crossley, 1981-IV) also indicate that φ = 45° for certain combinations of the layer resistivities and thicknesses, even when $\alpha_1 > \sqrt{2}$. One would prefer to have reliable geological information before resorting to these alternative ways of interpreting a phase angle of 45°.

Two-Layer Model

The two-layer model has traditionally been assumed to contain three independent parameters ρ_1 , h_1 and ρ_2 , but one might wish to extend the number to seven by including ϵ_1 , μ_1 , ϵ_2 and μ_2 as unknowns. Even with three parameters (ρ_1 , h_1 , ρ_2) the model is ambiguous, as only two data values (ρ_a , φ) are available at any one frequency. We therefore should consider the possible assumptions that may be made concerning the interpretation.

From a practical point of view the most useful two parameters of a two-layer model are h_1 and ρ_1/ρ_2 (or β_1). Unfortunately the measured quantities $|Z_1|$ and $\arg Z_1$, which lead to ρ_a and φ via equations (65) and (66), cannot be written in terms of h_1 and β_1 alone because the quantity α_1 (necessary to compute the factor Q_1) contains the product $h_1/\sqrt{\rho_1}$. As a result, it appears impossible to resort to a single set of type-curves, i.e. (ρ_a , φ) against α_1 and β_1 , and for this reason we briefly consider two popular alternative assumptions, which are treated more fully in Jones and Telford (1981-III) and Powell and Jensen (1981-II). A single set of curves is nonetheless feasible for the two-layer case, as demonstrated by Mathieson and Crossley (1981-IV), provided one of the following two cases is assumed. We will ignore values of $\alpha_1 > \sqrt{2}$ as the phase $\varphi \approx \pi/4$ ($\arg Q_1 \approx 0$) which leads to a difficult interpretation problem.

Case A: ρ_1 assumed known

The amplitude $|Q_1|$ is known from ρ_a via the equation

$$\rho_a = \rho_1 |Q_1|^2 \quad ,$$

so that in Figure 8 one can uniquely relate a specified value of β_1 with a known α_1 . Also $\arg Q_1$ is known from

$$\varphi = \pi/4 + \arg Q_1$$

and one then obtains, from Figure 9, two possible values of α_1 for each β_1 selected. Comparing these with values (α_1 , β_1) from Figure 8, it should be possible to uniquely identify (α_1 , β_1) and hence h_1 and ρ_2 . If no agreement between the parameters can be found, then perhaps one should seek a solution for a different choice of ρ_1 (which could be found independently by a small-scale DC resistivity survey). Failing this, the model is inappropriate, and the choice is then one of including additional parameters (ϵ_1 , μ_1 , ϵ_2 , μ_2) or a third layer.

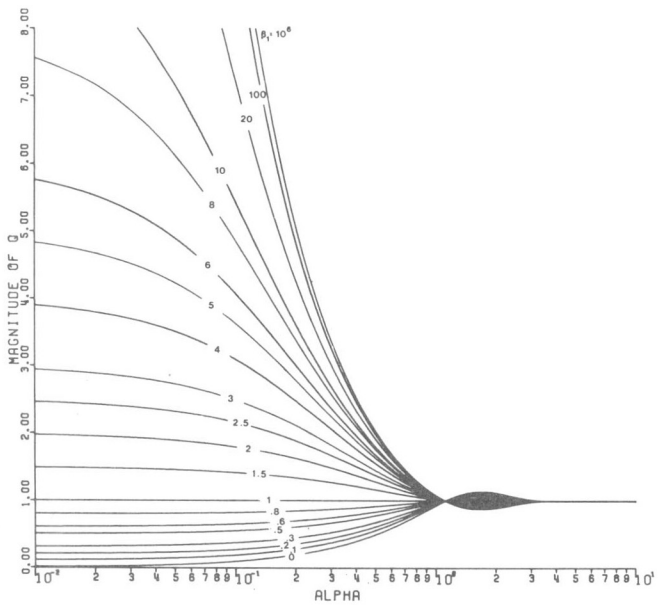

Figure 8. *Amplitude of Q_1 as a function of α_1 for all values of $\beta_1 = \sqrt{\rho_2/\rho_1}$ in a two-layer model.*

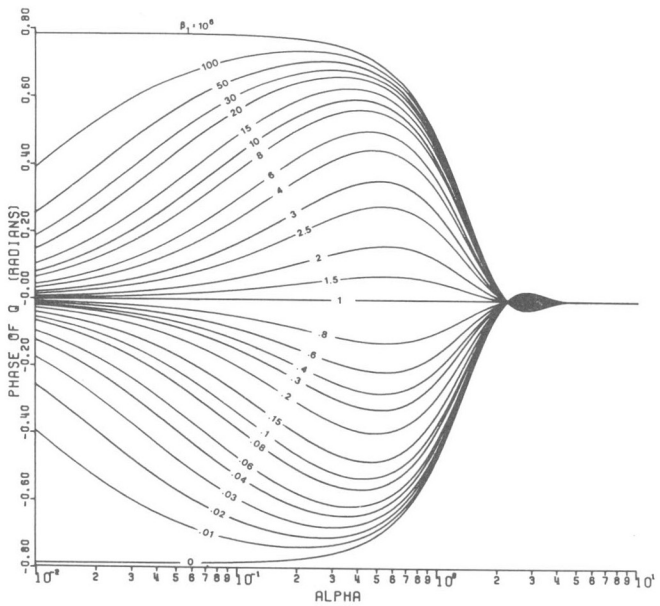

Figure 9. *As Figure 8 but phase of Q_1 plotted.*

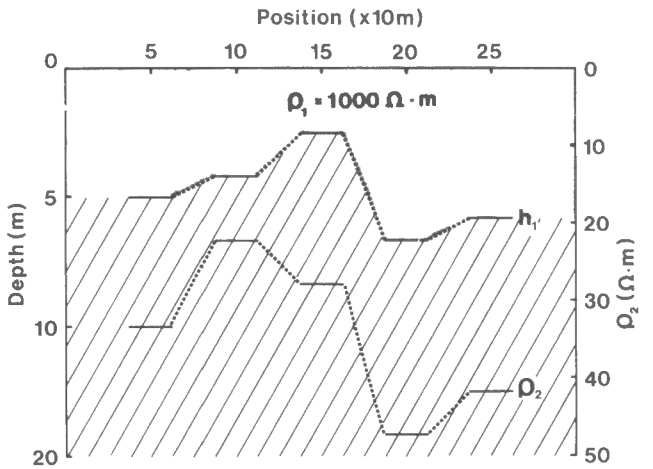

Figure 10. The problem of lateral changes in thickness h_1 *(upper curve) or resistivity* ρ_2 *(lower curve) in a typical two-layer interpretation for stations located 50 m apart. The dashed lines are assumed to bridge disjointed sections but a simultaneous solution for all stations could yield significantly different parameters.*

Case B: ρ_2/ρ_1 assumed known

Occasionally, from geological considerations, one may have an idea of the resistivity contrast and no means of determining ρ_1 directly. In this case, the phase φ and hence arg Q_1 will now yield two possible values of α_1 for the chosen value of β_1. Unfortunately, a unique value of α_1 for the model cannot be found from Figure 8 because ρ_1 is not known, and therefore these are two possible values of $|Q_1|$ appropriate to those known values of α_1. Both solutions will lead to the same value of ρ_a.

Models With 3 or More Layers

With effectively only two data from measurements in the VLF band, the interpretation of M-layered models with (2M-1) parameters (i.e. ρ_m and h_m for each layer and ρ_m for the last) becomes very problematical unless a good idea of the structure already exists. It then becomes a question of guessing all but two parameters and varying the free parameters to attempt to fit the observations. This can, however, be a useful exercise if no solution is found unless parameters which were assumed known are required to change. Very often there are multiple solutions to the M-layered problem and interpretation must be made with this in mind. Failure to do so could result in a physically meaningless solution. Mathieson and Crossley (1981-IV) discuss the question of the visibility of a layer in these models.

Interpretation by type-curves can be a tedious procedure, as so many curves are required for a three (or more) layered model and the most common application has been to the relativly well-defined problem of a thawed permafrost layer (Hoekstra et al. 1975). Mathieson and Crossley (1981-IV) consider the detection of a water table layer in a geologically simple environment and show that the surface measurements can be altered by the presence of even a shallow third conductive layer. In such cases the need for additional controls, such as those provided by drilling or a DC resistivity or seismic survey, becomes especially important.

Models With Lateral Structure

One problem that arises in all the interpretations of VLF, LF, and MT resistivity surveys is the continuity of structure from one measurement location to another, as shown in Figure 10. Such a problem could be approached using finite-element numerical integration, as described for instance by Ku (1976), but this is an expensive method computationally. The vertical contact problem treated by Telford et al. (1977) may possibly be adaptable to multiple contacts, but the only alternative appearing in the literature is the sinusoidal interface of Hughes and Wait (1975). Teemull and Crossley (1981-VI) have investigated the possibility of finding the parameters of such a model from two dimensional field profiles, but the synthesis of arbitrary lateral structure using this method also leads to extensive computational manipulation.

Combined VLF, LF Interpretation

This topic is treated more fully by LaFleche and Jensen (1981-V) for ground wave impedance measurements. Essentially, the interpretation is similar to that in MT, but, instead of plotting ρ_a as a function of frequency and therefore obtaining a sounding curve, with two frequencies the best possible approach would seem to be direct numerical inversion, either by a Monte-Carlo simulation or through an extension of the technique of Mathieson and Crossley (1981-IV). The advantages of two frequencies are probably best realized in cases where the electromagnetic skin depths lie on either side of the depth of an interface or interfaces of a model.

SUMMARY

This brief discussion of the theory of the VLF resistivity method rests heavily on the pioneering work of Wait (1962). Nevertheless certain aspects of the problem, such as the geometry of the source fields, the possibility of displacement currents affecting surface impedance measurements and an outline of interpretational procedures, have been described in an attempt to summarize the present situation for this geophysical technique. In particular there is a significant improvement to VLF interpretation to be gained by using the LF signals, which are easy to receive in Canada, and then using numerical rather than graphical interpretation.

ACKNOWLEDGEMENTS

The author would like to thank W. M. Telford and O. G. Jensen for many helpful comments on certain aspects of the above discussion. T. Warn and M. Ritchie, of the Department of Meteorology of McGill University, gave assistance in producing Figures 1 and 2.

REFERENCES

Arcone, S.A.
1978: Investigation of a VLF airborne resistvity survey conducted in northern Maine, Geophysics, 43 (7), 1399-1417.

1979: Resolution studies in airborne resistivity surveying at VLF, Geophysics, 44 (5), 937-946.

Barlow, H.M. and Brown, J.
1962: Radio Surface Waves, Clarendon Press, Oxford.

Barringer, A.R.
1972: (and 1973), Geophysical exploration method using the vertical electric components of a VLF field as a reference; Canadian Patent No. 1 261 732; US Patent Nos. 3 594 633 and 3 763 419.

Collett, L.S. and Becker, A.
1967: Radiohm method for Earth resistivity surveying; Canadian Patent No. 795 919.

Hoekstra, P.
1978: Electromagnetic methods for mapping shallow permafrost, Geophysics, 43 (4), p. 782-787.

Hoekstra, P., Sellmann, P.V. and Delaney, A.J.
1975: Ground and airborne resistivity surveys of permafrost near Fairbanks, Alaska, Geophysics, 40 (4), p. 641-656.

Hughes, W.J. and Wait, J.R.
1975: Effective wave-tilt and surface impedance over a laterally inhomogeneous two-layer Earth, Radio Science, 10 (11), p. 1001-1008.

Jones, A.G. and Hutton, R.
1979a: A multi-station magnetotelluric study in southern Scotland - I. Fieldwork, data analysis and results, Geophys. J. R. astr. Soc., 56, p. 329-349.

1979b: A multi-station magnetotelluric study in southern Scotland - II. Monte-Carlo inversion of the data and its geophysical and tectonic implications, Geophys. J. R. astr. Soc., 56, p. 351-368.

Jones, D. and Telford, W.M.
1981: Mapping bedrock terrain with the EM16R - VLF unit; in Geophysical Applications of Surface Wave Impedance Measurements, L.S. Collett and O.G. Jensen (eds.), Geological Survey of Canada, Paper 81-15, Report V, p. 35-48.

Kamas, G.
1977: Time and Frequency User's Manual, NBS Technical Note 695, G. Kamas (ed.), U.S. Department of Commerce, Washington, 210 pp.

Keller, G.V. and Frischknecht, F.C.
1966: Electrical Methods in Geophysical Prospecting, International Series in Electromagnetic Waves, Vol. 10, Pergamon, Toronto, 523 pp.

Kraus, J.D. and Carver, K.R.
1973: Electromagnetics, McGraw-Hill, Montreal.

Ku, C.C.
1976: Numerical inverse magnetotelluric problems, Geophysics, 41 (2), p. 276-286.

Lorrain, P. and Corson, D.R.
1970: Electromagnetic Fields and Waves, W.H. Freeman, San Francisco, 706 pp.

Mathieson, C.C. and Crossley, D.J.
1981: Interpretation of single frequency VLF data; in Geophysical Applications of Surface Wave Impedance Measurements, L.S. Collett and O.G. Jensen (eds.), Geological Survey of Canada, Paper 81-15, Report V, p. 49-65.

Mathur, R.K. and Telford, W.M.
1981: Magnetotelluric phase measurements; in Geophysical Applications of Surface Wave Impedance Measurements, L.S. Collett and O.G. Jensen (eds.), Geological Survey of Canada, Paper 81-15, Report V, p. 87-93.

Nichols, E. and Telford, W.M.
1981: A phase-measuring magnetotelluric instrument; in Geophysical Applications of Surface Wave Impedance Measurements, L.S. Collett and O.G. Jensen (eds.), Geological Survey of Canada, Paper 81-15, Report V, p. 95-102.

Olhoeft, G.R.
1975: The electrical properties of permafrost, Ph.D. thesis, Department of Physics, University of Toronto.

Patra, H.P. and Mallick, K.
1980: Geosounding Principles 2 : Time - Varying Geoelectric Soundings, Elsevier, New York, 615 pp.

Powell, B.W. and Jensen, O.G.
1981: Radiohm mapping of permafrost; in Geophysical Applications of Surface Wave Impedance Measurements, L.S. Collett and O.G. Jensen (eds.), Geological Survey of Canada, Paper 81-15, Report V, p. 19-33.

Singh, R.P. and Lal, T.
1981: Wave-tilt characteristics of TE-mode waves, Can. J. Earth Sci., 18, p. 382-385.

Sinha, A.K.
1977: Influence of altitude and displacement currents on plane-wave EM fields, Geophysics, 42 (1), p. 77-91.

Stratton, J.A.
1941: Electromagnetic Theory, McGraw-Hill, New York.

Teemull, F. and Crossley, D.J.
1981: Inversion of VLF data for simple lateral inhomogeneities; in Geophysical Applications of Surface Wave Impedance Measurements, L.S. Collett and O.G. Jensen (eds.), Geological Survey of Canada, Paper 81-15, Report V, p. 79-86.

Telford, W.M., Geldart, L.P., Sheriff, R.E. and Keys, D.A.
1976: Applied Geophysics, Cambridge University Press, 860 pp.

Telford, W.M., King, W.F. and Becker, A.
1977: VLF mapping of geological structure, Geological Survey of Canada, Paper 76-25, 13 pp.

Van Ngoc, P., Telford, W.M. and Becker, A.
1976: Magneto-telluric trials, Carswell Dome, Saskatchewan, Research Note 76-1, Mineral Exploration Research Institute, (IREM/MERI), Montreal.

Wait, J.R.
1962: Electromagnetic Waves in Stratified Media, International Series in Electromagnetic Waves, Vol. 3, Pergamon, Toronto, 372 pp.

Wait, J.R.
1971: Theory of Ground Wave Propagation; in Electromagnetic Probing in Geophysics, J.R. Wait (ed.), Golem Press, Colorado.

Wait, J.R.
1978: Concise theory of radio transmission in the Earth-ionosphere wave-guide, Rev. Geophys. and Space Phys., 16 (3), p. 320-326.

II

RADIOHM MAPPING OF PERMAFROST

B.W. Powell* and O.G. Jensen+
* Amok, Ltd.
+ Laboratory in Applied Geophysics, McGill University

Powell, B.W. and Jensen, O.G., Radiohm mapping of permafrost; in Geophysical Applications of Surface Wave Impedance Measurements, L.S. Collett and O.G. Jensen editors; Geological Survey of Canada, Paper 81-15, p. 19-33, 1981.

Abstract

The ground's surface impedance to electromagnetic waves is a measure of its local subsurface conductivity structure. Recently, geophysical instruments capable of the measurement of surface wave impedance at very-low, low and medium radio frequencies both on the ground and from airborne platforms have been developed and demonstrated to provide for rapid reconnaissance surveys of the earth's near surface conductivity condition. This paper explores the particular application of these geophysical methods in the mapping of permafrost, a problem of importance to the industrial development in Canada's extensive arctic and sub-arctic regions. Surface wave impedance measurements are shown to be useful in distinguishing permafrost from unfrozen soils, for delineating its occurence and in determining its depth and thickness. Survey results from tests conducted in the discontinuous permafrost zone near Fort Simpson and in the continuous zone at Norman Wells and near Tuktoyaktuk, Northwest Territories, Canada are compared to results obtained from both seismic and DC resistivity surveys with geological control being provided by drill-hole logs. Interpretations of the data based upon computer numerical inversions and manual fittings to Powell's two-layer master curves are shown to expose permafrost structures. For delineation of permafrost occurence, two useful indices are also provided. The surface wave impedance methods are found to be especially useful for the reconnaissance mapping of permafrost in continuous and discontinuous zones.

Résumé

L'impédance caractéristique du sol aux ondes électromagnétiques est une mesure de la structure de sa conductivité superficielle. On a récemment mis au point et fait la démonstration d'instruments géophysiques capable de mesurer l'impédance caractéristique de la surface à très basses, basses et moyennes fréquences tant au sol que dans les airs. On peut ainsi procéder à une reconnaissance rapide de la conductivité superficielle de la Terre. Le présent article examine l'application spécifique de ces méthodes géophysiques à la cartographie du pergélisol, problème important pour le développement industriel des immenses régions de l'Arctique et du Nord canadien. On y démontre que les mesures de l'impédance caractéristique du sol sont utiles: elles permettent de distinguer le pergélisol de sols non gelés, de délimiter son étendue ainsi que sa profondeur et son épaisseur. Les résultats d'essais effectués dans la zone de pergélisol discontinu près de Fort Simpson et dans la zone de pergélisol continu à Norman Wells et près de Tuktoyaktuk, dans les Territoires du Nord-Ouest (Canada), sont comparés à des données obtenues par des évaluations sismiques et des analyses de résistivité au courant direct, le contrôle géologique étant assuré par des rapports de sondage de mines. On démontre que les interprétations des données fondées sur les inversions numériques par ordinateurs et sur l'ajustement manuel aux abaques d'interprétation de deux couches de Powell font apparaître les structures de pergélisol. Deux indices utiles pour la détermination de la présence du pergélisol sont également donnés. On a trouvé que les méthodes faisant intervenir l'impédance caractéristique du sol étaient particulièrement utiles pour l'établissement de cartes des zones continues ou discontinues de pergélisol.

INTRODUCTION

With the expansion of the resource-based industrial development in northern Canada, the detection and delineation of permafrost structures has become a very important problem. In its solution, the methods and techniques of geophysics play a particularly useful role because the alternative, direct inspection of the soil section by means of drilling, is very expensive when applied over large areas. While geophysical methods cannot hope to replace direct inspection completely, wherever decisions for development have been made and precise questions of an engineering nature must be explicitly answered they do offer the attractive possibility of rapid reconnaisance in the search for probable development sites. Until recently, two geophysical methods have been most broadly applied to the permafrost problem: seismic refraction surveying and galvanic resistivity profiling and sounding. That these methods have been so often used is understandable because the geophysical properties which most distinguish permafrost structures from normal soils are their high elastic wave velocity and their very high DC resistivity. Of these two

properties, the very high DC resistivity of permanently frozen soils perhaps offers the most reliable indicator, if only because the seismic velocity of permafrost is not very dissimilar from that of many consolidated bedrock materials. Resistivity surveying is presently most widely accepted as the reconnaissance tool for detecting and delineating permafrost.

The additional costs of developing and continuing industrial activity in regions of permafrost occurrence have many aspects. For example, at the Iron Ore Company of Canada's mine site, Schefferville, Quebec, permafrost occurs discontinuously in the iron formations being exploited. The peculiar viscoelastic properties of the permafrozen ore make blasting for its fragmentation and removal and handling particularly difficult. A similar condition arises at the Cassiar Asbestos mine in northern British Columbia. For construction in the northern regions, the detection and delineation of permafrost is essential. "The record of the past shows many failures of construction on permafrost ... Consequences of encountering unexpected conditions during construction include lost construction time schedules, improvised foundation re-design, carrying of work unexpectedly into severe fall and winter weather, very large cost increases, delay in beneficial occupancy, heavy repair and maintenance expenses, and disruption of operations." (Linell and Johnston, 1973).

Determination of permafrost thickness in the continuous permafrost zone can be useful for determining the potential for the presence of gas hydrates in and immediately below the permafrost horizon, and is necessary in the design of safe casing strings for drilling and production operations and the establishment of adequate foundations for drilling rigs. Also, the presence of permafrost can introduce very large "statics" errors into reflection seismic exploration data. Accurate correction for these statics errors is required in order that reflection trace stacking can be accomplished for the reduction of noise, and so that the seismic sections produced can reveal the subtle stratigraphic petroleum traps, which often exhibit only a few milliseconds of interval time anomaly. The thickness of a permafrost structure cannot be easily determined using seismic refraction data, whether obtained from separate refraction surveys or through an interpretation of the first breaks of the reflection records, because the bottom of the permafrost represents a velocity inversion. Moreover, the bottom interface is very often gradational and consequently offers no strong acoustic impedance contrast and therefore provides a poor signal reflection (Hnatiuk and Randall, 1975).

The presence of permafrost presents serious obstacles to the servicing of town sites with water supply and sewage and waste removal. Culverts and conduits, even when well insulated, often ice-up in passing through permafrost. Obviously, the detection of permafrost occurrence would be of great help in the routing of community services.

The establishment of the infrastructure necessary to industrial development in the the Yukon and in western part of the Northwest Territories to provide permanent roads, railways, and pipelines for the shipment of petroleum, gas and mineral slurries and for airports and shipping ports is most seriously affected by permafrost occurrence. Because of the large extent and breadth of this area of development, it becomes essential to have access to very economical, or more properly, cost-effective methods of delineating and determining permafrost structures. Seismic refraction methods and the DC resistivity sounding, while applicable to the problem, are often slow (and consequently expensive), imprecise (hence requiring redundant follow-up work), and largely limited to use in the very short northern summer season. The need for a rapid and simple geophysical methodology is clear, and toward that end this article and the thesis from which it derives (Powell, 1978) is directed.

The essential purpose of the study (See also Hoekstra et al., 1975.) is to determine the efficacy of surface-wave impedance mapping based upon the ground Radiohm (Collett and Becker, 1967) and airborne E-Phase (Barringer, 1971) systems. Field studies at three test sites were conducted during the winter, spring, summer and early arctic autumn of 1973. The three sites studied were:

1. Fort Simpson, NWT, where a survey was conducted on a grid straddling the Mackenzie highway 15 miles south of the town site. This is a region of discontinuous permafrost.

2. Norman Wells, NWT, where a survey was conducted on a grid straddling the Canol Road, constructed during the Second World War. The area is one of continuous permafrost.

3. Tuktoyaktuk, NWT, where profiling was done across the Geological Survey of Canada's test site known as the "Involuted Hill", 15 miles south-east of "Tuk". Thick permafrost occurs generally in this region.

All Radiohm measurements were obtained in using VLF (very low frequency) transmissions at 18.6 kHz from station NLK, Jim Creek, Washington, while the airborne E-phase surveys employed various LF (low frequency) navigation and MF (medium frequency, broadcast band) transmitters.

The Electrical Properties of Permafrost

Upon freezing, there is a radical change in the electrical resistivity of terrestrial soils and sediments due to the loss of mobility of the free ions in water solution. The DC resistivity of soils can easily increase by 4 or 5 orders of magnitude with freezing and consequently, DC resistivity sounding has been used to advantage in detecting permafrost (Dement'ev, 1959; Ogilvy, 1967).

Perhaps of greater importance to the interpretation of Radiohm surface-wave impedance measurements is the fact that the dielectric characteristics of ice also depend very strongly upon the presence of impurities, which are commonly a part of soil materials (Addison 1967; Olhoeft, 1975). The propagation constant of a surface guided electromagnetic wave depends upon the electrical conductivity, the magnetic permeability and the dielectric permittivity of the ground material as shown by Crossley, (1981-I),

$$\gamma = \sqrt{j\mu\omega(\sigma + j\epsilon\omega)}$$

where, for a real material, the dielectric permittivity is often best described as a complex quantity,

$$\epsilon = \epsilon' + j\epsilon'' , \quad j = \sqrt{-1}$$

The imaginary component of the permittivity is descriptive of a dielectric energy-loss mechanism which for any frequency is not distinguishable from the ohmic loss due to the finite electrical resistivity of the ground materials. As Crossley (1981) shows, the energy loss mechanism is

often characterized by the "loss tangent",

$$\text{loss tangent} = \frac{\omega\epsilon'' + \sigma}{\omega\epsilon'}$$

For unfrozen sediments and rocks, the electrical conductivity, σ , exceeds the dielectric equivalent "conductivity" $\omega\epsilon''$, for frequencies $f = \omega / 2\pi < 10^5$ Hz. Effectively, then, at VLF, the loss within an unfrozen ground may be entirely ascribed to the finite electrical resistivity of the materials. However, for frozen sediments and permafrost, Olhoeft (1975) has determined that the dielectric loss mechanism begins to dominate at frequencies as low as 1 Hz. Consequently, for VLF surface-wave impedance measurements, the energy being extracted from the EM surface-guided wave through dissipation in natural ice and clay permafrosts, for example, is almost entirely due to the dielectric loss mechanism, and therefore, the contrast in equivalent material resistivity between unfrozen and frozen sediments may not be so evident as in the case of DC resistivity measurements.

It will soon be seen, however, that an approach to interpretation which ascribes the lossiness entirely to the electrical conductivity at any one frequency of measurement still permits the identification and delineation of permafrozen sediments. If several very different frequencies were to be used in a delineation survey, it would be advantageous to attempt to separate out the dielectric effect. Moreover, because this effect dominates in frozen materials, the extension of surface wave-impedance surveys by use of many independent frequencies could be very helpful in resolving an identification of permafrost.

INSTRUMENTATION

For the Radiohm measurements, the convenient Geonics Ltd. model EM16R receiver was used in all ground surveys. This instrument combines a sensitive ferrite-cored coil antenna for reception of the horizontal-transverse magnetic field signal (H_y) along with two buffered high impedance ground probes for the measurement of the oscillating electrical potential over a 10 m radial separation, which is due to the tangential electrical field (E_x) on the ground surface. The AC voltages, derived from the H-field antenna and as the difference potential between the ground probes, are amplified and phase shifted in order to accomplish a comparison of their relative phase and amplitudes. In use, varying the rotation of a potentiometer allows the H-field derived signal to be phase shifted until it is 180° out-of-phase with the E-field derived signal. The amplitude of the E-field derived signal is adjusted by varying a gain-controlling potentiometer until its amplitude is brought to precise equivalence with that of the H-field derived signal. The two signals are then summed and reduced to 1.6 kHz frequency by means of a ring demodulator. The sum signal is applied to a small loudspeaker loaded with a tuned resonant tube. By iteratively adjusting the calibrated phase-shifting and gain-controlling potentiometers, the two signals can be brought to cancel one another, producing a zero sum signal and consequently an audio null. The relative phase angle between the surface E and H fields, measured in degrees, and the scaled, squared ratio of the field amplitudes, measured in ohm-metres, can be read directly from the adjustment potentiometer dials. Because the buffered probes have a very high input impedance, claimed to be about 14 MΩ at 20 kHz, electrical contact resistance with the ground is not expected to be problematical, even when the ground is frozen. LaFleche (1979; LaFleche and Jensen, 1981-V), however, has determined that the effective capacitance of the buffer amplifiers is somewhat higher than the specified 0.5 pF, apparently about 3 pF, and consequently, at 20 kHz, the effective input impedance might be lower than specified by about a factor of six. In any case, even a 2 MΩ input impedance can accommodate a large contact resistance and source impedance without materially affecting the surface-wave impedance measurement. Scott (personal communication) has shown that surface-wave impedance measurement obtained under the condition of coupling the probes to the ground surface only through a relatively large capacitance provides for very similar results as produced under the normal direct resistive coupling. Consequently, one should not expect that this very convenient instrument is much affected by the ground condition except in very exceptional circumstances.

To provide some control for comparison of the Radiohm measurements of the ground's apparent resistivity, DC resistivity soundings using a Schlumberger electrode array and resistivity profiling using a Wenner array were employed. The resistivity meter used for this purpose was the McPhar model R-103 receiver, the current being supplied by a Huntec LoPo IP transmitter modified to deliver a square wave of 0.3125 Hz.

The Barringer E-Phase® airborne system effectively obtains a measurement of the electric wavetilt (Crossley, 1981-I) as the ratio of the vertical E field to the horizontal-radial (ie. on a radius away from transmitter) E field. The wavetilt is directly proportional to the surface-wave impedance. Actually, the E-Phase system obtains a measurement which involves only that part of the horizontal E field which is in quadrature phase relative to the vertical E field because, typically, the in-phase component of the horizontal component is so much smaller than the vertical E field that it is very difficult to determine their ratio. Over homogeneous ground, the phase angle of the surface wave impedance is just 45° and, consequently, the in-phase and quadrature components of the horizontal E field (as measured relative to the vertical E field) must have identical amplitudes, each being $1/\sqrt{2}$ of the total horizontal field amplitude. Even though the amplitudes of these two phase components are typically very similar, it is technically a much easier problem to establish the quadrature ratio and it is for this reason that only the quadrature ratio is provided as measurement. However, the quadrature part of the wavetilt only properly establishes the equivalent quadrature component of the surface-wave impedance, which is normally scaled by $\sqrt{2}$, as a means to estimating the actual surface-wave impedance. This fixed scale factor is correct only under conditions of a 45° phase angle (ie. for homogeneous ground) and yields an overestimate of the ground impedance for larger phase angles and an underestimate for lower phase angles. Care must therefore be taken when comparing the airborne E-Phase survey results to those obtained by the Radiohm ground surveys.

A Barringer E-Phase airborne survey using low and medium frequency transmissions was flown for the Geological Survey of Canada over the Ft. Simpson test site by Barringer Research. In this same area, a seismic refraction survey was conducted by Dr. J. Hunter of the GSC, using the 12 channel SIE model RS4 refraction seismograph as part of the active geophysical terrain survey program under the direction of L.S. Collett during the summer of 1973. Some shallow holes were also drilled in order to provide some absolute geological control for the several geophysical surveys.

The use of several geophysical methods at each of the survey test sites allowed for the judgement of the relative merits of each technique in the detection and delineation of permafrost structures. Moreover, the continuation of

the project through all seasons in the northern environment led to the exposure of several seasonally-related problems pertinent to each method. For example, it was discovered that, in winter, a null adjustment of the Radiohm instrument was not easily obtained. The phenomenon might have been due, in part, to the complexity of the propagation paths of the VLF transmissions between the NLK transmitter and the Fort Simpson test site. However, it was also determined that part of the problem arose due to the electrical isolation of the instrument from the ground. The Geonics EM16R instrument establishes its case as reference common for the E-field potential measurements and, in winter, this reference is not well coupled to the ground midway between the electrical probes. Consequently, the E field difference signal's mean or reference level could freely wander. In normal summer operation, the reference is coupled through the operator into the ground and, when the instrument is properly lain on the ground, directly from the instrument case to the ground via a much lower resistance direct path. This same effect can alternately be explained as the direct antenna pick-up by the isolated instrument and, when he is holding the instrument, the operator himself. Apart from this particular problem, no significant operational difficulties were encountered in using the Geonics EM16R during surveying in any season and in all but the very most inclement weather.

Several problems were discovered relevant to the DC resistivity sounding and profiling for permafrost. For example, during winter surveys, the high contact resistance between the current electrodes and the ground caused substantial difficulties. Several obvious approaches were taken to overcome this problem: long, steel rods were eventually driven deeply into the ground and very high transmitter voltages were used, typically exceeding 1 kV, in order to obtain an adequate current level of about 50 mA. This led, of course, to a rapid drain on the batteries due to the high power (typically 50 W) required to support the necessary current. Eventually, this power, which was largely dissipated at the contact between the electrodes and the ground, would cause some melting and a consequent decrease of the contact resistance. The transmitter itself was unable to control a constant current under these conditions of variable contact resistance, and it was found necessary to ride the current control rheostat manually.

Another obvious problem derives from the inefficiency of energy storage batteries at the low winter temperatures typical in the Canadian north. In general, more batteries were needed and longer, heavier and stronger electrodes were required. Many more heavy tools for the insertion and extraction of probes had to be carried and consequently, the progress of the resistivity surveys in winter was extraordinarily slow. Along with some minor electronics problems experienced by the resistivity receiver, perhaps due to the low water vapour content of the winter air allowing for electrostatic charges to build up within the circuitry, the resistivity surveys were found to be extremely inconvenient for permafrost surveying in winter.

On the other hand, summer brought a complementary series of problems. Access difficulties, of course, were chief amongst these as swamps and bogs are common throughout the permafrost regions of Canada. Also, a technical problem is encountered when trying to pass any current through the high resistivity permafrost structure in summer, because the current field distributes itself through the very low resistivity surface thaw layer which may be only about 30 cm thick. In overcoming this problem, large electrode spacings were required which led to increased power consumption in supporting the necessary current levels.

MAPPING DISCONTINUOUS PERMAFROST

The Fort Simpson, NWT test site (Fig. 1) lies in a region of discontinuous permafrost; that is, there is no continuous layer of permanently frozen soil subsurface. Various climactic, hydrological, geological and botanical conditions lead to the existence of permanently frozen soils in certain areas and their non-existence in others. As well, human activities such as land clearing and road construction can upset the delicate thermal regime in zones of discontinuous permafrost, causing local and permanent melting of permafrost structures. Because of the discontinuity of the permafrost structures at the Fort Simpson test site and the recent construction of a permanent road, it offered an ideal location for developing detection and delineation techniques. The problem of detection and delineation largely involves the recognition of some geophysically measurable parameter which is closely associated with permafrost occurence. In this region, the primary aim of the geophysical surveys was not to establish elaborate models of the permafrost but rather to determine its depth and horizontal extent. However, it was found necessary to obtain interpretations of the Radiohm measurements revealing the permafrost thickness as well.

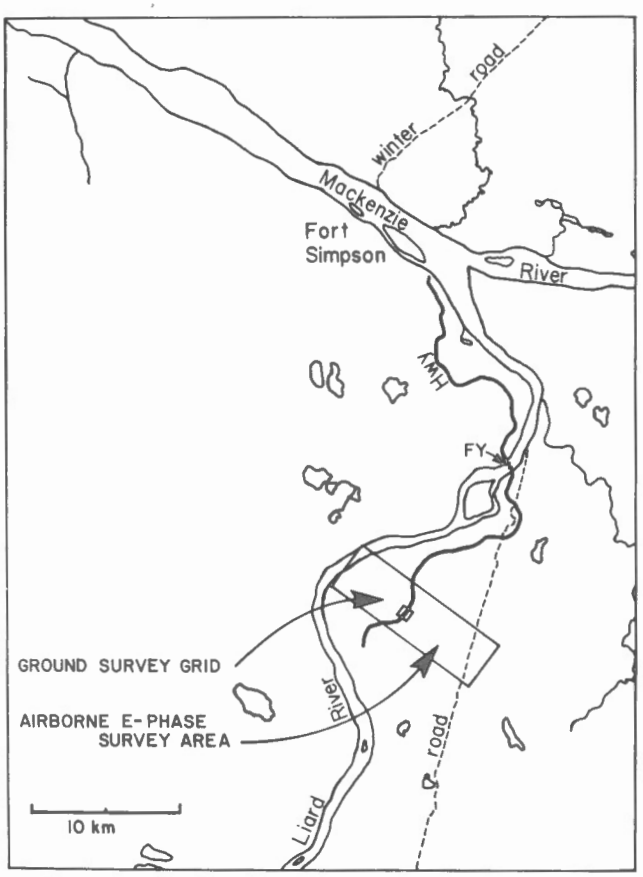

Figure 1. The location of the test site at Fort Simpson, N.W.T. The ground survey grid straddles the Mackenzie highway; the airborne survey area extends beyond the ground survey.

An extensive ground resistivity profiling was accomplished during March and June, 1973 using a Wenner array with a 15 m interelectrode spacing. This array configuration was deemed optimum for detection and delineation of the most usual permafrost occurences in this area. A contour map showing the apparent resistivities determined by these Wenner profilings is shown in Figure 2. For comparison, two Radiohm surveys accomplished in the winter, March 1973 (Fig. 3a) and summer, June 1973 (Fig. 3b) are shown in which the E-to-H phase angle obtained from the surface wave-impedance measurements at 18.6 kHz are shown. A reasonable indication of a permafrost structure as a thick high resistivity layer overlying a low resistivity unfrozen halfspace would be a high phase angle (well beyond 45°) in the Radiohm measurements and, obviously, a high DC resistivity in the Wenner profile measurements. The different results derived from the two Radiohm surveys and their lack of evident correlation with the more conventional DC resistivity survey brings into question the possibility of using the VLF wave-impedance measurement in the observation of discontinuous permafrost.

Inversion Modelling

In discontinuous permafrost zones, one would expect the permafrost structures to be relatively thin and probably much less than one skin depth considering their high resistivity and the 18.6 kHz EM wave frequency. Consequently, a more elaborate interpretation of the Radiohm results is required before the method could be discounted. With the intention of obtaining an optimum thin-layer model for the permafrost layer, a model-based inversion of the Radiohm data employing the well-known Marquardt's Lambda method (Marquardt, 1963; Ku, 1976) was obtained. By this method, inversion is performed by regression to an analytical expression which represents a general preconceived model of the physical system, giving rise to the measured data. As the criterion for the optimization of the model parameters, the sum of the squared errors between the data and the particular analytical expression is minimized. A simple horizontal layering model was used in which the permafrost layer

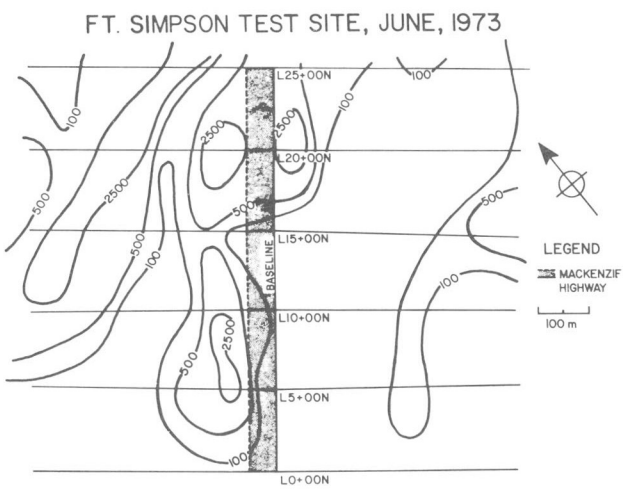

Figure 2. *A contour map of Wenner-array resistivity profiles at the Forth Simpson test site. The inter-electrode spacing was 15 m. Contours of apparent resistivities are shown: 100 Ω.m, 500 Ω.m and 2500 Ω.m.*

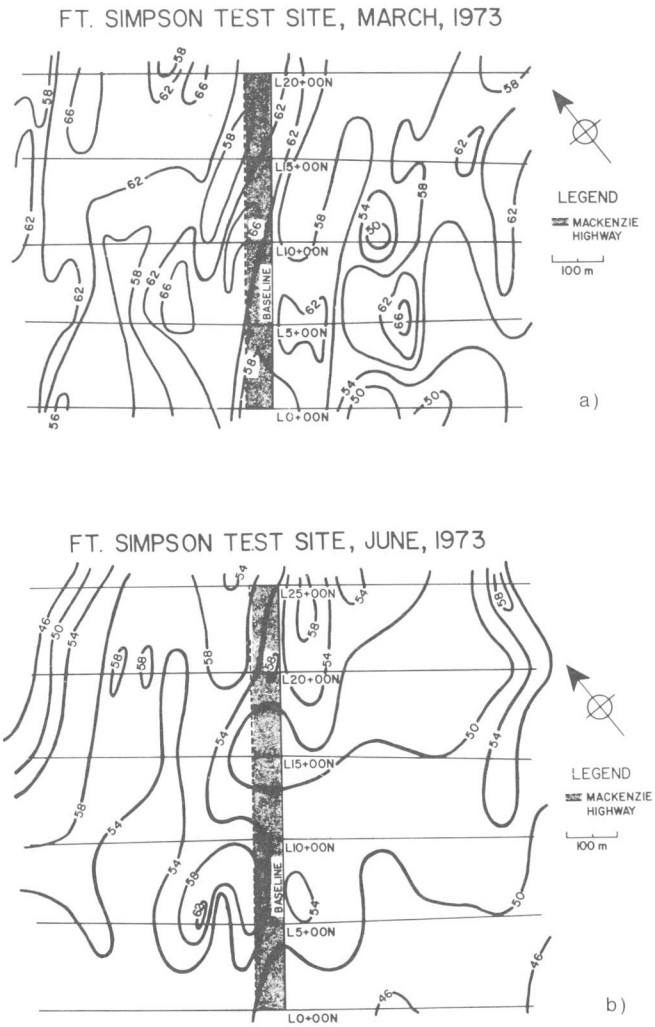

Figure 3. *The phase angle of the complex surface impedance as measured by the Radiohm method.*
a) *A winter survey, March, 1973.*
b) *A summer survey, June, 1973. The contour interval is 4°.*

overlies a conductive unfrozen layer. For the interpretation of the summer measurements, a thin, highly conductive surface layer must be added to the model. In principle then, five model parameters are properly involved: ρ_0, ρ_1, ρ_2, h_0, h_1, the resistivities of the first, second and third layers and the thicknesses of the first and second layers. For the winter measurements, we let $\rho_0 = \rho_1$. It was also assumed, generally, that $\rho_1 \gg \rho_2$, which allows us to establish (See Crossley, (1981-I).) that

$$\tanh \gamma_1 h_1 \cong \gamma_1 h_1 \quad .$$

In, winter, when the surface layer is frozen we assume

$$\gamma_0 = \gamma_1$$

so that

$$\tanh \gamma_0 (h_0 + h_1) \cong \gamma_1 (h_0 + h_1)$$

so that the expression immediately above holds. The analytical expression representing the apparent resistivity of the winter model is then, very simply,

of the winter model is then, very simply,

$$\rho_a = \rho_1 \left| 1 + \gamma_1 (h_1 + h_2) \right|$$

the summer model's proper expression being somewhat more complex. Practically, inversions were computed only for the winter model with a subsequent correction being applied to take into account the conductivity-thickness product of the very thin surface thaw layer.

Marquardt's Lambda method of solving least-squares inverse problems is basically one which combines the straightforward Gauss' least squares method and the method of steepest descent, with the immediate weighting towards one or the other method being selected at each iteration, in order to accelerate the convergence while at some distance from solution and to decelerate the convergence near solution so as not to overshoot or oscillate about the desired solution. It was also found necessary to add constraints of acceptability to the parameters being sought, so that the solution could not stray from reasonableness.

Generally, the constrained Marquardt method provided very fast convergence to least squares solutions. Figure 4 shows the results of such solutions made for each Radiohm measurement; the depth of the frost (i.e. seasonal frost plus permafrost) is contoured. A reasonable interpretation of this contour map is that thick frost represents a high probability of a local occurence of a permafrost structure, while low depth extent represents a low probabilty of permafrost occurence. Regarded in this way, this interpretation does show a reasonable level of correspondence with the results of the standard Wenner resistivity survey.

Type Curves as an Aid to Interpretation

A criticism of the use of inversion methods is that they are bound to access to computers and, while more and more powerful portable computers and calculators are becoming available which could be carried into the field to aid in the immediate interpretation of geophysical measurements, it would be useful to create some relatively simple measure which is easily calculable from the Radiohm measurements and which is a reliable indicator of the presence of a permafrost structure. Herein lies the advantage of the conventional geophysical type-curve catalogue appropriate to the particular geophysical measurement and the problem at hand. Powell (1978)

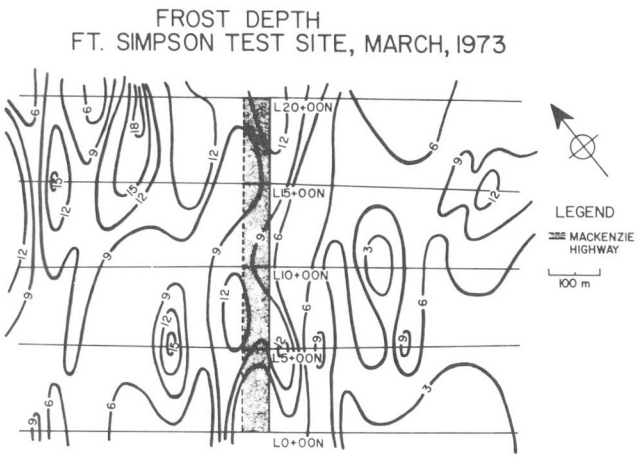

Figure 4. The depth extent of the seasonal and permafrost as determined by a constrained least squares inversion of data obtained during the winter survey, March, 1973. The contour interval is 3 m.

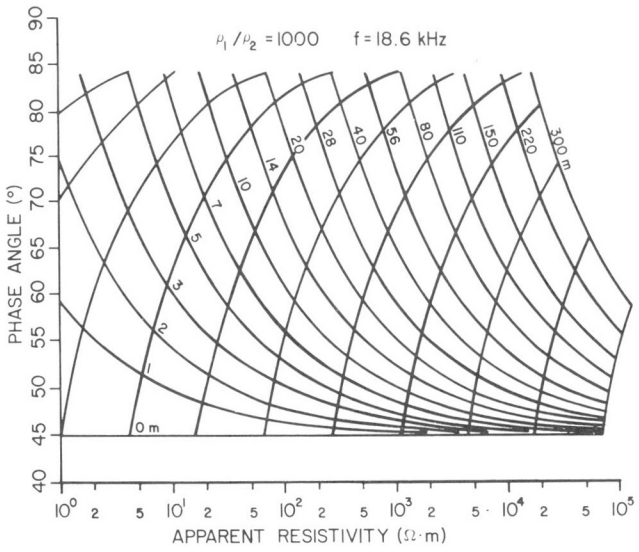

Figure 5. Powell's (1978) first solution master curves for the interpretation of Radiohm measurements in terms of a two-layer model. A resistivity contrast of 1000 is assumed. The frequency of the surface wave is 18.6 kHz.

obtained such a catalogue of two-layer master curves for the interpretation of Radiohm measurements as a model having a high resistivity layer overlying a low resistivity layer. An example of a pair of such master-curves is shown in Figures 5 and 6, for reference, for which $\rho_1/\rho_2 = 1000$. For these curves, one family of lines are representative of constant first layer thickness h_1 ; the second family of crossing lines represent the second layer resistivity ρ_2 , which of course also establishes the first layer resistivity. It has been assumed that there are no dielectric losses.

Two curve sets arise because two solutions exist for the generating equations. The general form of the two-layer solution (Powell, 1978; Crossley, 1981-I) obtains the surface wave impedance according to Wait's (1962) recursive form as

$$Z = \left[\frac{j\mu_1\omega}{\sigma_1 + j\omega\epsilon_1} \right]^{1/2} \cdot Q$$

where

$$Q = \frac{\gamma_1 + \gamma_2 \tanh \gamma_1 h_1}{\gamma_2 + \gamma_1 \tanh \gamma_1 h_1} \quad ;$$

μ_1 , σ_1 and ϵ_1 represent the magnetic permeability, the electrical conductivity and the dielectric permittivity respectively for the frozen layer (seasonal frost plus permafrost) of thickness h_1 . γ_1 and γ_2 are the complex propagation constants having the general form, in layer i,

$$\gamma_i = \sqrt{\mu_i \epsilon_i \omega^2 - j\mu_i \sigma_i \omega}$$

where the particular subscripts, here, represent the frozen layer and the underlying conductive halfspace (See Crossley, 1981-I; Wait, 1962.). For these solutions, we assume that $\mu_i = \mu_0$, the magnetic permeability of free-space, and that ϵ_i is purely real, so that there is no dielectric loss.

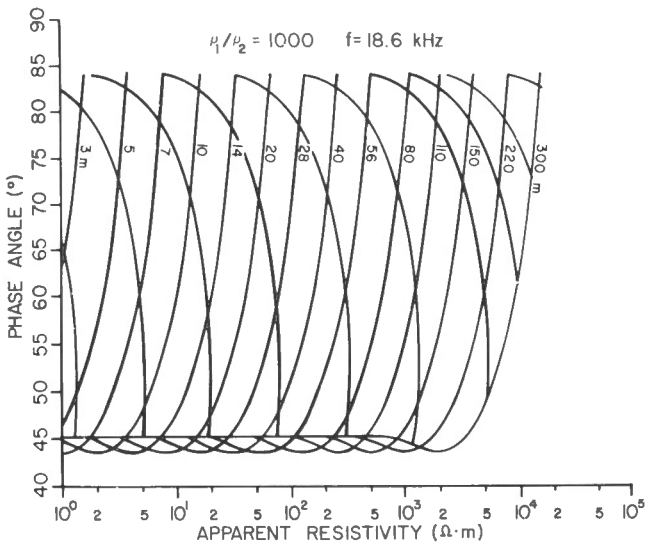

Figure 6. *Powell's second solution master curves for the interpretation of Radiohm measurement in terms of a two-layer model. A resistivity contrast of 1000 is assumed. The frequency of the surface wave is 18.6 kHz.*

In this case, the magnitude of σ_1 is typically very much larger than that of the $j\omega\epsilon_1$, and consequently

$$Z \cong \sqrt{\frac{j\mu_0\omega}{\sigma_1}} \cdot Q \quad .$$

The measurements provided by the Geonics EM16R Radiohm instrument are given in the terms of the apparent resistivity of an equivalent halfspace, determined according to the form

$$\rho_a = \frac{1}{\mu_0\omega}|Z|^2$$

and the phase angle of the complex impedance

$$\varphi = \tan^{-1}\frac{Im(Z)}{Re(Z)}$$

In Wait's recursion formalism, Q = 1 for a homogeneous halfspace and evidently, then, over a homogeneous ground structure,

$$\rho_a = 1/\sigma_1$$

and

$$\varphi = \pi/4$$

For the two-layer model, the first solution condition generally obtains when $\gamma_1 h_1$ is small enough that $\tanh \gamma_1 h_1 \cong \gamma_1 h_1 \ll \gamma_2 / \gamma_1$, and the form for Q reduces to

$$Q \cong \frac{\gamma_1 + \gamma_1\gamma_2 h_1}{\gamma_2}$$

from which one may determine that

$$\rho_a = \frac{Q^2}{\sigma_1}$$

and

$$\varphi = \pi/4 + \tan^{-1}\frac{Im(Q)}{Re(Q)}$$

The second solution generally obtains when $\gamma_1 h_1 \gg$ arc $\tan(\gamma_1/\gamma_2)$ and Q, which can be written in the form

$$Q = \tanh(\gamma_1 h_1 + \tan^{-1}(\gamma_1/\gamma_2))$$

reduces to $Q = \tanh \gamma_1 h_1$, which can be substituted into the forms immediately above to obtain ρ_a and φ. Transition between these two solutions arises where $\tanh(\gamma_1/\gamma_2) \simeq \gamma_1 h_1$.

The first solution curves are appropriate for geological conditions in which h_1 is sufficiently thin and, consequently, a general form for these curves was sought in terms of a power series expression of the form

$$\varphi - \pi/4 = a\rho_a^b$$

The shape of these curves in the linear phase vs. log apparent resistivity plot is evidently similar for a broad range of frost depths, and a regression analysis using all such curves for which $\rho_1/\rho_2 \gg 1000$, representative of an occurence of permafrost, obtained

$$-0.502 < b < -0.506 \quad .$$

For convenience, the exponent was set to be $b = -1/2$. The value of a, of course, depends strongly upon the first layer's thickness, so this is the parameter which, in fact, mostly distinguishes the various curves. The consistency of the exponent b led to the development of a simple measure for the indication of permafrost called the "permafrost index":

$$PMFI_1 = \rho_a^{1/2}(\varphi - \pi/4)$$

which can be shown to depend upon the frozen layer's thickness, h_1, as

$$PMFI_1 \simeq (2\mu_0\omega h_1^2)^{1/2}$$

for moderate depth extent. In discontinuous zones one expects only a moderate depth of the frozen zone, perhaps not exceeding 15 m and in these conditions, the permafrost index could offer an excellent indication of the occurrence of permafrost, with its magnitude being directly proportional to its depth extent. A second permafrost index has also been considered for which the occurrence effect is arbitrarily enhanced as

$$PMFI_2 = \rho_a(\varphi - \pi/4) \quad .$$

This index, of course, does not provide a magnitude which is directly relatable to the frozen zone's thickness.

Figures 7 and 8 show $PMFI_2$ contoured for all measurements made at the Fort Simpson test site during March and June, 1973. Geological comparison was made available through the frost logging of certain drill holes, as shown in Figures 9a, b, c.

The Effect of Underlying Bedrock

The presence of resistive bedrock within the depth of detectability of the 18.6 kHz surface wave impedance measurements would present a substantial deviation from the simple two-layer permafrost model. The effect of an underlying bedrock formation with a 2000 Ω.m resistivity at a depth of 30 m and of 39 m is shown in Figure 10. The permafrost layer, with an effective resistivity at 18.6 kHz of 2000 Ω.m is varied in thickness from 1.5 to 30 m in 1.5 m steps, and the conductive sub- permafrost layer has been set to a resistivity of 50 Ω.m in this example. The apparent resistivity and phase angles, as would be measured over the structure, are shown. In comparing these simulated measurements with the form of the first solution type curves, one sees that the presence of the bedrock layer would lead to the underestimation of the permafrost layer's thickness.

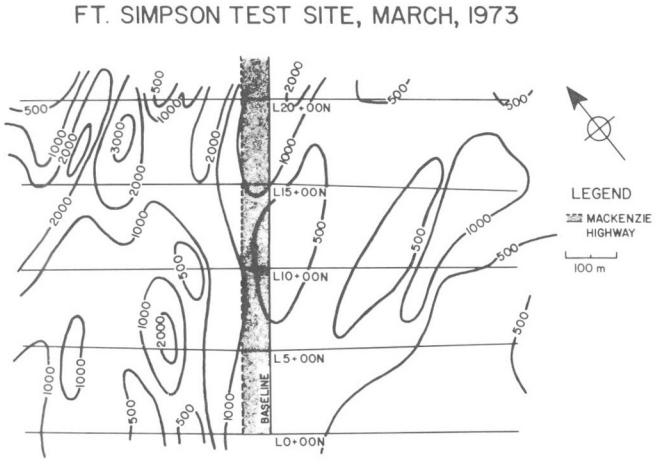

Figure 7. Contours of the permafrost index $PMFI_2$ as computed from the Radiohm measurements made during the Winter survey, March, 1973. The contours are (100, 200, 500, 1000, 2000) Ω.m .

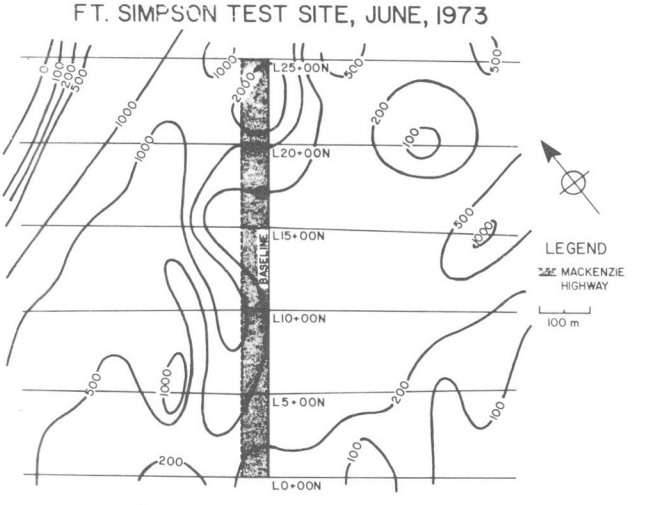

Figure 8. Contours of the permafrost index $PMFI_2$ as computed from the Radiohm measurements made during the Summer survey, June, 1973. The contours are (500, 1000, 2000, 3000) Ω.m .

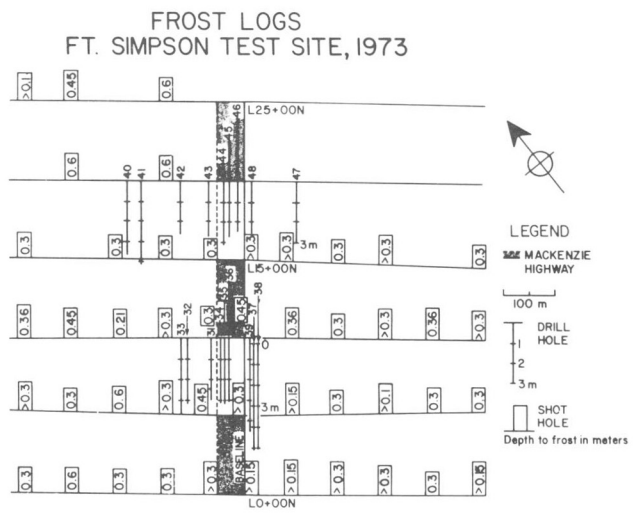

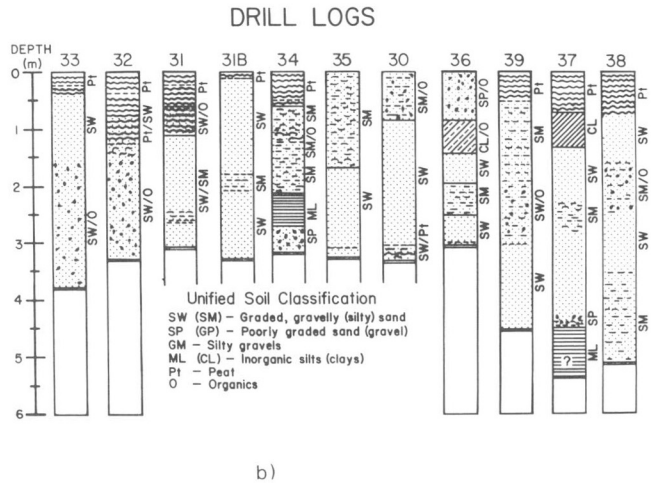

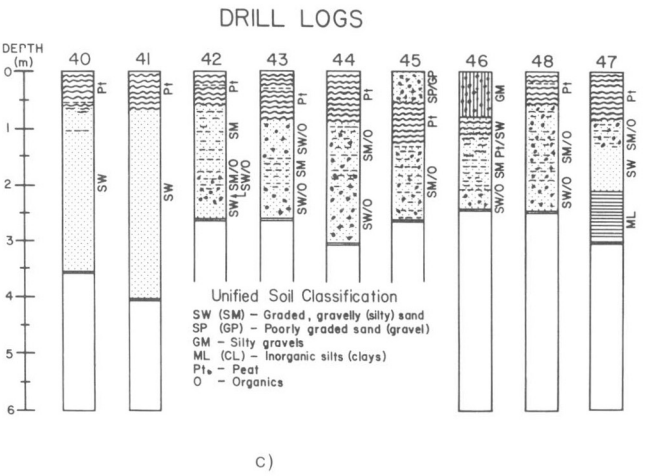

Figure 9. *Drill-hole and seismic shot-hole frost logs for the Fort Simpson test site.*
a) *The numbered hole sites and their depths are indicated.*
b) *Details of the frost logs for holes #30 to #39.*
c) *Details of the frost logs for holes #40 to #48.*

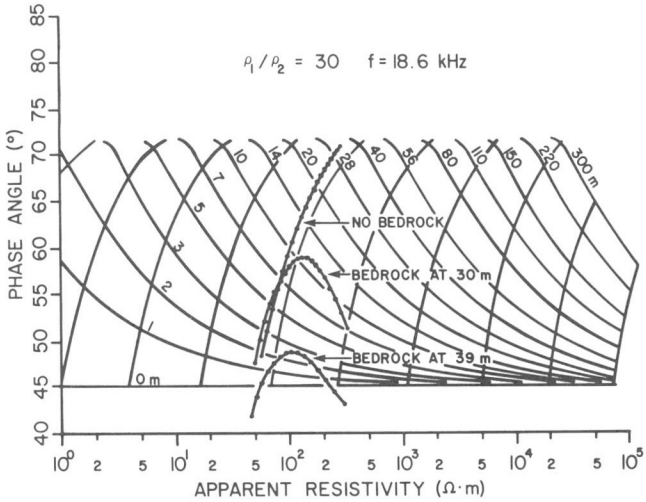

Figure 10. A scatter diagram of paired apparent resistivity and phase angles superimposed on Powell.s (1978) first solution master curves for a resistivity contrast of 30. A third resistive bedrock layer at 30 m and 39 m depth with a thickness of between 1.5 and 30 m (1.5 m interval is shown) affects the apparent resistivity/phase angle measurement as shown. Effects of no bedrock, bedrock at 30 m and bedrock at 39 m are shown.

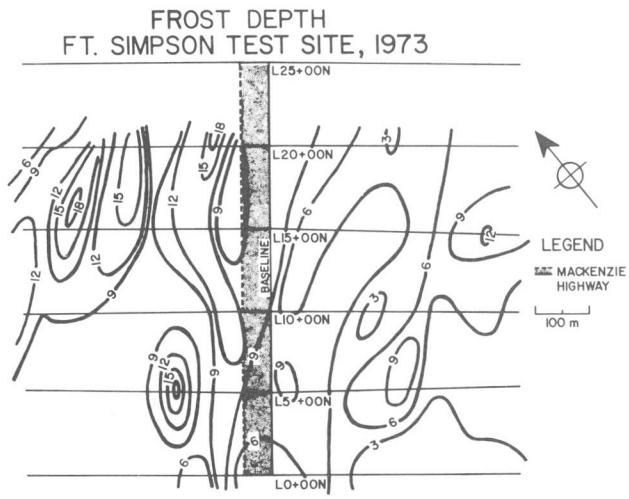

Figure 11. The frost depth at the Fort Simpson test site as interpreted using Powell.s master curves, first solution, with an assumed resistivity contrast of 30. The contour interval is 3 m.

The Effect of a Surface Thaw Layer

The interpretation procedures discussed above are appropriate to a two-layer model, in which the upper layer represents the high-resistivity frozen soils, and the lower layer, a deep uniformly conductive unfrozen soil section. It has already been suggested that a correction to interpretations based upon this model can be made in order to account for a thin surface thaw layer. Powell (1978) obtained a "thaw-layer transformation", which properly accounts for this thin layer, providing the permafrost thickness $h_1 \gg h_0$, the overlying thaw-layer's thickness. Taking $h_0 = 0.1\, h_1$ as a typical condition in midsummer at the Fort Simpson test site, Powell determined that the summer thaw layer introduces a fairly consistent additional phase shift of 10° and, providing the observed phase angle exceeds 45°, the apparent resistivity measurement is almost unaffected. Consequently, the interpretation for occurence based upon the permafrost index in this area could be reasonably corrected by subtracting a fixed 10° from the particular summer measurements of phase angles. Of course, these exact correction values are probably appropriate only to the discontinuous permafrost conditions in the particular area around Fort Simpson, NWT. To obtain correction factors appropriate to other areas, a preliminary three-layer modelling of the typical ground-soil structure should be conducted based upon a series of reconnaissance measurements.

Inversion Using the Two-layer Type Curves

Before one can select which pair of type curves (i.e. representing either the first or second solution) are appropriate to a survey region, one must establish a first reliable estimate of the typical permafrost thickness. At the Fort Simpson test site, no permafrost layer thicknesses exceeding about 15 m were to be expected (Judge, 1973). The transition between first and second solutions occurs for shallower permafrost depths with low permafrost resistivity. Assuming a permafrost resistivity of only 500Ω.m, certainly unrealistically low, the depth for transition between the two solutions becomes about 20 m. Since permafrost resistivities in this area were expected to well-exceed 500 Ω.m and the depth extent was not expected to exceed 15 m, the appropriate interpretation solution should fall well within the first solution regime.

Olhoeft's (1975) measurements indicate that, upon freezing, the resistivity at VLF for unconsolidated sediments increases approximately 30 fold. For the range of phase angles observed at the Fort Simpson test site, all measurements lay within the first solution two-layer master curves for a contrast of 30. The appropriate interpretation curve for this contrast has already been presented in Figure 10 above. In use, then, the phase angle and apparent resistivity establish coordinates on the interpretation type curves, and at these coodinates, the permafrost thickness and subpermafrost resistivity can be determined. Figures 11 and 12 show the interpreted frost depth and sub-permafrost resistivity respectively, contoured over all measurements at the Fort Simpson test site. It is notable that, as expected, the interpreted thickness shows much similarity to the map of $PMFI_2$ (Fig. 7) the contour map determined by the computer inversion (Fig. 4), and also to the map derived from the Wenner DC resistivity profiling survey (Fig. 2). Because a higher resistivity contrast was assumed for the Marquardt method optimized numerical inversion, it has provided permafrost thicknesses about 10% lower than those derived from the manual inversions using the first solution type curves. Their close similarity does, however, show that the thickness determination is remarkably insensitive to the actual resistivity contrast, there being a factor of 30 difference in the contrast between the permafrost resistivity and that of the unfrozen sub-layer as assumed in these two different approaches to interpretation.

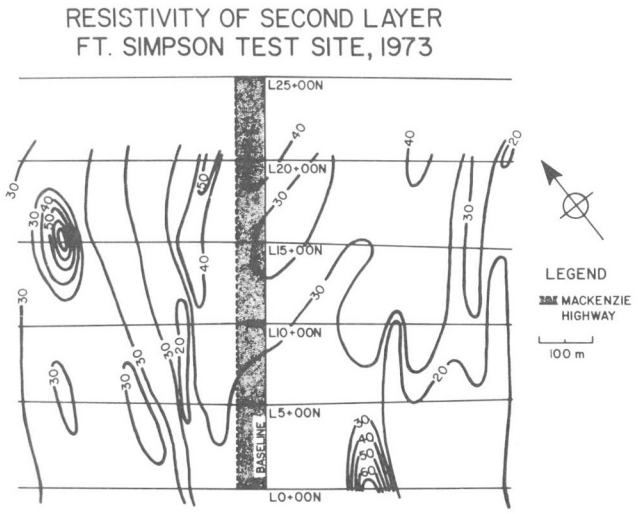

Figure 12. The resistivity of the sub-permafrost layer as interpreted using Powell.s curves. The contour interval is 10 Ω.m.

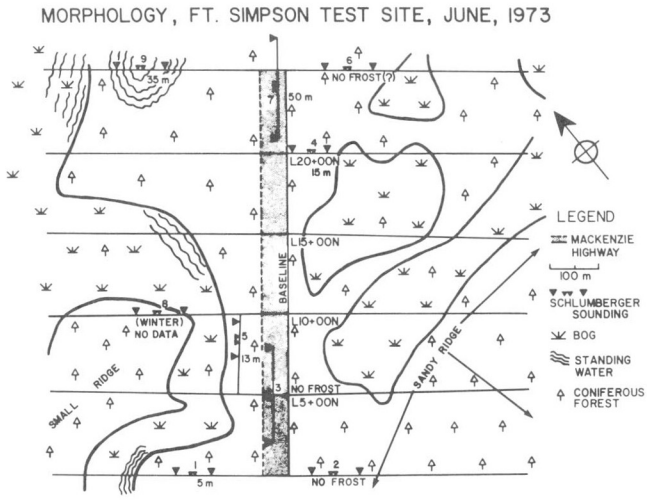

Figure 13. A morphology map of the Fort Simpson test site as mapped during the Summer survey, June, 1973. Nine locations of Schlumberger resistivity soundings are indicated with the depths to the base of the permafrost as obtained by the Zohdy (1974) inversion.

Resistivity Sounding

In order to test the Radiohm interpretations for the depth extent of the permafrost layer, DC resistivity soundings using a Schlumberger electrode configuration were conducted at several sites in the test area where the Radiohm surveys had suggested a relatively constant depth and where, as well, the Wenner resistivity profiling had found little spatial character in apparent resistivity. The data for each sounding were fitted to three- and four-layer resistivity master curves (Orellana and Mooney, 1966) manually and were also applied in computer inversions using an interactive program due to Zohdy (1974).

Nine soundings were conducted at the locations shown on the morphology map of the Fort Simpson test site (Fig. 13). The depths to the base of the permafrost in metres, as obtained by the computer inversions and confirmed as plausible by manual fittings of the sounding data to the master curves, are noted at the location of each sounding on the morphology map (Fig. 13). Horizontal layer model solutions were found to be impossible for sounding N°8, which was conducted during the winter, when generally consistent resistivity data could not be obtained. Also, the data from sounding N°6 could not be inverted to a solution, although its general form seemed to be quite characteristic of a no permafrost condition. Soundings N°7 and N°9 apparently produced unrealistically deep permafrost layers which, according to Judge (1973), must be held suspect. It would therefore appear that the success rate in DC resistivity sounding in this discontinuous permafrost zone does not much exceed 50%. However, the two soundings showing no frost were in fact corroborated by the conditions observed in nearby holes drilled for seismic shots. In comparison the various approaches for interpreting the Radiohm data (Figs. 4, 7, 8, 11, 12) of course show a continuity of either permafrost depth extent or permafrost index. Disappointingly, the resistivity sounding surveys do not provide the corroborative evidence to clearly demonstrate that the Radiohm measurements are capable of yielding a permafrost delineation.

The Airborne E-Phase Mapping

The Geological Survey of Canada contracted for the Barringer E-Phase system to be flown over an area several times larger than that of the ground survey, using LF source signals derived from two navigation beacons, with frequencies of 139.8 kHz and 375 kHz and the AM-broadcast band transmission at 690 kHz from CBU, Vancouver. The wavetilts at each frequency can in principle determine a characteristic apparent resistivity according to the normal formulas (Crossley, 1981-I) which, of course, corresponds to the actual resistivity of a homogeneous ground structure. Also, the first-solution two-layer curves can be directly used in a depth-of-permafrost interpretation if properly scaled according to the skin-depth ratios appropriate to the E-Phase frequency as, generally,

$$\frac{h(f)}{\delta(f)} = \frac{h(18.6\ \text{kHz})}{\delta(18.6\ \text{kHz})} \quad .$$

Figure 14 shows a portion of an E-Phase survey flight-line that approximately corresponds to the ground survey line 20+00 N. The lack of comparability between the apparent-resistivity profiles at the three different frequencies is probably evidence of an anistropy due to the imperfectly horizontal layering and the different azimuthal directions to the three transmitters. The results of this survey show an unexpectedly low resistivity over the permafrost zone which had been previously well-delineated by the ground surveys. At these higher frequencies, the dielectric-loss effect is enhanced and thus the low apparent resistivity measurements might only indicate a region of anomalously high dielectric lossiness. Also, because the particular E-Phase survey system was incapable of resolving the relative phase between the horizontal and vertical components of the E field (for determination of an apparent ground resistivity, a 45° phase angle must be assumed), it is probable that resistivities are being seriously underestimated wherever the relative phase angles are low.

Such a condition could very easily arise for these higher frequencies in the permafrost zone of the ground survey area. Consequently, while the E-Phase system offers the convenience of rapidly surveying large areas, its lacking phase measurement can lead to misinterpretations of the permafrost occurrence. For accurate permafrost delineation, a wavetilt measurement of both the in-phase and quadrature components of the horizontal component of the E field would seem to be necessary.

Seismic Velocity Survey

As a final control on the Radiohm surveys, the results of a seismic refraction survey in the search for high velocity zones was provided by Dr. J. Hunter of the Geological Survey of Canada (Hunter, 1973). Using the 12 channel SIE RS4 refraction seismograph with a 10 m geophone spacing, Hunter obtained refractor velocities as high as 3990 $m \cdot s^{-1}$ in permafrost zones and as low as 1600 $m \cdot s^{-1}$ elsewhere. Generally (Fig. 15), there was a correspondence between the high seismic velocity zones and the regions of high enhanced permafrost indices PMFI , as shown earlier in Figures 7 and 8. Since the seismic method is regarded as a high reliability indicator of permafrost occurence in these regions where the soil section is typically very deep, the seismic surveys are taken to offer strong corroborative evidence that the permafrost index and the inversion results from the Radiohm surveys do, in fact, delineate permafrost in the discontinuous zone.

MAPPING THIN CONTINUOUS PERMAFROST

Two other less extensive Radiohm surveys to obtain surface- wave impedance measurements over continuous permafrost were conducted at a test site traversing the Canol Road west of Norman Wells, N.W.T., and over a permafrozen hill south-east of Tuktoyaktuk. In their undisturbed state, the soils of the Norman Wells area are known to be everywhere frozen apart from the thin summer thaw layer to at least 10 m of depth. However, part of the survey had been burned out in a forest fire some years before the surveys were conducted. Also, the Canol Road

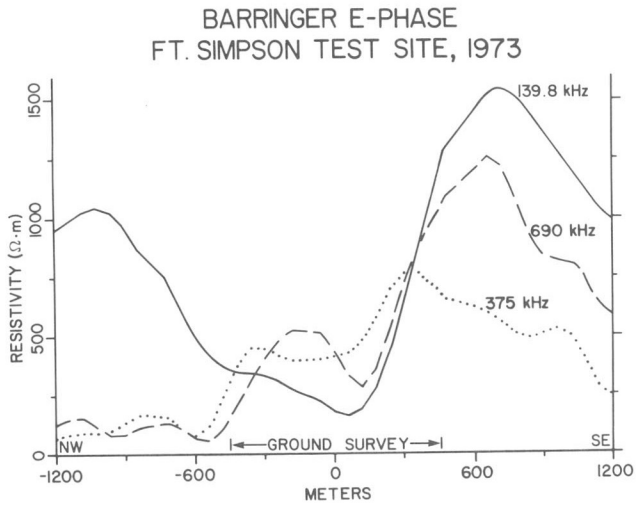

Figure 14. *A profile of apparent resistivity as measured at 3 frequencies by the Barringer E-phase airborne systems. The airborne survey was conducted in April, 1973. The profile corresponds to line 20 + 00 N of the ground survey.*

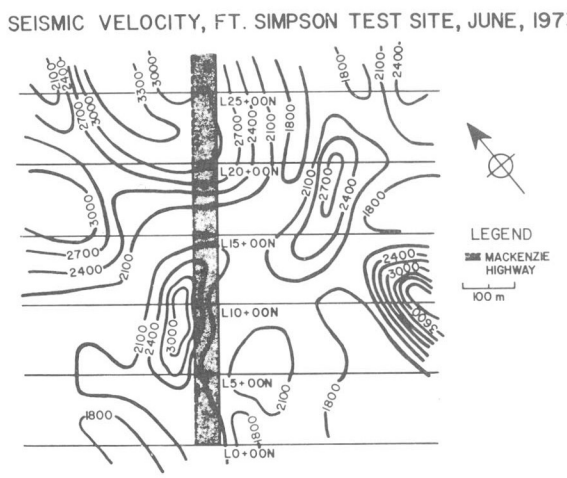

Figure 15. *Seismic velocity survey at Fort Simpson, N.W.T. conducted by Dr. J.A. Hunter, Geological Survey of Canada, June, 1973. These results have been provided courtesy of Dr. Hunter.*

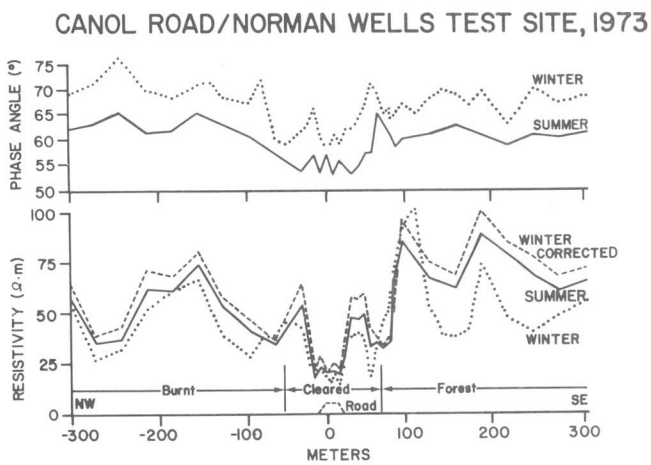

Figure 16. *The apparent resistivity and phase-angles determined from Radiohm measurements obtained in Winter and Summer surveys across the Canol Road at the Norman Wells test site, 1973.*

grade had been in place and somewhat used in this area for over 30 years. The burn zone and road have disturbed the soil cover to the extent that melting of the permafrost has taken place in these zones and, in fact, the permafrost immediately beneath the road has generally undergone partial to complete melting. (Kurfurst, et al., 1973).

Figure 16 shows Radiohm profiles on a line crossing the Canol Road. Using the method discussed earlier in this paper and by Powell (1978), the winter measurements were transformed into equivalent summer measurements (denoted winter corrected) by effectively adding a thin surface thaw layer of low resistivity. Here, where permafrost underlies the thaw layer almost everywhere, the validity of this correction procedure is clearly demonstrated by the evident correspondence of winter corrected and summer wave impedance measurements.

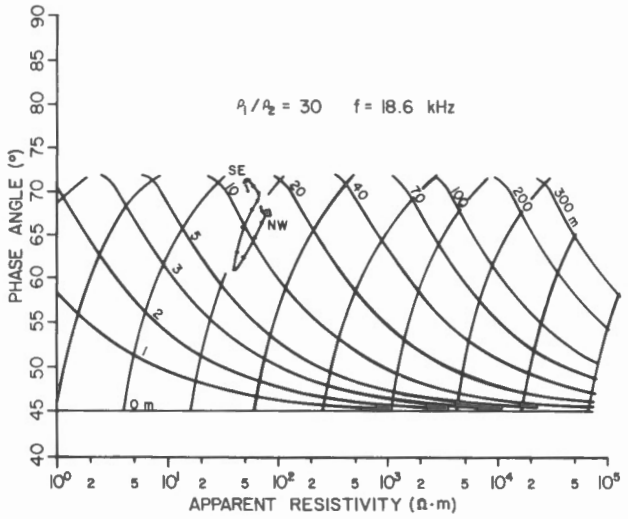

Figure 17. A scatter diagram of measurements made along one line traversing the Canol Road, superimposed on a Powell two-layer, first solution master curve set for a resistivity contrast of 30. The spatial sequence of the measurements is indicated.

All individual station measurements of the apparent resistivity and phase angle are overlain on a first-solution two-layer interpretation curve for a resistivity contrast ratio of 30 (Fig. 17). This particular representation shall be called a "scatter diagram", which provides a measure of internal consistency of the measurements. For the scatter diagram shown in this figure, local averaging of the adjacent complex surface-wave impedance measurements was applied in order to enhance the relative continuity of the data along the profile. Permafrost depths are seen to decrease towards the road through the burned forest zone from a depth of perhaps 13 m to about 7 m on the road itself. As the profile crosses the clearing to the south-east of the road in the forest shade, the permafrost depth rapidly increases again to about 13 m, as is typical of the forested zone. The disturbance of this subarctic landscape by fire and road construction has a clear and lasting effect on the permafrost thickness. These Radiohm interpretations were confirmed by Schlumberger soundings which revealed a permafrost thickness of about 15 m southeast of the road in the forested zone and about 11 m northwest of the road in the burned zone.

Thick Continuous Permafrost

On the arctic coast near Tuktoyaktuk, N.W.T., the permafrost is known to be continuous and everywhere deep, often exceeding 300 m (Hunter, 1973).

Clear ice structures are common, such as ice wedges and lenses and the unique pingo, an enormous surface frost-heave. The temperatures of the permanent ice is often well below the freezing point, perhaps -8 to -10°C in the upper regions of the ice. Consequently, ion mobility is effectively completely stopped and the DC resistivity of the pure, clear ice is correspondingly enormous, sometimes exceeding 10^7 Ω.m .

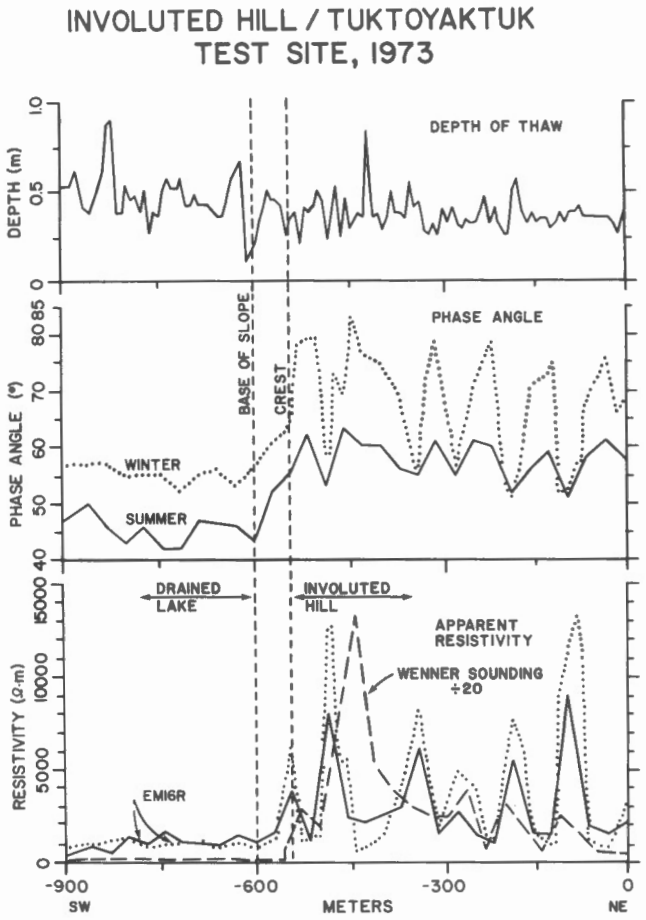

Figure 18. Summer (August, 1973) and Winter (April, 1973) Radiohm measurements along a line intercepting the "Involuted Hill" test site near Tuktoyaktuk, N.W.T. The phase angles and apparent resistivities measured are shown. Above, the depth of the summer surface thawed layer is shown.

The test site was centered on the "Involuted Hill", which is an ice-cored pingo-like hill surrounded by essentially flat terrain. On the south and west, the hill is flanked by an old lakebed, the lake having been drained some years earlier during petroleum exploration activity in the area. The lakebed itself offered a very interesting structure for our surveys since it is known that, beneath lakes, the permafrost is much thinned due to the enhanced heat transfer from the lake into its bed during the short summer season. In fact, drilling in the deepest part of the lakebed penetrated the base of the permafrost at only 30 m thickness, evidenced by artesian water flow.

Figure 18 shows summer (August, 1973) and winter (April, 1973) Radiohm profiles as taken on a line intercepting the hill. The late summer thaw layer was also probed in order to reveal its actual extent as shown on the Figure 16 above. The thaw zone is typically about 30 cm thick but was found to be almost 1 m thick on the sunny southwest side of the hill in the drained lakebed.

Figure 19 shows the Radiohm apparent resistivity measurement as superimposed above the drill-log diagram (Scott, 1975) derived from an extensive geological drill-hole survey of the Involuted Hill.

In this region, the extreme thickness of the permafrost layer requires that the second-solution master curves be applied in any interpretation for thickness and subpermafrost resistivity. On the other hand, the data were considered to be very consistent and appropriate for a computer inversion using the Marquardt's Lambda method. The least-squares optimized numerical inversion obtained, station-by-station, an estimate of the permafrost layer's thickness and a measure of sub-permafrost layer resistivity as shown in Figure 20. The permafrost thicknesses so-determined correspond reasonably well to the drill-log evidence in that no holes to 100 m depth on the hill succeeded in penetrating the permafrost layer. Also, based upon thermal gradient measurements, Mackay (personal communcication) estimated permafrost depths of 300 m in the area.

The inversions do obtain a rather striking correlation between the subpermafrost resistivity estimate and the depth estimate which indicates that these two solution parameters are highly interdependent. Perhaps the interdependence relates to the fact that, for the extremely high electrical resistivities which are expected to represent the clear ice, the dielectric loss mechanism certainly dominates the ohmic loss, and this effect has not been properly included in the inversion model.

CONCLUSIONS

Wave-impedance measurements made on the ground surface using the Radiohm method at VLF can effectively delineate the distribution and help in estimating the thickness of both discontinuous and continuous permafrost structures. Where permafrost surveys of a reconnaissance nature require a convenient and simple technique which can be rapidly and economically used in the study of relatively large areas, the Radiohm system is especially useful. For very large area surveys, the equivalent wavetilt systems operating from airborne platforms show promise, particularly if capable of measuring both the relative in-phase and quadrature components of the horizontal electric field.

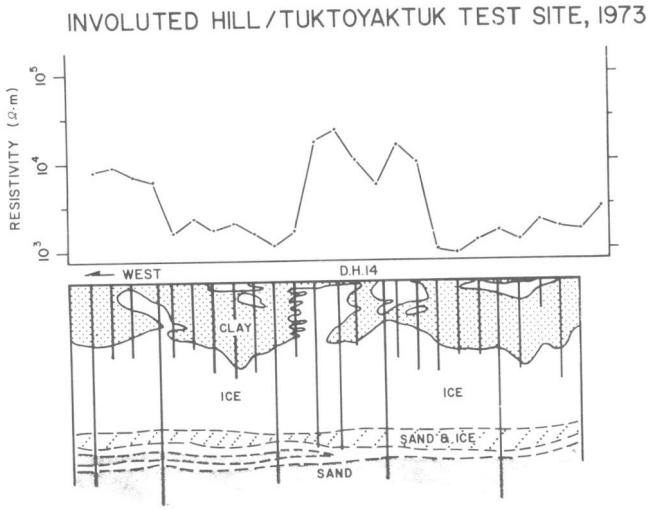

Figure 19. *Summer Radiohm apparent-resistivity measurements shown in relation to a drill-hole-frost-log interpretation. The shallow permafrost is well delineated by the high apparent resistivities.*

Because the present commercial wavetilt systems are limited to measuring only the quadrature component of the E field, the interpretation of their data in terms of a complex surface-wave impedance is ambiguous in such a way that a clear expression of permafrost is not always observable.

Several approaches to interpretation of the surface-wave impedance have been demonstrated involving both contemporary model-based numerical inversion methods and the traditional geophysical type-curve catalogues for the appropriate permafrost structural models. Also, two very useful field calculable indices $PMFI_1$ and $PMFI_2$, the first of which obtains a measure proportional to the depth of the permafrozen layer and the second of which enhances the delineable boundaries of permafrost structures, have been proposed. Geological control through drill-logs and geophysical control by means of seismic refraction surveys and DC resistivity profiling and sounding have established the validity of the interpretations and the reliability of the permafrost indices.

The ground surface-wave impedance measurements using only a single frequency in the VLF band do not offer much versatility in interpretation. It is, for example, impossible to distinguish a dielectric loss from an ohmic loss, and hence the actual electrical conductivity of structures is inseparable from their dielectric hysteresis. Moreover, a single frequency provides for only one complex measurement at each station, which allows an interpretation for only two independent parameters of a model.

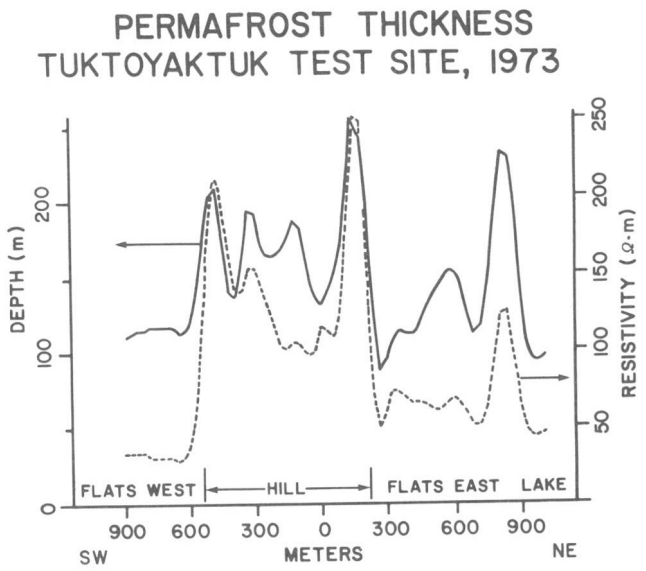

Figure 20. *A two-layer interpretation for the depth to the base of the permafrost as obtained by least-squares inversion of the Radiohm measurements made at the Tuktoyaktuk test site. The solid line indicates permafrost thickness; the dashed line indicates the resistivity of the sub-permafrost soils. Note that the two curves are closely correlated; this is an artifact of the least squares inversion indicating that the two parameters being sought are not independent.*

Consequently, only very simple geological structures can be properly resolved. The limited scope for structural interpretations and the difficulty of distinguishing dielectric from conductivity properties could be removed, in principle, through access to a broad range of independent measurement frequencies. It would be of major advantage to have a Radiohm-type instrument available that is capable of making simultaneous surface-wave impedance measurements in the VLF, LF and MF bands.

Practically, it has become obvious that the Radiohm surveys are best adapted to winter surveys in the permafrost zones, for then the surface seasonal frost combines with the underlying permafrost to provide a very resistive surface layer. The structure of the geophysical interpretation model can then often be limited to involve only a layer of undetermined thickness and high resistivity overlying a conductive halfspace. Approximate methods of transforming measurements from summer surveys for which the surface thaw layer introduces a need for some additional interpretation model complexity, into winter-like measurements has been obtained as an aid to the simplification of interpretation procedures.

Although a very comprehensive study of permafrost surveying by means of wave-impedance measurements has been accomplished in demonstrating the efficacy of these geophysical methods, the absolutely thorough assessment has not yet been achieved. Subsequent studies should be undertaken to explore the problem of thick permafrost in greater detail, to consider the use of a broader band of signal frequencies, and to evaluate the residual dielectric loss effect. With the rapid rate of northern development making increasing demands upon the earth scientists to provide detailed information on permafrost occurence and formation in the support of the essentially careful engineering studies preceding any construction, continuing research into these geophysical methods is of pressing importance.

ACKNOWLEDGEMENTS

The authors gratefully acknowledge the invaluable aid, advice and cooperation of several people: W.J. Scott, L.S. Collett, J. Hunter and P. Kurfurst of the Geological Survey of Canada, A. Becker of Ecole Polytechnique, P. Hoekstra of Northern Engineering Services, Ltd., J.D. McNeil of Geonics, Ltd., E. Bahar of the University of Illinois, J. Slankis of Texas Gulf, Inc., and C.C. Ku of McGill University. The surveys were conducted under the direction and with the logistical support of the Geological Survey of Canada during 1973 when one of us (B.W.P.) was in their employ.

The authors thank McGill University, the National Research Council of Canada, who through research grant A9017 and Energy Mines and Resources Canada who under research agreement GS1135- D13-4-4375 provided the essential financial support of this project.

REFERENCES

Addison, J.R.
1967: Electrical properties of saline ice, Ph.D. thesis, Dept. of Physics, McGill University.

Barringer Research Ltd.
1971: Technical note for the interpretation of the E-Phase system, TR71-188, Barringer Research Ltd., 304 Carlingview Dr., Rexdale, Ontario.

Collett, L.S. and Becker, A.
1967: Radiohm method for earth resistivity surveying, Canadian patent no. 795 919.

Crossley, D.J.
1981: The theory of EM surface wave impedance measurements; in Geophysical Applications of Surface Wave Impedance Measurements, L.S. Collett and O.G. Jensen (eds.), Geological Survey of Canada; Paper 81-15, Report V, p. 1-17.

Dement'ev, A.I.
1959: Principles of geocryology (Part II), Nat. Res. Council, Canada, Tech. Trans. 1287.

Hnatiuk, J. and Randall, A.G.
1975: Determination of permafrost thickness in northern wells, Paper presented at the Joint Annual Meeting of the Geological Association of Canada, the Mineralogical Association of Canada and the Geological Society of America, Waterloo, Ontario, May 15-17, 1975, (abstract) Abstract With Programs, Vol. 7, No. 6, GAAPBC 7 (1), The Geological Society of America, Boulder, p. 782.

Hoekstra, P., Sellman, P.V. and Delaney, A.
1975: Ground and airborne resistivity surveys of permafrost near Fairbanks, Alaska, Geophysics, 40, 4, p. 641-656.

Hunter, J.A.
1973: The application of shallow seismic methods to mapping of surficial materials; in North American Contribution to Permafrost -- Second International Conference, Yakutsk, U.S.S.R., National Academy of Sciences, p. 527-534.

Judge, A.S.
1973: Deep temperature observations in the Canadian north, in North American Contribution to Permafrost -- Second International Conference, Yakutsk, U.S.S.R., National Academy of Sciences, p. 35-40.

Ku, C.C.
1976 Numerical inverse magnetotelluric problems, Geophysics, 41, 2, p. 276-286.

Kurfurst, P.J., Isaacs, R.M., Hunter, J.A. and Scott, W.J.
1973: Permafrost studies in the Norman Wells region, N.W.T.; in Proceedings of the Symposium on the Geology of the Canadian Arctic, Saskatoon, J.D. Aitken and D.J. Glass (eds.), Canadian Society of Petroleum Geologists, Calgary, 368 pp.

LaFleche, P.T.
1979: Wave impedance measurements at 60 kHz, M.Sc. Thesis, Laboratory in Applied Geophysics, McGill University.

LaFleche, P.T. and Jensen, O.G.
1981: Wave impedance measurements at 60 kHz; in Geophysical Applications of Surface-Wave Impedance Measurements, L.S. Collett and O.G. Jensen (eds.), Geological Survey of Canada, Paper 81-15, Paper V, p. 67-78.

Linell, K.A. and Johnston, G.H.
1973: Engineering design and construction in permafrost regions: a review; in North American Contribution to Permafrost -- Second International Conference, Yakutsk, U.S.S.R., National Academy of Sciences, p. 553-576.

Marquardt, D.W.
1963: An algorithm for least squares estimation of non-linear parameters, J. of Soc. Indust. Appl. Math., 11, 2, p 431-441.

McNeil, J.D., Jagodists, F.L. and Middleton, R.S.
1973: Theory and application of the E-Phase airborne resistivity method, Proc. Symp. Electromag. Explor. Meth., Paper 19, University of Toronto.

Ogilvy, A.A.
1967: Geophysical studies in permafrost regions in the U.S.S.R., Mining and groundwater geophysics, Geol. Survey of Canada, Econ. Geol. Report No. 26, p. 641-650.

Olhoeft, G.R.
1975: The electrical properties of permafrost, Ph.D. thesis, Dept. of Physics, University of Toronto.

Orellana, E. and Mooney, H.M.
1966: Master tables and curves for vertical electrical sounding over layered structures, Interciencia, Madrid, 150 pp.

Powell, B.W.
1978: Radiohm mapping of permafrost, M.Sc. Thesis, Laboratory in Applied Geophysics, McGill University.

Scott, W.J.
1975: VLF resistivity (Radiohm) survey, Agricola Lake area, District of Mackenzie, Geological Survey of Canada, Paper 75-1, Part A, p. 223-225.

Wait, J.R.
1962: Electromagnetic waves in stratified media, International Series of Monographs in Electromagnetic Waves, Vol. 3, Pergamon, Toronto, 372 pp.

Zohdy, A.R.
1974: A computer program for the automatic interpretation of Schlumberger sounding curves over horizontally stratified media, U.S. Dept. Commerce Natl. Tech. Inf. Service, Springfield, VA. 22161, as U.S. Geol. Survey Rept. USGS-GD-74-017, PB-232-703.

III

MAPPING BEDROCK TERRAIN WITH THE EM16R-VLF UNIT

D. Jones* and W.M. Telford+
* MPH Consulting, Ltd.
+ Laboratory in Applied Geophysics, McGill University

Jones, D. and Telford, W.M., Mapping bedrock terrain with the EM16R-VLF unit; in Geophysical Applications of Surface Wave Impedance Measurements, L.S. Collett and O.G. Jensen editors; Geological Survey of Canada, Paper 81-15, p. 35-48, 1981.

Abstract

Mapping of bedrock terrain is often required in engineering and mineral exploration work, but the present seismic and four-electrode resistivity methods are slow and expensive. Electrical inductive measurements may usually be made much faster, permitting fairly accurate overburden depth soundings in areas where there is a distinct contrast in the conductivity between overburden and bedrock.

Using field measurements of apparent resistivity and phase angle with the Radiohm (EM16R) VLF equipmentand an estimation of conductivity contrast (from scatter diagrams). An intepretation may be carried out to give bedrock depth and the resistivity of the two layers using either a graphical method or an interactive computer based technique. Theoretical model studies show good correlation with interpretive techniques.

Résumé

L'établissement de cartes de terrains du socle est souvent requis en génie et en exploration minière, mais les méthodes sismiques et les méthodes de résistivité à quatre électrodes sont lentes et onéreuses. Il faut habituellement beaucoup moins de temps pour effectuer des mesures électriques inductives permettant des sondages en profondeur assez précis du mort-terrain dans des régions où il existe une différence marquée entre la conductivité du mort-terrain et celle du socle.

Grâce aux mesures de la résistivité apparente et à l'angle de phase, mesurés par des appareils Radiohm (EM16R) TBF, ainsi qu'à une estimation de la différence de conductivité (à partir des graphiques de dispersion), on peut réaliser une interprétation donnant la profondeur du socle et de la résistivité des deux couches en se servant soit d'une méthode graphique soit d'une méthode interactive informatisée. Les études effectuées sur le modèle théorique font apparaitre une bonne corrélation avec les techniques d'interprétation.

INTRODUCTION

Overburden, frequently but by no means always more conductive than barren bedrock, has long been a problem in exploration geophysics. Base metal exploration, engineering and groundwater geophysics are affected by the presence of overburden, since it may entirely obscure or seriously distort the response of interesting structures in the bedrock and/or introduce spurious anomalies due to variations in thickness.

Although depth of bedrock may be determined by shallow drilling and by geophysical techniques such as shallow refraction seismic and resistivity sounding, these operations are slow and expensive and would not be considered in mapping large areas. Furthermore, only resistivity, the least reliable of the three, provides any information on the electrical characteristics of the overburden.

The aim of this work was to develop a relatively cheap and fast geophysical method for mapping bedrock terrain. An electrical type of measurement appears to satisfy these requirements, provided the instrument does not use elaborate electrode arrays as in DC resistivity. An alternative is the Cagniard type of magnetotelluric sounding (Cagniard, 1953; Crossley, 1981-I), from which an apparent resistivity and phase angle may be obtained, both being particularly diagnostic of layered (one-dimensional) structure. The horizontal H field is detected by a suitably oriented coil sensor on the ground. Although the orthogonal horizontal E field requires a pair of electrodes in ground contact, their separation is generally constant and relatively small, since the expanding spread necessary for resistivity sounding is replaced by a variable frequency.

Magnetotellurics has mainly been employed for deep sounding at frequencies of 10^{-3} - 1 Hz, although for overburden - bedrock measurements (1 - 100 m) it is feasible to use frequencies in the audio range and probably higher. At present, however, only ρ_a may be determined directly, while the phase angle φ must be extracted through elaborate analysis of analog or digital records. Furthermore, there is no suitable equipment readily available.

In the VLF range (15 - 25 kHz) a commercial instrument - the EM16R from Geonics Ltd. - has been designed to receive ground wave signals from high power transmitters normally used for navigation (Crossley, 1981-I). These units detect orthogonal horizontal E and H fields, the former detector consisting of two electrodes containing pre-amplifiers spaced 10 m apart, the azimuth being in-line with the transmitter. The output is an apparent resistivity in the range 10 - 30000 Ω.m and phase angle 0 - 90°. Thus the EM16R is quite suited to measurements of overburden characteristics. In many locations, it may be possible to detect two or more VLF stations at different azimuths, indicating possible anisotropy or lateral changes in structure in addition to the desired one-dimensional geometry. On the other hand, the VLF frequency band is not sufficiently broad to produce a true sounding in the MT sense.

VLF THEORY

General

The theory of VLF propagation and penetration of the subsurface has been treated elsewhere and in this volume (Wait, 1962; Keller and Frischknecht, 1966; Crossley, 1981-I) Briefly, the EM16R instrument measures apparent resistivity and phase angle in the forms

$$\rho_a = \frac{1}{2\pi f \mu_0}\left|\frac{E}{H}\right|^2 = \frac{1}{2\pi f \mu_0}|Z_0|^2 \qquad (1)$$

$$\varphi = \tan^{-1} Z_0$$

where E and H are orthogonal, horizontal, electric and magnetic fields, mV/km and gammas (or nT) respectively, whose direction is determined by the VLF transmitter location with respect to the site, f is the frequency in Hz, and Z_0 is a complex surface impedance, in ohms, in the site vicinity.

In homogeneous isotropic ground, ρ_a is the true resistivity and the phase angle is 45°. Over stratified ground having several layers of different resistivity and thickness, ρ_a is a function of these parameter and the phase generally will not be 45°, depending particularly on the nature of the top bed which controls the depth of wave penetration. It is not possible to determine thickness and resistivity of the several beds with this equipment.

In the vicinity of lateral changes in structure (dipping contacts, dikes, etc., ie. two- and three-dimensional geometry), the ρ_a and φ values will also be affected, in a more complex fashion. The treatment of data becomes more difficult and measurements in at least two azimuths, preferably orthogonal, are necessary, as mentioned previously.

Displacement Currents

In the previous section, the relations for ρ_a and φ were derived from a plane wave simplification of the diffusion equation, in which displacement currents were considered insignificant. The latter assumption seems reasonable for frequencies $\leqslant$ 5 kHz, but at 20 kHz in ground of resistivity greater than 20 kΩ.m, it may not be valid (For a more complete treatment, see Crossley, 1981-I.)

Theoretically, the addition of a term containing displacement current modifies the diffusion equation, so that the propagation constant becomes

$$\gamma = -\sqrt{i\omega\mu\sigma - \omega^2\epsilon\mu}$$

where $\mu = \mu_0 = 4\pi \times 10^{-7}$ H.m^{-1}, the permeability of free space, $\omega = 2\pi f$, σ is the ground conductivity, in S.m^{-1}, and ϵ is the dielectric permittivity in F.m^{-1}. As developed previously (Crossley, 1981-I, equations (99)-(100)), this leads to a modified value for both ρ_a and φ in homogeneous ground

$$\frac{\rho_a'}{\rho} = \frac{1}{\sqrt{1+\omega^2\epsilon^2\rho^2}}$$

and

$$\tan\varphi = \sqrt{1+\omega^2\epsilon^2\rho^2} - \omega\epsilon\rho \simeq 1 - \omega\epsilon\rho \qquad (2)$$

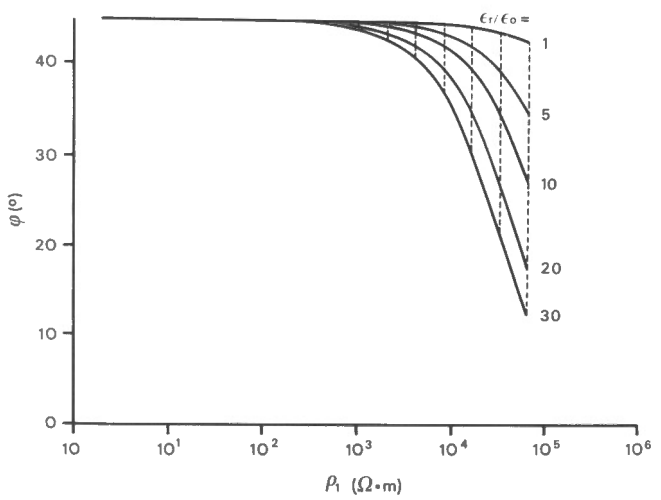

Figure 1a. Variation of phase angle with resistivity for a variety of dielectric constants and homogeneous earth.

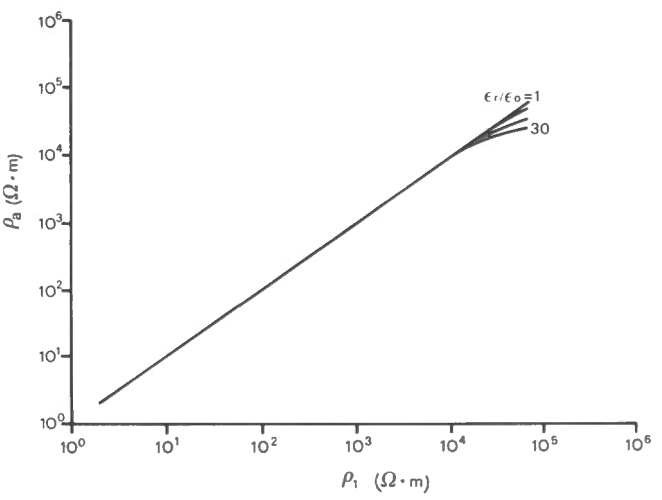

Figure 1b. Variation of apparent resistivity with resistivity for a variety of dielectric constants.

for vertical incidence (i.e. $\theta = 0°$; see Crossley (1981-I).), where ρ is the actual ground resistivity. Consequently, both parameters would appear smaller than their proper value, the phase angle being more affected. Figures 1a and b illustrate this modification in somewhat different plots from Crossley's (1981-I) Figure 7.

Whether an appreciable displacement current component exists has not been resolved by field measurements. As an example, assume f = 20 kHz, ρ = 20 kΩ.m , $\epsilon = 10\,\epsilon_0 \simeq 9 \times 10^{-11}$ F.m^{-1} , then $\omega\epsilon\rho = 0.2$. The value of φ is decreased to $\sim 39°$ or 13%, while ρ_a is only 2% smaller. If $\omega\epsilon\rho = 5$ (f = 20 kHz, $\rho = 4.4 \times 10^5$ Ω.m , $\epsilon = 9 \times 10^{-11}$ F.m^{-1}), $\varphi = 2.5°$, ρ_a = 40 kΩ.m . If either pair of values were obtained in a field measurement, they would merely indicate a highly resistive two-layer structure with $\rho_2 > \rho_1$.

Although one might suggest an appreciable dielectric effect due to a large value of ϵ rather than ρ, this implies a considerable amount of water since most rocks are listed as having values less than $10\,\epsilon_0$. The water, however, would surely lower ρ by several orders of magnitude, making the product $\omega\epsilon\rho$ insignificant.

The presence of an appreciable dielectric effect, although an interesting problem, is not significant in this work, since the measured field resistivities were generally less than 3000 Ω.m except in one small section in the first survey area.

TWO LAYER MODEL

This is the desirable structure in the present study; its response to a plane wave has been given previously (Crossley, 1981-I, Fig. 8a). Three parameters describe this model completely - resistivity of the bottom bed ρ_2, resistivity and depth of the overburden ρ_1 and h_1 . After measuring ρ_a and φ in the field, the structure remains indeterminate unless we know one of these parameters. Either ρ_1 or ρ_2 could be found separately with a very shallow or deep sounding which would require additional measurements with a different instrument. The depth h_1 might be known at a few locations, but this is not a significant possibility.

If neither ρ_1 or ρ_2 have been measured directly, we may make an estimate of one or the other, or possibly their ratio, to solve the problem. It is easy to show that when the values of ρ_1 and ρ_2 are considerably different ($\rho_1/\rho_2 \geqslant 10$ or $\leqslant 0.1$, say) a 100% error in the ρ_2/ρ_1 estimate will produce a smaller change in h than a similar error in estimating ρ_1 or ρ_2 individually.

However, if we use the ratio ρ_2/ρ_1 an ambiguity arises. There are two possible solutions for h_1 and ρ_1 , as discussed by Crossley (1981-I) and originally noted by Wait (1962). This ambiguity is illustrated in Figures 2a and b, where φ is plotted against ρ_a for various values of h_1 and ρ_1 with a fixed ratio of 30 for ρ_2/ρ_1 and f = 20 kHz. Two plots are required for clarity; when the phase angle reaches a maximum deviation from $\pi/4$ radians, the curves are folded back and become asymptotic to $\pi/4$. In fact, these are three-dimensional surfaces, the third axis being ρ_2/ρ_1 or ρ_1 .

As an example, with $\varphi = 27.5°$, ρ_a = 1000 Ω.m, Figure 2a gives $\rho_1 \simeq 900$ Ω.m, $h_1 \simeq 82$ m, while Figure 2b makes $\rho_1 \simeq 80$ Ω.m, $h_1 \simeq 3$ m. In the first case, ρ_2 becomes 27 kΩ.m , in the second 2400 Ω.m . (Either set of values is quite practical at 20 kHz since the respective skin depths would be about 30 m and 600 m.)

Both solutions are rather insensitive to changes in ρ_2/ρ_1 , where φ is close to $\pi/4$ radians ; at small phase angle, however, they are strongly affected. For a complete range of ρ_2/ρ_1 , the curves retain their characteristic shapes ($0 \leqslant \rho_2/\rho_1 \leqslant \infty$), although the phase angle deviation from $\pi/4$ radians increases with the contrast and, of course, the phase range is from $\pi/4$ to $\pi/2$ radians for $\rho_2/\rho_1 < 1$.

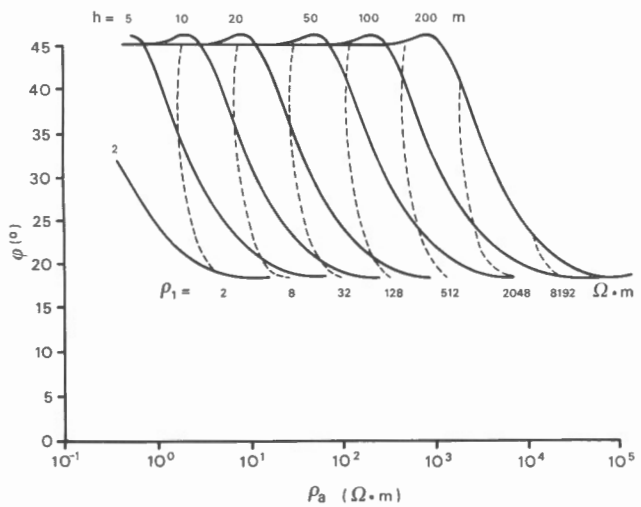

Figure 2a. Two layer curves. Resistivity contrast ρ_2/ρ_1 = 30. Solution 1.

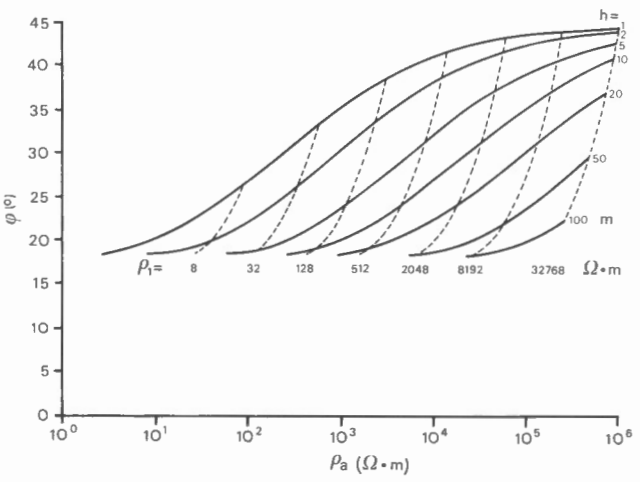

Figure 2b. Two layer curves. Resistivity contrast ρ_2/ρ_1 = 30. Solution 2.

Graphical Interpretation

Although it is a straightforward procedure to use these curves, a large suite is required to cover the range of ρ_2/ρ_1 , and it is attractive to condense these. The equations for ρ_a and φ may be written in several forms (Crossley, 1981-I, etc.), one pair of which is reproduced below

$$\sqrt{\frac{\rho_a}{\rho_1}} = \frac{1+\sqrt{m}\tanh \gamma_1 h_1}{\sqrt{m}+\tanh \gamma_1 h_1} \qquad (3)$$

and

$$\tan(\varphi - \pi/4) = \frac{-\sin\sqrt{2}\,|\gamma_1|h_1}{\sinh 2(|\gamma_1|h_1/\sqrt{2} + \tanh^{-1}\sqrt{m})} \qquad (4)$$

where $\sqrt{m} = \gamma_2/\gamma_1 = \sqrt{\rho_1/\rho_2}$.

Since the curves in Figure 2a, b are similar for constant $\sqrt{m}$ except for a lateral shift with depth, if we make φ constant, the product $|\gamma_1|h_1$ is constant, and

$$|\gamma_1|h_1 = |\gamma_1'|h_1' = \text{constant} \quad ;$$

and since $|\gamma_1|h_1 = \sqrt{\mu\omega/\rho_1}h_1$, we have $h_1 \propto \sqrt{\rho_1}$. Similarly, in the first equations, $\tanh|\gamma_1|h_1$ is constant, so $\sqrt{\rho_a} \propto \sqrt{\rho_1}$. That is, for constant φ and ρ_2/ρ_1 , h_1 and ρ_a increase proportionally with ρ_1 and $h_1 \propto \sqrt{\rho_a}$, so that

$$h_1' = \sqrt{\frac{\rho_a'}{\rho_a}}\, h_1$$

This permits a reduction of the various two-layer curves to a single set, with ρ_a and φ as ordinates and plotting curves of constant ρ_2/ρ_1 and ρ_1 for fixed h_1 . The result is displayed in Figure 3. As an example of its use, we assume the following:

$\rho_a = 1000\ \Omega.m$,

$\varphi = 20^\circ$,

$\rho_2/\rho_1 = 30.$

After locating the point for ρ_a and φ we move along the 20° horizontal line to intersect the $\rho_2/\rho_1 = 30$ curve. There are, of course, two possibilities and vertical lines from there to the abscissa give $\rho_a' = 1200\ \Omega.m$ and $60\ \Omega.m$.

Then, since the curves are for $h_1 = 10$ m, we find

$$h_1' = \sqrt{\frac{\rho_a'}{\rho_a}}\, h_1 = 11 \text{ m} \quad \text{or} \quad 2.5 \text{ m}$$

and

$$\rho_1' = \frac{\rho_a'\rho_1}{\rho_a} = 216\ \Omega.m \quad \text{or} \quad 11\ \Omega.m$$

(where ρ_1 was found from the original intersection of ρ_a and φ). Finally,

$$\rho_2' = 6\,500\ \Omega.m \quad \text{or} \quad 330\ \Omega.m$$

Figure 3 may also be used at other frequencies, since

$$|2\pi\mu f/\rho_1|h_1 = |2\pi\mu f'/\rho_1'|h_1'$$

However, if f' requires measuring in a different direction than f , because of station location, possible anisotropy - as mentioned in the introduction - may produce an error in h_1'.

Scatter Diagrams

There remain two unresolved problems, to select the correct resistivity contrast and the correct solution from two possible in each case. Again, the fact that the variation in ρ_2/ρ_1 does not affect the general curve shapes suggests a method of estimating the proper ratio.

By plotting the field station data on the same scale as is used on the two-layer curves, the scatter of the phase angle readings will indicate the minimum possible resistivity contrast. Such plots (See also Powell and Jensen, 1981-II.) are shown in Figures 4a and b, where a minimum phase angle of about 19° is superimposed on curves for $\rho_2/\rho_1 = 30$ and 20. In the latter case, several scatter points lie below the minimum phase angle which is approximately 22°. Of course, the data would also fit curves with larger ρ_2/ρ_1 . Clearly, any available controls from the survey area should be used as an aid to fitting the data to proper ρ_2/ρ_1 values and also for selecting one of the two solutions (which generally produce widely different values of h_1).

The scatter diagrams may also provide trends in h_1 or ρ_1 . For a simple two-layer structure the data will be closely clustered about a point; where ρ_1 is inhomogeneous, the trend would lie roughly on a curve of constant depth. Dipping bedrock with homogeneous ρ_1 may be indicated by trends of constant layer resistivity for which the data fit would be clearly better for one solution than the other. Although this type of analysis is useful, it is not very practical for large scale surveys.

Two-Layer Mathematical Solution

It is possible to obtain the two solutions of the two-layer problem mathematically. Rewriting equation (4) with

$$x = |\gamma_1|h_1/\sqrt{2} \quad , \quad y = \tanh^{-1}\sqrt{m} \quad , \quad K = \tan(\varphi - \pi/4)$$

we have

$$K = -\sin 2x/\sinh 2(x+y).$$

where K has been measured and estimated. For a conductive overburden, K is negative, and

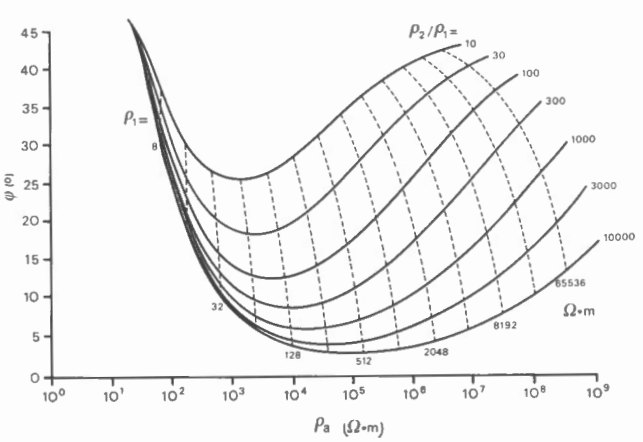

Figure 3. *Two layer curves. Contrast depth* h_1 *, variable* ρ_2/ρ_1 .

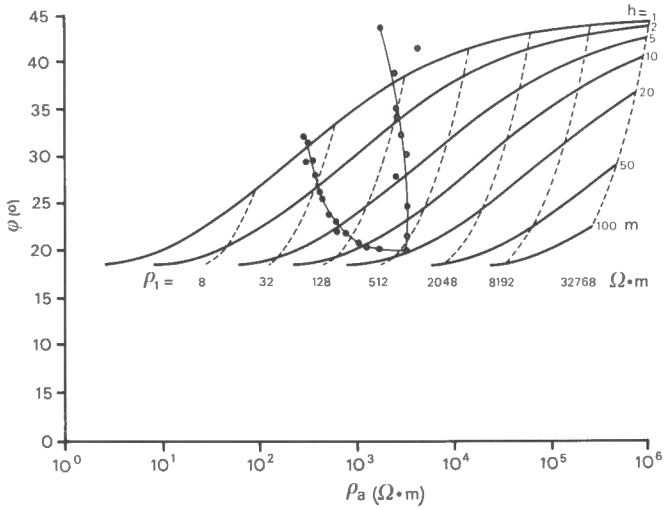

Figure 4a. *Solution 2 curves, ρ_2/ρ_1 = 30 with scatter diagram overlaid.*

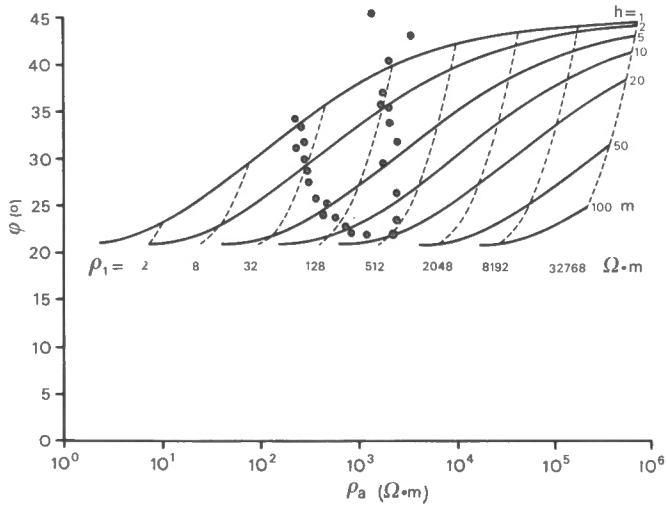

Figure 4b. *Solution 2 curves, ρ_2/ρ_1 = 20 with scatter diagram overlaid.*

$$K = \sin x \cos x / \sinh(x+y) \cosh(x+y)$$

We can solve for x by expanding the functions in series, truncating after three terms, by several methods. Graffe's root square technique gave 9 roots of the equation, 7 of which were either complex or negative. The two positive real roots, approximatly equal to solutions obtained graphically, were then refined by Newton's method of successive approximations which is given by

$$x_{n+1} = x_n - \frac{f(x)}{f'(x)}$$

where x_n is the approximate value from Graffe's method, x_{n+1} is the calculated value for the second iteration, $f(x) = K \sinh 2(x+y) - \sin 2x$ and $f'(x) = \partial f/\partial x$.

It is thus possible to refine the two results, compared to the graphical values, convergence generally being obtained after 2 to 5 iterations.

Filtering of Field Data

Low pass filtering of field data may be useful when there is excessive geologic (generally high frequency) noise. Filtering was performed on the complex surface impedance measurements. In the time domain, the filter is a series of discrete weighting coefficients and is combined with a data series using a convolution operator, as in the relation

$$z_t = g_t * f_t = \sum_k g_k f_{t-k}$$

where g_t = input data series
f_t = filter
k = filter length
z_t = output series.

Since z is complex, f and g are transferred by Fourier transformation into the frequency domain in which convolution corresponds to multiplying frequency - amplitude curves and adding frequency - phase curves. Filtered z data is then returned to time domain by inverse Fourier transformation and the modified ρ_a and φ data extracted from z .

Model Studies

Theoretical results were developed for a number of models, simulating common geological features associated with the overburden - bedrock structure, as an aid to interpretation of field surveys. The impedance network numerical method was used: this technique has been described elsewhere (Slankis, 1970; Ku et al., 1973; Doborzynski, 1974; Kisak, 1976) and will not be dealt with here. The accuracy, compared to the few possible analytical solutions, appears to be about ±10%. The following models were considered:

1. Horizontal bedrock with isotropic layer resistivity. This is a trivial case and gives the expected result for h_1 and ρ_1, within ±10%. Since the scatter diagram is a single point, there are no trends and either solution is equally probable.

2. Horizontal bedrock with anisotropic overburden. Model and calculated values are shown in Figure 5a. The minimum phase angle is about 22° and the scatter diagram was a good fit on only one of the curve sets for ρ_2/ρ_1 = 20, where the trend indicated a constant h_1 , as is clear from Figure 5b. Interpreted results for h_1 and ρ_1 are compared with the corresponding model parameters in Figure 5c. Values for h_1 are within 10%, but the ρ_1 data show a larger discrepancy and a large variance.

3. Dipping bedrock with isotropic layer resistivity. Model and data profiles are shown in Figure 6a. The value $\varphi_{min} \simeq 19°$ suggests $\rho_2/\rho_1 \simeq 30$; one set of such curves with the scatter diagram is shown in Figure 6b. Both solutions would be considered, since the left hand part of the scatter diagram fits a ρ_1 trend in 6b, while the right flank would fit a different ρ_1 trend on the second set of ρ_2/ρ_1 curves (not shown). Calculated and observed parameters are shown in Figure 6c.

In the vicinity of φ_{min} there is poor agreement with the model, particularly for ρ_1 : this is where the two possible solutions overlap. Again the h_1 results are better than those for ρ_1 .

4. Bedrock anticline. This model resembles the previous; the data are folded about the middle of the profile, however, and the results are better than for the dipping bedrock case.

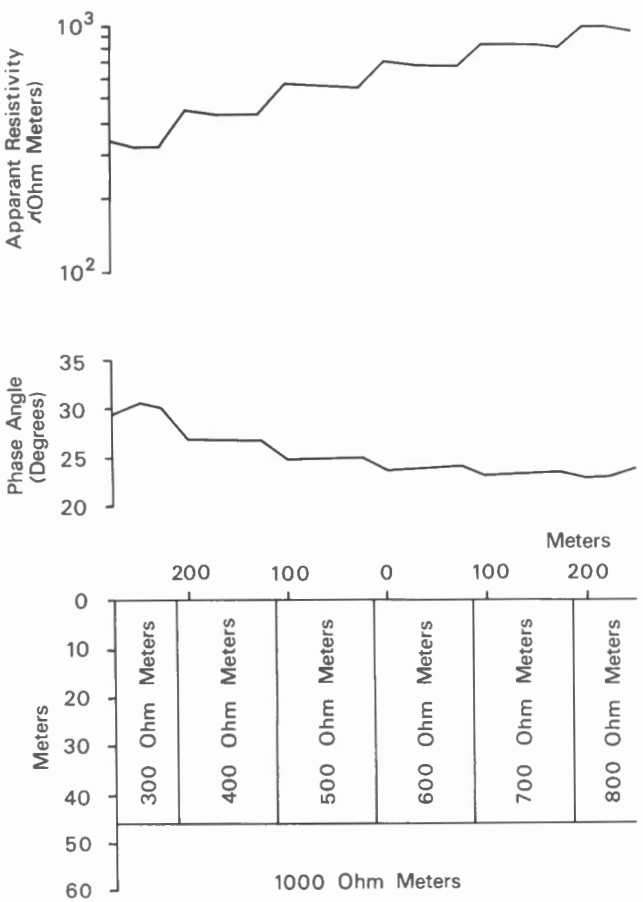

Figure 5a. Model of anisotropic first layer resistivity and horizontal bedrock with profiles.

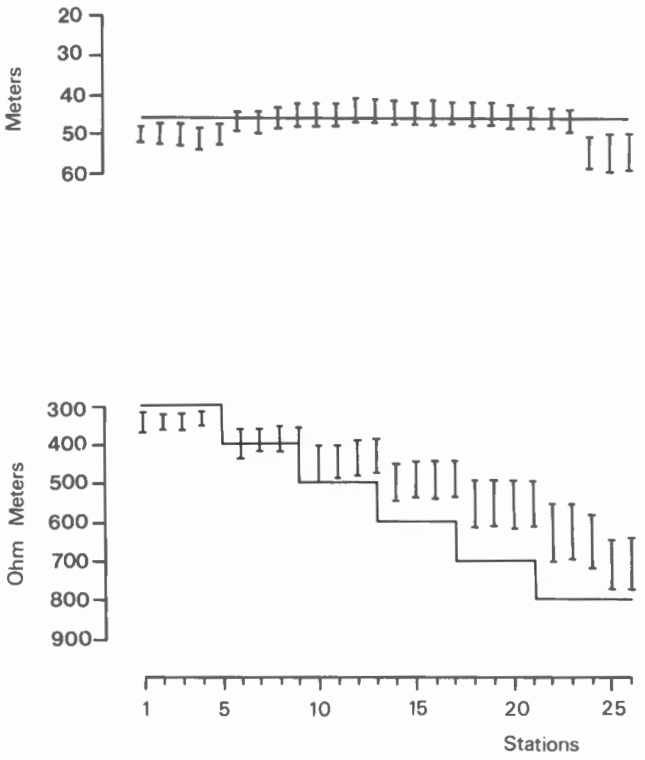

Figure 5c. Model of Fig. 5a. Comparison of interpreted and model parameters.

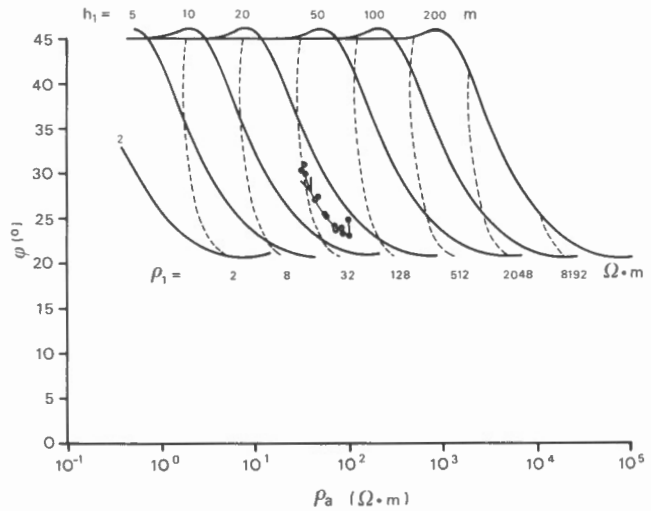

Figure 5b. Model of Fig. 5a. Solution 1 curves, ρ_2/ρ_1 = 30 with scatter diagram overlaid.

5. Vertical bedrock step. Figure 7a displays an abrupt change in ρ_a and φ at the step and suggests a profile over a vertical contact. However, the scatter diagram (not shown) is different in character from that for a step and the trend suggests constant ρ_1 rather than h_1. Figure 7b compares ρ_1 and h_1 profiles with the model. Again results for h_1 agree with the model better than those for ρ_1, although the latter are diagnostic of the step.

6. Vertical bedrock contact under horizontal isotropic overburden. Profiles of ρ_a are similar to those for DC or MT resistivity over a contact; along with the scatter diagram they suggest a change in ρ_2/ρ_1 over the profile. The resultant fit is similar and somewhat better for h_1 than in the previous example, while the ρ_1 profile provides evidence of the contact.

7. Vertical dike under horizontal isotropic overburden. The profiles here suggest a double contact of steep dip and are not reproduced.

Summarizing the model results, it is found that the calculated data for these common structural features fit well when the models are essentially one-dimensional (80% of all stations within 10% of correct values, 60% within the error tolerance). In the vicinity of two-dimensional structures there was poor correlation, although this did not persist for more than about 100 m (4-8 times their depth) either side of the anomaly. The estimation of resistivity contrast produced reasonable results in all cases, while the observation of trends in the scatter diagrams generally permitted discrimination between the two possible solutions for ρ_1 and h_1.

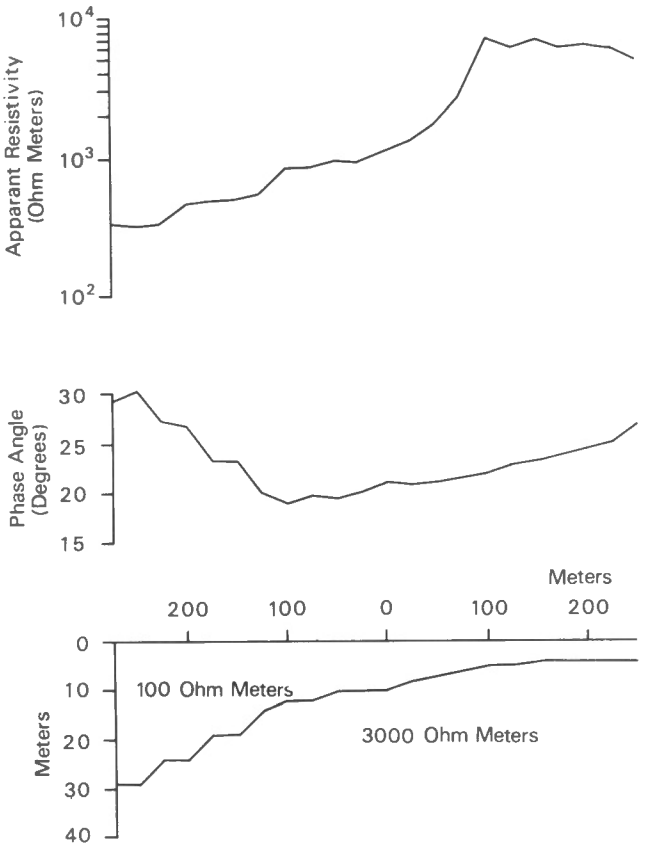

Figure 6a. Model of dipping bedrock with profiles.

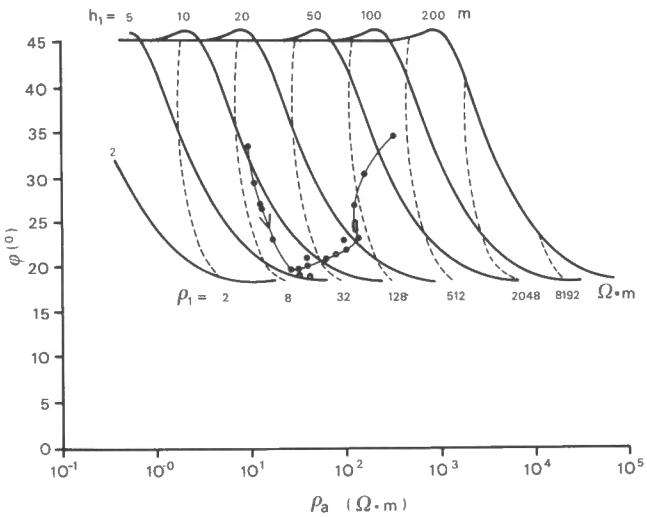

Figure 6b. Model of Fig. 6a. Solution 1 curves, ρ_2/ρ_1 = 30 with scatter diagram overlaid.

Procedure for Interpretation

Based on the preceding it is possible to process large quantities of data by following the sequence outlined below.

a) If necessary, apply a low pass filter to reduce geologic noise.

b) Plot scatter diagrams of selected profiles.

c) Using the scatter diagrams and information from the survey area (bedrock drill holes, overburden resistivities, evidence of two-dimensional structures from profiles, etc.) estimate ρ_2/ρ_1 and select the correct solutions.

d) Compute depth and resistivity of overburden.

e) Compare results with area control information.

f) Repeat c) to e) where necessary.

FIELD SURVEYS AND INTERPRETATION

Field results are presented from four surveys carried out during 1966-67. These areas provided some external control for a more comprehensive estimation of the interpretation results, particularly bedrock depth estimates: they also displayed a considerable variation of data to test the interpretation procedure. Unfortunately, information on ρ_1 was available in only one of the four areas.

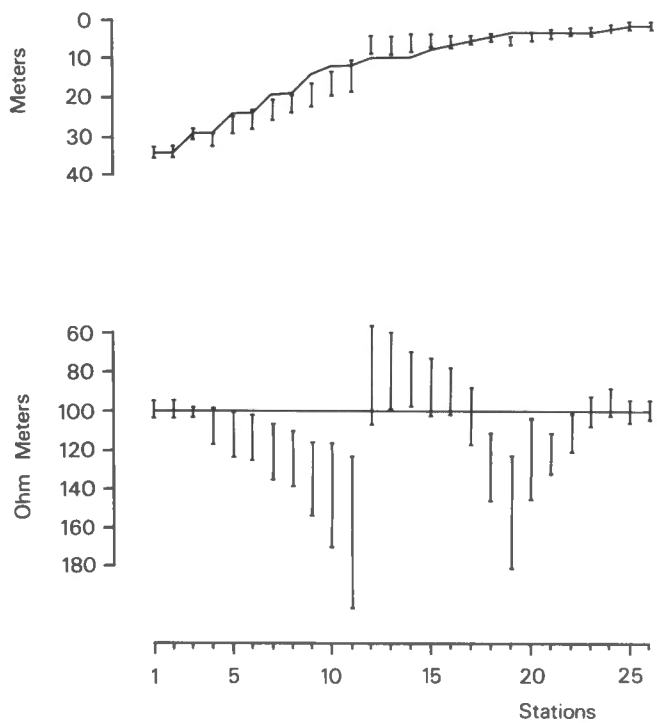

Figure 6c. Model of Fig. 6a. Comparison of interpreted and model parameters.

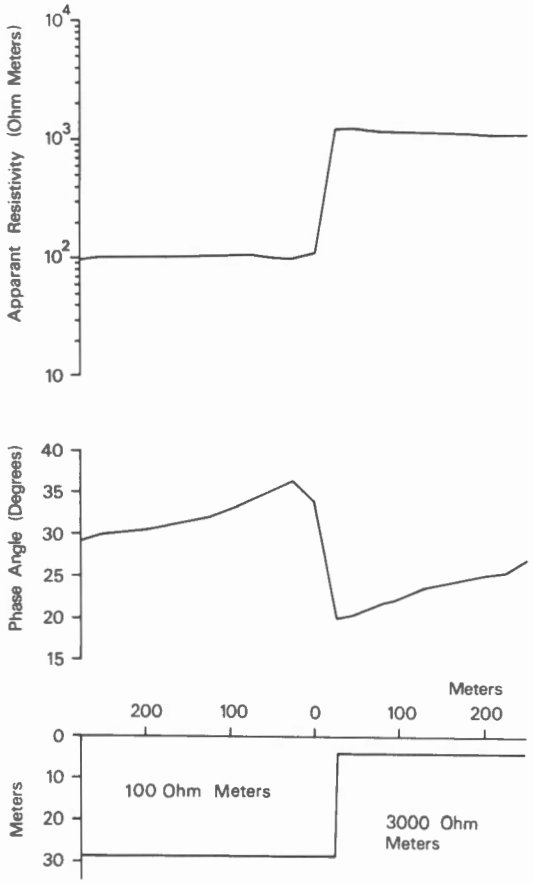

Figure 7a. Model of vertical step with profiles.

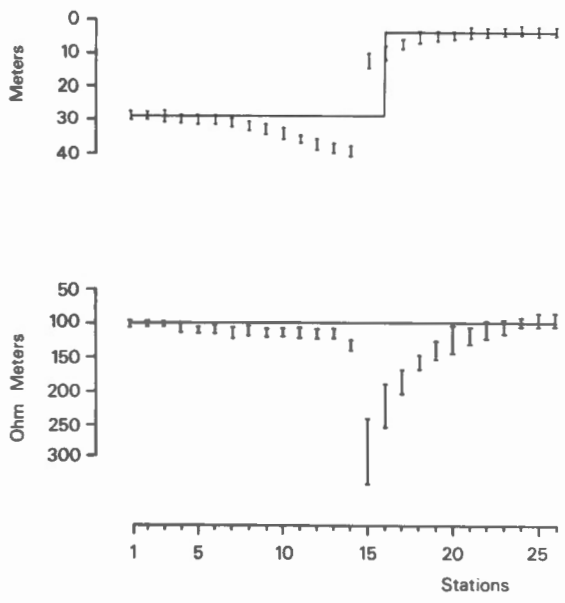

Figure 7b. Model of Fig. 7a. Comparison of interpreted and model parameters.

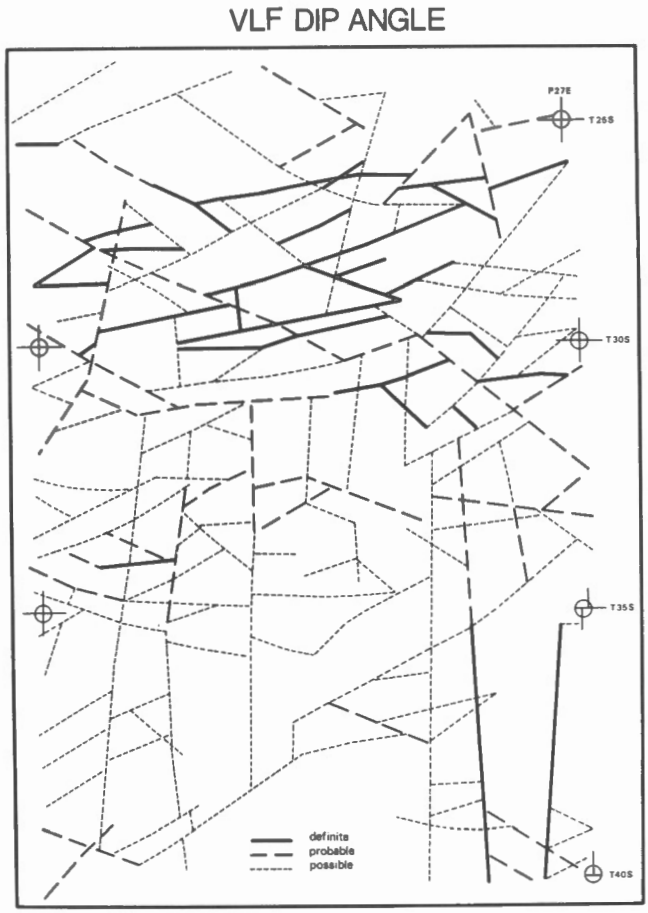

Figure 8. Area #1. VLF dip angle grid map.

Dip angle surveys were carried out with the EM16 instrument in the first three areas, in addition to the EM16R measurements, as an additional aid to interpretation. As is well known (Paterson and Ronka, 1971; Telford et al., 1977) the VLF dip angle technique is useful for mapping shallow structures, such as thin sheets, contacts, etc..

Area Nº 1

On a grid approximately 1500 m N-S by 1000 m E-W, profiles were run N-S at 50 m spacing with stations every 20 m. The area is quite flat (15 m maximum relief) with swampy sections containing creeks in the north and southeast portions, the remainder being dry. Overburden is glacial till with thin muskeg cover in the northern one-third of the grid and there is no outcrop. Shallow drilling indicated sandstone bedrock, fine to coarse grained, with minor hematite staining: thin brecciated bands through the sandstone were noted in the northern part of the grid. Bedrock control was provided by 31 drill holes.

The VLF dip angle grid map, shown in Figure 8, was compiled from two stations - Cutler, Maine and Jim Creek, Washington - which were roughly 90° in azimuth. Structures are classified as definite, probable and possible. There is a strong E-W trend in the northern section, while the remainder is predominantly N-S, particularly evident in the SE corner: these linear trends coincide with creeks in the swampy ground and indicate a possible lithologic change.

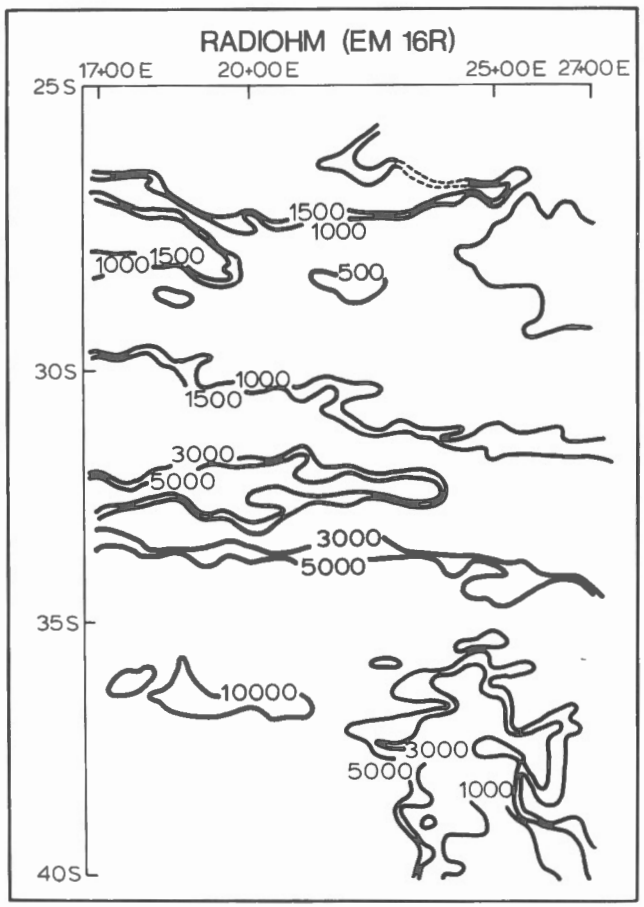

Figure 9. Area #1. EM16R contour of constant apparent resistivity ρ_a .

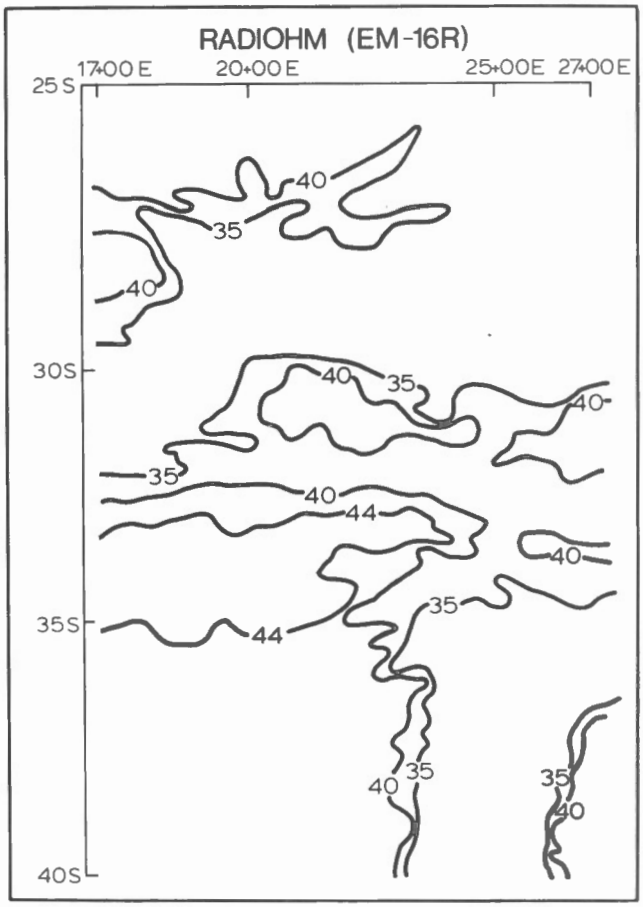

Figure 10. Area #1. EM16R contour of constant place angle φ .

Contours of ρ_a and φ, using the Jim Creek transmitter and the EM16R instrument, are displayed in Figures 9 and 10. Maximum variations in ρ_a and φ were 75 - 30000 Ω.m (EM16R upper limit) and 15°- 50°, both parameters increasing generally to the south. Initially the ρ_a and φ data were interpreted separately. Figure 9 appears to have three main zones.

1) An area of $\rho_a < 1000$ Ω.m trending E-W and enclosing all the major E-W anomalies shown in Figure 8, in the northern part of the grid.

2) Area about 400 m south of the first with $\rho_a \simeq 1000$-5000 Ω.m and E-W trend.

3) Two zones in the southern 30% of the grid separated by 5000 Ω.m contours. The SW corner shows steadily increasing resistivity, while in the SE section $\rho_a < 3000$ Ω.m coinciding with the swamp.

It is suggested that leaching of the sandstone and/or south dip of the conductive brecciated zones may be the cause of the increase of ρ_a and φ from north to south.

The phase contours in Figure 10 generally indicate an overburden more conductive than bedrock and show four zones which correlate with the areas in Figure 9. A sharp gradient of φ between the zones again suggests lithologic changes.

After filtering the data, scatter diagrams were prepared, as illustrated by the plots for line 24+00E in Figure 11. Stations 1-25 (Fig. 11a) have a vertical trend, fitting an interpretation curve with $\rho_2/\rho_1 = 10$ and following a line of constant ρ_1 in the second solution version. In Figure 11b, stations 26-44, the φ values are generally larger, so $\rho_2/\rho_1 < 10$: the first 10 stations show a trend which matches constant ρ_1 for $\rho_2/\rho_1 = 5$. Stations 36-44 appeared to fit a first solution constant depth trend. However, this produced a value of $h_1 \simeq 200$ m which was quite unrealistic and the second solution was used instead. In Figure 11c, data points 45-60 gave a reasonable fit for $\rho_2/\rho_1 = 10$, second solution, constant h_1 trend. Stations 61-73, Figure 11d, have lower φ values and were fitted to a second solution constant h_1 for $\rho_2/\rho_1 = 20$.

The changes in scatter diagram character - at stations 25, 36, 45 and 61 - coincide with grid areas where gradients of φ and ρ_a are pronounced. Similar analysis, employing the procedure outlined previously, was carried out for all stations.

Location of the geologic control - 25 percussion (to bedrock) and 6 diamond drill holes - is shown in Figure 12. Although the coverage is far from uniform, it overlaps to some extent the zones which appeared to be distinctly different. Correlation of interpreted with true depths

is given in Table 1. Within the error estimate (based on variance of instrument readings), 67% of these well agree with the drill hole data. Stations with poor correlation are mainly where phase angles are 44° to 46°, when it is difficult to use the present method successfully because the curves are convergent. Complete maps of the grid for interpreted h_1 and ρ_1 values are not shown. The latter cannot be assessed, since there is no information on ρ_1 .

Area Nº 2

The grid for this area is identical to the previous, except that the NS lines are 1000 rather than 1500 m. The east half is entirely flat, with about 70% standing water - swamp which produced relatively low ρ_a and φ readings. The west half, however, was mainly dry with appreciable relief; phase angles were in the range 50 - 60°, associated particularly with high ρ_a to the north.

The VLF dip angle map, compiled from Cutler and Jim Creek stations, displayed a rather complex structural pattern with no obvious trends. Horst and graben block faulting had been suggested, but not substantiated. High ρ_a readings in the northwest grid corner were outlined by the VLF, but no conductors appeared within this block.

The range of EM16R readings was 1000 - 11000 Ω.m and 28 - 60° for ρ_a and φ respectively, both decreasing to the east and south. Using the ρ_a data, an attempt to divide the grid into smaller sections appeared to outline three zones.

1) Low lying wet ground with $\rho_a < 1000$ Ω.m, where bedrock was generally quartz-feldspar-gneiss with some deeper breccia zones.

2) Similar to the first, with $\rho_a \simeq 1000$ - 3000 Ω.m, the larger values due to ground relief.

3) Northwest corner with $\rho_a > 3000$ Ω.m .

The phase angle map appeared more complex than that for ρ_a; areas with $\varphi > 50°$ coincided mainly with high zones and the gradient was quite sharp between 45° to 50°. The remaining grid area suggested two zones - one mainly in the northeast, where $\varphi > 40°$, associated with $\rho_a < 1000$ Ω.m, and the second for $\varphi < 40°$, correlating with the second zone above.

Scatter diagrams, constructed after low-pass filtering, exhibited numerous trends, generally more complex and less

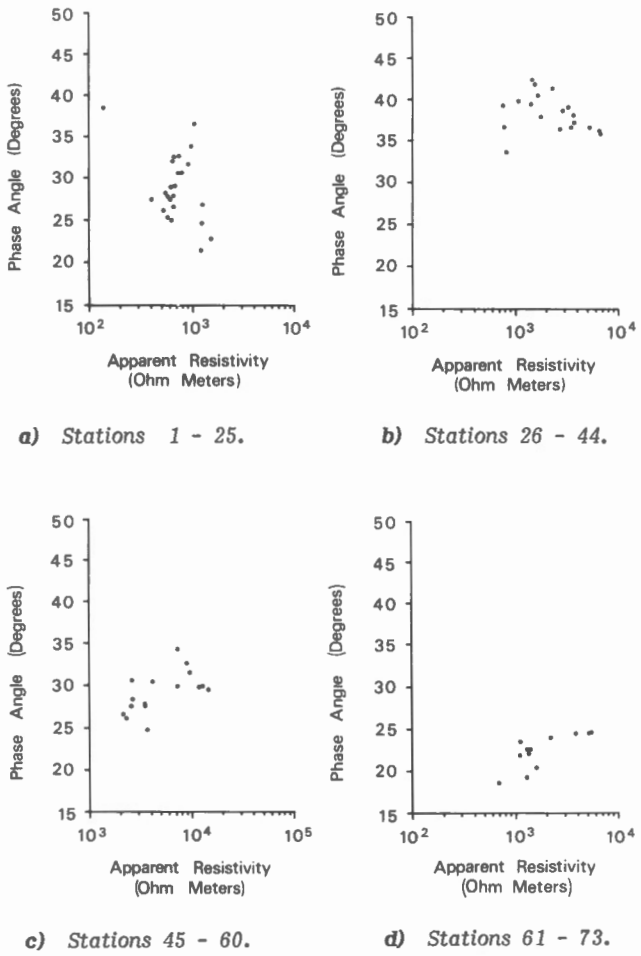

Figure 11. Area #1, profile 24+00E, scatter diagrams.

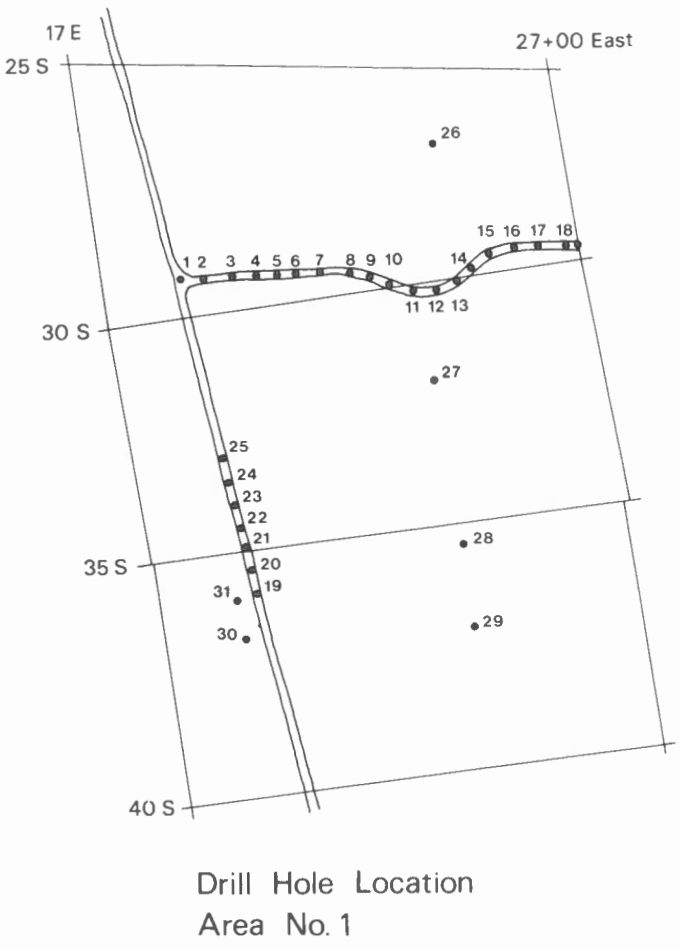

Figure 12. Area #1. Drill hole location map.

Table 1. Comparison of drill hole bedrock depths with interpreted depths for area N° 1.

Drill Hole	Depth	Interpreted Depth	Error Estimated
1	14.6 m	14.0 m	± 1.5 m
2	14.6	13.5	1.9
3	14.6	13.5	1.9
4	13.4	20.0	2.3
5	13.4	15.0	1.5
6	12.1	6.0	1.0
7	12.1	6.0	1.0
8	13.4	8.0	1.3
9	11.9	11.0	1.0
10	14.6	16.0	2.0
11	11.5	11.0	1.0
12	14.6	10.0	2.5
13	13.4	12.5	1.7
14	11.3	11.5	1.9
15	11.9	11.0	1.5
16	11.2	10.0	1.0
17	7.3	8.0	1.0
18	8.5	12.0	2.5
19	5.5	7.5	1.0
20	8.5	13.0	2.5
21	7.3	8.5	1.1
22	11.4	12.5	1.5
23	11.3	10.5	1.3
24	11.5	10.5	1.3
25	11.3	11.0	1.0
26	20.0	16.0	3.0
27	15.0	14.0	1.7
28	6.0	6.0	1.0
29	15.0	6.0	1.0
30	6.0	7.5	1.3
31	14.0	12.0	1.5

persistent than was the case in area N° 1. There were 52 percussion holes, mainly in the northern half of the grid, to provide bedrock depth control; no additional resistivity data were available.

Table 2 compares drill hole and interpreted depths. Holes 1-10 and 27-31 show extremely poor correlation. All were located in the western part of the grid where ρ_a and φ were abnormally large. Here the resistive overburden is about 4 m thick and effectively transparent to the VLF signal. It is evident that a deeper interface has been mapped. The remaining 37 holes correlated quite well except for cases where $\varphi \simeq 45°$; otherwise 70% of these stations agreed within the error tolerance.

Area N° 3

Located immediately north of N° 2 with a common baseline, the grid here was 1000 m N-S and about 650 m E-W, with 50 m spacing between N-S lines and stations 20 m apart. The overburden is mainly dry glacial till; maximum relief is about 45 m. VLF dip angle data obtained from Cutler and Jim Creek indicate a minor trend approximately N-S, with no discontinuous features. Horst and graben faulting has also been suggested in this area.

EM16R data ranged from 100 - 3000 Ω.m and 34°- 70° for ρ_a and φ respectively. The resistivity contours outline several zones where both ρ_a and φ are

Table 2. Comparison of drill hole bedrock depths with interpreted depths for area N° 2.

Drill Hole	Depth	Interpreted Depth	Error Estimated
1	5.8 m	20.0 m	±3.0 m
2	6.7	20.0	3.1
3	6.4	20.0	3.5
4	4.6	20.0	2.7
5	3.9	20.0	2.9
6	3.1	20.0	3.6
7	3.6	20.0	3.9
8	3.1	20.0	2.6
9	4.3	20.0	3.3
10	7.0	9.0	1.7
11	6.7	6.0	1.0
12	5.5	2.0	0.7
13	5.1	4.5	0.8
14	5.5	5.3	0.5
15	3.6	3.5	0.7
16	3.6	3.5	0.7
17	2.6	3.0	0.7
18	3.4	4.0	0.9
19	3.4	4.5	1.0
20	5.5	5.5	1.1
21	4.6	4.3	0.7
22	5.3	5.5	1.2
23	4.9	4.5	0.9
24	3.7	4.0	0.7
25	4.0	4.0	0.7
26	4.0	6.0	1.5
27	5.8	12.5	1.7
28	5.8	15.0	1.9
29	6.1	16.0	1.6
30	4.8	10.0	1.3
31	5.5	7.0	1.5
32	5.5	8.0	1.9
33	5.2	5.0	0.9
34	7.3	2.0	0.3
35	8.8	2.0	0.2
36	9.7	2.0	0.2
37	9.45	3.5	0.5
38	6.1	4.5	0.7
39	6.4	3.5	0.5
40	6.1	3.0	0.2
41	6.4	4.5	0.9
42	6.2	6.0	0.5
43	5.8	6.0	0.5
44	4.9	4.5	0.6
45	3.4	3.8	0.3
46	4.4	4.5	0.3
47	2.9	4.0	0.4
48	1.1	2.0	0.3
49	3.7	3.0	0.4
50	2.1	2.0	0.2
51	3.8	4.0	0.4
52	4.6	4.3	0.5

large, resembling the northwest block in area N° 2 adjoining this grid. These zones are surrounded by areas of lower ρ_a, with generally a high gradient between them. Some correlation with the VLF map is evident. The phase angle contours, as in area N° 2 are more complex, although where φ falls between 45°- 50°, $\rho_a > 1000$ Ω.m mainly and where $\varphi > 50°$, the ρ_a values are mostly less than 1000 Ω.m. Scatter diagrams displayed very complex trends.

Table 3. Comparison of drill hole depths with interpreted depths for area Nº 3.

Drill Hole	Depth	Interpreted Depth	Error Estimated
1	5.2 m	6.0 m	±0.9 m
2	4.0	12.5	1.5
3	3.1	15.0	1.7
4	3.1	20.0	2.0
5	3.1	20.0	2.0
6	4.6	12.5	1.7
7	3.7	4.0	0.4
8	4.1	4.5	0.6
9	4.0	3.5	0.5
10	3.7	3.5	0.5
11	3.1	2.8	0.4
12	4.0	8.0	0.7
13	4.0	12.5	1.3
14	4.3	12.5	1.5
15	3.7	12.5	1.4
16	3.1	10.0	1.1
17	4.3	5.0	0.6
18	4.3	3.5	0.4
19	5.2	5.0	0.4
20	5.2	5.0	0.5
21	4.9	5.0	0.3
22	5.2	6.0	0.6
23	6.1	6.5	0.6
24	6.7	15.0	1.1
25	6.4	15.0	0.9

Following the usual interpretation, routine maps of h_1 and ρ_1 were constructed. Drilling control was provided by 25 percussion holes, located on a NE-SW line in the SE grid section. Correlation with interpreted h_1 values is available in Table 3. Holes 2-6, 12-16, 24, 25 - or 12 of 25 - compare very badly: they are generally located where ρ_a and φ are high, conditions similar to area Nº 2. In fact, they are associated with small zones which are essentially three-dimensional and hence not amenable to reasonable analysis of this type.

Area Nº 4

Compared to the other three, this area provided a quite different test for bedrock mapping. It is approximately 2.5 km E-W by 1 km N-S, with profile lines spaced 125 m striking N-S and station spacing 30 m. A profile was also carried out on the E-W baseline which was shifted north for about 400 m at the west end of the grid to avoid a deep swamp. The area is flat within about 8 m, with a fine-grained clay surface overburden underlain by a sand and gravel layer above bedrock. Clay thickness varied from 9 -30 m, but was generally within 15 - 25 m and its resistivity was approximately 20 Ω.m. The sand and gravel bed, with a much larger resistivity, varies in thickness from 0 - 30 m, is generally thinner in the south-central section of the grid and is absent in only a few small areas.

Figures 13 and 14 display sand-gravel and bedrock depths respectively, compiled from earlier drilling and seismic data. Although the skin depth in the clay bed at VLF frequencies - about 17 m - is generally too small to permit detection of the bedrock, it was thought that the clay/sand-gravel interface might be shallow enough for mapping in some areas.

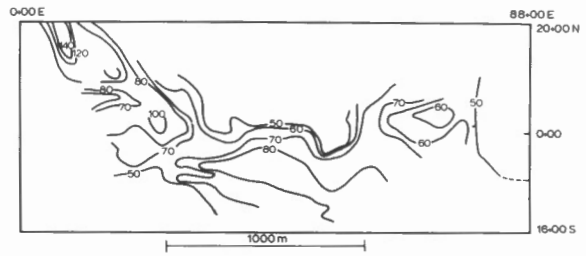

Figure 13. Area #4. Contours of interface between sand and gravel and clay beds in overburden compilation from drilling data.

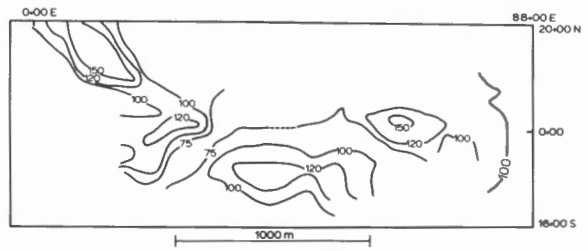

Figure 14. Area #4. Contours of bedrock depth. Compilation from seismic and drilling data.

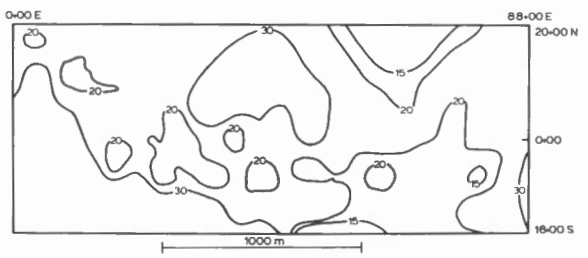

Figure 15. Area #4. EM16R contour of constant ρ_a .

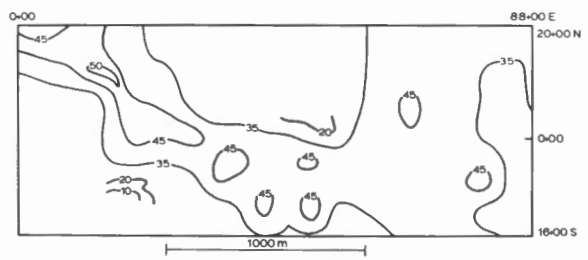

Figure 16. Area #4. EM16R contour of constant φ .

The ρ_a and φ data from the EM16R survey are shown in Figures 15 and 16. As expected, both are quite uniform. Phase angles larger than 45º, however, appear in the NW part of the grid, where the sand-gravel bed is known to be about 30 m below surface (Fig. 13). Thus the highly conductive section must be contained in the clay, presumably a water (probably saline) horizon.

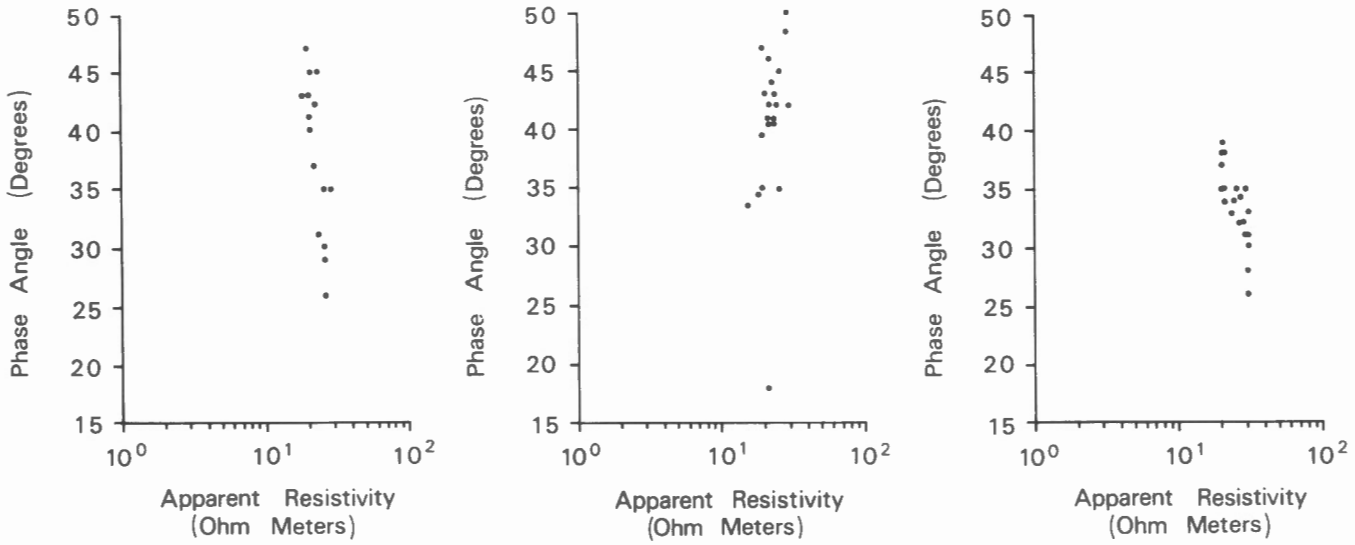

a) Profile 16 + 00E, stations 1-27. *b) Profile 56 + 00E, stations 1-17.* *c) Profile 80 + 00E, stations 1-24.*

Figure 17. *Area #4, scatter diagrams.*

Scatter diagrams for profiles 16E, 56E and 80E are illustrated in Figures 17a-c. All have a first layer resistivity trend which fits a first solution curve, generally for $\rho_2/\rho_1 = 5$. A few abnormally low φ values are doubtless produced by rock stacks at the south end of the lines.

Figure 18 displays contours of ρ_1 which are quite uniform at about 20 m. Interpreted ρ_2 contours appear in Figure 19; these are generally uniform as well, except in the NW corner where the conductive sections appeared to be contained in the clay. Depth contours of the $\rho_2 - \rho_1$ interface are seen in Figure 20. Compared with Figure 13 the contour shapes, if not the depths, are mainly similar and there is fair depth correlation over the eastern part of the grid where the sand-gravel bed is shallower and 60% of the interpreted depths are within 10% of the values from drill data. As the latter were obtained by considerable interpolation, they are not exact.

In the NW grid area there is no apparent fit, since the sand-gravel bed is considerably deeper than the skin depth: of the stations for which $\rho_2 < \rho_1$, 90% are located where the sand and gravel is at least 27 m deep. Furthermore, the skin depth here is considerably decreased by the conductive bed. As mentioned previously, this must be contained within the impermeable clay and there is no indication of its existence from drill data.

Although this EM16R survey failed to map the bedrock, it provided information about the overburden constituents. Obviously it would be necessary to employ frequencies lower than VLF to penetrate deep conductive overburden of this type. This situation is just the reverse of that in the western zone of area N° 2, where higher frequencies would be required to reduce the penetration of this resistive cover.

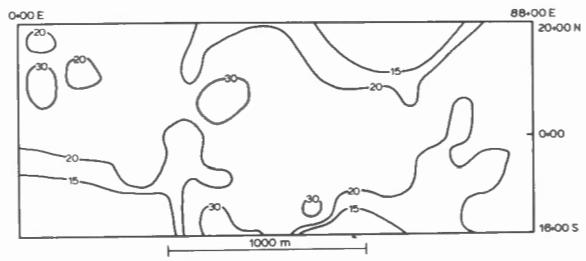

Figure 18. *Area #4. EM16R contours of constant upper bed resistivity* ρ_1.

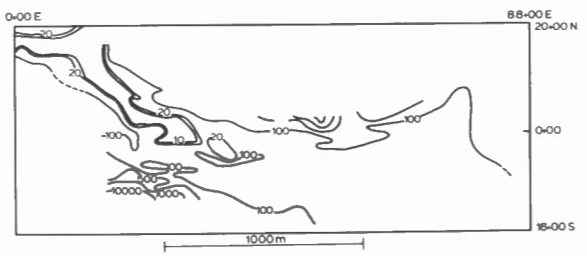

Figure 19. *Area #4. EM16R contours of constant lower bed resistivity* ρ_2.

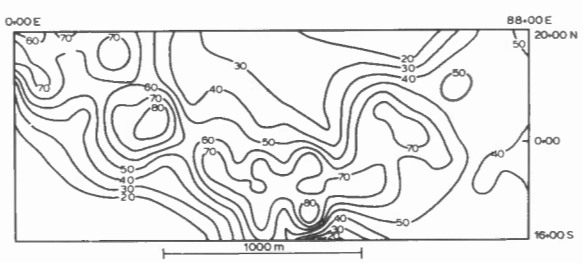

Figure 20. *Area #4. EM16R contours of depth to interface between first and second layers.*

CONCLUSIONS AND RECOMMENDATIONS FOR FUTURE WORK

The interpretation procedure applied to EM16R data from the four field areas produced first and second layer resistivities and first layer depths for a two-layer structure. No other specific information was available in regard to the first two parameters: where the true bedrock depths were known, 60-70% of the interpreted values agreed within the estimated error. Poor correlation may be due to several limitations in the method.

a) The phase measurement is particularly significant. When $\varphi \simeq 45°$ it is difficult to select a value of ρ_2/ρ_1, since the interpretation curves are bunched, data trends are unclear and the possible error in h_1 increases greatly. This is also true for very small (and large) phase readings, ie. approaching 0° and 90°.

b) The presence of additional layers in the overburden, or in bedrock if the skin depth is sufficiently large.

c) The presence of two-dimensional structures located as in b).

These limitations, particularly the first two, might be reduced in several ways. Additional control information from the survey area is, of course, most important. Shallow DC resistivity soundings, to determine at least ρ_1 and possibly h_1 where it is small, would be a useful supplement. However, a complete additional survey, since resistivity is slow and more expensive than EM16R, would be quite impractical.

It seems attractive to develop additional equipment similar to the EM16R to extend the frequency range sufficiently to permit measurement of ρ_1 - when it is large and/or h_1 small - and h_1 where the overburden is highly conductive. This would require a high frequency limit in the order of several MHz in the first situation and a low frequency ~100 Hz in the second.

Extension of the VLF frequency to 60 kHz, employing the WWVB transmitter, is reported in another paper (LaFleche and Jensen, 1981-V). The AM broadcast band might be used for the high frequency limit, but it is not generally available in remote areas. A portable low power source might be suitable. For low frequencies, MT type equipment operating in the low audio range is presently available; although not yet manufactured commercially, it probably will be. It does not, however, provide direct measurement of phase angle. Although this may be difficult, some development is in progress (Mathur and Telford, 1981-VII; Nichols and Telford, 1981-VIII)

ACKNOWLEDGEMENTS

The research which this article summarizes was supported by the EMR Canada through Research agreements 1135-D13-4-39/76 and 4-99-77.

The authors would like to thank the following people for aid in this work: Brian Powell, Dennis Teskey, Colin Mathieson, Pandeli Papazis, Jacques Liard, for valuable suggestions and help, and Amok Ltd., Saskatoon, Saskatchewan, and the Mineral Exploration Research Institute, Montreal, Quebec, for permission to use field data.

REFERENCES

Cagniard, L.
1953: Basic theory of the magneto-telluric method of geophysical prospecting, Geophysics 18, p. 605-635.

Crossley, D.J.
1981: Theory of EM surface wave impedance measurements; in Geophysical Applications of Surface Wave Impedance Measurements, L.S. Collett and O.G. Jensen (eds.); Geological Survey of Canada, Paper 81-15, Report V, p. 1-17.

Doborzynski, Z.B.
1974: Prospecting with multi-frequency tellurics, M.Sc. thesis, McGill University, Montreal.

Keller, G.V. and, Frischknecht F.C.
1966: Electric Methods in Geophysical Prospecting, Pergamon Press of Canada.

Kisak, E.
1976: Finite element analysis of telluric and magnetotelluric response over resistivity anomalies and topographic effects, Ph.D. thesis, McGill University, Montreal.

Ku, C.C., Hsieh, M.S. and Lim, S.H.
1973: The topographic effect in electromagnetic fields, Can. J. Earth Sci. 10, p. 645-656.

LaFleche, P.T. and Jensen, O.G.
1981: Wave impedance measurements at 60 kHz; in Geophysical Applications of Surface Wave Impedance Measurements, L.S. Collett and O.G. Jensen (eds.); Geological Survey of Canada, Paper 81-15, Report V, p. 67-78.

Mathur, R.K. and Telford, W.M.
1981: A study of magnetotelluric phase measurements; in Geophysical Applications of Surface Wave Impedance Measurements, L.S. Collett and O.G. Jensen (eds.); Geological Survey of Canada, Paper 81-15, Report V, p. 87-93.

Nichols, E.A. and Telford, W.M.
1981: Magnetotelluric phase instrumentation; in Geophysical Applications of Surface Wave Impedance Measurements, L.S. Collett and O.G. Jensen (eds.); Geological Survey of Canada, Paper 81-15, Report V, p. 95-102.

Paterson, N.R. and Ronka, V.
1971: Five years of surveying with the VLF-EM method, Geoexploration 9, p. 7-26.

Powell, B.W. and Jensen, O.G.
1981: Radiohm mapping of permafrost; in Geophysical Applications of Surface Wave Impedance Measurements, L.S. Collett and O.G. Jensen (eds.); Geological Survey of Canada, Paper 81-15, Report V, p. 19-33.

Slankis, J.A.
1970: Telluric and magnetotelluric surveys at 8 Hz, Ph.D. thesis. McGill University, Montreal.

Telford, W.M., King, W.F. and Becker, A.
1977: VLF mapping of geological structure, Geological Survey of Canada, Paper 76-25, 13 pp.

Wait, J.R.
1962: Electromagnetic Waves in Stratified Media, International Series in Electromagnetic Waves, Vol. 3, Pergamon, Toronto, 372 pp.

IV

INTERPRETATION OF SINGLE FREQUENCY VLF DATA

C.C. Mathieson* and D.J. Crossley+
* Gulf Canada, Ltd.
+ Laboratory in Applied Geophysics, McGill University

Mathieson, C.C. and Crossley, D.J., Interpretation of single frequency VLF data; in Geophysical Applications of Surface Wave Impedance Measurements, L.S. Collett and O.G. Jensen editors; Geological Survey of Canada, Paper 81-15, p. 49-65, 1981.

Abstract

Interpretation of VLF resistivity data collected on the ground by instruments such as the Geonics EM16R system poses several interpretation problems. The major one is a limitation of the data to only two independent quantities, apparent resistivity and phase angle (between electric and magnetic field components), at any wave frequency. This fact, coupled with effectively only one VLF transmitting frequency at a single reciever location, means that the possibilities of decoding resistivity structure in the ground are severely limited to simple horizontally-layered models with two or three layers.

This paper describes a novel graphical approach to interpretation which allows all possible two-layer situations to be represented on a single contour map. Where more precise model parameters are required the use of a simple numerical procedure, described in this paper, is encouraged.

Résumé

L'interprétation des données TBF de résistivité mesurées au sol par des instruments tels que le Geonics EM16R pose plusieurs problèmes. La plus importante de ces difficultés provient du fait que ces données se limitent à seulement deux quantités indépendantes, la résistivité apparente et l'angle de phase (entre les composantes des champs électrique et magnétique), à n'importe quelle fréquence. Ces données jointes à l'utilisation d'une seule fréquence de transmission TBF captée en un seul point de réception signifie que les possibilités de décodage de la structure de résistivité du sol sont sérieusement restreintes et se limitent à des modèles simples à deux ou trois couches horizontales.

Ce compte rendu décrit une nouvelle démarche graphique pour parvenir à l'interprétation. Cette approche permet de representer toutes les structures de terrains à deux couches sur une seule carte de contours. On conseille d'utiliser une simple démarche numérique (décrite dans cette communication) quand des paramètres plus préçis sont requis.

INTRODUCTION

As outlined by Crossley (1981-I), the limitation involved in the interpretation of VLF resistivity data for horizontally layered media lies in the restricted amount of data available. A VLF transmitter broadcasts at only one frequency and there are only two components of the wave impedance Z_1 at the air-ground interface which can be measured at any location, namely its magnitude $|Z_1|$ and phase angle arg Z_1 . These are converted to apparent resistivity (ρ_a) and phase lag (φ) of the horizontal magnetic field component H_y to the horizontal electric field component E_x, via the relations

$$\rho_a = \frac{1}{\omega\mu_1}|Z_1|^2 \quad ; \quad \varphi = \frac{180}{\pi} \arg Z_1 \qquad (1)$$

(I-equations (65) and (66)).

VLF transmitting stations operate within a relatively small band of frequencies 15-23 kHz (Crossley, 1981-I, Table 1) and so the electromagnetic skin depth

$$\delta = \sqrt{\frac{2}{\omega\mu\sigma}} \qquad (2)$$

within any electrically homogeneous region of the ground varies by only 20% within the above frequency limits for a fixed value of μ, the absolute magnetic permeability and σ, the electrical conductivity. For this reason there is little to be gained by operating a VLF receiver at more than one frequency except either to select the strongest of the several possible signals available at any one time or to investigate the effect of transmitter direction on the ground conductivity. In practise one is seldom able to receive well more than two VLF stations at a single location in Canada, these being Cutler, Maine (17.8 kHz) and Jim Creek, Washington (18.6 kHz) (Crossley, 1981-I, Figure 1) and these are too close in frequency to significantly affect the skin depth (2).

Accepting the limitation that only one pair of observations (ρ_a , φ) is available at any ground measurement location, using for example the Geonics EM16R (modified) receiver which measures E_x via two

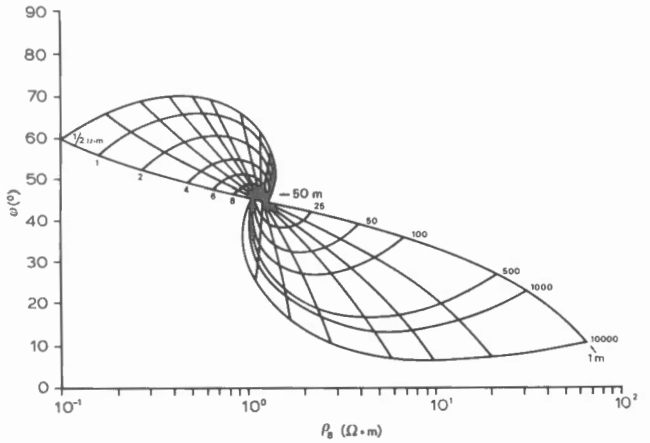

Figure 1. Phase angle as a function of apparent resistivity showing contours of h_1 *and* ρ_2 *; two-layer model with* ρ_1 = 12 Ω.m.

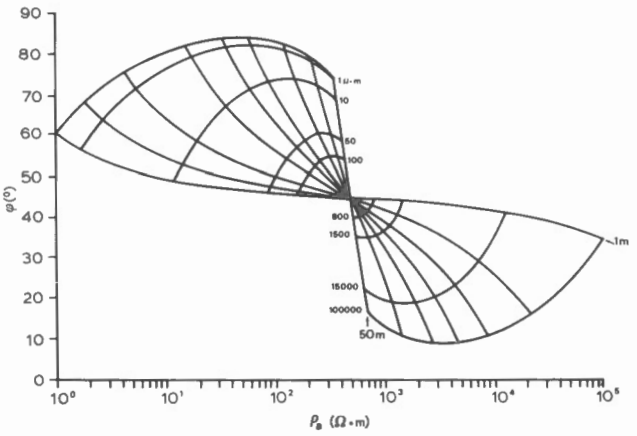

Figure 2. As Figure 1 but ρ_1 = 480 Ω.m.

probes 10m apart in line with the transmitter and H_y via a coil at right angles to E_x, one has to identify which parameters of the ground can be determined. If the ground is considered to be a homogeneous half space extending from depth $z = 0$ to $z = \infty$, with uniform resistivity ρ_1 (Ω.m), free-space values of $\epsilon = \epsilon_0$ (the electric permittivity) and $\mu = \mu_0$, the solution

$$\rho_a = \rho_1 \quad ; \quad \varphi = 45° \qquad (3)$$

is unambiguous. Clearly the measured value of φ will indicate whether this condition (3) is met and hence whether ρ_a can be taken as the resistivity of the ground everywhere. We will see later that for more complicated models situations can arise where $\varphi = 45°$ and yet ρ_1 may not be equal to ρ_a, but one would have to have clear evidence for preferring a more complicated model.

It should be recognised that measurements of (ρ_a, φ) are seldom better than (± 10%, ±1°) and therefore any measured phase angle within $\varphi = 45° \pm 1°$ can usually be taken to represent homogeneous ground. Furthermore the ground is homogeneous only to a depth of approximately δ (equation (2)), for beyond this depth the above errors in measurement completely dominate any structural information about the model that would be present in accurate data. An additional consideration which may be relevant rests on the assumption that VLF theory generally omits to consider displacement currents in the ground. These can modify the current density at high enough frequencies and resistivities (Crossley, 1981-I, equation (86)), to an extent controlled by the size of the non-dimensional parameter

$$\nu = \omega \epsilon \rho \qquad (4)$$

(Crossley, 1981-I, equation (56)). If $\nu \ll 1$ then displacement currents can be ignored but if ν is greater than about 0.1 significant deviations of ρ_a and φ from their values in (3) can occur even when ρ_1 is everywhere uniform (Crossley, 1981-I, equations (96) and (97)). In the present paper, it will be assumed that $\nu \ll 1$ and we will investigate the interpretation of (ρ_a, φ) for horizontally stratified Earth models with two and three uniform layers.

GRAPHICAL INTERPRETATION

Two-Layer Models: Known ρ_1

We assume the Earth has two layers, the upper with thickness h_1, resistivity ρ_1 and the lower with resistivity ρ_2 and free-space values of ϵ_0, μ_0 are assumed throughout. The surface wave impedance Z_1 is then given by

$$Z_1 = (i\omega\mu_0\rho_1)^{\frac{1}{2}}\, Q_1 \quad , \qquad (5)$$

where the correction factor Q_1 is

$$Q_1 = \frac{\beta_1 + \tanh(\alpha_1\sqrt{i})}{1 + \beta_1 \tanh(\alpha_1\sqrt{i})} \quad . \qquad (6)$$

The subsidiary parameters (α_1, β_1) will become quite important to our discussion and are given by

$$\left.\begin{aligned} \alpha_1 &= \sqrt{\frac{\omega\mu_0}{\rho_1}}\; h_1 \\ \text{and} \\ \beta_1 &= \sqrt{\frac{\rho_2}{\rho_1}} \quad . \end{aligned}\right\} \qquad (7)$$

As discussed in (Crossley, 1981-I) the apparent resistivity and phase can be related to the three parameters (ρ_1, h_1, ρ_2) by combining (1), (5) and (6)

$$\rho_a = \rho_1 |Q_1|^2 \quad ; \quad \varphi = 45° + \frac{180}{\pi} \arg Q_1 \qquad (8)$$

where the amplitude and phase are functions of α_1, β_1. There is then no obvious way of extracting h_1 and ρ_2/ρ_1, the most useful parameters of the model, from (8) without specifying ρ_1.

In (Crossley, 1981-I) it is shown that, by referring to the curves of $|Q_1|$ and arg Q_1 versus α_1 (Crossley, 1981-I, Figures 6 and 7), the assumption of known ρ_1 is enough to uniquely specify the other two parameters (h_1, ρ_2/ρ_1) or (α_1, β_1). We can however construct more useful type-curves for this purpose as follows:

Step 1. Choose a value of ρ_1
2. Select ranges for h_1, e.g. 1-50 m and ρ_2, e.g. 1-10 Ω.m
3. Compute (α_1, β_1) from (7)
4. Compute Q_1 from (6)
5. Compute (ρ_a , φ) from (8)
6. Plot (ρ_a , φ) as functions of (h_1, ρ_2) (9)

As examples of this procedure we show the curves for ρ_1 = 12 Ω.m and ρ_1 = 480 Ω.m in Figures 1 and 2. These values, as well as others used here, are relevant to field values found later. It is evident from these two figures that, with the exception of phase angles near 45°, there is a unique relationship between (ρ_a, φ) and (h_1, ρ_2) for a given ρ_1 , as claimed above. Armed with a selection of such characteristic curves, for all possible situations one might encounter in the field, it is possible to interpret a wide range of (ρ_a , φ) in terms of a two-layer model.

Figures 1 and 2 show however that not all values of (ρ_a , φ) can be interpreted as a two-layer model. For example values for (ρ_a, φ) of (10 Ω.m, 20°) or (10^4 Ω.m, 70°) lie well outside any of the overlapping contours. This is due to the fact that the curves of arg Q_1 versus α_1 (Crossley, 1981-I, Figure 7) show maxima or minima for every value of β_1 (except 0 and ∞). We can express this result mathematically by finding the maximum or minimum of arg Q_1 as a function of α_1 . From (6),

$$\arg Q_1 = \tan^{-1}\left(\frac{2q\, e^p \sin p}{q^2 - e^{2p}}\right) \qquad (10)$$

(Crossley, 1981-I, equation (77)), where

$$p = \sqrt{2}\,\alpha_1 \quad , \quad q = \frac{\beta_1 - 1}{\beta_1 + 1}$$

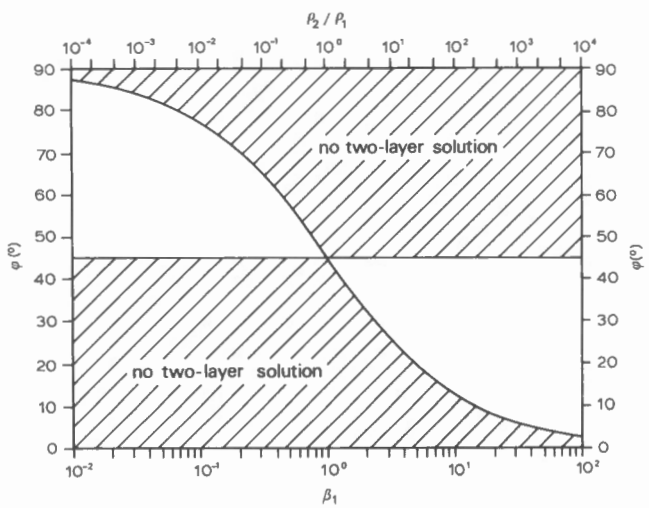

Figure 3. *The maximum and minimum phase angle associated with a specified resistivity contrast for a two-layer model. Unacceptable solutions lie in the shaded regions.*

It can be shown that the partial derivative

$$\frac{\partial}{\partial \alpha_1}(\arg Q_1) = \sqrt{2}\,\frac{\partial}{\partial p}(\arg Q_1)$$

vanishes when

$$q = \pm \sqrt{\frac{1-\tan p}{1+\tan p}}\; e^p \quad . \qquad (11)$$

A minimum value of q occurs when $\tan p = 1$, or α_1 = 0.555, at which value we find β_1 = 1 and arg Q_1 = 0 for a homogeneous ground situation. The utility of (11) lies in the fact that β_1 has either a maximum or minimum value, determined from the relation

$$\beta_1 = \left(\frac{1+q}{1-q}\right) \quad ,$$

according to whether we take the + or the - sign for q . At the same time the phase angle can be calculated from (8) for those values of α_1, β_1 which satisfy (11). A plot of this phase angle is shown, in Figure 3, as a function of ρ_2/ρ_1 which has a minimum value for phase angles less than 45° and a maximum acceptable value for phase angles greater than 45°. As examples of the use of this figure, a measured phase of 60° implies a resistivity contrast of less than 0.18 for any value of ρ_1 , whereas a phase of 30° implies a contrast of at least 5.5. We therefore have a useful method of veryifying immediately whether a measured phase can be due to a particular two-layer model or whether a third layer is required.

Two-Layer Model - Known ρ_2/ρ_1

As explained in (Crossley, 1981-I), it may be possible that the resistivity contrast can be deduced from geological considerations and this leads to an ambiguity in the interpretation for ρ_1 and h_1 . In this case useful type-curves for interpretation can be constructed as follows.

Step 1. Choose a value for ρ_2/ρ_1
2. Select ranges for ρ_1, e.g. 1-10 Ω.m and h_1, e.g. 1-50m.
3. Compute α_1 , β_1 from (7)
4. Compute Q_1 from (6)
5. Compute (ρ_a , φ) from (8)
6. Plot (ρ_a , φ) as a function of (ρ_1 , h_1). (12)

Two typical sets of curves produced by this procedure are shown in Figure 4 for a conductive over resistive layer with ρ_2/ρ_1 = 10 and in Figure 5 for a resistive over conductive layer with ρ_2/ρ_1 = 0.1. It can be seen that the maximum and minimum phase angles agree with those estimated from Figure 3 and that two possible solutions are possible depending on whether one is on the 'back' or 'front' surface defined by the intersecting contours. Provided one is in the acceptable phase angle range of Figure 3 two possible solutions then exist for every value of apparent resistivity, despite the appearance of Figures 4 and 5 which suggests the overlap is restricted only to the central portions of the figures. There is no a priori method of distinguishing the most geologically reasonable of the two mathematically valid solutions, although in practise one of the two solutions often contains an extreme (high or low) value for either ρ_1 or h_1 , therefore leading to the rejection of that model.

Two-Layer Model: Master Curves

In both of the above cases one cannot proceed with interpretation without a set of type curves covering a representative selection of possible values for either ρ_1 or ρ_2/ρ_1 . During the course of this analysis it was realized that one can plot a value of ($|Q_1|$, φ) on a graph for any combination of (α_1 , β_1) from equations (6)-(8). If these values of ($|Q_1|$, φ) are then contoured over the (α_1 , β_1) space it should be possible to deduce the appropriate model parameters from any measured values of (ρ_a , φ). The single set of master curves for the ranges ($10^{-4} \leqslant \alpha_1 \leqslant 10^1$); ($10^{-3} \leqslant \beta_1 \leqslant 10^3$) is shown in Figure 6 and an enlargement of the central portion ($0.1 \leqslant \beta_1 \leqslant 10$) is shown in Figure 7 for more detailed interpretation. Figure 6 is reproduced in a larger version included with this volume.

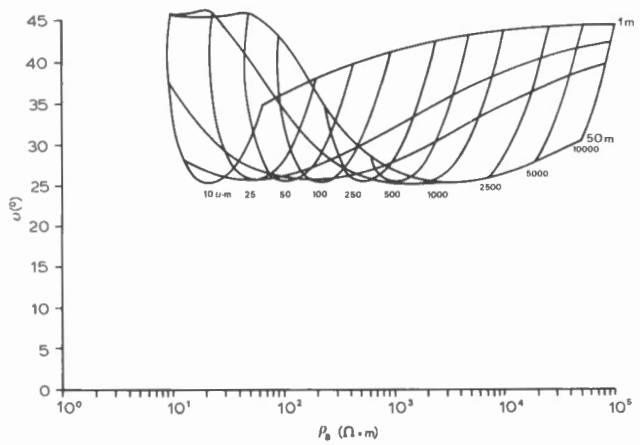

Figure 4. Phase angle as a function of apparent resistivity showing contours of constant ρ_1 *and* h_1 *; two-layer model with* $\rho_2/\rho_1 = 10$.

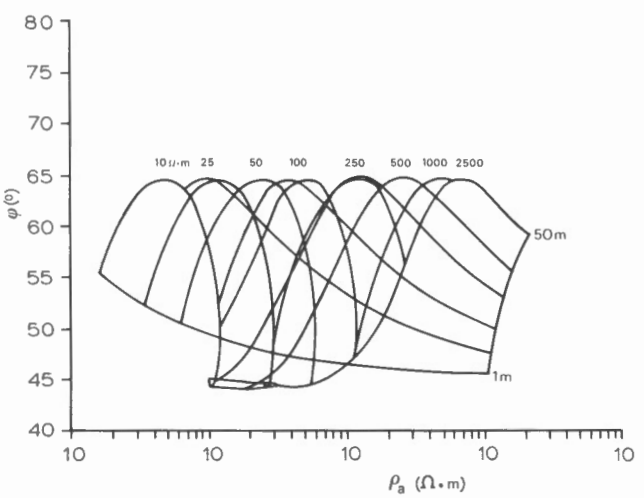

Figure 5. As Figure 4 but $\rho_2/\rho_1 = 0.1$.

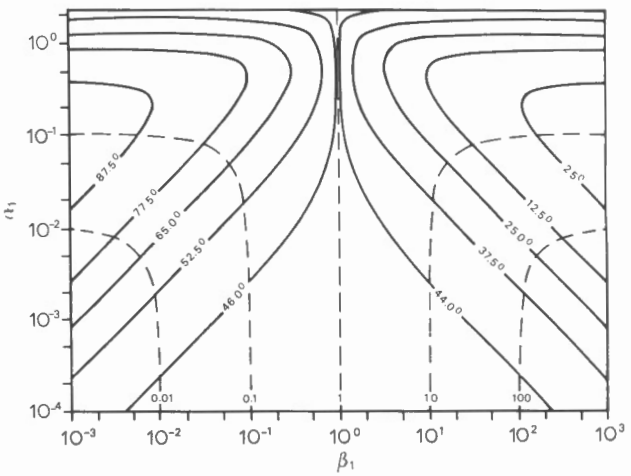

Figure 6. Master curves for two-layer VLF resistivity interpretation showing contours of φ *(solid) and* $|Q_1|$ *. (dashed) for various combinations of* (α_1, β_1).

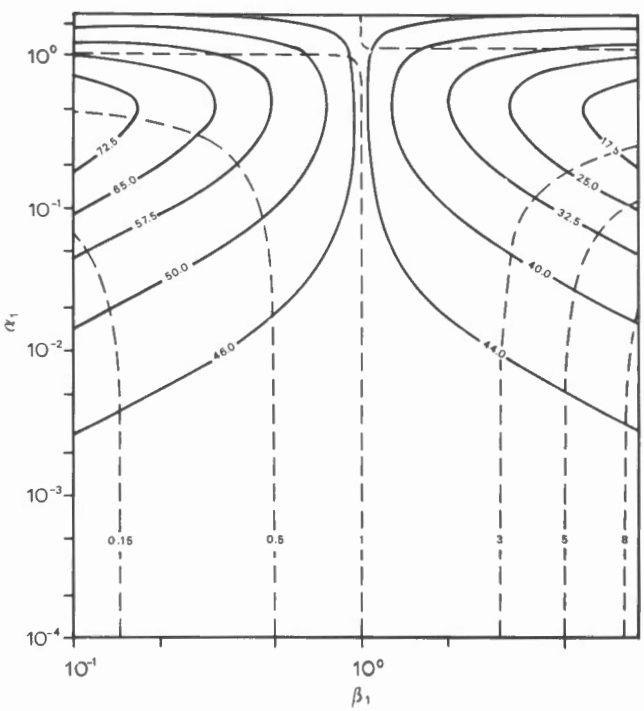

Figure 7. Enlargement of the central portion of Figure 6.

Interpretation of any two layer model can be realized with use of these master curves by the procedure outlined in Table 1. To increase the utility of this table the equations (7) and (8) are written out at the appropriate places, and the subscript 1 is omitted from α_1 , β_1 and $|Q_1|$.

Table 1. Use of master curves for two-layer VLF resistivity interpretation; it is assumed that ρ_a and φ are measured.

	Known ρ_1		Known ρ_2/ρ_1
Step 1	Compute $\|Q\|$ from $\rho_a = \rho_1 \|Q\|^2$	Step 1	Locate intersection of (β , φ) to give α
2	Locate intersection of ($\|Q\|$, φ) to give β	2	Read the value of $\|Q\|$
3	Read the value of α	3	Compute ρ_1 from $\rho_a = \rho_1 \|Q\|^2$
4	Compute h_1 from $\alpha = \sqrt{\omega \mu_0 / \rho_1}\, h_1$	4	Compute h_1 from $\alpha = \sqrt{\omega \mu_0 / \rho_1}\, h_1$
5	Compute ρ_2 from $\beta = \sqrt{\rho_2 / \rho_1}$	5	Compute ρ_2 from $\rho_2 = \beta^2 \rho_1$

Three-Layer Models

Interpretation of a three-layer model, which contains the five parameters ρ_1, h_1, ρ_2, h_2 and ρ_3, is not an easy task given only two observed quantities (ρ_a , φ). Computationally the forward problems is a simple extension of the two-layer case, where instead of (6) we find

$$Q_1 = \frac{\beta_1 Q_2 + \tanh(\alpha_1 \sqrt{i})}{1 + \beta_1 Q_2 \tanh(\alpha_1 \sqrt{i})} \qquad (13)$$

and

$$Q_2 = \frac{\beta_2 + \tanh(\alpha_2 \sqrt{i})}{1 + \beta_2 \tanh(\alpha_2 \sqrt{i})} \quad , \qquad (14)$$

where $\beta_2 = \sqrt{\rho_3 / \rho_2}$ and $\alpha_2 = \sqrt{(\omega \mu_0 / \rho_2)}\, h_2$. The apparent resistivity and phase angle continue to be given by equation (8). In attempting to reduce the number of variables the most common assumption is to specify the ratios h_2/h_1 and ρ_3/ρ_1 so that one attempts to find ρ_1 , h_1 and ρ_2 as for the two-layer model.

An example of three-layer type curves for the case where h_2/h_1 and $\rho_3/\rho_1 = 1$ is shown in Figures 8 and 9 for Q_1 and arg Q_1 respectively as a function of α_1 (defined as before). Both curves again indicate that difficult interpretation problems can be expected when $\alpha_1 > \sqrt{2}$ and it is clear their characteristics are radically different from the two-layer situation. This is especially true of the phase angle which now exhibits both a maximum and a minimum value for a specified value of β_1 so that no straightforward division between acceptable and non-acceptable models exists in the sense of Figure 3.

It is also evident that the number of possible, equally valid, solutions increases to as many as four for phase angles close to 45° (arg $Q_1 = 0$ radians). This ambiguity is not surprising in view of the added complexity of the model and the limitations of VLF resistivity data become rather apparent at this stage. Further testimony to this fact can be found by examining a slightly different model, $h_2/h_1 = 3$ and $\rho_3/\rho_1 = 1$, as shown in Figures 10 and 11. The curves are not only quite different from the previous model but also different from the two-layer curves shown in (Crossley, 1981-I). One important aspect of three-layer curves is that a phase angle of 45° can occur for models totally unlike a homogeneous ground situation.

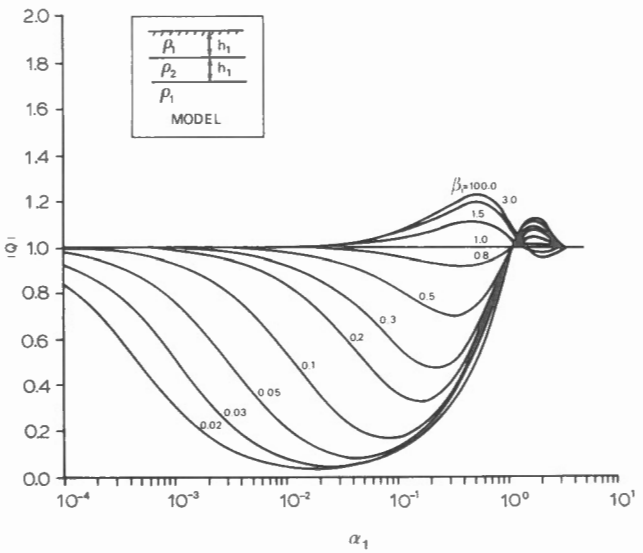

Figure 8. *Amplitude of Q_1 as a funtion of α_1 for selected values of β_1 ; two-layer model with $h_2 = h_1$ and $\rho_3 = \rho_1$.*

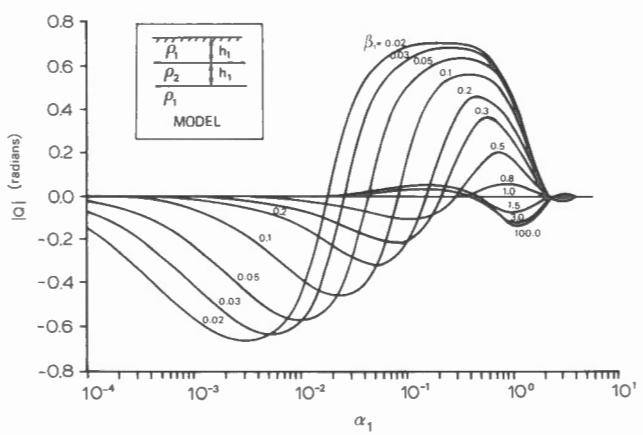

Figure 9. *As Figure 8 but phase of Q_1 plotted.*

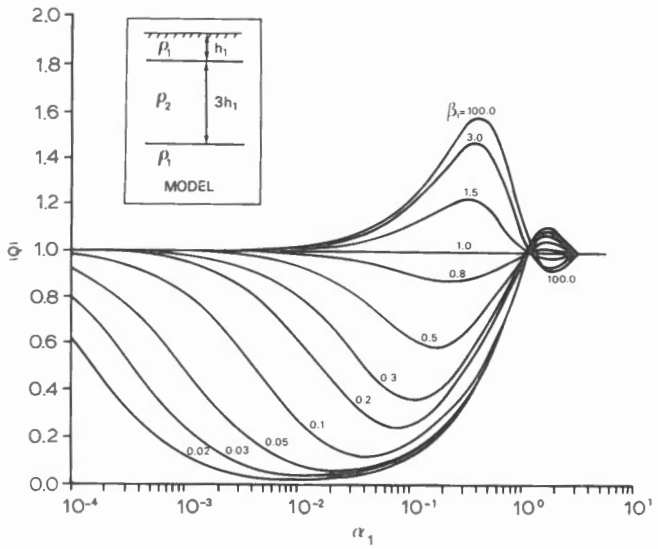

Figure 10. As Figure 8 but with $h_2 = 3h_1$.

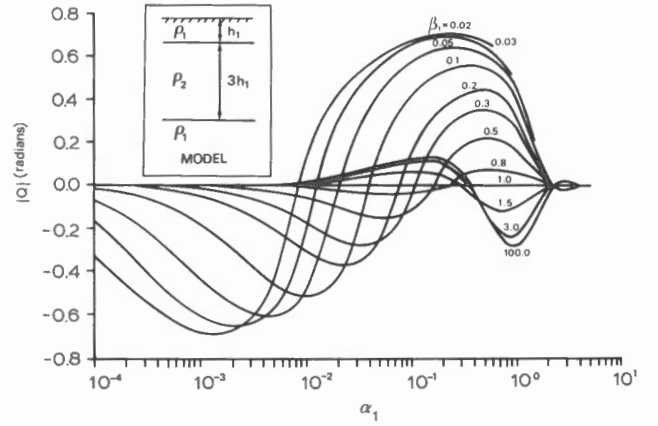

Figure 11. As Figure 10 but phase of Q_1 *plotted.*

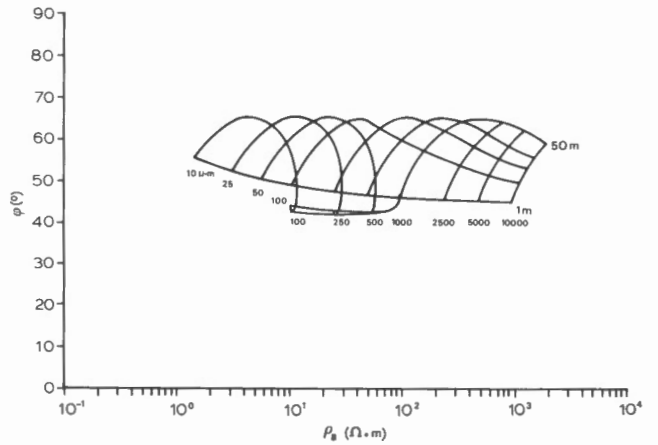

Figure 12. Phase angle as a function of apparent resistivity showing contours of constant ρ_1 *and* h_1 *; three-layer model with* $h_2 = 3h_1$, $\rho_2 = .025\,\rho_1$ *and* $\rho_3 = .01\,\rho_1$.

More elaborate graphical interpretation is possible for the three-layer situation, for example in Figure 12 the variation of phase angle with resistivity is shown for the specific combination of $h_2/h_1 = 3$, $\rho_3/\rho_1 = 1$ and $\rho_2/\rho_1 = 0.025$ which would correspond to a curve with $\beta_1 = 0.16$ in Figures 10 and 11. As in Figures 4 and 5, there are clearly two different solutions for any two observed pairs of data (ρ_a , φ) but it is not difficult to find parameter combinations which can yield up to four possible solutions giving the same values for (ρ_a , φ).

Even if one were restricted to, say, 10 values for any one parameter, or parameter ratio, this would lead to 1000 type-curves for any geophysical situation (10 for h_2/h_1 x 10 for ρ_3/ρ_1 x 10 for either ρ_1 or ρ_2/ρ_1). This is a formidable number for any field interpretation but it is possible to reduce this number by one dimension (i.e. to 100 in the above) by using the master curve technique developed for the two-layer models. To do this requires that $|Q_1|$ and φ be contoured as functions of α_1 and β_1 for specific values of the ratios h_2/h_1 and ρ_3/ρ_1 , an example being shown in Figure 13 where those ratios are both taken to be unity. Interpretation for the remaining parameters proceeds exactly as in Table 1. The number of master curves is still substantial and it is clear that a numerical technique of some sort would be preferable to an extensive set of curves similar to any of the above. We therefore turn to one approach to solving VLF resistivity interpretation numerically which requires the use of linearized iteration to improve certain 'guesses' to the model.

NUMERICAL INVERSION

General Procedure

The linearization of any geophysical interpretation problem has been discussed very concisely by Jackson (1972) and Wiggins (1972). One requires a means of generating theoretical data c_i ($i = 1,2 \ldots n$) from a model containing parameters p_j ($j = 1,2 \ldots m$) through geophysical theory represented by a function f_i , i.e.

$$c_i = f_i(p_j) \quad , \qquad i = 1,2 \cdots n \tag{15}$$

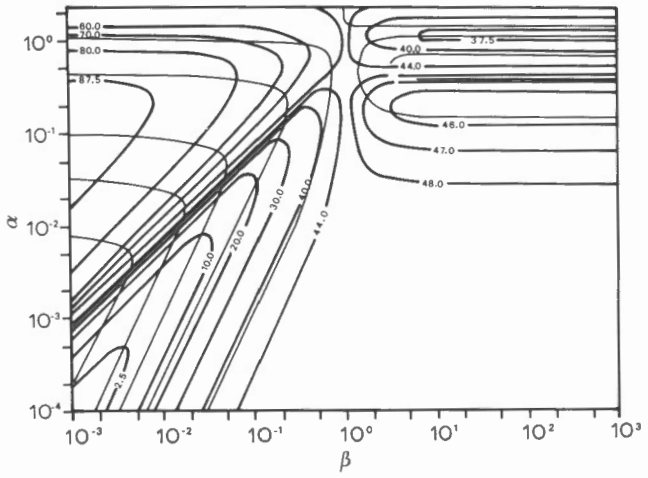

Figure 13. Master curves for three-layer VLF resistivity interpretation showing contours of φ *and* $|Q_1|$ *for various combinations of* (α_1, β_1) *with* $h_2 = h_1$ *and* $\rho_3 = \rho_1$.

Table 2. Algorithm for solving a two-layer resistivity model using VLF data (ρ_a, φ) measured at a single frequency.

Step 1. Known ρ_1 : select values for h_1 and ρ_2/ρ_1 (typically 50 each) and compute a parameter matrix of pairs (α_1, β_1).

Known ρ_2/ρ_1 : select values for ρ_1 and h_1 (typically 50 each) and assemble in a parameter matrix of pairs (ρ_1, h_1).

Step 2. Compute (ρ_{ac} , φ_c) for each element of the parameter matrix and calculate the objective function

$$E^2 = \left(\frac{\rho_{ac} - \rho_a}{\rho_a}\right)^2 + \left(\frac{\varphi_c - \varphi}{\varphi}\right)^2$$

where (ρ_a , φ)are observed data. Save initial parameters for which E^2 is a minimum.

Step 3. If E^2 is less than some prescribed value, or if the specified number of iterations has been reached, go to Step 8.

Step 4. Compute the elements of the partial derivative matrix A using the formulae in the Appendix. Find A^{-1} and assemble the vector ΔC.

Step 5. Update the parameters by the operation $\widehat{\Delta P} = A^{-1}\Delta C$.

Step 6. Compute new data (ρ_{ac}, φ_c) using updated parameters and find the quantity E^2 as in Step 2.

Step 7. Go to Step 3 replacing initial parameters by updated parameters.

Step 8. Compute parameter variances from

$$\text{var}(\widehat{\Delta P}) = (A^{-1})(A^{-1})^T \text{var}(\Delta C)$$

and print out the complete solution.

which may, or may not be, a linear function of p_j . A Taylor series expansion of c_i about some initial set of parameters $p_j^{(0)}$ leads to the linear equations

$$c_i - c_i^{(0)} = \frac{\partial f_i}{\partial p_j}\Big|_{p_j^{(0)}} (p_j - p_j^{(0)}) \quad . \quad i = 1,2 \ldots n \qquad (16)$$

We desire the calculated data $c_i^{(0)}$ to be as close as possible to observed values o_i (= 1,2... n) and can therefore write (16) as a matrix equation

$$\Delta C = A \Delta P \quad , \qquad (17)$$

where ΔC is an ($n \times 1$) vector with elements $o_i - c_i^{(0)}$, A is an ($n \times m$) matrix whose (i,j)th element is the partial derivative appearing in (16) and ΔP is an ($m \times 1$) vector containing corrections $p_j - p_j^{(0)}$ to the initial parameters. If (15) is already linear in p_j , then (17) will lead immediately to an estimated solution

$$\widehat{\Delta P} = H \Delta C \quad , \qquad (18)$$

where H is the generalized inverse of A. For the simple case when n=m , $H = A^{-1}$ where the inverse A^{-1} can be determined uniquely provided A is non-singular.

Should (15) be non-linear in the neighbourhood of the initial parameters $p_j^{(0)}$, then successive applications of (18) will be necessary to effect a stable solution for p_j . One advantage of this matrix approach is that the variances of the parameters are available through the expression

$$\text{var}(\widehat{\Delta P}) = H H^T \text{var}(\Delta C) \quad , \qquad (19)$$

where var(ΔC) can be taken as the statistical variances of the observed data, σ_i^2. An essential requirement of the method is the need for reasonable initial parameter values to ensure the iteration sequence moves in the desired direction towards a solution.

Application to Two-Layer Models

As for graphical interpretation, it is assumed that either ρ_1 or ρ_2/ρ_1 will be known so that there are two free parameters to be fitted to two available data, i.e. n = m = 2 and $H = A^{-1}$ as discussed above. We are able to implement the general inversion scheme providing the partial derivatives contained in the matrix A can be calculated. This can be achieved numerically by the approximation $\partial f_i / \partial p_j = \Delta c_i / \Delta p_j$ for Δp_j equal to a small fraction (e.g. 0.01) of the current value of p_j . In the present case an analytic form is quite straightforward and we find, by differentiating expression (6), the required derivatives shown in the Appendix.

It is clear from Figures 1 and 2 (or 4 and 5) that the variations of (ρ_a , φ) with the parameters h_1 and ρ_2/ρ_1 are very non-linear, especially in the region where $\varphi \approx 45°$, so one therefore needs a reasonable starting model before the inversion will converge. This is provided by pre-calculating theoretical values of (ρ_a , φ) for a range of values of (α_1 , β_1) using equations (6)-(8) and then finding the pair of values (α_1 , β_1) which yields the smallest difference between (ρ_a , φ) as observed and as pre-calculated. In effect one is solving by a combination of trial and error followed by iterative improvement. The complete algorithm is outlined in Table 2 for either of the

Table 3. Numerical simulation of VLF resistivity inversion for two-layer models. All resistivities are in Ω.m, depths in m.

Case I: f = 17.8 kHz ; ρ_1 = 500 ; ρ_2 = 4000 ; h_1 = 5
ρ_a(exact) = 2996.13 ; ρ_a(input and output) = 3000
φ (exact) = 38.02° ; φ (input and output) = 38°

Method	Trial	Starting Parameters ρ_2	Starting Parameters h_1	Final Parameters ρ_2	Final Parameters h_1	Iterations	Mean Square Error
Known ρ_1	1	5000	5.0	4010 ± 3%	5.0 ± 7%	3	$.5 \times 10^{-8}$
		ρ_1	h_1	ρ_1	h_1		
Known ρ_2/ρ_1	1	500	5.0	501	5.0	0	$.5 \times 10^{-7}$
	5	700	13.0	501 ± 3%	5.0 ± 10%	3	$.2 \times 10^{-8}$
	7	400	0.6	501 ± 3%	500 ± 10%	2	$.5 \times 10^{-7}$
	9	2000	80.0	3327 ± 1%	215 ± 3%	2	$.4 \times 10^{-6}$

Case II: f = 17.8 kHz; ρ_1 = 4000; ρ_2 = 500; h_1 = 5
ρ_a(exact) = 554.2 ; ρ_a(input and output) = 550
φ (exact) = 47.78° ; φ (input and output) = 48°

Method	Trial	Starting Parameters ρ_2	Starting Parameters h_1	Final Parameters ρ_2	Final Parameters h_1	Iterations	Mean Square Error
Known ρ_1	1	500	5.0	492 ± 2%	5.4 ±17%	1	$.1 \times 10^{-5}$
		ρ_1	h_1	ρ_1	h_1		
Known ρ_2/ρ_1	1	500	120.	485 ± 1%	102 ± 3%	2	$.1 \times 10^{-6}$
	2	500	130.	485 ± 1%	102 ± 3%	3	$.1 \times 10^{-7}$
	19	600	60.	485 ± 1%	102 ± 3%	3	$.2 \times 10^{-6}$
	33	6000	25.	3933 ± 2%	5.4 ±17%	2	$.9 \times 10^{-8}$
	41	5000	0.2	3933 ± 2%	5.4 ±17%	1	$.4 \times 10^{-6}$

two initial assumptions. It will be noticed that if ρ_1 is known, the parameters (α_1 , β_1) are more convenient to use in the inversion, whereas if ρ_2/ρ_1 (i.e. β_1) is known one has to revert to ρ_1 and h_1 . Although it was not necessary in the present case, one could weight either or both the parameters and the data so that the dimensions of quantities such as ρ_1 and h_1 are comparable (e.g. Jackson 1972). A simpler procedure is simply to weight the matrix A itself by pre-multiplication with a diagonal matrix W with elements $W_{ii} = 1/A_{ii}$, i = 1,2. In step 5 (Table 2) we then have

$$\Delta\hat{P} = (WA)^{-1} W \Delta C \quad .$$

A common problem which arises in practise with this adjustment method is the situation in which the solution diverges at the first iteration due to an unsatisfactory pair of starting parameters. If this is caused by a very non-linear portion of the curves of (ρ_a , φ) as functions of the parameters, then the grid of starting values can usually be intensified in this neighbourhood with some success. If, however, the true solution lies at, or close to, a maximum or minimum phase value or any portion of the above curves where derivatives are close to zero, A will be ill-conditioned and no solution found. One should then be satisfied with the chosen initial value which is often fairly close to the correct solution. Naturally the appearance of negative parameter values is also unacceptable.

It will also be apparent that if ρ_2/ρ_1 is known there are two possible solutions for any given (ρ_a , φ) and Step 2 (Table 2) should be appropriately modified to retain several sets of starting parameters to ensure that both local minima of E^2 are determined. It has been found necessary to often include more than 10 such starting sets for the above purpose. Selection of the shallow or deep solution in this case has to be made on geologic grounds.

Table 3 shows several examples of the inversion for known model using a combined forward and then inverse algorithm as in Table 2. Cases I and II differ only by having the resistivities ρ_1 and ρ_2 interchanged. The exact values of (ρ_a, φ) derived from the models were rounded off to realistic field values before being used as input values to the inversion program. In all cases except for an abnormal program termination, the calculated output and input values of (ρ_a, φ) were virtually the same. Several interesting points concerning the results should be mentioned:

(i) convergence is achieved, if at all, in very few iterations,
(ii) calculated values of the model parameters are not sensitive to the particular starting model chosen (in the known ρ_2/ρ_1 method) and
(iii) the known ρ_2/ρ_1 method displays more numerical quirks than the known ρ_1 method.

For example, the second solution requires several attempts to find numerically (9 attempts in Case I, 33 attempts in Case II), assuming the same starting grid density as in the known ρ_1 method. This is due to the presence of two unequal local minima of the objective function E^2 and the desired solution happens to be not the global but a local minimum. Such problems can be dealt with to a certain degree by various procedures used in non-linear optimization methods (eg. Adby and Dempster, 1978) although the problem of many local minima is difficult to treat satisfactorily by any efficient algorithm.

Application to Three-Layer Models

Any numbers of layers can be included in the model and an inversion achieved provided only two free parameters have to be determined. For three layers there are two obvious choices in which parameters are assumed beforehand, viz., either

(i) known h_1 and assumed ratios ρ_2/ρ_1 , ρ_3/ρ_1 ; find ρ_1 , h_2 ,
or

(ii) known contrast h_2/h_1 and assumed ratios ρ_2/ρ_1 , ρ_3/ρ_1 ; find ρ_1 , h_1 (or h_1).

It is obvious that incorrect choices of the assumed parameters will lead to considerable difficulty in finding any solution which is geologically reasonable. Also there are many more possible solutions than for the two-layer model which not only adds to the problem of finding the desired minima but also increases the possibility of solutions lying on or close to maxima or minima of the curves of $|Q_1|$ and $\arg Q_1$ (Figures 8-11). If this happens then the partial derivates become very small and unstable inversions can occur. Considerable care is required to find the appropriate parameters for a three-layer situation and, whenever possible, maximum use should be made of geologic control and subsidiary geophysical information such as a DC resistivity survey or the monitoring of LF as well as VLF stations.

Combined Graphical-Numerical Interpretation

One way of avoiding the problems of the density of the starting grid and the singularity of A when starting near a maximum or minimum value in the iteration is to choose the starting model graphically and refine the solution by linearized iteration. This is a particularly attractive scheme for two-layer interpretation, as Table 1 can be used quickly and conveniently in conjunction with the master curves, Figures 6 and 7, as input to the numerical algorithm in Table 2. The advantages are two-fold: first, to give the operator an immediate idea of which starting parameters are reasonable for the particular data (this is especially important for the known ρ_2/ρ_1 method with its ambiguous solutions) and second, to avoid storing large arrays in the main computer program. This latter feature would then enable the numerical algorithm to operate well within the memory of current field operational microprocessors.

All these advantages would apply equally to three-layer interpretation, providing the master curves were chosen sufficiently carefully to reduce the number required for field use.

TRANSPARENCY OF A LAYER

It is evident from the preceeding discussion that the interpretation of apparent resistivity and phase is not unique, in the sense that one could choose any number of layers in the model to find a satisfactory fit to the data. In addition, certain combinations of resistivity and thickness of a layer could render that layer either very prominent or very insignificant for the interpretation. There is a general 'rule of thumb' in electrical sounding that the conductivity-thickness product controls the 'visibility' of a layer, which will now be discussed.

Analysis of the Hyperbolic Tangent Function

In an M-layer model, the correction factor for the m'th layer can be found by generalising equation (13) to

$$Q_m = \frac{\beta_m Q_{m+1} + \tanh(\alpha_m\sqrt{i})}{1+\beta_m Q_{m+1}\tanh(\alpha_m\sqrt{i})} \quad , \qquad (20)$$

as discussed in (I). The complex argument of the tanh( ) function can be written $(1+i)\alpha'_m$, where $\alpha'_m = \alpha_m/\sqrt{2}$, and the real imaginary parts are then

$$\mathrm{Re}\left(\tanh(\alpha_m\sqrt{i})\right) = \frac{\sinh(2\alpha'_m)}{\cosh(2\alpha'_m)+\cos(2\alpha'_m)} \qquad (21a)$$

and

$$\mathrm{Im}\left(\tanh(\alpha_m\sqrt{i})\right) = \frac{\sin(2\alpha'_m)}{\cosh(2\alpha'_m)+\cos(2\alpha'_m)} \qquad (21b)$$

From this last equation the imaginary component is seen to vanish when $2\alpha'_m = N\pi$, where N is an integer, which is equivalent to $h_m = N\pi\delta_m/2$. This repeating condition (N= 0,1,2...) gives the amplitude and phase curves their 'bulging' character at certain values of α_m . If α_m is small, equations (21a,b) reduce to

$$\mathrm{Re}\left(\tanh(\alpha_m\sqrt{i})\right) \approx \alpha'_m \qquad (22a)$$

and

$$\mathrm{Im}\left(\tanh(\alpha_m\sqrt{i})\right) \approx \alpha'_m \quad , \qquad (22b)$$

whereas for α_m large

$$\mathrm{Re}\left(\tanh(\alpha_m\sqrt{i})\right) \approx 1 \qquad (23a)$$

and

$$\mathrm{Im}\left(\tanh(\alpha_m\sqrt{i})\right) \approx 0 \quad . \qquad (23b)$$

Furthermore the imaginary part is a two-valued function of α'_m in the range $0 \leq \alpha'_m \leq \pi/2$, which gives rise to an ambiguity of solution in certain cases.

Analysis of the Correction Factor

Returning to (20), we can write

$$Q_{m-1} = \frac{\beta_{m-1}+\tanh(\alpha_{m-1}\sqrt{i})}{1+\beta_{m-1}\tanh(\alpha_{m-1}\sqrt{i})} \qquad (24a)$$

and

$$Q_m = 1 \quad , \qquad (24b)$$

by assuming α'_m is large so equations (23a,b) hold. The m'th layer, represented only by its resistivity contained in β_{m-1} , then effectively masks the lower layers. The opposite extreme is to take α'_m small, in which case

$$Q_m \approx \beta_m Q_{m+1} \qquad (25a)$$

which leads to

$$Q_{m-1} = \frac{\sqrt{\rho_{n+1}/\rho_{n-1}}\, Q_{m+1} + \tanh(\alpha_{m-1}\sqrt{i})}{1+\sqrt{\rho_{n+1}/\rho_{n-1}}\, Q_{m+1} \tanh(\alpha_{m-1}\sqrt{i})} \qquad (25b)$$

and the m'th layer is absent from the solution.

At this point the analysis becomes more straightforward if we let $Q_{m+1} = 1$, which indicates that the m'th layer is very opaque and α'_{m+1} is large. We then have, for the m'th layer

$$Q_m \approx \frac{\beta_m + \tanh(\alpha_m\sqrt{i})}{1+\beta_m \tanh(\alpha_m\sqrt{i})} \qquad (26)$$

and this layer becomes transparent when $\alpha_m \to 0$, i.e. from (25a)

$$Q_m \to \beta_m \quad , \quad (\alpha_m \approx 0) \quad . \qquad (27)$$

This can be seen in Figure 14 which shows the magnitude of Q_m as a function of α'_m. The curves of β_m and $1/\beta_m$ are symmetric about $|Q_m| = 1$ and the limiting condition (27) is satisfied. From this figure it appears that (27) is a reasonably good approximation for α'_m in the range $0 \leqslant \alpha'_m \leqslant 10^{-2}$, so we might enquire whether there is a condition on α'_m which is relevant to a nearly transparent layer.

It is shown in the Appendix that equation (26) has the components

$$|Q_m|^2 = \frac{e^{2p} + 2qe^p \cos p + q^2}{e^{2p} - 2qe^p \cos p + q^2}$$

and

$$\xi_m = \arg Q_m = \tan^{-1}\left(\frac{2qe^p \sin p}{q^2 - e^{2p}}\right)$$

where $p = \alpha_m\sqrt{2}$ and $q = (\beta_m - 1)/(\beta_m + 1)$. After some manipulation shown in the Appendix an explicit expression for p can be extracted

$$p = \tan^{-1}\left(\frac{\pm 2|Q_m| \sin \xi_m}{|Q_m|^2 - 1}\right)$$

or, replacing Q_m by β_m as in (27),

$$\alpha'_m \approx \frac{\beta_m \xi_m}{|\beta_m^2 - 1|} \quad , \qquad (28)$$

where we have assumed that α'_m, p and ξ_m are small. This expression relates the near transparency of any layer m to the phase shift ξ_m generated between the electric and magnetic field components. The smallest phase shift that can be detected by surface measurement is about 1°, so we can set $\xi_m = \pi/180$ and give the condition for a layer to be transparent as

$$\alpha'_m \leqslant \alpha'_{min} \qquad (29)$$

where

$$\alpha'_{min} = \frac{\pi}{180} \cdot \frac{\beta_m}{|\beta_m^2 - 1|} \qquad (30)$$

Also shown in Figure 14 are two lines representing 45° ± 1° phase angles computed as a function of α'_m. A quick graphical check for any layer is to see if the computed values (α'_m, β_m) lie within the 45° ± 1° zone; if so, the layer is transparent, if not, the layer contributes significantly to the interpretation.

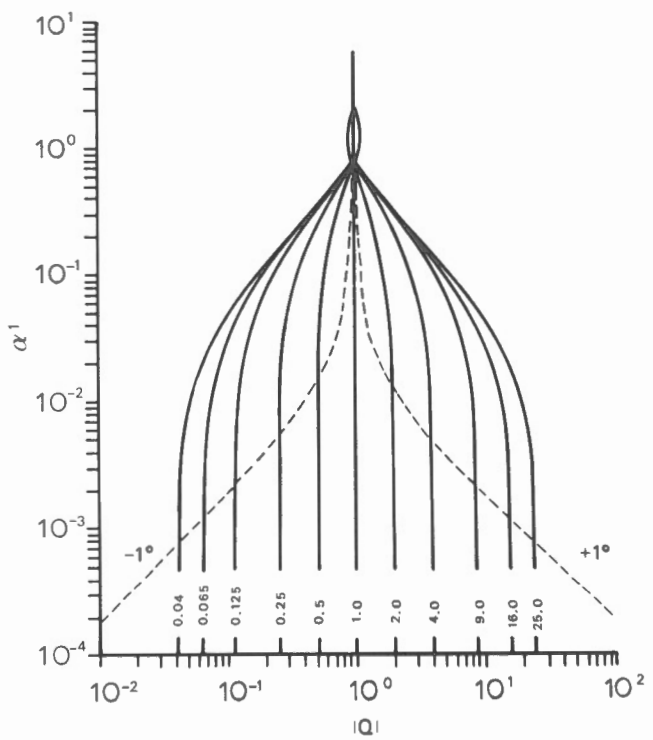

Figure 14. Amplitude of Q_m for an arbitrary layer m as a function of α'_m for values of $0.4 \leqslant \beta_m \leqslant 25$.

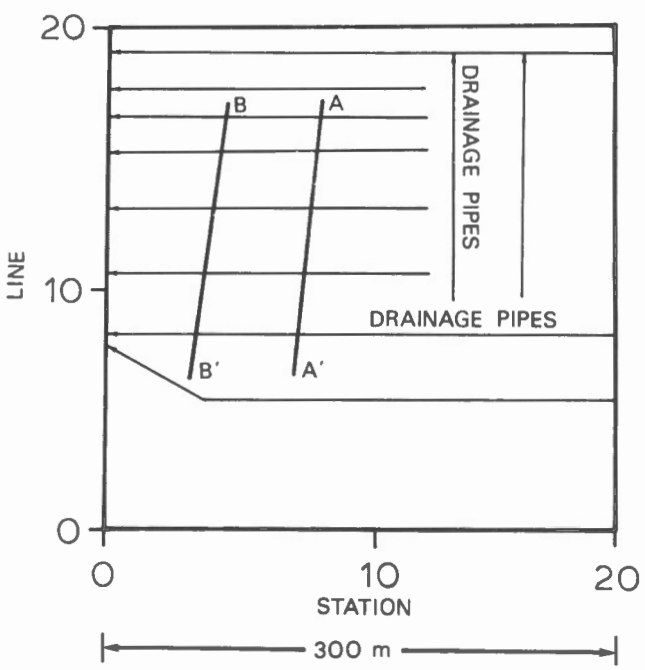

Figure 15. Location of drainage pipes in the survey area at St. Anne-de-Bellevue.

FIELD RESULTS AT ST. ANNE-DE-BELLEVUE, QUEBEC

This area is a cornfield located in the MacDonald Campus of McGill University at coordinates (45°25' N; 73°56' W). The geology of the area consists of an alluvial deposit of sandy loam covering a layered sequence of clays which overlies a limestone basement at depth (Chieng, 1976). The area is interesting because of a system of horizontal pipes installed to study groundwater drainage (Fig. 15). The pipes, buried at depths of 1 to 1.5 m (Fig. 16), divide the topsoil into a dry upper layer and a water-saturated lower layer. At the time of the survey the water table was found to be at approximately the depth of the pipes (Chieng, 1976).

The VLF survey used a Geonics EM16R receiver monitoring the 17.8 kHz Cutler transmitter and has taken over a grid of 20 lines and 20 stations spaced 100ft. apart. Contour maps of ρ_a and φ are shown in Figures 17 and 18 and indicate a relatively uniform resistivity structure for the area. The only significant anomalies are at station '0', due to a buried gas pipeline 10 ft. below the surface, and a minor high at line 16 station 18 due to a wire fence. Averaging over all the (ρ_a , φ) values gives ρ_a = 29.5 ± 8.7 Ω.m and φ = 27.2 ± 7.0° which is indicative of increasing resistivity with depth.

A representative station (line 7, station 4) was chosen as the centre of a small-scale hammer seismic survey using a 300ft. spread with profiles running both N-S and E-W. The mean of the two directions yielded a three-layer model with the following parameters: $V_1 \approx 1500 ft.s^{-1}$, $h_1 \approx 10ft$, $V_2 \approx 4100 ft.s^{-1}$, $h_2 \approx 45ft$ and $V_3 \approx 8000 ft.s^{-1}$. These are consistent with the geology mentioned above.

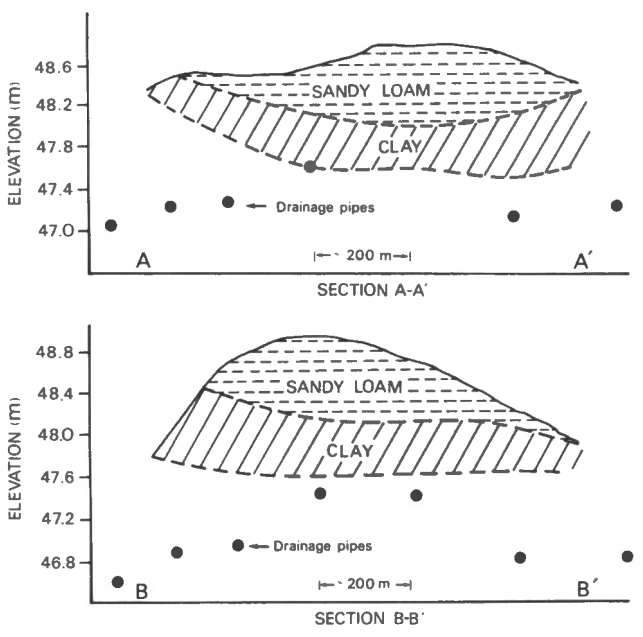

Figure 16. *Cross-sections of topsoil and drainage pipes from Figure 15.*

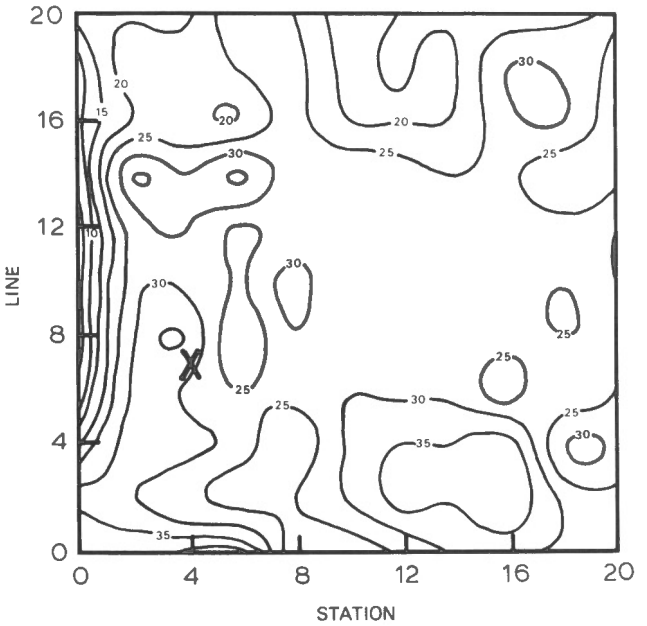

Figure 17. *Contour map of the apparent resistivity at St. Anne-de-Bellevue. Seismic and DC resistivity surveys centered at X (line 7, station 4). Grid size 100 ft. × 100 ft.*

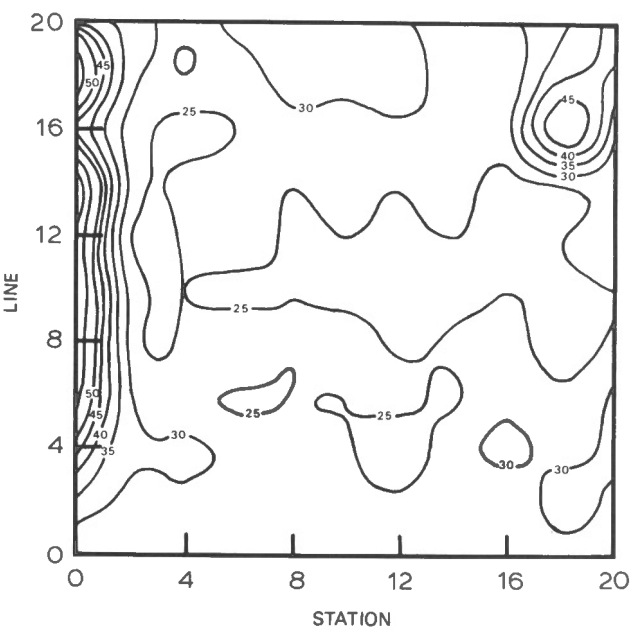

Figure 18. *Contour map of the phase angle at St. Anne-de-Bellevue.*

Further control was obtained with a Wenner DC resistivity sounding at the same location (line 7, station 4) using electrode spacings of 1-100 ft., again in both N-S and E-W directions. Three distinct layers were found and solutions for the parameters using master curves yielded the values $\rho_1 \approx 480$ Ω.m, $h_1 \approx 0.9m$, $\rho_2 \approx 12$ Ω.m, $h_3 \approx 3\text{-}9m$ and a large (indeterminate) value for ρ_3 .

As a result of these preliminary surveys it was decided to interpret the VLF data in two stages:

(i) two-layer models with ρ_1= 12 Ω.m, ρ_2/ρ_1 = 15,
(ii) three-layer models with h_1= 0.9m, ρ_2/ρ_1 = 0.025, ρ_3/ρ_2 = 40 and h_2/h_1 = 3, ρ_2/ρ_1 = 0.025, ρ_3/ρ_2 = 40.

The values given are assumed fixed throughout the inversion.

Two-Layer Interpretation

We first ignore the thin top layer (480 Ω.m, 0.9m) and invert the (ρ_a , φ) values with a starting value for ρ_1 of 12 Ω.m. This was later charged to 14 Ω.m and 25 Ω.m to assess the effect on the solution of an incorrect value for this first layer resistivity. Line 7 was selected as a representative profile and the inversion was performed numerically as outlined above. It was found that although the solutions for (h_1 , ρ_2) were not very sensitive to a change of ρ_1 from 12 Ω.m to 14 Ω.m, when ρ_1 was set to 25 Ω.m these parameters were significantly altered even to the extent that at some stations a two-layer solution could not be obtained.

To test the second possible situation, a contrast for ρ_2/ρ_1 of 15 was selected on the basis of the electrical sounding and extreme values for ρ_2/ρ_1 of 10 and 40 were also attempted. As mentioned above this inversion method is more prone to errors in the starting model than the known ρ_1 method; this was borne out in practise when the results of the three values for ρ_2/ρ_1 (above) were compared. Only for a value of 15 for the resistivity contrast were the parameters h_1 and ρ_2 at all well-behaved. In particular the shallow solution often yielded negative depths whereas the deeper solution gave reasonable values even for the higher contrast of ρ_2/ρ_1 = 40.

The two-layer solutions are summarized by comparing the h_1 , ρ_2 and ρ_1 values for line 7 in Figure 19. In general the most acceptable solutions were obtained with a value of ρ_1 = 12 Ω.m which was about midway between the shallow and deep solutions, $\rho_1 \approx$ 5 Ω.m and 20 Ω.m respectively, for the known ρ_2/ρ_1 method. The major interface occurs at about 4 to 5m for the known ρ_1 method but varies considerably between about 1m for the shallow to 15m for the deep solutions of the known ρ_2/ρ_1 method. One would have to conclude that the known ρ_1 method yields a better approximation to the DC resistivity section (assuming the top layer is missing) because the known ρ_2/ρ_1 method leaves it unclear as to whether the shallow or deep interpretation is better (Fig. 20).

Three-Layer Interpretation

The first method assumes that h_2/h_1 is known; in this case it was taken to be the lowest value, i.e. 3, obtained from the DC sounding, and contrasts of ρ_2/ρ_1 and ρ_3/ρ_2 were taken to be 12/480 (0.025) and 480/12 (40) respectively. The computed parameters ρ_1 and h_1 gave the

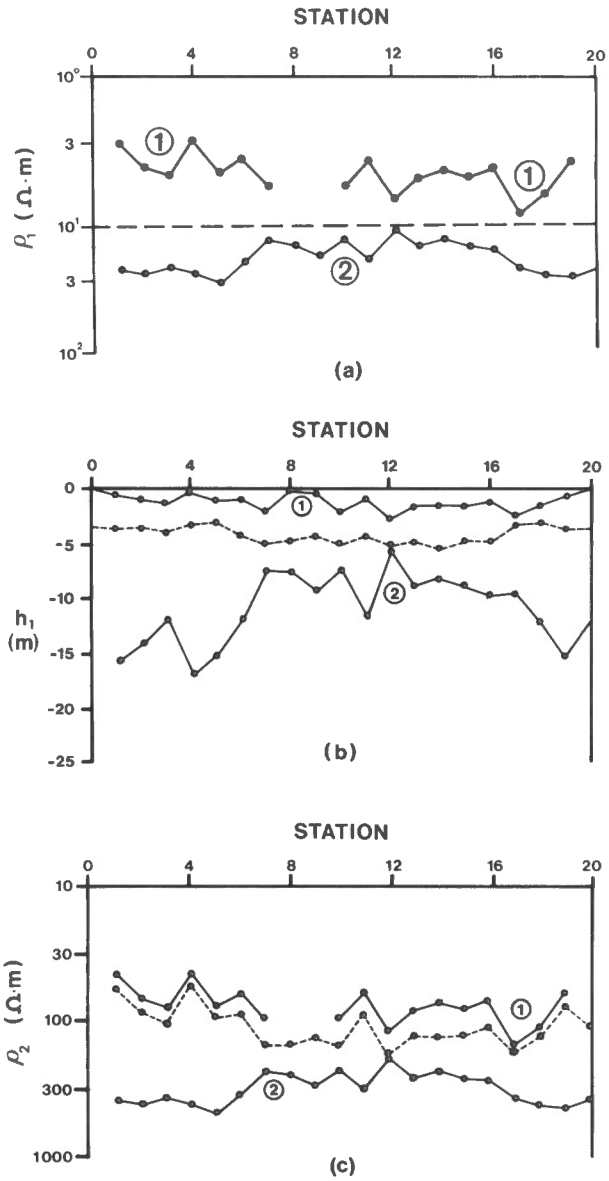

Figure 19. *Comparison of profiles for line 7, St. Anne-de-Bellevue; + is the known ρ_1 method and 1, 2 are the shallow and deep solutions of the known ρ_2/ρ_1 method. **a)** values of ρ_1 , **b)** values of h_1 and **c)** values of ρ_2 .*

results for line 7 shown in Figures 20 (d)-(e) where the averages of all station parameters are shown. Only the deep solution is displayed because the shallow solution gave values of h_1 very close to zero. The second method, assuming h_1= 0.9m and with the same resistivity contrasts, might be expected to yield better agreement with the DC resistivity values but it can be seen that the effect of fixing h_1 is to force ρ_2 and h_2 to substantially differ from the control solution. In this case there is some advantage in allowing h_1 to remain flexible in the inversion, unlike the two-layer situation where the knowledge of ρ_1 is clearly a superior choice.

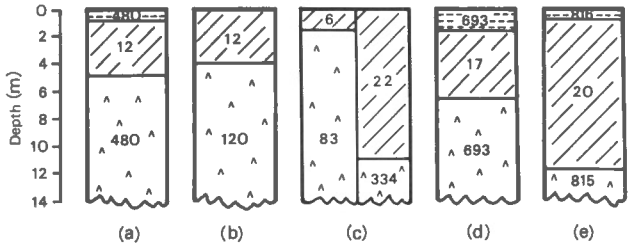

Figure 20. *Comparison of results for St. Anne-de-Bellevue survey. Numbers shown are average resistivities (Ω.m) for line 7.*
a) *DC resistivity (control):* $h_1 = 0.9m$, $h_2 \sim 5m$,
b) *two-layer VLF resistivity (known* ρ_1 *):* $h_1 = 4m$,
c) *two-layer VLF resistivity (known* ρ_2/ρ_1 *): left is shallow solution,* $h_1 = 1.6m$; *right is deep solution,* $h_1 = 11m$,
d) *three-layer VLF resistivity (known* h_2/h_1 *):* $h_1 = 1.7m$, $h_2 = 5m$ *and*
e) *three-layer VLF resistivity (known* h_1 *):* $h_1 = 0.9m$, $h_2 = 11m$.

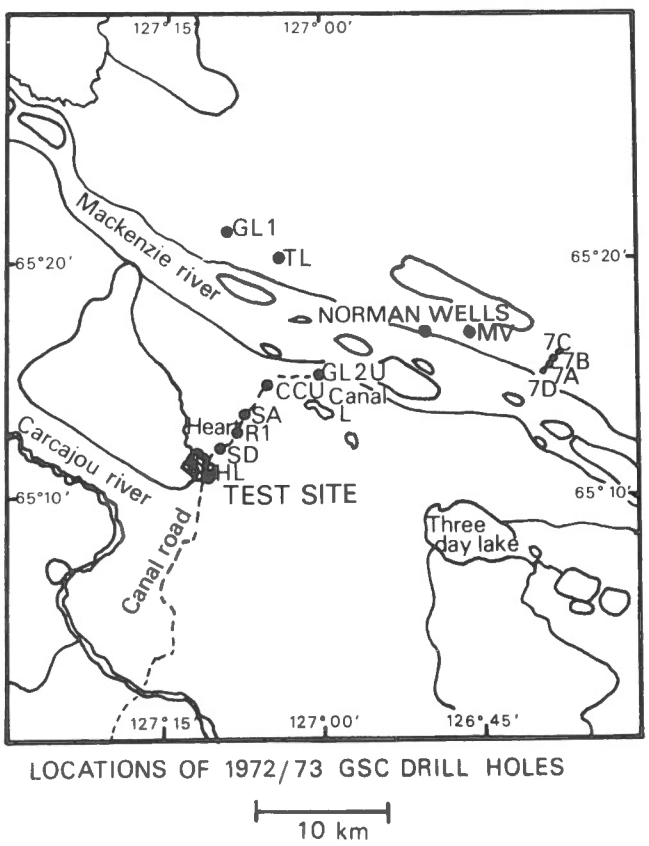

Figure 21. *Location of the Norman Wells site and related drill holes (after Kurfurst et al., 1973).*

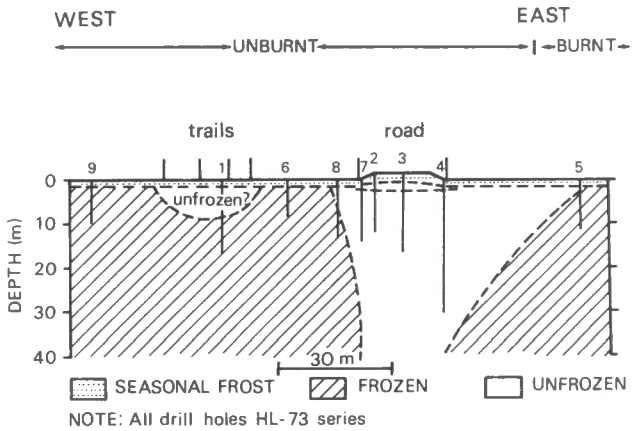

Figure 22. *Profile at drill site HL, based on drill hole results (after Kurfurst et al. 1973).*

FIELD RESULTS: HEART LAKE, NORMAN WELLS

The survey area ia about 9 miles west of Norman Wells on the MacKenzie River, located on Map 96 E/3, coordinates 84-86; 30-32 in the vicinity of Heart Lake (Fig. 21). Both silt and organic soil types can be found in the area and the overburden composition in the HL-33 series holes is mainly one of a clay silt classification overlying a clay-shale bedrock which is highly weathered (Kurfurst et. al., 1973). A cross section of the area determined from drill holes is shown in Figure 22 and contains several interesting features which disturb the electrical properties of the near surface permafrost. The west side of the area is virgin vegetation covering permafrost over bedrock, the simplest to model, whereas the east side has experienced lightening-caused fires that destroyed the vegetation and left thawed topsoil over permafrost over bedrock. In between is a road built over the topsoil which should have lead to melting of the permafrost in its vicinity.

As a preliminary to the VLF survey several DC resistivity soundings were taken in the area using both the Schlumberger and Wenner array methods. The results of these surveys are discussed in detail in Mathieson (1980) and can be summarized as indicating a three-layer model with parameters $\rho_1 = 1000\ \Omega.m$, $h_1 = 1.25m$, $\rho_2 = 2500\ \Omega.m$, $h_2 = 18.2m$ and $\rho_3 = 15\ \Omega.m$. We therefore expect in general to find permafrost of relatively high resistivity down to a depth of about 20m, when the conductive bedrock is reached; the extent to which this model is affected by the local anomalies should be reflected in the detailed VLF resistivity results.

A typical line across the area taken with the EM16R equipment and using the Jim Creek 18.6 kHz transmitter is shown in Figure 23. The phase angle shows a very consistent value of about 61° whereas the apparent resistivity varies from a low of about 10 Ω.m over the road to about 70 Ω.m over certain narrow zones in both the E and W sides of the road. These values are typical over the whole survey. As for the St. Anne de Bellevue site, interpretation of the VLF data proceeds by finding a suitable two-layer model and then extending this to a three-layer model in an attempt to find a thin surface layer, in this case thawing of the permafrsost.

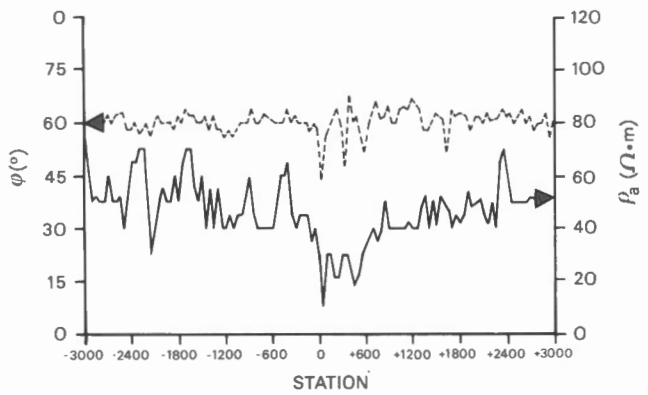

Figure 23. *Profiles of apparent resistivity (solid line) and phase (dashed line) at line 0, Norman Wells test site. Note that the E-W directions are reversed in comparison with Figure 22.*

Two-Layer Interpretation

An initial value of ρ_1 = 1050 Ω.m was chosen for the first inversion of the data and the (h_1 , ρ_2) values are computed in profile form for line 0 in Figure 24. The road can clearly be seen in the vicinity of station -600 (east) as a thinning of the top layer from the bottom (Fig. 24b). If a thaw had occurred in the surface layer, one would expect a three-layer model with the bottom of the permafrost layer remaining at a fixed depth and an upper low resistivity layer appearing. Therefore we have a clear case of a misleading two-layer interpretation due to an insufficiently sophisticated model.

Assuming ρ_2/ρ_1 is known (a value of 0.0625 was chosen) yields profiles for line 0, shown also in Figure 24, which give in this case a clear agreement between the shallow solution and the known ρ_1 results. The deep solution, on the other hand, predicts the major permafrost bedrock discontinuity better even though the resistivities of both layers are on the low side.

Three-Layer Interpretation

In this test area it is clear that a two-layer model is insufficient to delineate the thin surface layer of thawed permafrost that is suggested by the more detailed DC results (Mathieson, 1980). As for the survey at St. Anne de Bellevue, two three-layer models were tried, the first with a fixed values of h_1 = 1.25m, ρ_2/ρ_1 = 2.5 and ρ_3/ρ_2 = 0.006 which yielded a sensible result only for the deep solution . When the contrast method was tried (h_2/h_1 = 14.5, ρ_2/ρ_1 = 2.5, ρ_3/ρ_2 = 0.006) no reasonable solutions could be found. The three-layer solution is compared with the two-layer solutions and the DC resistivity results in Figure 25, again averaging all the results for line 0. It can be seen there is a definite boundary between partially thawed and unthawed permafrost which warrents the three layer solution, but heavy reliance has been placed on the available controls in the area for this VLF resistivity interpretation to be justified.

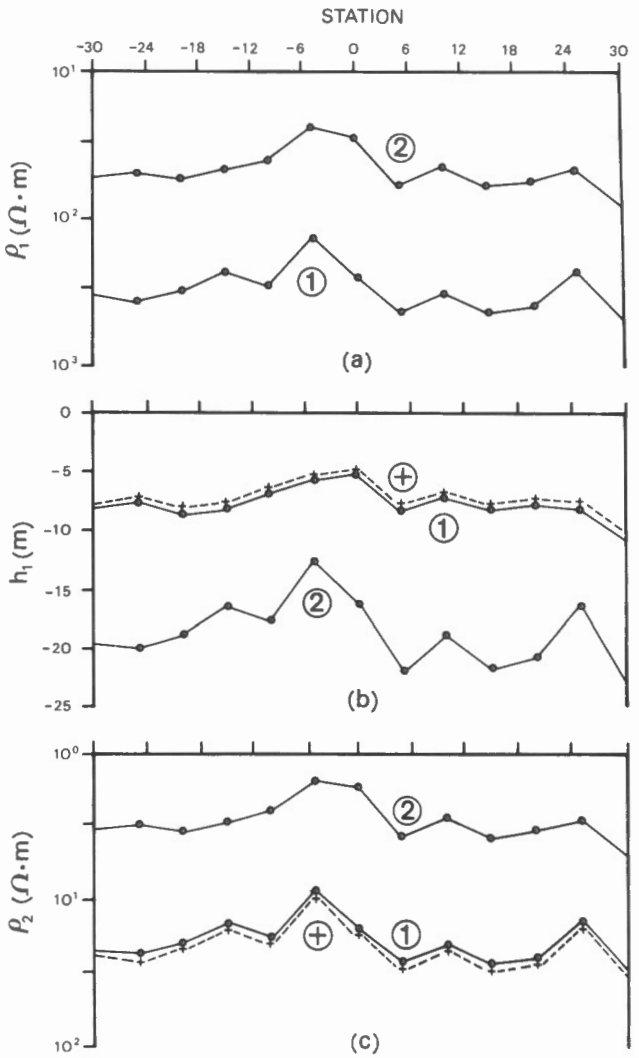

Figure 24. *Comparison of profiles for line 0, Norman Wells, + is the known ρ_1 method and 1, 2 are the shallow and deep solutions of the known ρ_2/ρ_1 method.* ***a)*** *values of ρ_1 ,* ***b)*** *values of h_1 and* ***c)*** *values of ρ_2.*

DISCUSSION

It is apparent from the field results that VLF resistivity interpretation is most reliable for a two-layer model with ρ_1 known. If only the contrast ρ_2/ρ_1 is assumed, then the choice of the shallow or deep solution is not necessarily a clear one, especially where the two solutions lie either side of the solution with ρ_1 known as at St. Anne de Bellevue. This ambiguity is aggravated in both field examples because no two-layer model is really sufficient to describe the geology and one must resort to a three-layer model to find a near surface layer.

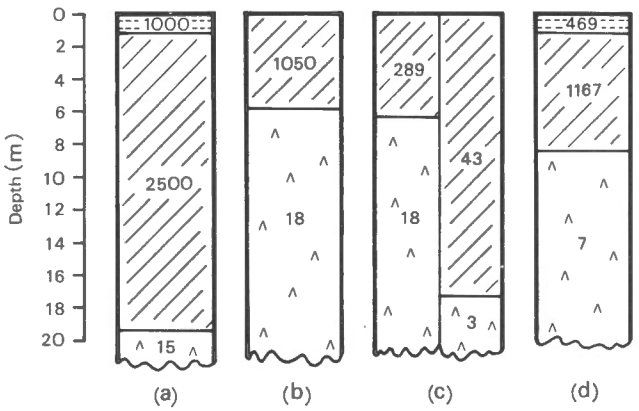

Figure 25. *Comparison of results for Norman Wells survey. Numbers shown are average resistivities (Ω.m) for line 0 (E-W).*

a) *DC resistivity (control):* $h_1 = 1.25m$, $h_2 = 18.2m$,

b) *two-layer VLF resistivity (known* ρ_1*):* $h_1 = 5.9m$,

c) *two-layer VLF resistivity (known* ρ_2/ρ_1*): left is shallow solution,* $h_1 = 6.4m$*; right is deep solution,* $h_1 = 17.4m$ *and*

d) *three-layer VLF resistivity (known* h_1*):* $h_1 = 1.25m$, $h_2 = 7.2m$.

We might enquire whether this thin surface layer can be considered transparent by the treatment above. For the St. Anne de Bellevue survey we take the surface layer ($\rho_1 = 480\ \Omega.m$, $h_1 = 0.9m$, $\rho_2 = 12\ \Omega.m$) to have the parameters ($\alpha_1' = 0.0109$, $\beta_1 = 0.158$) which lead to a point is outside the $45° \pm 1°$ lines in Figure 14. Further confirmation that the layer is not transparent is obtained by evaluating α'_{min} from equation (30) which is 0.0028, hence by (29) the conjecture is proven and a three-layer model is indicated.

Let us repeat this for the Norman Wells survey where we take the values as given by the DC resistivity sounding, i.e. $\rho_1 = 1000\ \Omega.m$, $h_1 = 1.25m$, $\rho_2 = 2500\ \Omega.m$, $h_2 = 18.2m$ and $\rho_3 = 15\ \Omega.m$. Applying equations (29) and (30) we find

layer 1: $\alpha_1' = 0.0107$, $\beta_1 = 1.58$, $\alpha'_{min} = 0.0185$ (transparent),

layer 2: $\alpha_2' = 0.099$, $\beta_2 = 0.08$, $\alpha'_{min} = 0.0011$. (not transparent).

Reducing this model to a two layer structure with parameters $\rho_1 = 1050\ \Omega.m$, $h_1 = 10m$ and $\rho_2 = 4.1\ \Omega.m$ yields

layer 1: $\alpha_1' = 0.084$, $\beta_1 = 0.0625$, $\alpha'_{min} = 0.0011$ (not transparent),

as expected. This analysis should obviously be done for each station individually rather than a global average as outlined here.

When one comes to perform a three-layer inversion, provided it is warranted by reasoning such as the above, it is obvious that extreme care in selecting the fixed parameters must be exercised. Unless good control data is available it would seem that a three-layer interpretation is rather unreliable for VLF data and the use of a second, preferably LF, transmitter would be invaluable for determining thin surface layers.

Finally it has to be acknowledged that the above interpretation suffers from the drawback of using horizontally layered models rather than realistic laterally varying models. This is especially true for the Norman Wells survey, where adjacent stations give quite different vertical structure. Attempts to overcome this limitation are described elsewhere (Teemull and Crossley, 1981-VI).

SUMMARY

We have shown that it is possible to construct a single family of master curves for the interpretation of all two-layer VLF resistivity measurements of apparent resistivities and phase angle. These should be useful not only as a direct aid to field interpretation but also as a means of commencing a least squares inversion for more accurate interpretation.

Application of numerical methods to three-layer field situations shows the severe limitations of the VLF method using only one frequency unless such good subsidiary control is available as to seriously question the reliability of the VLF technique. Hopefully more extensive ground survey use of the 60 kHz LF signal in Canada, which we advocate, will permit more secure interpretation than currently possible.

ACKNOWLEDGEMENTS

The research which this article summarizes was supported by the EMR Canada through Research Agreements 1135-D13-4-39/76, 4-99-77 and 58-4-78, and by the NSERC Operating Grant A4240.

The authors would like to express sincere thanks to W. Scott, formerly of the GSC Ottawa, for help in acquiring the field data and for various discussions on the VLF resistivity method.

REFERENCES

Adby, P.R. and Dempster, M.A.H.
1978: Introduction to Optimization Methods, Chapman and Hall, London, 204 pp.

Chieng, S.T.
1976: The effects of subsurface basin depths and drainage rate on water levels, M.Sc. Thesis, MacDonald College, McGill University.

Crossley, D.J.
1981: The theory of EM surface-wave impedance measurement; in Geophysical Applications of Surface-Wave Impedance Measurements, L.S. Collett and O.G. Jensen (eds.), Geological Survey of Canada, Paper 81-15, Report V, p. 1-17.

Jackson, D.D.
1972: Interpretation of inaccurate, insufficient and inconsistent data, Geophys. J. R. Astr. Soc. 28, p. 97-109.

Kurfurst, P.J., Isaas, R.M., Hunter, J.A. and Scott, W.J.
1973: Permafrost studies in the Norman Wells Region, N.W.T.; in Proceedings of the Symposium on the Geology of the Canadian Arctic, Saskatoon, J.D. Aitken and D.J. Glass (eds.), Canadian Society of Petroleum Geologists, Calgary, 368 pp.

Mathieson, C.C.
1980: Graphical and numerical interpretation of VLF resistivity studies, M.Sc. Thesis, McGill University.

Teemull, F. and Crossley, D.J.
1981: The interpretation of lateral inhomogeneities in ground VLF resistivity data; in Geophysical Applications of Surface-Wave Impedance Measurements, L.S. Collett and O.G. Jensen (eds.), Geological Survey of Canada, Paper 81-15, Report V, p. 79-86.

Wiggins, R.A.
1972: The general inverse problem: implication of surface waves and free oscillations for Earth structure, Reviews of Geophysics and Space Physics, 10, 1, p. 251-285.

APPENDIX - DERIVATION OF MATHEMATICAL RESULTS

Correction Factor

The two-layer correction factor, equation (6), is

$$Q_1 = \frac{\beta_1 + \tanh(\alpha_1\sqrt{i})}{1 + \beta_1 \tanh(\alpha_1\sqrt{i})} \quad , \qquad (A1)$$

where α_1 , β_1 are given by (7). It is convenient to define subsidiary parameters

$$p = \sqrt{2}\,\alpha_1 \quad , \qquad q = \frac{\beta_1 - 1}{\beta_1 + 1}$$

so that (A1) becomes

$$Q_1 = \frac{e^{(1+i)p} + q}{e^{(1+i)p} - q} \quad .$$

Rationalising and extracting the magnitude and phase we find

$$|Q_1|^2 = \frac{e^{2p} + 2qe^p \cos p + q^2}{e^{2p} - 2qe^p \cos p + q^2} \qquad (A2)$$

and

$$\arg Q_1 = \tan^{-1}\left(\frac{2qe^p \sin p}{q^2 - e^{2p}}\right) \quad . \qquad (A3)$$

Partial Derivatives

Differentiating (A2) and (A3) with respect to p and q results in the expressions

$$\frac{\partial|Q_1|^2}{\partial p} = \frac{4qe^p}{(e^{2p} - 2qe^p\cos p + q^2)^2}\left\{q^2(\cos p - \sin p) - e^{2p}(\cos p + \sin p)\right\} \qquad (A4)$$

$$\frac{\partial|Q_1|^2}{\partial q} = \frac{4e^p \cos p\,(e^{2p} - q^2)}{(e^{2p} - 2qe^p\cos p + q^2)^2} \quad , \qquad (A5)$$

$$\frac{\partial(\arg Q_1)}{\partial p} = \frac{2qe^p\left[q^2(\sin p + \cos p) + e^{2p}(\sin p - \cos p)\right]}{(e^{4p} - 2q^2e^{2p}\cos 2p + q^4)} \qquad (A6)$$

and

$$\frac{\partial(\arg Q_1)}{\partial q} = \frac{-2e^p \sin p\,(e^{2p} + q^2)}{(e^{4p} - 2q^2e^{2p}\cos 2p + q^4)} \quad . \qquad (A7)$$

From these we can quickly establish the required derivatives. For the known ρ_1 method,

$$\left.\begin{aligned}
\frac{\partial\rho_a}{\partial\alpha_1} &= -\frac{2\rho_1}{\alpha_1}|Q_1|^2 + \rho_1\sqrt{2}\;\frac{\partial|Q_1|^2}{\partial p} \\
\frac{\partial\rho_a}{\partial\beta_1} &= -\frac{2\rho_1}{\beta_1}|Q_1|^2 + \frac{2\rho_1}{(1+\beta_1)^2}\;\frac{\partial|Q_1|^2}{\partial q} \\
\frac{\partial\varphi}{\partial\alpha_1} &= \frac{180\sqrt{2}}{\pi}\;\frac{\partial(\arg Q_1)}{\partial p} \\
\frac{\partial\varphi}{\partial\beta_1} &= \frac{360}{\pi(1+\beta_1)^2}\;\frac{\partial(\arg Q_1)}{\partial q}
\end{aligned}\right\} \qquad (A8)$$

and for the known ρ_2/ρ_1 method,

$$\left.\begin{aligned}
\frac{\partial \rho_a}{\partial \rho_1} &= |Q_1|^2 - \frac{p}{2}\ \frac{\partial |Q_1|^2}{\partial p} - \frac{\beta_1}{(1+\beta_1)^2}\ \frac{\partial |Q_1|^2}{\partial q} \\
\frac{\partial \rho_a}{\partial h_1} &= 2\rho_1 |Q_1|^2 + \sqrt{2\omega\mu_0\rho_1}\ \frac{\partial |Q_1|^2}{\partial p} \\
\frac{\partial \varphi}{\partial \rho_1} &= -\frac{180}{\pi \rho_1}\left[\frac{p}{2}\ \frac{\partial (\arg Q_1)}{\partial p} + \frac{\beta_1}{(1+\beta_1)^2}\ \frac{\partial (\arg Q_1)}{\partial q}\right] \\
\frac{\partial \varphi}{\partial h_1} &= \frac{180p}{\pi h_1}\ \frac{\partial (\arg Q_1)}{\partial p}
\end{aligned}\right\} \quad (A9)$$

These quantities form the components A_{11}, A_{12}, A_{21} and A_{22} of the partial derivative matrix .

Transparency Requirement

From (A2)

$$|Q_1|^2 - 1 = \frac{-4q\,e^p \cos p}{(e^{2p} + 2q\,e^p \cos p + q^2)} \quad ,$$

and using the identity

$$\sin \xi = \frac{\tan \xi}{\sqrt{1 + \tan^2 \xi}}$$

where $\xi = \arg Q_1$, we find

$$\sin \xi = \frac{2q\,e^p \sin p}{[(e^{2p} + 2q\,e^p \cos p + q^2)(e^{2p} - 2q\,e^p \cos p + q^2)]^{1/2}} \ .$$

Combining the above it follows without approximation that

$$\frac{\sin \xi}{|Q_1|^2 - 1} = -\frac{1}{2} \tan p \quad , \qquad (A10)$$

and generalisation to the m'th layer leads directly to equation (28).

V

WAVE IMPEDANCE MEASUREMENTS AT 60 kHz

P.T. LaFleche* and O.G. Jensen+
* Scintrex, Ltd.
+ Laboratory in Applied Geophysics, McGill University

LaFleche, P.T. and Jensen, O.G., Wave impedance measurements at 60 kHz; in Geophysical Applications of Surface Wave Impedance Measurements, L.S. Collett and O.G. Jensen editors; Geological Survey of Canada, Paper 81-15, p. 67-78, 1981.

Abstract

The geophysical use of the low-frequency (LF) 60 kHz carrier of the amplitude-modulated time code signal transmitted by station WWVB, Fort Collins, Colorado, for ground surface wave-impedance measurements in Canada is demonstrated. A prototype instrument is described, which was designed and constructed in order to provide measurements of the appropriate electric and magnetic field vector amplitudes, along with the relative phase between them. This instrument proved to be rugged and reliable in field use, while providing highly reproducible measurements of the quantities necessary to the determination of the wave impedance on the ground surface. A calibration survey was conducted at the Kidd Creek Mine site in Timmins, Ontario. A subsequent survey at the Macdonald College Farm in Ste.-Anne-de-Bellevue, Quebec, using both the standard, very low frequency (VLF) receiver and the prototype LF instrument, has clearly established the advantage in obtaining measurements at a frequency well above 20 kHz. A three-layer geological model of this survey site is shown to be required in order to correspond measurements obtained at both frequencies.

Résumé

On a démontré que l'on peut, à l'aide de l'onde porteuse basse fréquence de 60 kHz du signal horaire à modulation d'amplitude transmis par la station WWVB, Fort Collins, Colorado, mesurer, au Canada, l'impédance caractéristique de la surface du sol. On a décrit un prototype d'instrument conçu et construit pour mesurer des amplitudes appropriées de vecteurs des champs électriques ou magnétiques ainsi que leur différence de phase. Cet instrument s'est avéré résistant et sûr sur le terrain, tout en offrant des mesures faciles à reproduire des quantités nécessaires à la détermination de l'impédance caractéristique de la surface du sol. Une étude de calibration a été effectuée sur le terrain, à la mine Kidd Creek à Timmins (Ontario). Une étude réalisée par la suite à la ferme du collège Macdonald à Ste.-Anne-de-Bellevue (Québec) dans laquelle on a utilisé le récepteur standard de très basse fréquence (TBF) et l'instrument prototype BF, a clairement démontré les avantages qu'il y a à obtenir des mesures à une fréquence dépassant nettement 20 kHz. Le compte rendu démontre ensuite qu'il faudrait avoir recours, pour ce site, à un modèle géologique à 3 couches pour faire correspondre les mesures obtenues aux deux fréquences.

INTRODUCTION

Following the formalism of Wait (1962), Crossley (1981-I) has obtained relationships for the surface-wave impedance of very low frequency (VLF) and low frequency (LF) surface-guided electromagnetic (EM) waves under the influence of a halfspace crust which is structured in its electrical conductivity. He has also shown that the commonly derived geophysical measurements of the apparent resistivity of the halfspace and the phase lag between the electric (E) and the magnetic (H) field vectors depends upon the subsurface electrical permittivity, ϵ , and the magnetic permeability, μ . Conductivity, σ , permittivity and permeability each differently affect the wave impedance at different frequencies in a way that very strongly depends upon the subsurface distribution of these geophysical properties. For a simple halfspace ground structure in which the permittivity and permeability are those of free space, i.e. ϵ_0 and μ_0 respectively, the apparent resistivity measure is just the inverse of the electrical conductivity of the halfspace and the phase lag between the E and H field vectors is precisely $\pi/4$, irrespective of the wave frequency.

The exact relationship between the E and the H fields also depends upon the assumption that the air-space overlying the conductive halfspace is a non-conductive semi-infinite halfspace in which the permittivity , ϵ , and the permeability , μ , are representative of free space. Because the real conductivity, permittivity and permeability of the air-space are so similar to the equivalent free-space quantities, they do not give rise to any material difference in this result as obtained from the standard EM propagation theory. However, the effect of any real structure of the air-space above the surface must have a significant influence on the character of the wave propagation itself, particularly for EM waves whose wavelength is of the order of the shortest dimension of the spherical waveguide formed by the earth's surface and the ionospheric D and E layers in which the "surface-guided waves" are naturally

confined. Practically, at VLF and LF, this effect is almost insignificant and Crossley has shown that in the case of a uniformly conductive halfspace geophysical model, the actual form of the wave propagation, whether of plane-wave, inhomogeneous plane-wave, Zenneck-wave or wave-guided mode, has no influence on the surface wave-impedance measure. On the other hand, where there is additionally a material permittivity and permeability of the uniformly conducting halfspace, the surface-wave impedance does become frequency dependent and the air-space wave propagation is affected. For example, the apparent resistivity obtained by surface wave-impedance measurement over a halfspace of pure water (conductivity $\sigma = 2.0 \times 10^{-4}$ $S.m^{-1}$, $\epsilon = 80\epsilon_0$, $\mu = \mu_0$) would be an overestimate of the actual inverse conductivity at 20 kHz by almost 20% and the phase lag between the E and the H fields would be reduced to only 32° from the normal halfspace value of 45°. In ignorance of the frequency-dependent permittivity effect, these apparent resistivity and phase angle measurements could lead to an erroneous geophysical interpretation of a layered structure in which the conductivity decreases with depth (See Crossley (1981-I).).

One can avoid the problem of ambiguity in the source of the anomaly in apparent resistivity and phase lag through the measurement of the surface-wave impedance at more than one frequency since the frequency dependence of the permittivity effect and that of a layered conductive structure are quite dissimilar. The permittivity effect in pure water is probably greater than would be expected in any normal geophysical field condition since the effect is magnified for a given permittivity in a material of low conductivity. Even common fresh water shows a typical conductivity an order of magnitude greater than that of pure water due to the presence of minute concentrations of dissolved electrolytes. Consequently, the permittivity effect becomes masked by the dominating conductivity effect. However, one cannot reasonably ignore the permittivity effect when geophysically surveying in regions of extremely high apparent resistivity such as in the 1 MΩ.m volcanics of the Abitibi region of northern Quebec.

A somewhat similar condition could arise when surveying over a conductive body having a significant magnetic permeability. The apparent resistivity measurement would, in this case, underestimate the actual inverse conductivity and the phase angle would be reduced. Also, in the case of a permeable or permittive halfspace, the actual form or mode of propagation of the incident EM wave has a significant effect on the impedance measurement (Crossley, 1981-I). However, except when surveying in regions of massive magnetite deposits, the geophysicist would probably seldom encounter field conditions where the magnetic permeability effect is significant.

In principle, the various effects competing to modify the apparent-resistivity and phase-angle measurements from those representative of a uniform halfspace (i.e. conductivity variation, permittivity variation, permeability variation and the wave propagation mode condition) can be resolved through the use of a sufficient number of particular frequencies or a spectrum of frequencies in an interpretation constrained by a theoretical development complete in the necessary details. Such an approach to geophysical surveying and the subsequent interpretation of the measurements obtained is obviously intractable and consequently, some order of compromise is essential to practical geophysical use of surface-guided radio waves. Conventionally, two compromise solutions are now being applied: 1) the use of ultra-low frequency (ULF) magnetotelluric (MT) wave fields whose relatively long periods tend to accomplish large volume averagings of the subsurface geophysical properties and 2) the use of the 20 kHz-band VLF radio transmissions derived from the international communications-navigation network. In the MT method, the uncontrolled (direction and polarization) character of the natural sources is its most essential limitation while it does offer the apparent advantage of an available spectrum of frequencies. In the VLF methods, the azimuthal direction and polarization of the sources are quite precisely fixed but there is no sufficient bandwidth of frequencies to allow for any resolution of the competing effects on the geophysical wave-impedance measurements. It is, however, well known that many other useful artificial sources of surface-guided waves in the VLF (3 kHz to 30 kHz), the LF (30 kHz to 300 kHz) and the MF (medium frequency: 300 kHz to 3 MHz) radio bands present freely-available signals for geophysical use. The higher frequencies beyond the 20 kHz range of the VLF band have not been much explored for such use because the penetration of such EM fields into common geological structures is reduced as the square root of the reciprocal of the wave frequency and, most commonly, geophysicists are seeking methods of increasing the penetration of their methods in the search for mineral and petroleum resources. At the present time, no very convenient artificial lower frequency sources of VLF and ULF waves are available except from the 10 kHz band of frequencies of the Omega Navigation System (Kamas, 1977) which are not azimuthally fixed or from small portable active transmitters. However, in spite of the reduction in penetration, the higher frequencies in the LF band can be used to help resolve the source of any measured deviation from a simply-conductive halfspace structure.

With such a material advantage in mind, we shall here describe a prototype instrument which has been designed to make wave-impedance measurements in the LF band. The instrument makes use of the 60 kHz WWVB time code transmissions originating from the United States National Bureau of Standards transmitter in Fort Collins, Colorado. This instrument could be easily modified for use of several other international transmissions in the 40-91 kHz band of frequencies originating from the sources listed in Table 1.

Table 1. LF Transmissions which could be used in eastern Canada.

Station Code	Location	Frequency
JG2AS	Chiba, Japan	40 kHz
WWVB	Fort Collins, Colorado	60
MSF	Rugby, England	60
HBG	Prangins, Switzerland	75
DCF 77	Mainflingen, Germany	77.5
NSS	Annapolis, Maryland	88
FTA 91	St.Andre-de-Corcy, France	91.2

INSTRUMENT DESIGN

The 60 kHz radio signal is transmitted from station WWVB, Fort Collins, Colorado as a modified IRIG (Inter Range Instrument Group) H time code (Kamas, 1977) amplitude modulating the carrier which has an effective radiative power of only 13 kW. This gives rise to a free-space electrical signal in the Montreal region of eastern Canada of about 100 $\mu V.m^{-1}$. Both the source radiative power and the received signal level are much lower than the equivalent measures for the megawatt-plus VLF transmissions in the 20 kHz band. However, it is not the total radiative power or, in fact, the total signal level which is important to the signal's usefulness in geophysical measurement of the surface-wave impedance; rather, the signal power density, i.e. the power per bandwidth, determines the usefulness of the WWVB time-code transmissions. Whereas the VLF transmissions have a characteristic bandwidth of about 50 Hz, the WWVB transmission has a very narrow bandwidth of only about 1 Hz. Consequently, the power density for the 60 kHz signal is, at source, a factor of about 2 or less than that of a powerful 20 kHz band VLF transmission. The VLF transmission from station NLK (18.6 kHz, Jim Creek, Washington) travels almost 1000 km farther to Montreal than does the WWVB signal from Fort Collins and, since the reception of NLK in the locale is generally good, there was never any reason to doubt that the very narrow band WWVB time-code signal could be used in geophysical surface-wave-impedance measurements in eastern Canada. Moreover, since the WWVB time-code signal itself could be relatively easily demodulated at almost any time of the day or night on the McGill University campus, there was strong corroberative evidence of the sufficiency of the signal level.

Rather than design an original radio receiver, it was initially decided to employ a high-sensitivity, commercially available instrument for reception of the magnetic (H-field) signal. As a base for the geophysical instrument, the True Time Instruments Model 60-TLC WWVB time-code receiver along with its compatible Model A-60 FS ferrite-rod loopstick magnetic field antenna was used. The natural Q of the tuned antenna was determined to be approximately 70 and the subsequent preamplifier-line driver and radio frequency stages of the receiver increase the overall Q to about 1000. The antenna case itself is shielded against radio-frequency interference and also encloses an ultra-low noise transistor preamplifier. The preamplifier drives the RF stages of the time-code receiver which offers a further amplification, adjustable between about 500 and 10000.

In order that the antenna and receiver be together useful in establishing the magnitude of the H-field vector of the EM surface wave, their electronic circuitry must be both phase and amplitude stable in time and with variation in temperature. Generally, with careful operation, the True Time Instruments antenna and receiver operated admirably and essentially stably during the development and the subsequent field testing of the prototype instrument. The only truly bothersome problem in their operation involved the necessity for maintaining a rather large distance (at least 5 metres) between the H-field antenna and the receiver unit since the tuned pot-core inductors used in each amplifier stage themselves radiated a weak synchronous magnetic field. If the antenna and RF amplifier were in close proximity, this could cause a regeneration or feedback into the antenna. The specifications and circuit schematics for the True Time Instruments Model 60 TLC receiver and Model A-60 FS antenna can be found in their manual (True Time Instruments, 1976).

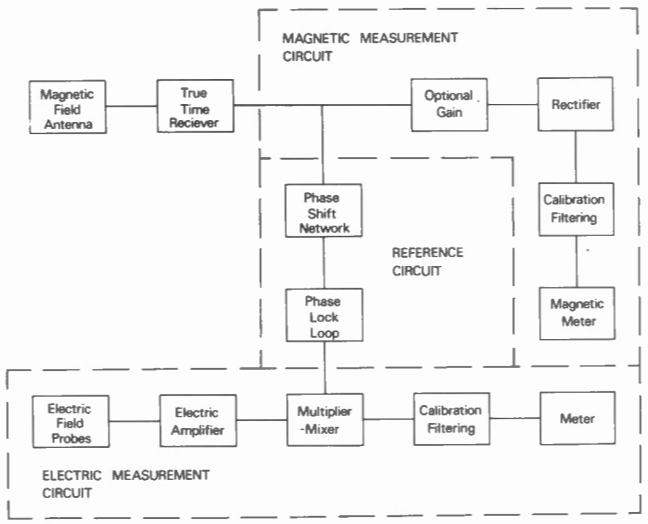

Figure 1. *A systems block diagram of the 60 kHz surface-wave impedance instrument. The circuitry is logically divisible into three sections: 1) the magnetic measurement circuit, 2) the electric measurement circuit and, 3) the reference circuit.*

The physical measurements essential for computing the wave impedance at the ground surface are: 1) a measurement of the amplitude of the horizontal-transverse oscillating magnetic field vector (H_y) in the air-space close to the ground surface; and 2) a measurement on the surface of the amplitude of the horizontal-radial oscillating electric field vector (E_x) and its phase lead relative to the magnetic field vector.

In order to be geophysically useful, a relative precision and reproducibility of the measurement of the ratio of the field amplitudes of about 5% and of the relative phase of about 1° are required. With careful design and by paying particular attention to the stability of the electronic components used, conventional electronic circuitry may be employed in achieving these requirements. A systems block diagram of the overall circuit as employed in the present prototype instrument is shown in Figure 1. This diagram shows the three basic functional modules of the circuit: 1) the magnetic field measurement circuit for determination of the magnetic field's amplitude, 2) the electric field measurement circuit for determination of the electrical field's amplitude and 3) the reference circuit for determination of the relative phase shift between the E and H fields. These circuit modules will now be described in some detail.

The Magnetic Field Measurement Circuitry

The True Time antenna-receiver pair provides a stable, linearly amplified H-field signal with a very high signal-to-noise ratio. Direct amplification, rectification and low pass filtering of this signal obtains a voltage proportional to the root-mean-squared amplitude of the H-field which is then applied through a calibration resistor to a sensitive, mirror-faced, taut-band galvanometer. A schematic of the circuitry used in the H-field amplitude measurement is shown in Figure 2. The input signal to the circuit is derived from the previously calibrated True Time RF receiver and either a) enters the amplifier-high-pass

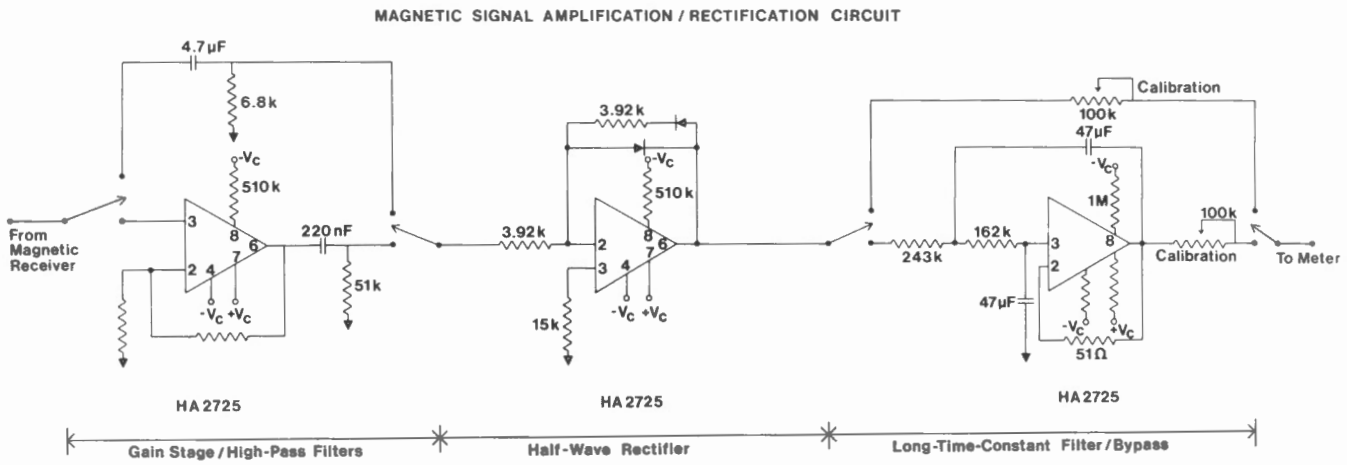

Figure 2. A schematic of the magnetic signal amplification/ rectification circuit. This circuit comprises three functional stages: 1) the gain/filtering stage, 2) the half-wave rectifier, 3) the long time-constant filter network.

filter stage in conditions of weak magnetic field strength, or b) bypasses this stage through a 50 Hz high-pass resistor capacitor pair. The amplifier, with gain 6.1, is based upon the standard voltage follower-with-gain design employing the Harris Semiconductor HA-2725 operational amplifier as the active element. These versatile operational amplifiers were used throughout the instrument, wherever possible, in standardizing the vulnerable components to those used in the True Time receiver with a view to ease of field maintenance. The output from the amplifier is delivered through a 50 Hz high-pass resistor-capacitor pair to the following precision half-wave rectifier circuit, whose design is due to Jung (1976). Apart from the expected non-linearity at very low signal levels, this rectifier circuit was found to provide extremely accurate rectification of the modulated 60 kHz signal. The output rectified signal is then normally passed into a long time-constant 2-pole filter which is based upon the Sallen and Key (1955) voltage-controlled- voltage-source design. A time constant of 66 s , with a maximally flat frequency response according to the Butterworth criterion, was used in the particular realization. The very long time constant was chosen in order to provide for an extremely stable voltage signal, proportional to the time-averaged rms amplitude of the H field, to the meter. However, during the orientation of the H-field antenna and general set-up of the instrument, this long time constant was found to be very inconvenient and a bypass was eventually provided directly to the meter from the rectifier. As well as aiding in the selection of the antenna orientation which provided for maximum signal strength, the bypass allowed for recognition of the WWVB time-code pulses which showed unequivocally that the instrument was properly receiving the 60 kHz signal. A certain small measure of filtering and damping is obtained from the meter's mechanical movement.

The Electric Field Measurement Circuitry

The E_x component of the oscillating electric field is necessarily continuous across the surface interface between the air and the ground. Its determination on the ground surface is, in principle, easily accomplished by the direct measurement of the oscillating potential between two probes separated along a line of radius centered on the source transmitter. The measured potential is then the product of the required electric field strength and the distance of radial separation between the probes. Because the surface electric field may vary quite rapidly horizontally, it is usually desirable to accomplish an electric field measurement with the minimum possible probe separation distance. The compromise between a high lateral resolution of the E field and an amplitude of electrical potential large enough to be accurately measured is most often dictated by the overall quality of the electronic circuitry employed in sensing the E field (See Fig. 3). Normally, wave-impedance measuring instruments are designed with a fixed probe separation of 10 m (Geonics Ltd., 1972).

It should be noted that any probe separation implies that the E-field measurements are representative of subsurface structures averaged over similar lateral distances. On the other hand, the H-field measurement is usually accomplished using a very compact loop antenna which essentially obtains the relevant measure at a point in space.

Station WWVB provides a typical free-space E-field signal in the Montreal region of about 100 $\mu V.m^{-1}$. This corresponds to an electric field of the order of 0.6 $\mu V.m^{-1}$ on the surface of a homogeneous halfspace ground having a conductivity of 0.1 $S.m^{-1}$. Because this signal level is so low, it was decided during the initial stages of the instrument design to use a potential probe spacing of 40 m which is four times that employed by the Geonics EM16R VLF Radiohm instrument. Larger separations became impractical because spurious electric fields on the ground surface due to various natural phenomena and the innumerable fixed frequency radio sources in the LF and MF bands could become so large as to saturate the E-field measuring electronics. With such a large probe separation, it is also important to place a buffer amplifier between the spike-probe which is inserted into the ground and the following electronics of the instrument. Otherwise a direct coupling of the WWVB signal into the probe lines themselves could occur and easily dominate the signal actually existing in the ground.

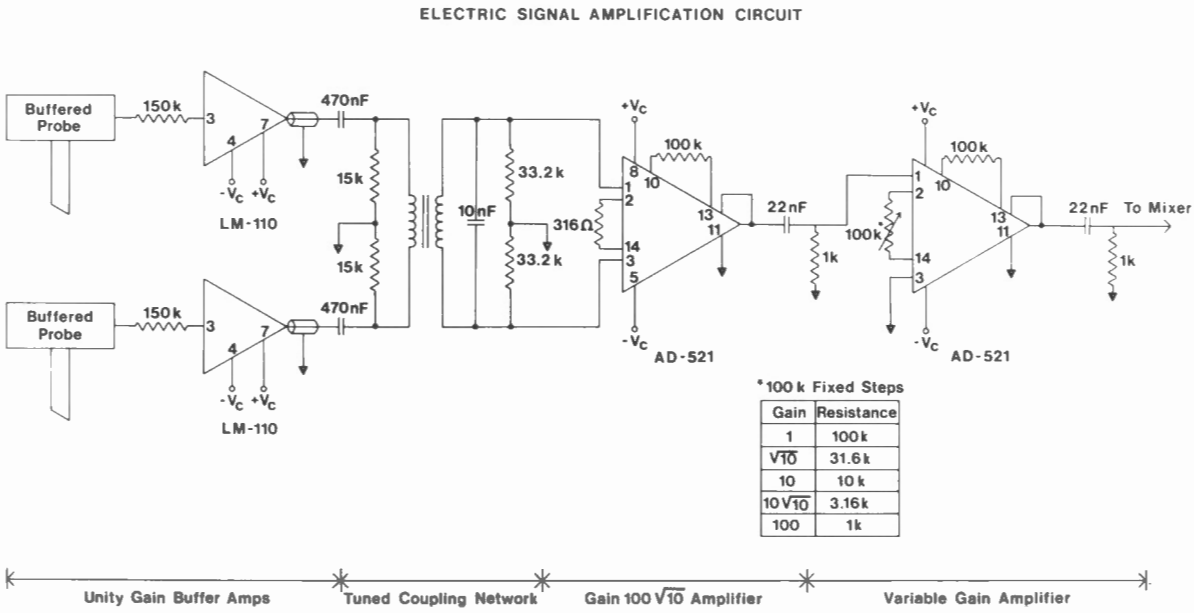

Figure 3. *A schematic of the electric signal amplification circuit. This circuit comprises four functional stages: 1) the buffer amplifiers, 2) the tuned coupling network, 3) the differential amplifier stage with fixed gain 316 and, 4) the variable gain amplifier stage.*

In the final design, both probes were buffered using unity gain amplifiers based upon the Fairchild Semiconductor μA110 committed voltage-follower video amplifier. This particular unit was selected because it offered an extremely high input resistance ($10^{12}\ \Omega$), a very low input capacitance (1.5 pF) and a low bias current (1 nA). As in all such amplifiers, the high frequency response is largely limited by the time constant, which is the product of the source-resistance and the input capacitance, but through its use of an extremely high open-loop gain, the μA110's bandwidth is about 25 MHz when receiving the input voltage signal through a low source resistance. Even when receiving the signal through a source resistance of 100 kΩ , the amplifier's bandwidth exceeds 1 MHz and, in fact, as used in the instrument, these buffer amplifiers had to be limited to a bandwidth of about 500 kHz, using the suggested method of adding a 150 kΩ series resistance on the input. This added source resistance normally dominates the probes' contact resistances and the effective ground source resistance in all but the very least conductive geophysical environments. As a result, the buffer amplifier's gain and phase characteristics are almost unaffected by ground condition. Eventually, using the 40 m probe separation, it was determined that no measurable phase lag at 60 kHz arose due to the E-field buffer amplifiers when surveying in regions where the surface resistivity exceeded 100 kΩ. m . This level of performance is better than that provided by the commercially-available buffered E-field probes.

The buffer amplifiers are placed within a thick tubular copper shield directly connected externally to the probe's spike and internally to the amplifier's input terminal. The output is presented to the subsequent instrument electronics through a four-conductor, shielded cable which also brings power and the reference common to the buffer amplifier from the central circuitry.

The electrical potential difference signal on the ground surface, which is due to the electromagnetic wave's radial electric field, is detected by the two buffered probes, each of which feeds a signal along the 20 m cables through matched 470 nF DC (and 60 Hz) - blocking capacitors onto the opposite ends of the primary windings of a tuned transformer as shown in Figure 3. An Analog Devices AD-521 true differential instrumentation amplifier receives the difference signal from the transformer secondary across which a 1 nF shunt capacitor provides for a rough tuning into the 60 kHz range. Precise tuning to pass the 60 kHz WWVB signal with no phase shift was made possible through the adjustment of a ferrite slug in the transformer core. This tuned circuit, providing a Q of 20 which will reject frequencies outside the 60 kHz band, was found to be necessary because strong asynchronous signals in the VLF, LF and MF bands would otherwise saturate the subsequent amplifiers in the electric field measurement circuitry.

In order to avoid the DC saturation or latch-up of the instrumentation amplifier, matched bias current paths through 33.2 kΩ resistors to the circuit common were provided from each of its inputs. The AD521 amplifier was operated with a fixed gain of 300, for which its small signal bandwidth is only about 100 kHz. Consequently, some further attenuation of E-field signals generated by the many AM-broadcast band radio transmitters was provided.

A second adjustable gain stage providing precisely calibrated 10 dB gain steps between 0 and 40 dB allows for sufficient adjustment to accommodate a fairly broad range of ground resistivity conditions. This amplifier, based upon the AD521 instrumentation amplifier operating in a single ended mode, provides a high-level signal proportional to the E field on the ground surface through AC-coupling into the synchronous demodulation circuitry which comprises the reference circuit and the multiplier-mixer of the electric field measurement circuit. It is most convenient to describe these functional circuit parts as a unit as follows.

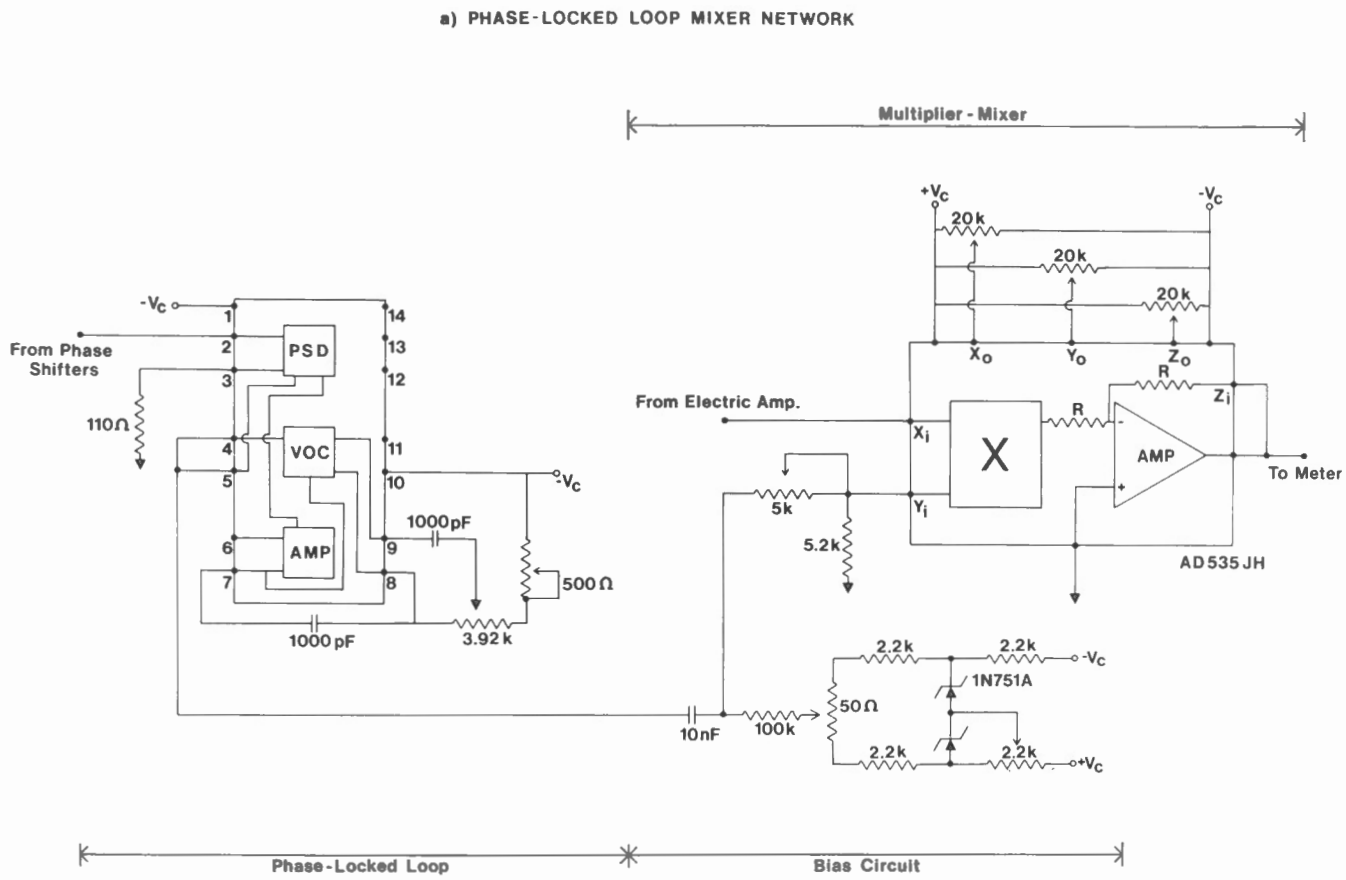

Figure 4. ***a)*** *A schematic of the phase-locked loop/mixer network. This circuit comprises three functional parts: 1) the phase- locked loop network, 2) the bias circuit and, 3) the multiplier/mixer.* ***b)*** *A schematic of the phase-shifting network.*

The Synchronous Demodulation Circuitry

Synchronous demodulation allows for a precise determination of the E-field signal amplitude and an accurate measurement of the phase lag between the E- and the H-field vectors. Many schemes for realizing synchronous demodulation with electronic circuitry are possible. However, all schemes essentially provide for three basic functions: a) a precisely calibrated phase shifting of a synchronous reference signal, b) a reversing switch driven synchronously with a reference signal, and c) an integration of the output from the reversing switch.

In this particular instrument, the reference signal is derived from the H-field measurement circuitry, phase-shifted by a series of three adjustable one-quadrant phase shifters (Jung, 1974) and applied as input to an integrated circuit, phase-locked loop. The National Semiconductors LM565 phase-locked loop integrated circuit provides a square wave output which is maintained coincident in phase and frequency with the input signal by means of an internal feedback loop which senses and corrects for any instantaneous phase difference between the input and output. Some control over the characteristics of this feedback loop is possible through the external placement of selected resistors and capacitors (See Figure 4 for the values used.). In the present application, these external components were chosen so that the phase-locked loop is free to slew in frequency by only about 10 Hz per second. This very strict condition ensures that phase stability is available even when very weak and possibly noisy H-field reference signals are provided as input. However, in all of our field testing outside of the Montreal urban agglomeration, the H-field signals received have been essentially noise-free and stable. The free-running frequency of the internal voltage-controlled oscillator, which is a component of the phase-locked loop circuitry, is fixed at 63 kHz although a frequency much closer to the 60 kHz WWVB signal could be substituted. In loosing synchronism, the phase-locked loop's output square wave will begin to drift in frequency toward 63 kHz at the rate of 10 Hz per second if it does not lock itself onto some other received frequency or again onto the 60 kHz WWVB signal. This configuration was found to provide for excellent stability in conditions of observable H-field signal but was sufficiently unstable in absence of real and measurable signal so as not to mimic real measurements.

The output synchronous square wave from the phase-locked loop is offset by a bias level equivalent to approximately one-half the (12 V) supply voltage. Because, in the demodulation circuit used in this instrument, the square-wave signal itself provides for synchronous switching of the amplified E-field signal by an electronic multiplication of the two signals, it is very important that the mean level of this square wave be within a few millivolts of the reference common potential. The appropriate rebiasing of the square wave is accomplished by the zener diode referenced bias circuit shown in Figure 4.

An analog multiplier based upon the Analog Devices AD533 non-linear transconductance integrated circuit was used to provide the function of switching or reversing the polarity of the input E-field signal twice per cycle. The precise moment of switching is governed by the moment at which the square wave changes polarity and this moment is adjustable via the phase-shifting circuitry so as to be either in coincidence with the polarity change of the E-field sinusoidal signal or shifted by 90°. When exactly coincident, the multiplied signal (H-field derived square wave times the E-field proportional sinusoid) output has a maximum DC component which is proportional to the sinusoid's amplitude. When exactly 90° phase-shifted, the multiplied signal output has zero DC component. These conditions are represented pictorially in Figure 5. In normal operation of the instrument, the phase is adjusted using one of the three one-quadrant phase shifters which has been calibrated to within 1° so as to obtain a minimum DC level of the multiplied signal. This process obtains a measurement of the phase lag between the E- and H-field signals. Using another of the phase shifters, which has been calibrated to provide an exact 90° phase shift of the square wave, the amplitude of the E-field signal is obtained as proportional to the DC level of the multiplier's output signal. The null signal and E-field amplitude signal are observed on a calibrated, mirror-faced, taut-band galvanometer; the phase is derived from a dial on the phase shifter's adjusting potentiometer. The third of the one-quadrant phase shifters is necessary to obtain a precise and fixed phase calibration of the synchronous demodulator.

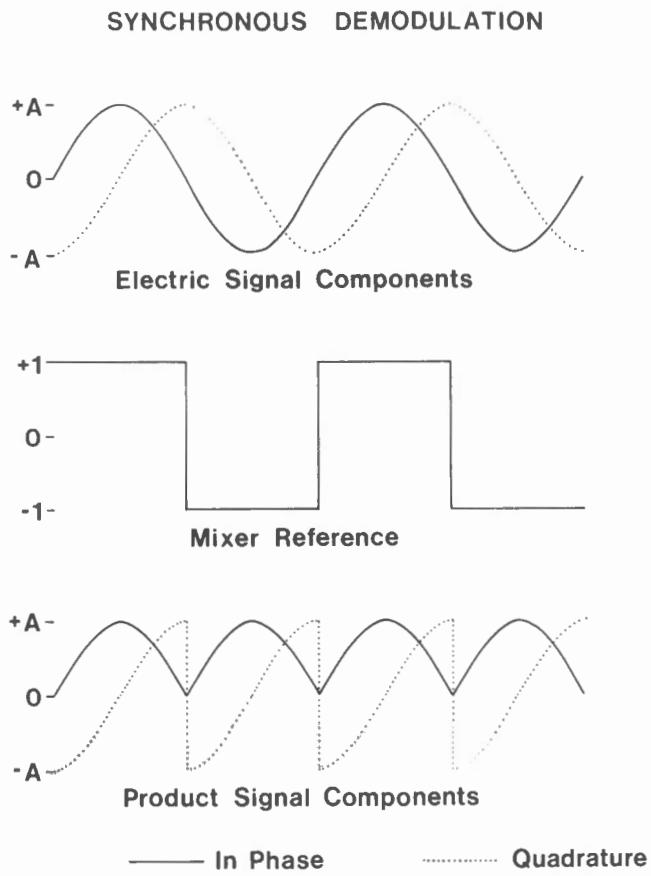

Figure 5. *The demodulation of sinusoidal components. The in-phase (solid line) and quadrature (dotted line) components (referenced to the mixer reference) of a general sinusoidal signal are multiplied by a square wave mixer reference signal which is synchronous in frequency and phase with the in-phase component of the sinusoid. The resultant demodulated signals are shown in which the demodulated in-phase component has a DC level proportional to the amplitude of the source sinusoid and the quadrature component has a zero mean. By adjustment of the phase of the mixer reference, the demodulated quadrature component's RMS amplitude can be brought to zero.*

The power necessary to drive the electronics is derived from two rechargable 12 volt gel-cell batteries with a 4 ampere-hour capacity. Fully charged, these batteries can provide several days of instrument operation. In any revised design of the instrument, some provision should be made to control the power supply voltages to some greater extent. The operational and instrumentation amplifiers employed in the design require dual supply voltages (12 V and -12 V, nominally referred to the circuit common) and will reject any drift or variation between the two supply voltages. The transconductance circuit employed in the multiplier-switch is also relatively insensitive to variations in supply voltages but the output square wave from the phase-locked loop has an amplitude which is directly proportional to the positive supply voltage. Thus, in the present configuration, as the supply voltage slowly drops, the synchronous demodulator provides an output measure of the E-field signal which increases in error. Over a period of days of operation, the battery supply voltage may drop by 5%, thus introducing a 5% underestimation of the E-field signal level, corresponding to a 10% underestimate of the equivalent apparent resistivity of the ground. By maintaining the batteries in a state of full charge, these errors were reduced to about 2 or 3% during the course of a day's measurements.

Instrument Operation

The instrument is operable in a manner analogous to the operation of the Geonics EM16R unit. The H-field antenna's loop axis is rotated in a horizontal plane about a vertical axis until the orientation which obtains the maximum H-field signal is determined. In practice, it is probably easier to determine the antenna orientation of minimum signal level and then rotate the antenna through 90° in alignment for maximum signal level. The electric probes are then inserted into the ground 40 m apart along a line perpendicular to the H-field antenna's axis. Since the measured components, E_x and H_y, of both the E- and H-field vectors vary only as the cosine of the misalignment angle with the fields and it is relatively easy to keep such angular errors to less than 10°, the errors in the measured field amplitudes seldom exceed about 1.5% in each case. Moreover, since it is in fact the ratio of the E-to-H field amplitudes which is the important measure, only the relative misalignment between the probe-line and the H-field antenna axis is material. This misalignment can easily be held to less than 5° by direct visual estimation, and consequently, ratio errors of no more than ±0.5% are expected in normal field use of the instrument.

The operator of the instrument can determine three essential measures of the field: the H-field amplitude, the E-field amplitude and the phase lag between the E and H fields. The H-field amplitude is directly available as a reading on the H-field meter. Usually, the most highly filtered (i.e. time averaged) signal is recorded. The observation of the E-field amplitude requires first that the E-to-H phase lag be determined. This is accomplished by varying the rotation of a pre-calibrated potentiometer controlling one of the phase shifters. When the potentiometer position corresponding to a minimum output from the synchronous demodulator as presented on the E-field meter is determined, the phase-lag measurement is obtained according to the potentiometer's scale. To obtain the actual E-field amplitude measurement, the reference signal presented to the synchronous demodular is further phase shifted by precisely 90° by use of a second pre-calibrated phase shifter. The filtered output signal from the synchronous demodulator is displayed on the E-field meter. The operator records the H-field amplitude, the phase lag and the E-field amplitude to complete a measurement of the local surface-wave impedance at 60 kHz. With practice, this whole process can be completed in about 10 minutes by a single operator. In its present configuration, the 60 kHz instrument is not quite as convenient to use as is the commercial EM16R VLF unit available from Geonics Inc..

CALIBRATION AND FIELD TRIALS

It is essential that any instrument used for geophysical purposes be calibrated absolutely so that it is possible to relate its measurements to real physical quantities and thus compare its measurements with those made by other instruments and other methods. For this instrument, the calibration procedure must obtain the meter deflections related to the E-field in $V.m^{-1}$ and the H-field in $A.m^{-1}$, as well as relate the phase angle measuring potentiometer's scale to degrees of phase lag. The obvious approach to calibration is to provide to the instrument's sensors predetermined magnetic and electric field signals having a precise 60 kHz frequency and a fixed relative phase. This direct approach turned out to be exceedingly difficult, largely because the input calibration signal levels must be so very small and yet accurately measurable in both frequency and phase. The required H-field signal amplitude must be typically less than 1 $\mu A.m^{-1}$ while the E-field signal must be represented by a potential difference between the two electric field probes of less than 100 μV. In a typical electronics laboratory and using conventional equipment, it is difficult to prevent a current signal generator from radiating some magnetic field directly. Furthermore, since the source signal must provide a controlled oscillating current to a Helmholtz coil pair for the creation of the calibration oscillating magnetic field,

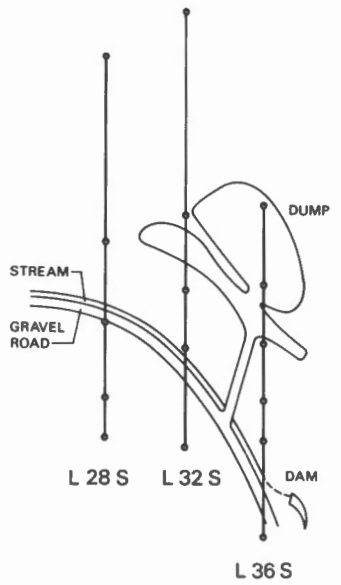

Figure 6. A plan view of the calibration test site near the Kidd Creek mine, Timmins, Ontario. For scale reference, L32S is 0.90 km in length.

one must somehow account for any mutually inductive coupling between this source coil and the various metallic conductors always present in a laboratory. Thus, the total magnetic field in which the antenna is placed for calibration is not very easily controlable in amplitude and phase. This proved to be the source of most of the difficulties in several attempted direct calibrations of the H-field antenna and it was decided to try instead indirect calibrations in the field.

As a calibration standard, a Geonics EM16R instrument was used following its own calibration by the Geonics laboratories. For this indirect approach to calibration, the intention was to compare the wave-impedance measurements of the Geonics instrument with those of the 60 kHz instrument in a region where the ground structure was demonstrably homogeneous. As a measure of the ground homogeniety, a phase angle of 45° in presence of a conductive and simple geological structure was established as the criterion. The difficulty here is in assuring that the observation of a 45° phase lag between the E and H fields is not due to a fortuitously complex structure rather than a nearly homogeneous geology. Good geological control through drilling was therefore essential.

Conditions which fulfilled the criterion of a simple geology in the form of a thick and reasonably conductive upper layer was found in the region of the Kidd Creek Mine in Timmins, Ontario. In his earlier surveys, Telford (1978) had shown that this area showed little anisotropy in resistivity measurements and generally was characterized by phase-lag measurements of near 45°. Moreover, drilling had revealed a conductive clay (σ = 0.05 S m^{-1}) overlying a varved clay and sand and gravel till with a total depth exceeding 30 m, or approximately twice the skin depth of the 20 kHz VLF electromagnetic waves. Geological cross-sections of the three lines which were surveyed are shown in Figures 6 and 7. Using the 17.8 kHz NAA signal

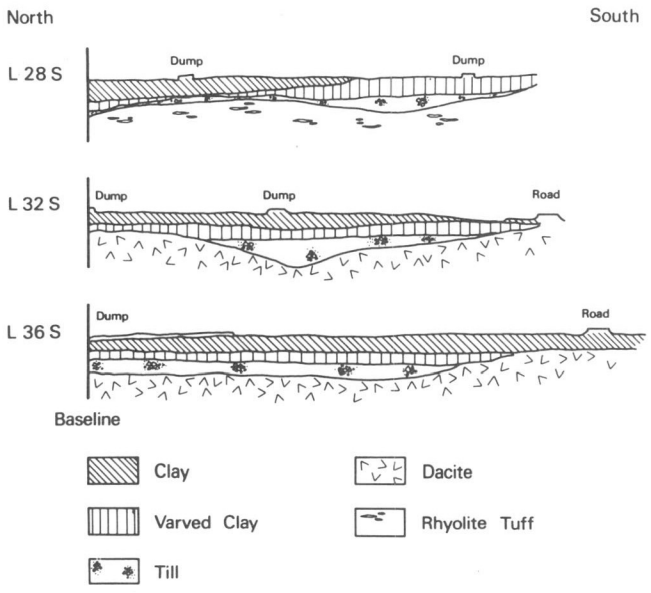

Figure 7. *Geological cross-sections of the calibration test site near Timmins, Ontario. The vertical and horizontal scales are identical.*

transmitted from Cutler, Maine, the Geonics EM16R obtained E-to-H phase angles of between 40° and 45° and an apparent resistivity of between 21 Ω.m and 28 Ω.m in all measurements. A particular station for which the Geonics instrument reproducibly obtained a phase angle of 45° and an apparent resistivity of 28 Ω.m was established as the calibration benchmark and the 60 kHz instrument was there adjusted to provide exactly equivalent measurements. A wave-impedance survey for comparison was then conducted over the whole region, using both instruments. A mean difference of +1.9° (±2.7°) in phase angle and of +2.2 Ω.m (± 4.4 Ω.m) in apparent resistivity measurements were obtained by the 60 kHz instrument in reference to the measurements obtained by the EM16R. The clear biases towards the higher phase angle and apparent resistivity should have been removed by a readjustment of the 60 kHz instrument. However, it should be noted that the phase errors were typically less than 2° and the mean relative apparent-resistivity errors were only about 8%, even though the azimuthal directions to the two transmitters (WWVB and NAA) were different by 165°. Measurement errors by the operator and a very slight degree of anistropy could easily account for discrepancies of this order.

The NLK 18.6 kHz VLF signal from Jim Creek, Washington could not be used in this survey area because the EM16R could not be brought to show a consistent phase-angle null. While factors peculiar to the NLK signal frequency and direction might account for some of these difficulties, it was taken to be a revelation that the 60 kHz instrument is at least as sensitive to weak signals as is the commercial VLF instrument.

Conditions were generally adverse during the two days of the calibration survey, which was conducted on October 4 and 5, 1979. The weather was cold and wet with scattered shower activity and the terrain presented dense bush in most places. These conditions conspired to provide a realistic field test of the prototype instrument. It was found to be rugged and reliable, though not nearly so convenient in use as is the very well-conceived Geonics EM16R instrument.

A second survey was conducted within the Macdonald College Farm site in Ste.-Anne-de-Bellevue, Quebec, where Mathieson and Crossley (1981-IV) had obtained wave-impedance measurements in a previous study. This second survey had two basic purposes: the first was to establish the stability of the 60 kHz instrument and to determine the reproducibility of its measurements; the second was to test the two- and three-layer interpretations of the VLF survey data as reported by Mathieson and Crossley (1981-IV).

For the purpose of testing the stability and reproducibility of the new instrument's measurements one station was chosen as a base station and a reference measurement was obtained there during a general survey of the area on October 3, 1979, the day preceding the Timmins calibration survey. A remeasurement was made on October 6, immediately following the calibration survey. Taking into account the adjustments which had been made during the Timmins calibration, it was determined that the repeated derived apparent resistivity measurements at the base station remained within about 2% and the phase angles were consistent to within 1°. Since these levels of reproducibility are within the limits of the operator's ability to read the instrument's meters and scales, the instrument was shown to be essentially stable and its measurements highly reproducible.

Table 2. A Comparison of VLF and LF interpretations: two-layer model.

	60 kHz				17.8 kHz			
Survey Station	ρ_a	φ	ρ_2	h_1	ρ_a	φ	ρ_2	h_1
Line 1/ 0(base)	12 Ω.m	37°	-	- m	23 Ω.m	28°	42	3.3 m
1	10	46	-	-	25	25	72	3.7
2	10	50	54	0.9	22	26	39	4.0
3	13	36	15	2.0	18	28	51	3.5
4	10	37	13	1.5	25	28	58	1.9
5	8	39	-	-	28	27	120	4.1
Line 2/ 6	10	46	9.8	0.6	31	20	140	4.0
7	10	43	17	3.1	35	20	150	4.0
8	8	34	16	2.6	30	20	92	4.7
9	8	36	16	2.7	20	22	120	4.0
10	8	35	6	4.7	26	21	180	3.7
11	6	40	8.5	1.0	29	19	150	4.0
12	8	42	13	0.7	28	20	68	3.7
13	11	42	14	0.7	32	22	88	3.6
14	13	42	10	0.0	32	24	68	3.3
15	10	45	14	2.0	22	26	45	3.1

The return from the Timmins calibration survey with an indirectly but absolutely calibrated instrument now allowed for a calibration of the survey measurements, which had been previously obtained at the Macdonald College Farm site. With absolute physical unit measures established, the 60 kHz survey measurements could be compared to those obtained several months earlier by Mathieson and Crossley (1981-IV). To the extent that one may assume that the ground conductivity conditions had remained similar between the spring and the fall of 1979 on this survey site, these 60 kHz measurements could offer a validity check of the interpretations based upon the VLF survey.

The 60 kHz survey of the Macdonald College Farm site obtained apparent resistivity measurements of about 10 Ω.m with phase angles typically less than 45°. A series of the measurements made during this survey are shown in comparison, in Table 2, to Mathieson's (1980; Mathieson and Crossley, 1981-IV) equivalent measurements derived from an earlier VLF survey.

An interpretation based upon a two-layer geological model assuming an upper layer resistivity of 5 Ω.m, the lowest apparent resistivities observed in the region being only 6 Ω.m at 60 kHz, was attempted in order to determine the lower layer's resistivity, ρ_2, and the upper layer's thickness, h . Using Mathieson's (1980) novel two-layer interpretation curves, the 60 kHz survey obtained values of these parameters which are also compared to the results of Mathieson's own VLF interpretation in Table 2.

Essentially, no quantitative correlation between these interpretations is evident and it was assumed that the reason for the disagreement was the inadequacy of the interpretation model. Also since in several cases no solutions having an upper layer resistivity of 5 Ω.m were possible based upon the 60 kHz survey measurements, an interpretation for a more complex three-layer geological model was attempted.

The soil section of the Macdonald College Farm site comprises a tilled sandy loam overlying a compacted clay subsoil in which the water table is maintained at 1.2 m to 1.5 m below the surface (Chieng, 1976). These soils overlie the electrically resistive Trenton limestone at a depth of about 30 m. A three-layer geological model for which the dry surface soil layer and the deep limestone layer were assigned similar resistivities and for which the water-saturated clay bed (layer 2) was constrained to have a thickness $h_2 = 10 \cdot h_1$ was used as a basis for the interpretation. The reasonableness of this geological model has been earlier established by Mathieson (1980), following a seismic refraction survey and a subsequent resistivity sounding. He found a clear seismic velocity discontinuity at about 3 m depth and his resistivity sounding established that the surface and bedrock resistivities were roughly equivalent with a 10:1 upper layer-to-second layer depth ratio being representative of the area. Table 3 compares interpretations of the VLF and LF survey data in determining both the second layer resistivity, ρ_2, and the upper layer's thickness, h_1, which also establishes the depth to bedrock as 11 h_1. Three assignments of the surface soil and bedrock resistivity have been applied.

In most cases, the model parameters derived from these interpretations are comparable for both surveys. However, only by reducing the assigned resistivities of the surface soil layer and the bedrock to an unrealistically low 100 Ω.m could the first layer depth be brought into some agreement with the depth to the 3 m seismic marker and then many solutions for the 17.8 kHz measurements were non-determinable. Whether or not the seismic marker actually corresponds to a resistivity contrast was never fully established.

Unfortunately, the Macdonald College Farm did not provide the ideal geophysical test site for the purpose of the VLF-LF systems comparison in spite of the apparent uniformity of the soil layering, the relatively constancy of the depth-to-bedrock and the control of the water table within the soil section. It had been expected that a

Table 3. A Comparison of VLF and LF interpretations: three-layer model.

1. $\rho_1 = \rho_3 = 480\ \Omega\cdot m$, $h_2 = 10\, h_1$

Station	60 kHz ρ_2	60 kHz h_2	17.8 kHz ρ_2	17.8 kHz h_2
L 1/0	12 Ω.m	18 m	16 Ω.m	14 m
1	8.1	19	25	17
2	9.4	23	9.4	15
3	12	15	11	22
4	12	16	17	24
5	8.1	18	14	22
L 2/6	9.4	21	9.4	12
7	9.4	19	9.4	12
8	8.1	15	9.4	13
9	8.1	16	8.1	15
10	8.1	16	9.4	13
11	5.8	16	9.4	11
12	8.1	19	8.1	14
13	11	19	12	14
14	12	20	14	17
15	9.4	20	12	22

2. $\rho_1 = \rho_3 = 100\ \Omega\cdot m$, $h_2 = 10\, h_1$

Station	60 kHz ρ_2	60 kHz h_2	17.8 kHz ρ_2	17.8 kHz h_2
L 1/0	9.0	5.2	9.0	5.4
1	7.8	7.2	7.8	3.0
2	7.8	8.4	7.8	4.1
3	9.0	4.5	9.0	5.4
4	9.0	4.9	9.0	4.9
5	6.3	5.1	8.4	2.3
L 2/6	7.8	7.2	1.4	0.6
7	8.4	6.8	-	-
8	5.3	4.1	-	-
9	5.3	4.2	3.2	1.6
10	5.3	4.1	-	-
11	4.0	4.5	-	-
12	5.3	5.8	-	-
13	7.8	5.9	-	-
14	9.0	6.4	2.6	0.8
15	7.8	6.5	7.3	4.1

comparison survey on this site would demonstrate the unequivocal requirement for a particular three-layer model in order to obtain any substantial quantative correlation between interpretations of the VLF and LF survey data. Rather, it was found that general agreement between the interpretations based upon the two surveys at the well-separated frequencies could be maintained for an uncomfortably large range (almost 5 to 1) of surface and bedrock resistivities. What has been demonstrated is that feasible geological interpretations can, in fact, show some evident correspondence when the complex wave-impedance measurements are made at these two, quite different, frequencies. Therefore, measurements at 60 kHz could usefully supplement those made in the VLF band and perhaps help in the resolution of the more complex, three-layer geological sections.

CONCLUSIONS

The viability of a geophysical wave-impedance measurement using the 60 kHz signal derived from the 13 kW WWVB transmitter in Boulder, Colorado have been clearly demonstrated. In spite of the low signal level available in northern Ontario and western Quebec, the measurements of the surface-wave impedance at 60 kHz proved to be reliable, providing a high level of reproducibility in the determination of the apparent resistivity and the phase lag between the field vectors. Throughout much of Canada, the WWVB signal is stronger than that available in the two test areas and consequently one could expect the performance of the prototype instrument to be more than adequate for geophysical use throughout western, central and south-eastern Canada. In the high arctic regions, the variability of the height of the ionspheric D and E layers might limit the usefulness of these signals in geophysical measurement although Powell (1978; Powell and Jensen, 1981-II), reported no special problems concerning the geophysical use of VLF signals for permafrost delineation surveys in the Tuktoyaktuk area of the Northwest Territories. In far eastern Canada and in the eastern arctic, it is also possible that the 60 kHz transmissions from Station MSF, Rugby, England, could offer an alternative source for wave-impedance measurements using the same instrument tuned to the same frequency. In the Montreal area, there was no evidence that the MSF signals disturbed geophysical measurement in using the WWVB signal or were in fact even observable. Crossley, however, (personal communication) has reported that the MSF signal provides a more reliable time code than does WWVB in central Newfoundland. One might therefore expect that this prototype instrument is geophysically usable Canada-wide and that reliable 60 kHz wave-impedance measurements can be relatively easily obtained everywhere in Canada providing a useful check of VLF measurements or as an adjunctive measurement making possible more complex interpretations.

Resistivity and phase angle have been seen to vary considerably between the 20 kHz and the 60 kHz wave frequencies even in the presence of apparently simple geological structures. At these separated frequencies, then, the measurements are often essentially independent and hence, in princple, four geophysical parameters could be established as representative of each measurement station. These parameters may correspond to any four of the five basic physical parameters representative of a three-layer geological structure; the paired measurements at VLF and LF could overdetermine the solution for a simpler two-layer geological model or provide some evidence of the permittivity and permeability of a halfspace-like geological structure.

In overburden and bedrock mapping, two-layer geological sections are often encountered. The substantial modification of the available VLF surface wave impedance measuring instruments to allow their use of the 60 kHz signals or the design and development of a new two-frequency instrument merits the consideration of the Canadian manufacturers of geophysical exploration and engineering instruments. The 60 kHz frequency does not, of course, extend the depth of our geophysical investigations and hence might not find much application in mineral exploration but the rapidly expanding interest in geophysical methods for the study of terrain, investigations of shallow geological structures, in the search for ground-water courses in agriculture, in geographical investigations, in problems of soil mechanics and geotechnology, in engineering site evaluation, etc. would ensure a ready market for such a versatile instrument. It

was a recognition of our own particular but not unusual need for this instrument that provided major stimulation for the development and construction of the prototype instrument and our investigations of its applications.

ACKNOWLEDGEMENTS

The research which this article summarizes was supported by the EMR Canada through Research Agreements 58-4-78 and 77-4-79. One of us (P.T.L.) received support in the form of scholarships from the Natural Science and Engineering Research Council and the Ministry of Education of the Province of Quebec.

The authors would like to acknowledge the invaluable assistance of the following people: Mr. J. Roy, Dr. R. Bazinet, Professors W. M. Telford and D. J. Crossley, Mr. M. Chouteau. and Dr W. J. Scott and Mr. L. S. Collett of the Geological Survey of Canada. Field assistance was provided by Mssrs. N. St.-Aubin and E. Nichols.

Field work was carried out in part at the Texasgulf mine site near Timmins, Ontario: Dr. T. R. Yu's assistance there was very necessary to the realization of the project.

REFERENCES

Chieng, S.T.
1976: The effects of subsurface basin depths and drainage rate on Water Levels, M.Sc.Thesis, Macdonald College, McGill University, Montreal.

Crossley, D.J.
1981: The theory of EM surface-wave impedance measurements; in Geophysical Applications of Surface Wave Impedance Measurements, L.S. Collett and O.G. Jensen (eds.), Geological Survey of Canada, Paper 81-15, Report V, p. 1-17.

Jung, W.G.
1974: IC Op-Amp Cookbook, Bobbs-Merril Co. Inc., New York, 591 pp.

Kamas, G.
1977: Time and Frequency User's Manual, NBS Technical Note 695, G. Kamas (ed.), U.S. Department of Commerce, Washington, 210 pp.

Mathieson, C.C.
1980: VLF resistivity interpretation, M.Sc.Thesis, McGill University, Montreal.

Mathieson, C.C. and Crossley, D.J.
1981: Graphical and numerical interpretation in VLF resistivity studies; in Geophysical Applications of Surface Wave Impedance Measurements, L.S. Collett and O.G. Jensen (eds.), Geological Survey of Canada, Paper 81-15, Report V, p. 49-65.

Powell, B.W.
1978: Radiohm mapping of permafrost, M.Sc. Thesis, Laboratory in Applied Geophysics, McGill University, Montreal.

Powell, B.W. and Jensen, O.G.
1981: Radiohm mapping of permafrost; in Geophysical Applications of Surface Wave Impedance Measurements, L.S. Collett and O.G. Jensen (eds.), Geological Survey of Canada, Paper 81-15, Report V, p. 19-33.

Sallen, R.P. and Key, E.L.
1955: A practical method of designing RC active filters, IRE Transactions on Circuit Theory, CT-2, p. 74-85.

Telford, W.M.
1978: Overburden-bedrock mapping: Case History 78-1, Mineral Exploration Research Institute (IREM/MERI), Case History 78-1, 7 pp., 19 maps.

Wait, J.R.
1962: Electromagnetic Waves in Stratified Media, International Series of Monographs; in Electromagnetic Waves, Vol.3, Pergamon, Toronto, 372 pp.

TECHNICAL PRODUCT INFORMATION AND MANUALS

Analog Devices
1978: Data Aquisition Products Catalogue; Analog Devices, Norwood, Mass.

Fairchild Semiconductor
1976: Linear Integrated Circuits Data Book

Geonics Ltd.
1972: Operating Manual for EM16R Direct Reading Ground Resistivity Meter, Geonics Ltd., Mississauga, Ont.

Harris Corp.
1977: Linear and Data Aquisition Products Catalogue

National Semiconductor Corp.
1976: Linear Data Book

True Time Instrument Co.
1976: Operating and Service Manual, WWVB Time-Code Receiver, Model 60 TLC, Manual 7-16, Santa Rosa, Ca., 44 pp.

VI

INVERSION OF VLF DATA FOR SIMPLE LATERAL INHOMOGENEITIES

F.A. Teemull and D.J. Crossley
Laboratory in Applied Geophysics, McGill University

Teemull, F.A., and Crossley, D.J., Inversion of VLF data for simple lateral inhomogeneities; in Geophysical Applications of Surface Wave Impedance Measurements, L.S. Collett and O.G. Jensen editors; Geological Survey of Canada, Paper 81-15, p. 79-86, 1981.

Abstract

A simple interpretation of VLF resistivity data is to subdivide the Earth into plane homogeneous layers with infinite horizontal extent. This method is somewhat suspect however if the actual interfaces are not horizontal, e.g. faults, because the point-to-point interpretatation avoids all consideration of lateral structure. Numerical techniques do exist for evaluating the response of arbitrary shaped conductors to plane electromagnetic waves, but they tend to be computationally expensive. In between the extremes is a method for representing an interface between two uniform homogeneous media as a Fourier series, i.e. a sum of suitably chosen harmonic functions.

The results indicate that certain parmeters of the interface, in particular its vertical characteristics such as depth, amplitude and resistivity contrast, can be well determined. The horizontal characteristics of the model, i.e. wavelength and phase, pose numerical difficulties which have not at the present time been overcome. Nevertheless, one advantage of looking for specific structures in a data set is that the structures can often be represented by a few (typically 2) independent parameters, thus avoiding the need for estimating the amplitude and phase of a large number of individual components.

Résumé

On peut faire une interprétation simple des données de résistivité TBF en subdivisant la Terre en couches horizontales homogènes infinies. Cette méthode devient quelque peu inexacte si les interfaces ne sont pas horizontales, par example s'il y a des failles. L'interprétation de point à point élimine en effet toute considération de structure latérale. Il existe des techhniques numériques pour l'évaluation de la réponse de conducteurs de formes arbitraires aux ondes électromagnétiques planes, mais elles exigent de très longs calculs. Entre ces deux extrêmes, il existe une méthode permettant de representer une interface entre deux milieux sous forme de serie Fourier (somme de fonctions harmoniques appropriées).

Les résultats indiquent que certains paramètres de l'interface, en particulier ses caractéristiques verticales telles que profondeur, amplitude, contraste de résistivité et d'amplitude peuvent être bien déterminées. Et pourtant, les caractéristiques horizontales du modèle, c'est-à-dire la longueur d'onde et la phase posent des difficultés numériques qui n'ont pas été encore surmontées. La recherche de structures spécifiques dans un ensemble de données, a pour avantage le fait qu'on peut souvent representer les structures par quelques paramètres indépendants (on en utilise habituellement 2). On évite ainsi d'avoir à évaluer la phase et l'amplitude d'un grand nombre de composantes individuelles.

INTRODUCTION

The interpretation of VLF resistivity data for horizontally stratified media was developed by Wait (1962) and a recent review given by Crossley (1981-I). For this type of model the interpretation is quite straightforward because the data is usually limited to only one pair of values, namely apparent resistivity (ρ_a) and phase angle (φ), at each measurement location and for each transmitter frequency. The narrow range of VLF transmitter frequencies (15 - 23 kHz) effectively restricts the number of measurements to one pair (ρ_a , φ) for the whole VLF band. Two convenient stations which can be used for Canada are Cutler, Maine (17.8 kHz) and Jim Creek, Washington (18.6 kHz). Higher available frequencies which yield significantly different resistivity information lie in the LF band, which for Canada means either Fort Collins, Colorado or Rugby, England (both at 60 kHz). LaFleche and Jensen (1981-V) describe an instrument to record this higher frequency data.

Interpretation of (ρ_a , φ) for resistivity sounding poses several problems in all but a simple 2-layer case (e.g. Mathieson and Crossley, 1981-IV). These problems are largely avoided in the MT method which is able to record wave impedance measurements at many distinct frequencies. As a survey device the VLF resistivity method can be quite useful in mapping lateral variations in the thickness of a near-surface layer. To a first approximation each station may be treated as if it were on semi-infinite layered half-space, although this will clearly be inaccurate if the layer thickness varies significantly between adjacent stations.

Various numerical techniques have been used to solve EM problems for inhomogeneous media. Coggon (1971) applied the finite element method to modelling a variety of isolated conductivity structures in a half-space, whilst the problem of two dimensional inhomogeneities buried in a conductive half sphere was treated using a finite difference method by Jones and Price (1970). An alternative approach is to use the transmission surface analogy which recognizes the similarity of the Helmholtz equation, as derived from the two dimensional Maxwell equations, to the transmission line and telegraphers equation. Swift (1971) applied this method to solving the problem of a plane electromagnetic wave incident on a layered medium having only lateral conductivity variations.

The only study intermediate between the simple, but restricted, plane layered model and the flexible, but costly, numerical methods is that of Hughes and Wait (1975). Their technique was to find the effect of small undulations of a sinusoidal boundary on the measurement of complex wave impedance and wave tilt at the Earth's surface. Certain quantities in their analysis were required to be small which allows the linear combination of many sinusoids to model a wide variety of two dimensional structures, for example a sedimentary basin or non-vertical fault contact.

We here investigate the possibility of inverting VLF resistivity data to search for parameters of a model which may be represented as a sum of sinusoidal undulations on a single boundary separating uniformly resistive media. Linearized inversion is used to improve initial parameter estimates and the method is applied to models which contain from 1 to 20 terms in the Fourier series representing the boundary.

EQUATIONS FOR A HARMONIC INTERFACE

We review the equations derived by Hughes and Wait (1975) and briefly examine the significance of the model parameters in the equations.

Apparent Resistivity and Phase for a Single Sinusoid

The model (Fig. 1) consists of a two-dimensional boundary whose equation

$$z'(x) = z_0 + z_1 \sin \nu x \qquad (1)$$

represents a single sinusoid of amplitude z_1 and wavelength $L = 2\pi/\nu$, buried at a mean depth z_0 below the air-ground interface. The boundary (1) is assumed to separate two homogeneous isotropic electrical media with values (σ_1 , ϵ_1 , μ_1) and (σ_2 , ϵ_2 , μ_2) for the conductivity, absolute dielectric permittivity and absolute magnetic permeability in the upper and lower layers respectively. In air these three parameters have the values (0, ϵ_0 , μ_0) and we shall assume in what follows that $\mu_1 = \mu_2 = \mu_0$.

The incident electromagnetic field is assumed to be propagated from a distant VLF transmitter at an angular frequency ω and so arrives at the air-ground interface as a plane wave. It is assumed that the single magnetic field component is parallel to the sinusoidal interface, taken to be the y direction, in accord with the requirements of polarization of VLF radio waves.

Assuming electrical homogeneity of a medium allows the magnetic and electrical fields to satisfy the wave equations

$$\nabla^2 \underline{H} = \gamma^2 \underline{H} \qquad (2a)$$

and

$$\nabla^2 \underline{E} = \gamma^2 \underline{E} \qquad (2b)$$

where

$$\gamma^2 = i\omega\mu_0\sigma - \omega^2\epsilon\mu_0 \qquad (3)$$

is the propagation constant. The general solution of (2a) for a two dimensional H-polarized EM wave propagating in the +x direction is

$$H_y = (A e^{-uz} + B e^{uz}) e^{-kx} \quad , \qquad (4)$$

where u and k are the vertical and horizontal wavenumbers which are related by

$$u^2 + k^2 = \gamma^2 \quad , \qquad (5)$$

(Crossley, 1981-I, equation (42)). On account of the nature of the boundary (1), Hughes and Wait (1975) assume that H_y in (4) can be expressed as a Fourier series

$$H_y(x,z) = \sum_{n=-\infty}^{\infty} H_{ny}(z)\, e^{-(in\nu + k)x} \quad . \qquad (6)$$

The complex coefficients $H_{ny}(z)$ can easily be deduced from (2a) and (3) to be

$$H_{ny}(z) = a_n e^{-u_n z} + b_n e^{u_n z} \quad , \qquad (7)$$

where

$$u_n^2 = \gamma^2 - (in\nu + k)^2 \qquad (8)$$

and a_n , b_n are constants to be found from the boundary conditions.

The two electric field components can be found from

$$\underline{E} = (\sigma + i\omega\epsilon)^{-1} \nabla \times \underline{H}$$

to be

$$E_x = \frac{1}{\sigma + i\omega\epsilon} \sum_n u_n (a_n e^{-u_n z} - b_n e^{u_n z})\, e^{-(in\nu + k)x} \qquad (9)$$

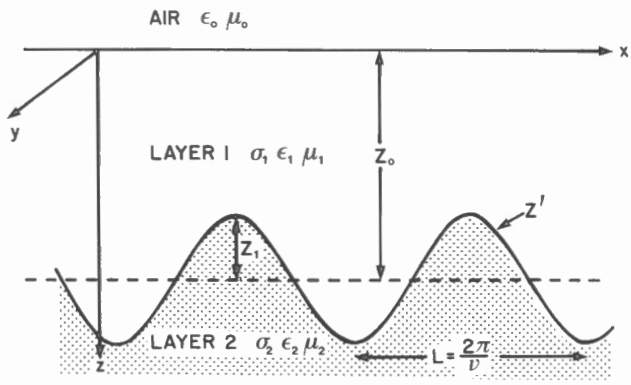

Figure 1. Section through a two-dimensional model with a single sinusoidal interface of the form $z'(x) = z_0 + z_1 \sin \nu x$.

and

$$E_z = -\frac{1}{\sigma + i\omega\epsilon}\sum_n (in\nu + k)(a_n e^{-u_n z} + b_n e^{u_n z})\, e^{-(in\nu + k)x} \qquad (10)$$

and the complex wave impedance at the surface is defined as

$$Z_1 = \left.\frac{E_x}{H_y}\right|_{z=0} \quad . \qquad (11)$$

We now introduce a second subscript m = 0, 1, or 2 to denote air, upper layer and lower layer of the model respectively. Then equations (6) to (11) should be modified to

$$H_{my} = \sum_n (a_{nm} e^{-u_{nm} z} + b_{nm} e^{u_{nm} z}) e^{-(in\nu + k)x} \qquad (12a)$$

$$E_{mx} = \frac{1}{\sigma_m + i\omega\epsilon_m}\sum_n u_{nm}(a_{nm} e^{-u_{nm} z} - b_{nm} e^{u_{nm} z}) e^{-(in\nu + k)x} \qquad (12b)$$

$$E_{mz} = -\frac{1}{\sigma_m + i\omega\epsilon_m}\sum_n (in\nu + k)(a_{nm} e^{-u_{nm} z} + b_{nm} e^{u_{nm} z})\, e^{-(in\nu + k)x} \qquad (12c)$$

where

$$u_{nm}^2 = \gamma_m^2 - (in\nu + k)^2 \qquad (13)$$

and

$$\gamma_m^2 = i\omega\mu_0\sigma_m - \omega^2\epsilon_m\mu_0 \quad . \qquad (14)$$

Notice that the horizontal wavenumber k is the same in all layers from the argument of continuity of $(\sigma + i\omega\epsilon)E_z$ (Crossley, 1981-I, equation (36)). The complex wave impedance should now be written in terms of the fields at the top of the first layer (m = 1), so that

$$Z_1(x) = \frac{1}{\sigma_1 + i\omega\epsilon_1}\,\frac{\sum_n u_{n1}(a_{n1} - b_{n1}) e^{-in\nu x}}{\sum_n (a_{n1} + b_{n1}) e^{-in\nu x}} \quad , \qquad (15)$$

where it is clear that Z_1 will now depend on horizontal position x above the interface. If we assume that the horizontal wavenumber k is related to the angle of incidence θ of the incoming wave by

$$k = \gamma_0 \sin\theta \quad , \qquad (16)$$

where $\gamma_0^2 = -\omega^2\mu_0\epsilon_0$ (Crossley, 1981-I, equation (52)), then the propagation constants u_{nm} (m = 0, 1, 2) can be determined from (13) once θ is specified. The complex impedance Z_1 then depends on the coefficients a_{n1} and b_{n1}.

Requiring all fields to vanish in the lower layer as $z \to +\infty$ leads to the result that $b_{n2} = 0$ (all n) and the requirement that all induced fields must decay as $z \to -\infty$ in air implies $a_{n0} = 0$ $(n \neq 0)$. Continuity of tangential $\underline{E}$ and H at the upper air-ground interface yields the relations

$$a_{n1} + b_{n1} = b_{n0} \quad , \; n \neq 0 \qquad (17)$$

and

$$b_{n1} = g_n a_{n1} \quad , \; n \neq 0 \quad , \qquad (18)$$

where

$$g_n = \frac{u_{n1}/u_{n0} - (\sigma_1 + i\omega\epsilon_1)/i\omega\epsilon_0}{u_{n1}/u_{n0} + (\sigma_1 + i\omega\epsilon_1)/i\omega\epsilon_0} \quad . \qquad (19)$$

Hughes and Wait (1975) also show that the same boundary conditions applied across the sinusoidal interface (1) serve to couple terms with different wavelengths in the E_x and H_y field expansions (12a,b). H_y is always tangential to (1) and thus always continuous, but it is easy to show that the requirement for tangential $\underline{E}$ to be continuous requires

$$\text{continuity of } (E_x + \nu z_1 E_z \cos\nu x) \qquad \text{at} \quad z = z_1 \, . \qquad (20)$$

Details of the derivation of expressions for a_{01}, b_{01}, can be found in Hughes and Wait (1975, Appendix A) and will not be reproduced here. Together with (17) and (18) these are sufficient equations to solve for all the quantities appearing in (15) and therefore, after appropriate summation, for Z_1.

There is an important restriction on the magnitude of z_1 which arises once a finite number of terms in the expansions (12a-c) are considered. To a good approximation only 3 values of n $(0, \pm 1)$ are required, provided

$$u_{n1} z_1 \ll 1 \quad , \qquad (21)$$

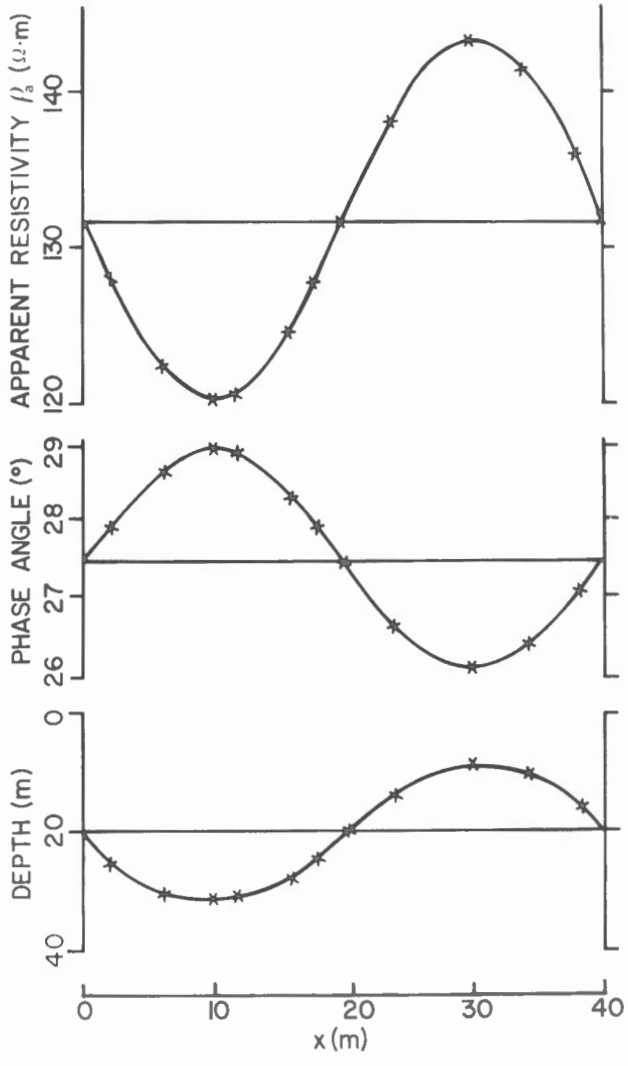

Figure 2. *Variations of ρ_a and φ above a single cycle of a two-layer model with sinusoidal interface. Model parameters are $z_0 = 20$ m, $z_1 = 10$ m, $L = 40$ m, $\rho_1 = 100$ Ω.m, $\rho_2 = 1000$ Ω.m, $\epsilon_1 = 9\epsilon_0$, $\epsilon_2 = 25\epsilon_0$.*

which leads to six linear equations connecting a_{n1} and b_{n1}. By referring to (13) it can be seen that (21) implies that z_1 be much less that the skin depth δ_1 $(= (2/\omega\mu_0\sigma_1)^{1/2})$ in either medium and that z_1 be much less than the wavelength L of the interface. Apparent resistivity and phase are then computed from Z_1 in the same way as for a plane layered model, i.e.

$$\rho_a = \frac{1}{\omega\mu_0}|Z_1|^2 \quad ; \quad \varphi = \arg Z_1 \ . \tag{22}$$

Discussion of the Model Parameters

Figure 2 shows the apparent resitivity and phase computed as a function of distance x along the sinusoidal interface. Values of the parameters are chosen to be the same as in Hughes and Wait (1975), but we used the frequency of the VLF transmitter at Cutler, Maine (i.e. 17.8 kHz). It can be seen that both ρ_a and φ are periodic with the interface, that the maximum and minimum values are not symmetric about the plane layered model ($z_1 = 0$) and that ρ_a is in phase with the interface but φ is not. The variation of ρ_a and φ with amplitude of the interface is shown in Figure 3 at x = 10 m, where it can be seen that the relationship is quite linear even for an extreme case ($z_1 = z_0$) where the second layer comes completely to the surface. Hughes and Wait (1975) show also that as the wavelength of the model is increased the maximum and minimum values of ρ_a and φ themselves show a maximum at L = 100 - 200 m (Fig. 4). This is, as Hughes and Wait (1975) note, due to the effect of skin depth in the two layers, whereas at large values of L both ρ_a and φ show extreme values which correspond to horizontally-layered models with $h_1 = z_0 \pm z_1$. The interface depth z_0 is obviously an important parameter in determining the amplitude of the excursions in (ρ_a, φ) which is observed at the surface. As Hughes and Wait (1975) note for fixed z_1, as z_0 increases, these variations decrease to the point where the two-layered model solutions are obtained.

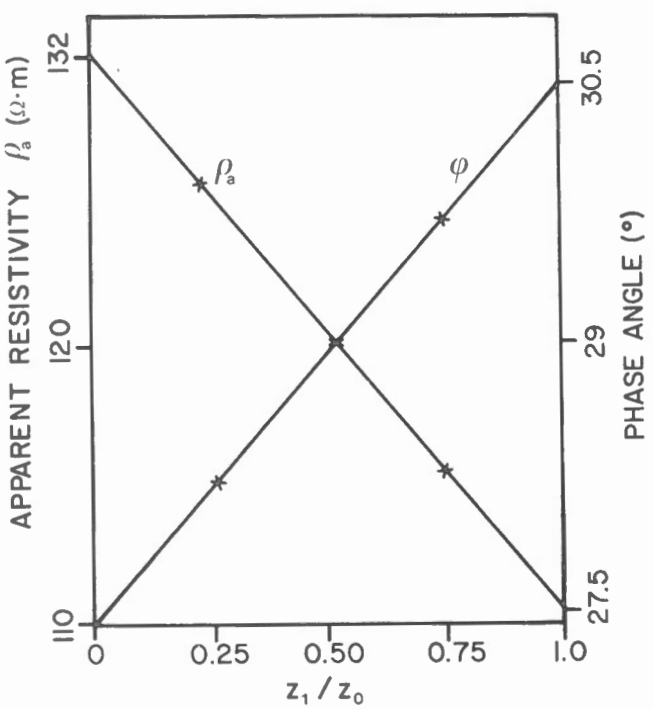

Figure 3. ρ_a and φ as functions of z_1, the amplitude of the sinusoidal interface. The other parameters are the same as for Figure 2.

Interface as a Fourier Series

Instead of (1) we can represent the interface as a Fourier series expansion of R sinusoids, each with amplitude z_r :

$$z'(x) = z_0 + \sum_{r=1}^{R} z_r \sin(r\nu x) \tag{23}$$

and frequency $r\nu$. The previous equations are then modified somewhat (Hughes and Wait, 1975, Appendix A), although the main effect of truncating the expansions is now to limit n to R terms. This is admissible providing

$$u_n z_r \ll 1 \ ; \ |n| \leqslant R \ ; \ 1 \leqslant r \leqslant R \ . \tag{24}$$

A further condition

$$(u_n + k)^2 > \gamma_0^2 \ , \tag{25}$$

ensures the fields induced by the interface decay away in air.

INVERSION FOR A SINGLE FOURIER COMPONENT

General Theory

We follow the style of Jackson (1972) and Wiggins (1972) in describing the estimation of M parameters p_j from N observed values o_i where there is a known functional relation between parameters and computed data c_i

$$c_i = f_i(p_j) \ , \ i = 1,2 \ldots N \ . \tag{26}$$

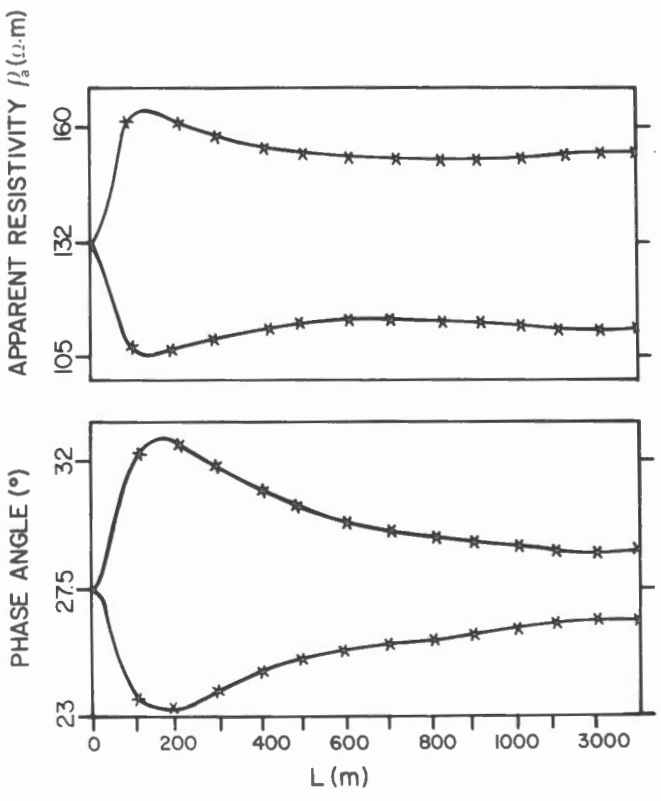

Figure 4. The maximum ranges of ρ_a and φ versus L, the wavelength of the sinusoidal interface. The other parameters are the same as for Figure 2.

Table 1. The influence of ψ on the parameters for a single harmonic component of the interface. In all tests $\epsilon_2/\epsilon_0 = 25$, $\epsilon_1/\epsilon_0 = 9$, $\rho_1 = 100\ \Omega.m$ and $L = 40$ m.

		Test 1		Test 2		Test 3	
Parameters	True	Initial	Final	Initial	Final	Initial	Final
z_0(m)	20	25	20.1	25	19.4	25	20.0
z_1(m)	10	12	13.7	12	-49.0	12	9.7
ρ_2 (Ω.m)	1000	1200	1067.1	1200	889.6	1200	1001.5
ψ (m)	0	2	2.0	2	1042.6	2	1.7

An acceptable least squares solution requires minimization of the sum of residuals $\sum_i (o_i - c_i)^2$ which leads to a formal matrix solution in the following way. We write (19) in terms of a parameter correction vector ΔP and a data vector ΔC

$$\Delta C = A \Delta P \tag{27}$$

then compute an estimated solution

$$\widehat{\Delta P} = (A^T A)^{-1} A^T \Delta C \quad , \tag{28}$$

assuming that the rank of matrix A is equal to $m \leq n$. The elements of ΔP and ΔC are $p_j^{(1)} - p_j^{(0)}$ and $o_i - c_i^{(0)}$ respectively where $^{(0)}$ denotes the initial approximation and $^{(1)}$ the updated parameter values. As usual A is the matrix of partial deviates $A_{ij} = \partial c_i / \partial p_j$ to be evaluated at the current value of the parameters. If the data contain errors which can be treated as independent statistical variances σ_i^2 , the estimated parameters $\widehat{\Delta P}$ have the variances

$$\text{var}\{\Delta P_k\} = \sum (H_{ki})^2 \sigma_i^2 \quad , \quad k = 1, 2 \ldots M \tag{29}$$

where H_{ki} is an element of the inverse matrix $H = (A^T A)^{-1} A^T$ appearing in (28). A further useful feature of the matrix formulation is the information density matrix S which is defined by the product AH. If we substitute from (28) back into (27) we find the recomputed data appears as

$$\widehat{\Delta C} = A \widehat{\Delta P} = AH\Delta C = S\Delta C \tag{30}$$

and S thus has the effect of smoothing the observed data during the fitting of the least squares estimates.

In the computation of H the critical numerical step is finding the inverse of the square matrix $B = (A^T A)$. Aside from problems with either data or parameters being linearly dependent (two or more rows or columns related) which leads to this matrix being singular, the elements of B often vary considerably in size due to the physical dimensions of the quantities involved being quite different. Instead of the theoretically preferred weighting procedure suggested by Wiggins (1972), the simpler scheme outlined by McKeeman (1962) has been found quite adequate for the present case. One simply forms a new matrix

$$B' = W B W \tag{31}$$

where W is a square diagonal matrix with elements $W_{jj} = (c / B_{jj})$ and c is a constant, often taken to be 0.5. The inverse of B' is simply $W^{-1} B^{-1} W^{-1}$ so that in practise H is unaltered if $(B')^{-1}$ is pre- and post-multiplied by W :

$$H = W(WA^T AW)^{-1} WA^T \Delta C \tag{32}$$

Any parameter which is poorly represented in the data will cause B' to be nearly singular regardless of scaling and the rank of B' , and hence that of A, falls below M. In this case the offending parameter is best removed from the inversion. A sound criteria for rejection of parameters can be established on examining the eigenvalues of A (e.g. Jackson, 1972).

The inversion needs an initial model to be supplied at the beginning and this is provided for in all cases by taking the parameters of an equivalent plane layered model ($z_1 = 0$) which satisfy (ρ_a, φ). These parameters can be determined by standard graphical or numerical methods (e.g. Mathieson and Crossley, 1981-IV).

Synthetic Data

The data are given by N observed values of (ρ_a, φ) as a function of the horizontal distance x, and the parameters involved in the model are z_0, z_1 , ρ_1, ρ_2 , ϵ_1/ϵ_0 , ϵ_2/ϵ_0 and L. An additional parameter ψ is introduced to give the phase of the interface with respect to the first observation point, considered to be $x = 0$. It is necessary to modify the field equations to accommodate this parameter which appears in the depth profile as

$$z'(x) = z_0 + z_1 \sin \nu(x + \phi) \tag{1a}$$

where the phase of the interface is $\nu\psi$. The modification appears as a replacement of x by $x + \phi$ in equations (12a-c).

There are potentially eight parameters involved in the inversion, of which one, ρ_1 , can in principle determined by independent means. During one test in which an inversion for four parameters (z_0, z_1 , ρ_2 and ψ) was attempted, it was noticed that the scaled matrix B' (equation (31)) was singular due to the interdependence of z_1 and L. If only a small fraction of a wavelength is interpreted, i.e. for $\nu x'$ small, we note from (1a) that $z' \approx z_0 + z_1 \nu x$ and so $z_1 \nu$ will always appear as a product. As a result one of these two parameters must be eliminated from the inversion and

we choose L because it can be estimated in principle as one half the distance between maxima of (ρ_a , φ).

Based on previous studies (see Crossley, 1981-I), it is clear that the dielectric constant does not play a large role in affecting (ρ_a , φ) at VLF (20 kHz), and we can therefore avoid numerical problems by omitting ϵ_1, ϵ_2 from the parameters to be determined. We therefore have four (z_0, z_1 , ρ_2 and ψ). A trial was then made to determine the three parameters (z_1, z_2 , and ρ_2) from a data set consisting of five pairs of (ρ_a , φ), i.e. N = 10 in the inversion, and for this trial setting the true phase ψ = 0 . The results, shown under 'test 1' of Table 1, indicate that when ψ is misrepresented as being 2m, i.e. 5% of L , then the errors in ρ_1 and z_2 are of comparable size. In 'test 2' of Table 1, we see that the result of using 5 pairs (ρ_a , φ) to try and estimate ψ from the data gives unacceptable results. Even with 21 pairs (ρ_a , φ) the values obtained, whilst quite good for z_0 , z_1 and ρ_2 show that ψ is poorly constrained (Table 1, test 3).

This parameter (ψ) is associated with a very small eigenvalue of the matrix A and hence poses numerical difficulties in the inversion. Without wishing to pursue this further we decided reluctantly to disregard ψ as a free parameter. The basic model has now been reduced to three well represented parameters, z_0, z_1 and ρ_2 , which considerably reduces the flexibility of the program while of course increasing its reliability.

We next wanted to find out the effect of omitting either apparent resistivity or phase information from the data set. A number of experiments were tried which indicated that the phase information was a more important contribution than apparent resitivity. Further details can be found in Teemull (1979).

In addition data values above the maxima and minima of the sinusoid (i.e. $x + \psi = L/4 , 3L/4$) were found to be more important than those at the inflection points $x + \psi = 0, L/2$. Another test used the original data with 25% random Gaussian noise added and the solution for 3 parameters was easily determined to within 5%. This accuracy is somewhat illusory for in a practical situation the parameters L and ψ would not be expected to be known exactly. The sinusoidal interface is not necessarily a unique solution even though a data set might suggest such an interpretation. For example, if one had a plane horizontal interface between layer 1 and a layer in which ρ_2 varied sinusoidally, the results would appear very similar (Fig. 5). These results are however approximate as (ρ_a, φ) were computed on a point-by-point basis.

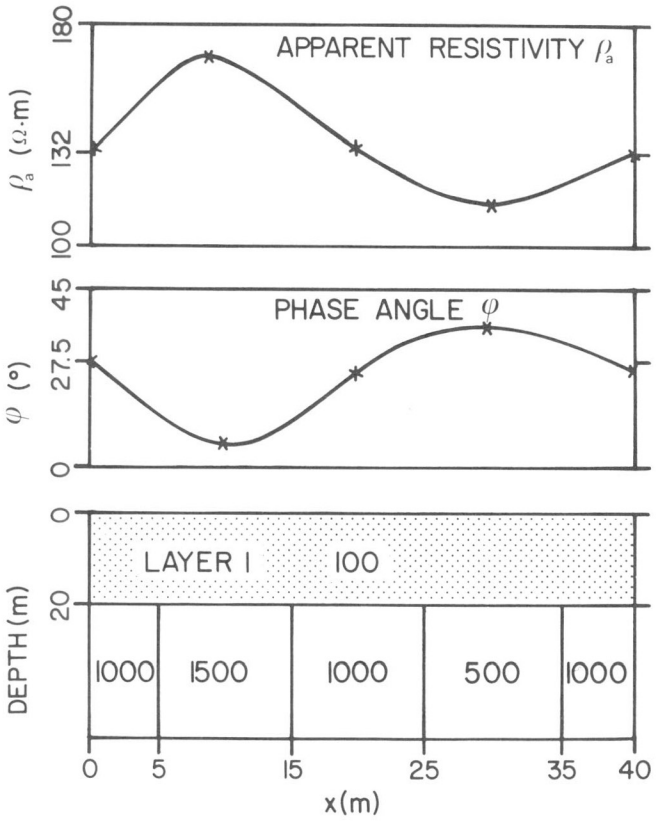

Figure 5. *Apparent resistivity and phase for a horizontal interface above blocks with varying resistivity. The stations are fortuitously located above the center of each block and the (ρ_a, φ) values obtained by simple two-layered interpretation. Other parameters are z_0 = 20 m, ϵ_2/ϵ_0 = 25, ϵ_1/ϵ_0 = 9.*

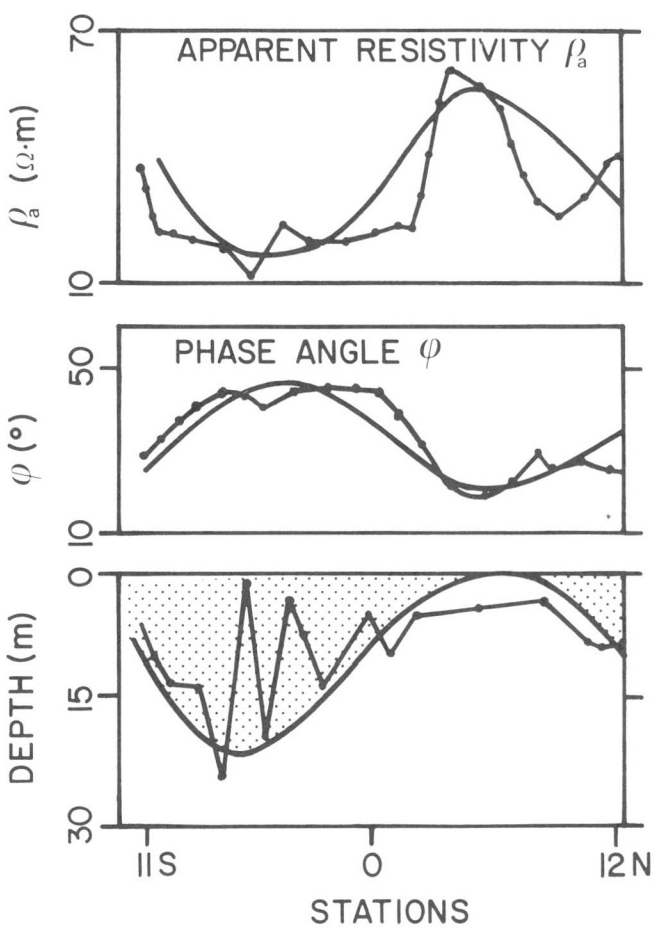

Figure 6. *Comparison of sinusoidal versus point-by-point interpretation of line 32, Timmons area.*

Application to Field Data

The observational data was obtained from an EM16R survey in the Timmins area using the Cutler VLF transmitter at 17.8 kHz. One profile of a N-S line "32" was chosen along which 24 stations were spaced at 100 ft intervals. From a previous interpretation in the area it was found that ρ_1 was close to 20 Ω.m, and the dielectric constants were assumed to be ϵ_0 for both layers. Inspection of the data (Fig. 6) lead to a selection of 2200 ft for L and 100 ft. for ψ. Initial values for z_0 and z_1 were taken to be the mean standard deviation of all the individual first layer depths, i.e. $z_0^{(0)}$= 9m, $z_1^{(0)}$= 5.5m and ρ_2 was the mean of all second layer resistivities, i.e. $\rho_2^{(0)}$= 180 Ω.m.

The initial attempt at inversion diverged, but a second attempt with $\rho_2^{(0)}$ = 90 Ω.m, gave the solution z_0 = 8.6m, z_1 = 15.8m and ρ_2 = 95.6 Ω.m. A comparison of the sinusoidal solution with a point-by-point plane layered model is shown in Figure 6.

INVERSION FOR A FOURIER SERIES MODEL

When dealing with an interface depth profile constructed from R Fourier coefficients, the quantities a_{n1}, b_{n1}, ($|n| \leqslant R$), though modified slightly from the single sinusoid case (see Hughes and Wait, 1975, Appendix A), are still quite straightforward to generate. The surface impedance given by (15) is then updated by letting the two sums run from $-R \leqslant n \leqslant R$.

Sloping Interface Model

An interface profile z' was generated using 20 terms in a series expansion

$$z'(x) = z_0 + \sum_{r=1}^{20} z_r \sin(2\nu\pi x/L) , \qquad (33)$$

where z_0= 20m and the periodicity of the structure is 600m. The coefficients z_r were generated from the amplitude spectrum of a unit step function, which has the form $1/\omega$, thus

$$z_r = \frac{A}{r\pi}(1 - \cos r\pi) , \qquad r = 1, 2 \ldots R, \qquad (34)$$

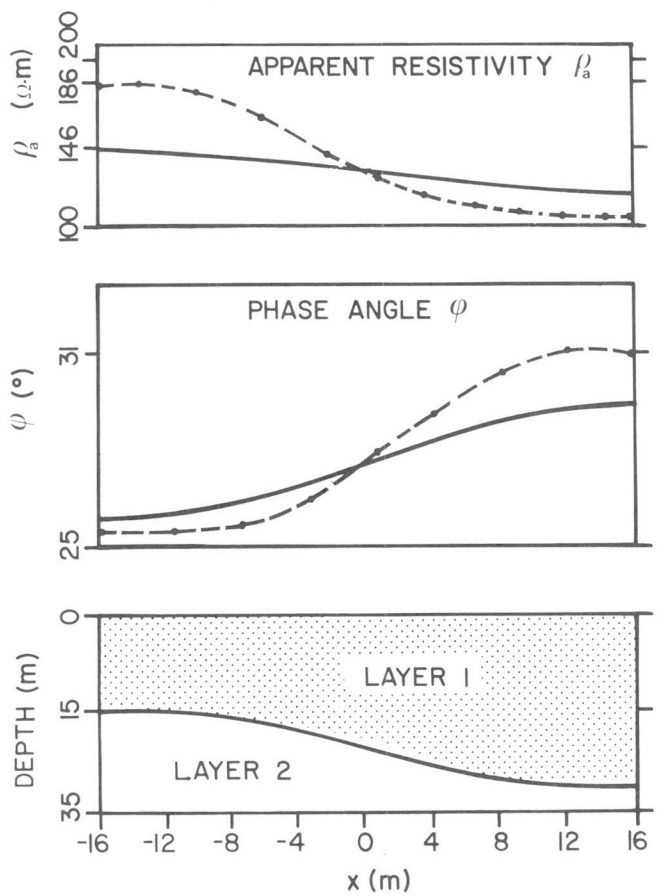

Figure 7. Apparent resistivity and phase generated by a sloping interface as the central portion of a long step function simulated by a 20-term expansion (solid lines). These are compared with the values simulated from a point-by-point data generation procedure (dashed lines).

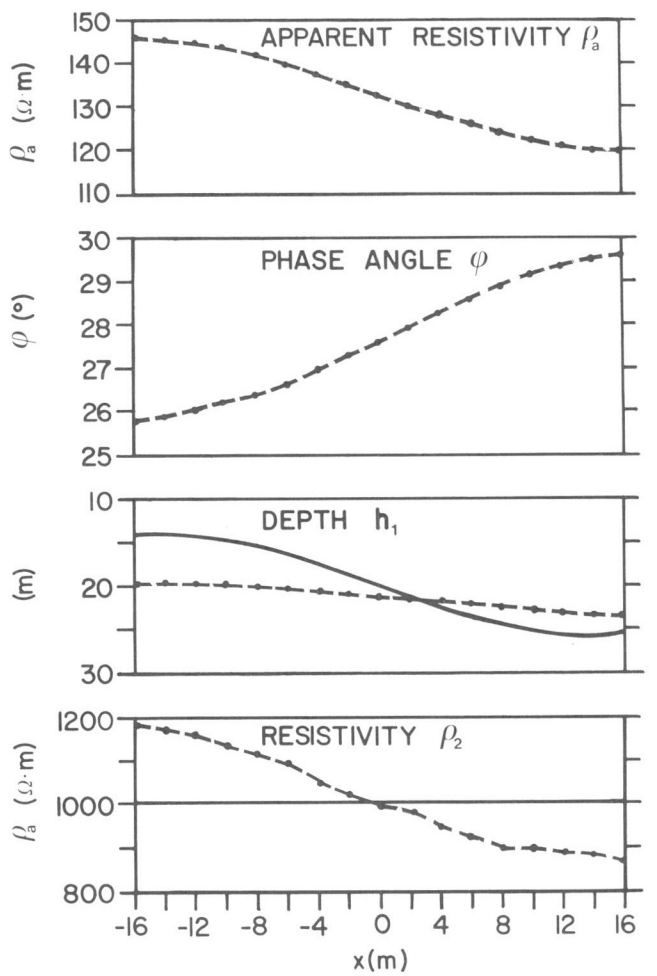

Figure 8. Inversion of synthetic data using a portion of a step function interface (solid lines) and point-by-point two-layer interpretation (dashed lines).

where A is the vertical amplitude of the step. Both the model and (ρ_a, φ) are shown in Figure 7 as a function of the distance x, for parameters $\rho_1 = 100\ \Omega.m$, $\rho_2 = 1000\ \Omega.m$, $\epsilon_1 = \epsilon_2 = \epsilon_0$, $A = 10m$. Only the central portion of the profile is shown and a comparison is made between the exact solution and a two-layer point-by-point interpretation. It can be seen that, as expected, the point-by-point interpretation over emphasises the vertical relief of structure. Similar examples are given in Hughes and Wait (1975) for structures with several hundred terms.

The next question is how to interpret such a structure as (34) which is made up of a considerable number of terms. Fortunately it is not necessary to find all the z_i's independently as they are obviously related via (34), therefore the step model has essentially seven parameters. As before ρ_1 will be assumed known and ϵ_1/ϵ_0, ϵ_2/ϵ_0 set to unity, which leaves four parameters z_0, ρ_2, A and L. If we assume L then the other three parameters are well determined in an inversion, as has been noted before. Of more interest is the point-by-point two-layer interpretation of this data shown in Figure 8, which indicates that much of the depth variation of h_1 along the profile has be ascribed to changes in ρ_2.

SUMMARY

It is clear that certain parameters in harmonic interface models are difficult to estimate from actual field observations. These are the dielectric constants of the two layers and the wavelength and phase of the structure which appear to be best estimated directly from the data. This may not always be possible however, especially in situations where the wavelength of the whole structure is much larger than the survey area.

Nevertheless, because fairly complicated functions such as a step can be characterized accurately by one or two parameters, i.e. amplitude and wavelength, inversion for particular categories of models is not as unwieldy as might be imagined. Most simple interfaces can be synthesized from similar formulae which suggests that the characteristic signatures of certain geological structures may be sought in field data either by direct inversion or a matched filtering technique.

ACKNOWLEDGEMENTS

The research which this article summarizes was supported by the EMR Canada through Research Agreements 4-99-77 and 58-4-78.

REFERENCES

Coggon, J.H.
1971: Electromagnetic and electrical modelling by the finite element method, Geophysics, 36, p. 132-155.

Crossley, D.J.
1981: The theory of EM surface wave impedance measurements; in Geophysical Applications of Surface-Wave Impedance Measurements, L.S. Collett and O.G. Jensen (eds.), Geological Survey of Canada, Paper 81-15, Report V, p. 1-17.

Hughes, W.J. and Wait, J.R.
1975: Effective wave tilt and surface impedance over a laterally inhomogeneous two-layer Earth, Radio Sci., 10, p. 1001-1008.

Jackson, D.D.
1972: Interpretation of inaccurate, insufficient and inconsistent data, Geophys. J. Roy. Astr. Soc., 28, p. 97-109.

Jones, F.W. and Price, A.T.
1970: The perturbations of alternating geomagnetic field by conductivity anomalies, Geophys. J. Roy. astr. Soc., 20, p. 317-334.

LaFleche, P.T. and Jensen, O.G.
1981: Wave-impedance measurements at 60 kHz; in Geophysical Applications of Surface Wave Impedance Measurements, L.S. Collett and O.G. Jensen (eds.), Geological Survey of Canada, Paper 81-15, Report V, p. 67-78.

Mathieson, C.C. and Crossley, D.J.
1981: Graphical and numerical interpretation in VLF-resistivity studies; in Geophysical Applications of Surface Wave Impedance Measurements, L.S. Collett and O.G. Jensen (eds.), Geological Survey of Canada, Paper 81-15, Report V, p. 49-65.

McKeeman, W.M.
1962: Algorithm 135, Crout with equilibrium and iteration, Comm. Assoc. Comput., Mach. 5, p. 553-555.

Swift, C.M.
1971: Theoretical magnetotelluric terrain response from two-dimensional inhomogeneities, Geophysics 36, p. 38-52.

Teemull, F.A.
1979: Inversion of VLF data for two-layer lateral inhomogeneities, M.Sc. thesis, McGill University.

Wait, J.R.
1962: Electromagnetic Waves in Stratified Media, Pergammon, Oxford.

Wiggins, R.A.
1972: The general linear inverse problem: implication of surface waves and free oscillation for Earth structure, Rev. Geophy. Space Phys., 10, p. 251-285.

VII

MAGNETOTELLURIC PHASE MEASUREMENTS

R.K. Mathur* and W.M. Telford+
* Institute of Petroleum Exploration, Government of India
+ Laboratory in Applied Geophysics, McGill University

Mathur, R.K. and Telford, W.M., Magnetotelluric phase measurements; in Geophysical Applications of Surface Wave Impedance Measurements, L.S. Collett and O.G. Jensen editors; Geological Survey of Canada, Paper 81-15, p. 87-93, 1981.

Abstract

The purpose of this work was to study the possibility of measuring phase differences between natural electric and magnetic (magnetotelluric) field detected at ground surface. Data from a magnetotelluric survey conducted at Pemberton, B.C., were employed for this purpose. Orthogonal E- and H-field analog data were combined to produce Lissagous ellipse figures, from which the phase was measured at various frequencies from 0.5 to 100 Hz. These results were compared with phase measurements from the same data, obtained by the maximum entropy method (MEM). Reasonable agreement between the two methods has been obtained, the maximum phase differences between Analog and MEM being about 5°.

Résumé

Cette étude visait à déterminer s'il est possible de mesurer les différences de phase entre les champs électrique et magnétique (magnétotellurique) naturels perçus à la surface du sol. A cette fin on a utilisé les données d'une étude magnétotellurique effectuée à Pemberton, C.-B. On a associé des données analogiques de champs E et H orthogonaux pour obtenir des figures elliptiques de Lissajou dont la phase a été mesurée à différentes fréquences de 0,5 à 100 Hz. Ces résultats ont été comparés aux mesures de phase des mêmes données obtenues par la méthode MEM (méthode d'entropie maximum). Il existe une corrélation satisfaisante entre les deux démarches, la différence de phase maximale entre les résultats obtenus par la méthode analogique et par la MEM étant d'environ 5°.

INTRODUCTION

The measurement of complex ground impedance Z_o and hence the determination of an apparent resistivity ρ_a and phase φ over one-dimensional (layered) and two-dimensional (dipping contacts dikes, etc., with long strike length) structures has been discussed elsewhere (See Cagniard (1953), Wait (1962), Keller and Frischknecht (1966), Porstendorfer (1975), etc. and in this volume, Crossley (1981-I), Powell and Jensen (1981-II), Jones and Telford (1981-III) and Mathieson and Crossley (1981-IV).). The respective values are, in any medium with permeability μ_o

$$Z = E/H\ ,\ \rho_a = |Z|^2/2\pi f\mu_o\ ,\ \varphi = \arg Z = \mathrm{Im}(Z)/\mathrm{Re}(Z)$$

Determination of ρ_a , involving the amplitude ratio of the electric to magnetic fields, is a relatively simple procedure. When using a controlled propagation source, such as VLF or LF transmitting stations, the phase measurement is straightforward as well, since the signals are constant in azimuth, more or less so in amplitude and in phase difference between E and H fields.

In MT surveys, however, only ρ_a has been measured directly. Because of the random character of the natural source, the phase is obtained from analysis of selected data recorded in the field. The present study was initiated to determine the possibilities of making a field measurement, at specific frequencies, of φ as well. Records from a survey carried out previously were analyzed in the laboratory for this purpose. Smith et al. (1961) have reported similar measurements at lower frequencies.

Source of Data

Data used for this study were obtained from the magnetotelluric surveys performed in the Mount Meagher geothermal area in British Columbia during the summers of 1976 and 1977 The aim of the project was to decipher hot spring zones and to study the geology of the area. The survey was carried out by the Department of Energy, Mines and Resources Canada and the Mineral Exploration Research Institute.

Figure 1 (Van Ngoc, 1976) shows the location of the sites in the Mount Meagher area along with a synthesis of the results. Two types of instruments were used, the magnetotelluric profiling instrument (MTP), Telemag 2, which measures the apparent 'scalar' resistivity in the direction of the survey line at 12 relatively high frequencies (1-2000 Hz) and the magnetotelluric sounding array (MTS) which records two orthogonal magnetic and telluric components simultaneously over a lower frequency band (0.01-100 Hz). The MTS records, after analysis of their data, produce apparent resistivity tensor and phase measurements which determine the electrical properties of structures to considerable depths, in two principal directions.

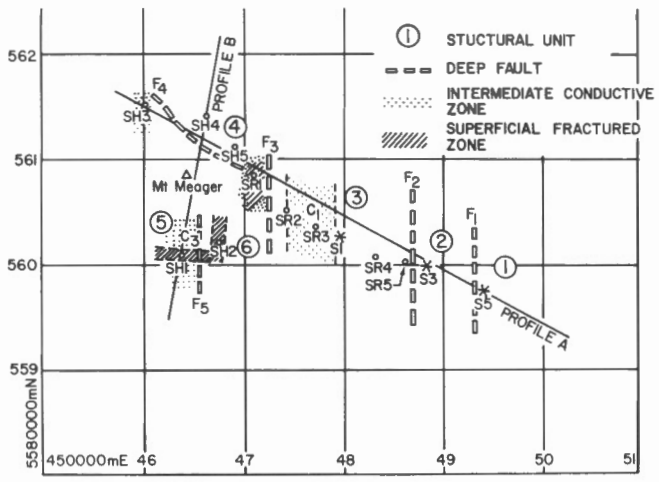

Figure 1. Location of MT sounding sites, area Mt. Meagher, B.C. A synthesis of the survey results is superimposed.

In summary, the survey indicated a first layer resistivity of about 1000-3000 Ω.m, 45-65 m thick which corresponds to gravels. This appears to be underlain by a conductive clay bed, 4-5 m thick and 2-5 Ω.m resistivity. At greater depths the layers appear anisotropic in both E-W and N-S azimuths, with resistivities in the range 500-20000 Ω.m (E-W) and 600-8000 Ω.m (N-S), below which a conductive horizon (15-600 Ω.m) appears at various depths from about 4 km to 40 km. which may indicate partially melted upper mantle or magma chambers. These geoelectric sections are illustrated in Figures 2a and 2b. Quality of the data is better illustrated by the ρ_a vs. T plot shown in Figure 3.

ANALOG PHASE MEASUREMENT

The original magnetic tape data from the Mount Meagher survey were recorded at 3 3/4 and 15/16 ips (inches/second), the former for higher frequency bands 1-1000 Hz and 0.1-20 Hz and the slower speed for 0.001-0.2 Hz signals. Portions of the tapes showing good quality data were selected for analog analysis after playback display on the oscilloscope. These were from sounding sites S1, S2 and SH1 (See Figure 1.).

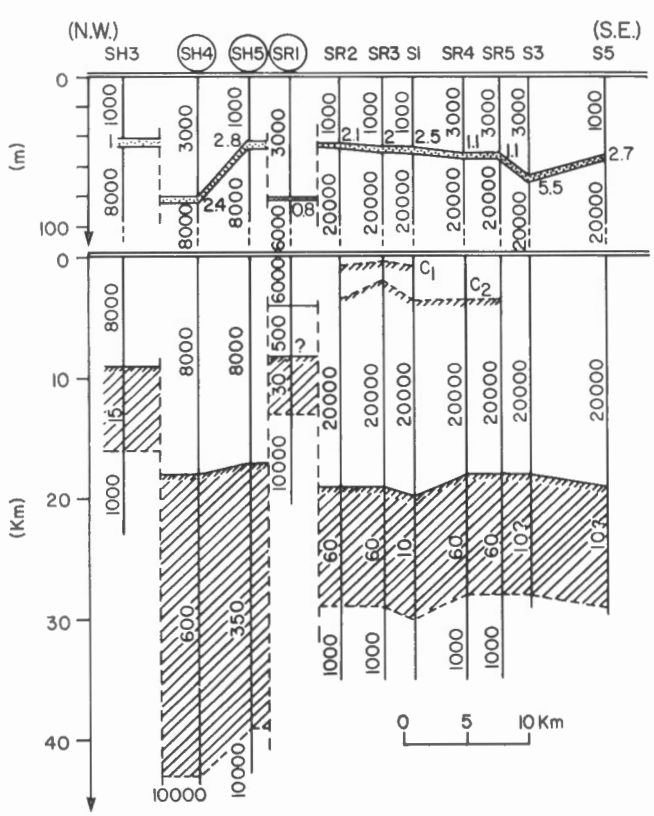

Figure 2a. Geoelectric section Profile A, Mt. Meagher, B.C.

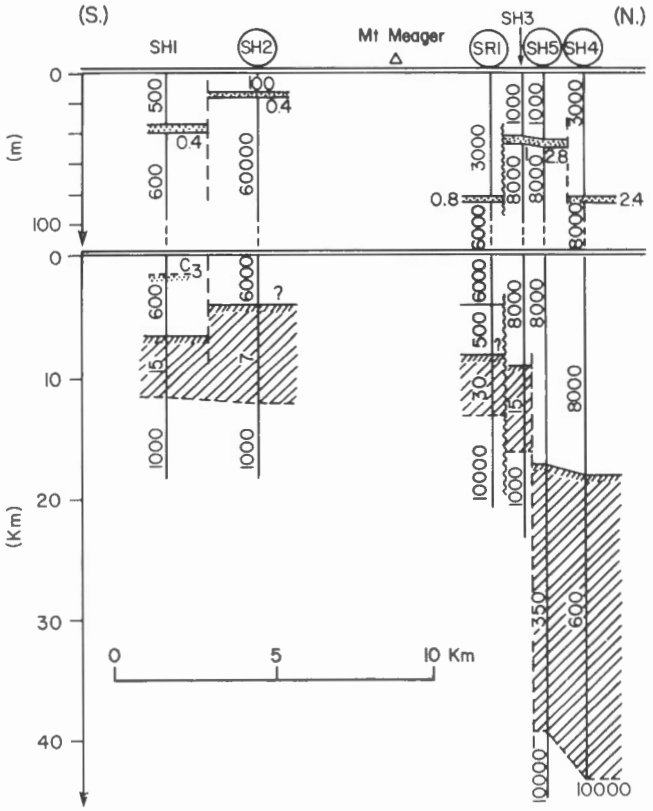

Figure 2b. Geoelectric section Profile B, Mt. Meagher, B.C.

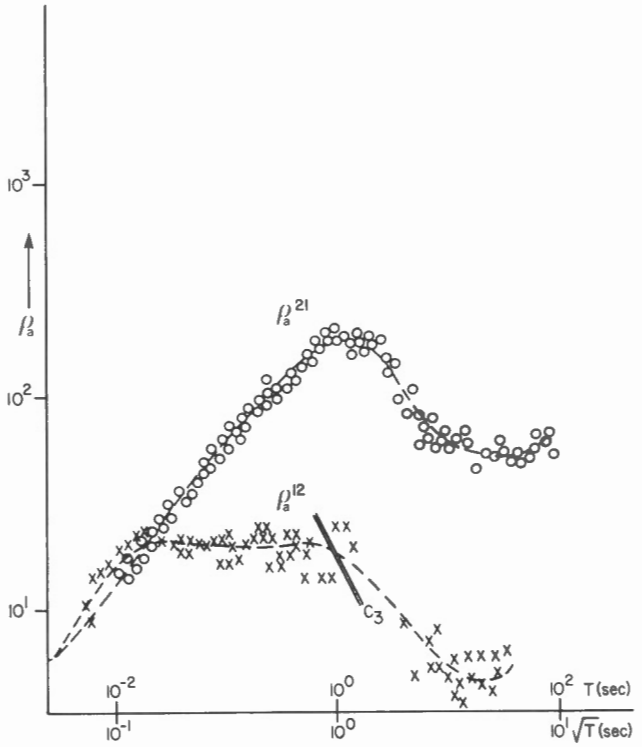

Figure 3. *MT curves of ρ_a vs. T, site SH1, for ρ_a 12(NS) and ρ_a 21(EW) soundings.*

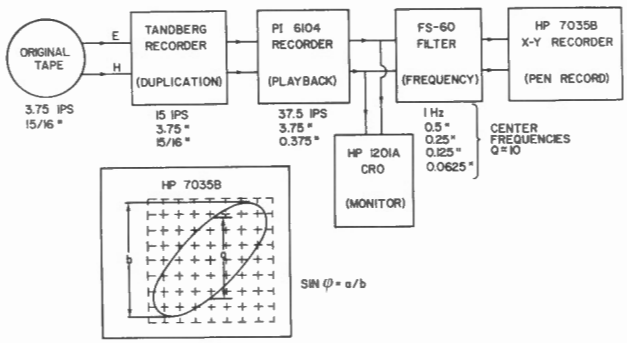

Figure 4. *Instrumentation for analog phase measurement block diagram.*

Instrumentation

Since the relative E-H phase was to be measured at particular frequencies in the sub-audio and audio range on an X-Y recorder (1 Hz maximum frequency), it was necessary to reduce the higher frequencies to accommodate the recorder plot. This was accomplished with the instrumentation sequence shown in the block diagram of Figure 4.

Selected data from the original tapes were transferred to the 4-channel Tandberg tape recorder. Generally it was operated at 15/16 ips, for 3 3/4 ips speed of the original tapes, providing a frequency division of four. Portions of these records were then transcribed on the Precision Instruments PI-6104 recorder which ran at 35 ips at all times. This instrument was then played back, through a band pass filter for frequency selection, to the oscilloscope and X-Y recorder. Playback at 35 ips reproduced the original frequency divided by four; at 3.75 and 0.375 ips the reduction would be forty and four hundred respectively. Thus the highest frequency from the original data which could be displayed on the X-Y recorder was 400 Hz.

The FS-60 active filter was used for the various selected frequencies (0.5, 1, 5, 10, 25, 40, 100, 200 and 400 Hz). This is known as a 3-step state variable filter with two parallel sections, as identical as possible, one for each of the E and H channels. It consists of a hybrid integrated circuit employing multiloop negative feedback tunable from DC to 10 kHz in high pass, low pass and band pass modes, the latter being used for this work. The center frequencies were 1, 0.5, 0.25, 0.125,and 0.062 Hz, obtained by connection of appropriate external resistors and capacitors. The filter Q was approximately 10. For clarification the equivalent frequency values and tape speeds are listed in Table 1.

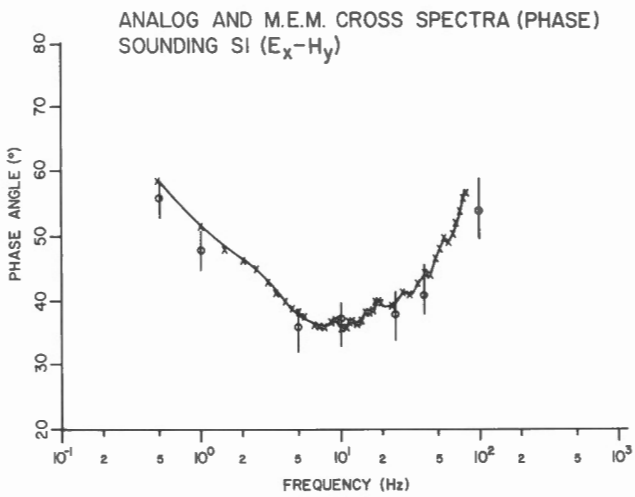

Figure 5. *Sounding SI (E_x-H_y). Analog and MEM cross spectra for phase angle.*

Table 1. Recorder and filter settings for analog phase measurements.

Frequency Record	Record/Playback Ratio	Frequency Playback
0.5 Hz	1 , 1/4	0.5 , 0.125
1	1 , 1/4	1 , 0.25
5	1/40	0.125
10	1/40	0.25
25	1/400	0.0625
40	1/40	1
100	1/400	0.25
200	1/400	0.5
400	1/400	1

Table 2. Signal magnitudes from MEM (maximum entropy method) analysis.

Sounding	Amplitude Range ('Very Fast' Records)	Average	Amplitude Range ('Fast' Records)	Average
S1 (E_x-H_y)	0.02 -0.07	0.05	0.001 -0.008	0.002
S1 (E_y-H_x)	0.002 -0.03	0.006	0.0003 -0.006	0.001
S2 (E_x-H_y)	0.01 -0.07	0.02	0.002 -0.02	0.003
S2 (E_y-H_x)	0.0003-0.01	0.002*	0.0002 -0.002	0.0003*
SH1 (E_x-H_y)	0.02 -0.08	0.05	0.002 -0.01	0.004
SH1 (E_y-H_x)	0.002 -0.01	0.005*	0.00002-0.0008	0.0001*

After selecting a frequency to be analyzed from the original records, adjusting the playback speed and filter to suitable values, the procedure was to study the scope ellipses and record them on the X-Y pen recorder when they showed reasonable amplitude and well defined shape. The phase shift was determined from the dimensions of the ellipse in the relation (See Figure 4.):

$$\varphi = \sin^{-1} a/b$$

PHASE DETERMINATION BY MAXIMUM ENTROPY METHOD

Burg (1967, 1968) introduced the maximum entropy method (MEM) of spectral analysis for stationary time-series data. This method determines the most unpredictable time series whose actual auto-correlation function agrees with all available estimates of the same function as determined from a data series. It provides a power spectral estimate which is a non-negative function of frequency and which agrees with the estimated autocorrelation values as required. MEM has several advantages over conventional methods of harmonic analysis. Greater resolution of harmonic peaks is obtained, the spectral window being data adaptive (Lacoss, 1971) and without sidelobes which could cause leakage between frequency components. The MEM offers an attractive procedure for obtaining high spectral resolution from short segments of data.

Because of the superiority in resolution of the maximum entropy method of spectral analysis over other techniques, it was utilized in this work to compare with the results obtained by the analog procedure, employing electronically selected harmonic components of the data record. To obtain the MEM cross-spectrum for two orthogonal electric and magnetic components, a solution of the multichannel prediction error system was used. Theory for this type of analysis is extensive and is not incorporated in this paper (e.g. See Tyraskis (1979).): the computer program used to obtain the required MEM cross spectra was provided by this source.

Magnetotelluric field data selected from the Mount Meagher survey and recorded on the FM recording system were digitized and the numerical record punched on computer cards. Each block contained 1024 data values. For the 4-channel recorded data, the four values E_x, H_y, E_y and H_x are printed on each card and each block then provides 1024/4 = 256 cards. For each sounding 10 blocks from the 'very fast' (1 Hz -1 kHz) and 'fast' (0.1 - 20 Hz) sections were used. In the first case the time for each block is 0.5 seconds, since the frequency of digitization is 512 Hz and the time for 10 blocks becomes 5 seconds. For 'fast' sections the corresponding values are 4 seconds, 64 Hz and 40 seconds.

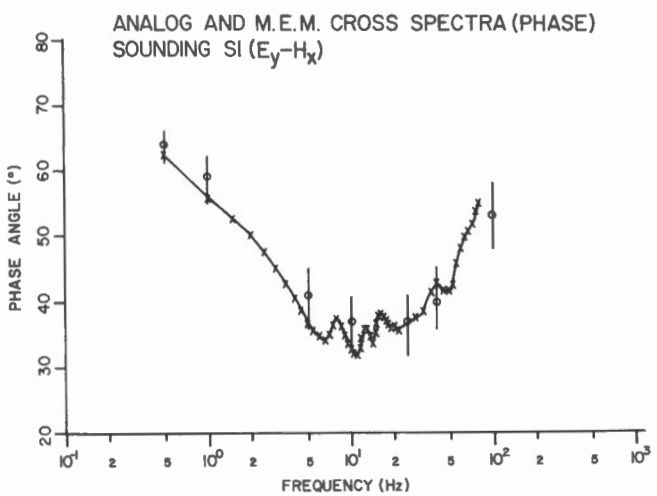

Figure 6. *Sounding SI (E_y-H_x). Analog and MEM cross spectra for phase angle.*

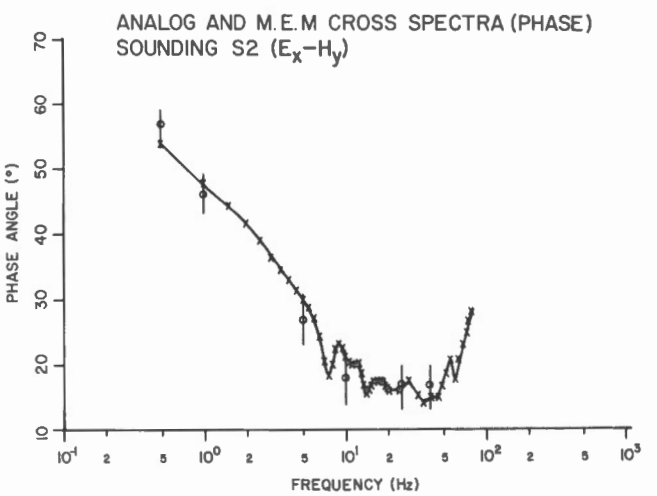

Figure 7. *Sounding S2 (E_x-H_y). Analog and MEM cross spectra for phase angle.*

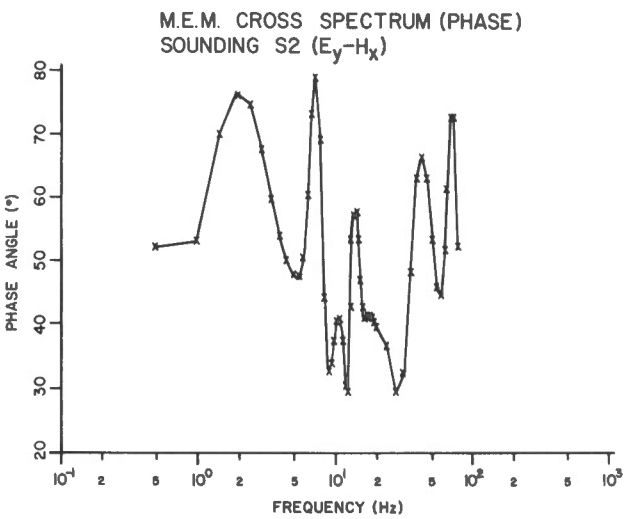

Figure 8a. Sounding S2 (E_y-H_x). MEM cross spectra for phase angle.

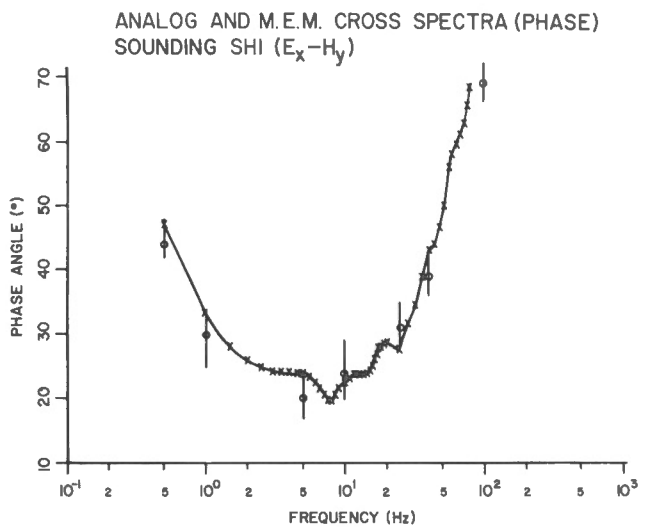

Figure 9a. Sounding SH1 (E_x-H_y). Analog and MEM cross spectra for phase angle.

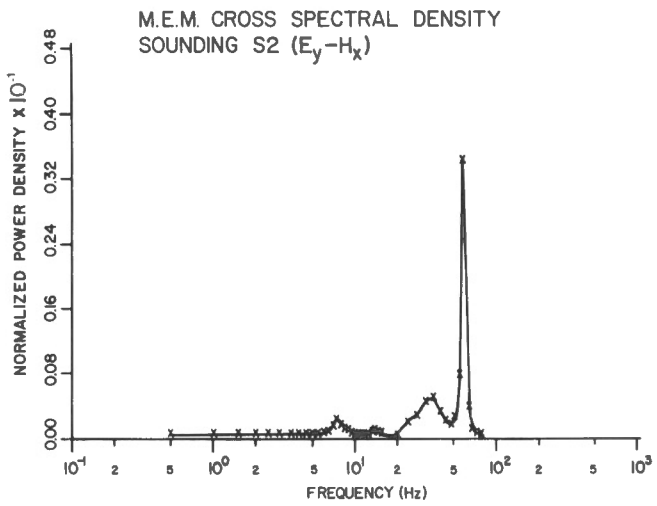

Figure 8b. Sounding S2 (E_y-H_x). MEM cross spectra of power density.

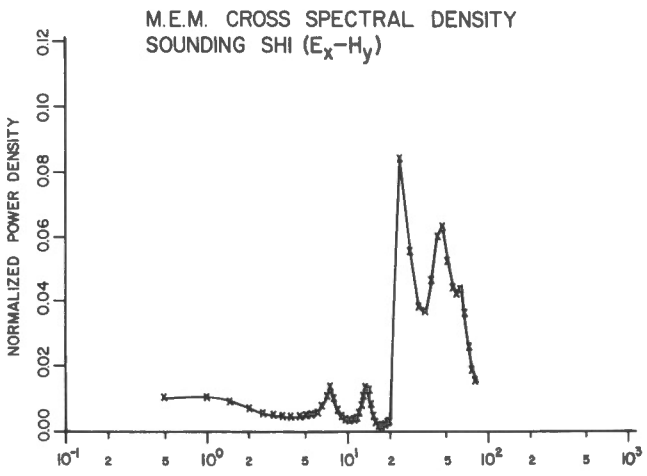

Figure 9b. Sounding SH1 (E_x-H_y). MEM cross spectra of power density.

Data cards for 10 blocks of each type were then processed by the computer program. The cross spectrum between orthogonal E and H fields was obtained in complex form, via Fourier transformation of the interchannel prediction-error filter coefficients obtained from the MEM program, to produce 65 harmonics corresponding to a frequency range from zero to the Nyquist frequency, the frequency interval between successive harmonics being constant. The Nyquist frequency is the inverse of twice the digitizing interval; a digital signal contains no genuine information higher than this frequency.

A separate program was used to convert real and imaginary parts of the complex cross correlation into amplitude ratios and phase differences between the orthogonal E and H components. Corrections were incorporated in this program for phase shift in the magnetic sensor, electric and magnetic field units (mV/100 m to mV/km and mV to gammas or nT) and gain settings of field amplifiers (Chouteau, 1976). The output, in the form of a computer plot, then consisted of magnitude (normalized power density) and phase angle, as a function of frequency.

RESULTS OF PHASE MEASUREMENTS

Results of the two methods of phase measurement have been combined in phase spectra plots, shown in Figures 5, 6, 7, 8a, 9a and 10. As can be seen from Figure 5, for example, E_x - H_y data are displayed from sounding S1 in the range 0.5 - 100 Hz. (Analog data could not be obtained at frequencies above 100 Hz because of low signal amplitudes.) Crosses indicate phase angles determined from the maximum entropy method of direct spectral analysis; circles represent average phase from analog analysis, with the bars showing the total range of values at a particular frequency.

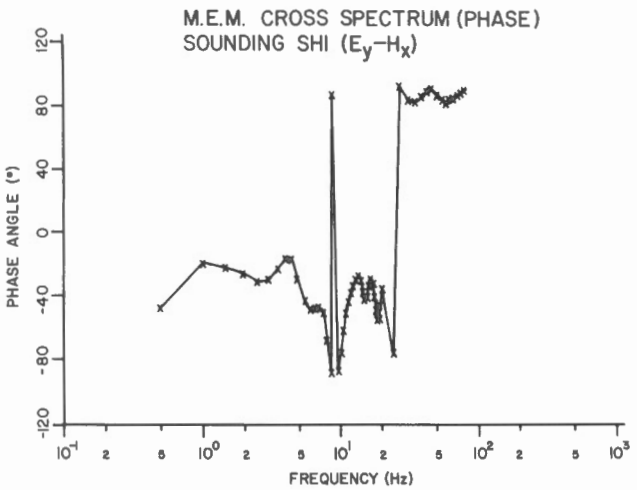

Figure 10. *Sounding SH1 (E_y-H_x). MEM cross spectra for phase angle.*

In Figures 8a and 10 there are no analog phase points to compare with the MEM phase spectra, since the E_y - H_x data from stations S2 and SH1 were generally too low and/or erratic in amplitude to produce reasonable ellipses. This is clear from the MEM magnitude spectra in Figures 8b and 9b. In the first the signal level is generally very low compared to the second. The same situation existed for E_y - H_x data at SH1. Further information related to signal amplitudes is given in Table 2.

Asterisks indicate the low amplitude for which analog phase spectra could not be obtained. The signal levels from E_x - H_y records (E-field EW, H-field NS) are considerably higher than the E_y - H_x orientations at these sites. Similarly the data amplitudes at 'very fast' (3 3/4 ips, frequency range 1-1000 Hz) speeds are consistently larger than at 'fast' speeds (0.1 - 20 Hz).

Phase values derived from the analog method show a reasonable agreement with the MEM spectra. The average error for 24 measurements at 6 frequencies (0.5, 1, 5, 10, 25, 40 Hz) is - 0.5° with a spread of + 4.5° to - 3.7°. The average range as shown by the bars is ±3.6° with a maximum of ±4.5°, minimum ±2.0°.

CONCLUSION

Based on this laboratory work, an attempt should be made to develop field instrumentation for direct phase determination at several frequencies in the range 8 - 3000 Hz, the audio-frequency range of the magnetotelluric spectrum (i.e. AMT). In AMT surveys the present method for measuring amplitude requires averaging at least three integration periods of about 30 seconds each. Where the signals are erratic this time may be doubled. A simultaneous phase integration is expected to take more time, if it can be done at all; in the present study it was necessary to select good data (relatively high amplitudes, low noise) for the analog recording. However, the possibilities are very attractive.

ACKNOWLEDGEMENTS

The research which this article summarizes was supported by the EMR Canada through Research Agreement 77-4-79.

The author would like to thank the Canadian Commonwealth Scolarship and Fellowship Committee for providing financial support in the form of a graduate scholarship during his attendance at McGill. Thanks are also due to Michel Chouteau for providing information on the previous survey work carried out pertinent to this thesis, and to P. Tyraskis for aid in applying the maximum entropy method.

REFERENCES

Burg, J.P.
1967: Maximum entropy spectral analysis, Paper presented at 37th Annual International Meeting, Society of Exploration Geophysicists, Oklahoma City, (abstract) Geophysics, 32, 6, p. 1093.

Burg, J.P.
1968: A new analysis technique for time series data; in Proceeings of the Nato Advanced Study Institute on Signal Processing With Emphasis on Underwater Acoustics, Enschede, Netherlands, National Defense Organization, The Hague, 2 vols.

Cagniard, L.
1953: Basic theory of the magnetotelluric method of geophysical prospecting, Geophysics 18, p. 605-35.

Chouteau, M.
1976: Acquisition et traitement des signaux large bande de frequence pour sondage magneto-tellurique minier et petroliere, M.Sc. Thesis, Ecole Polytechnique de Montreal.

Crossley, D.J.
1981: The theory of EM surface wave impedance measurements; in Geophysical Applications of Surface Wave Impedance Measurements, L.S. Collett and O.G. Jensen (eds.); Geological Survey of Canada, Paper 81-15, Report V, p. 1-17.

Jones, D. and Telford, W.M.
1981: Mapping bedrock terrain with the EM16R - VLF unit; in Geophysical Applications of Surface Wave Impedance Measurements, L.S. Collett and O.G. Jensen (eds.); Geological Survey of Canada, Paper 81-15, Report V, p. 35-48.

Keller, G.V. and, Frischknecht F.C.
1966: Electrical Methods in Geophysical Prospecting, International Series on Electromagnetic Waves, Vol. 10, Pergamon, Toronto, 523 pp.

Lacoss, R.T.
1971: Data adaptive spectral analysis methods, Geophysics 36, p. 661-675.

Mathieson, C.C. and Crossley D.J.
1981: Interpretation of single frequency VLF data; in Geophysical Applications of Surface Wave Impedance Measurements, L.S. Collett and O.G. Jensen (eds.); Geological Survey of Canada, Paper 81-15, Report V, p. 49-65.

Porstendorfer, G.
1975: Principles of Magneto-telluric Prospecting, Geopublication Associates, Gebruder Bonntraeger, Berlin-West, Stuttgart, 118 pp.

Powell, B.W. and Jensen, O.G.
1981: Radiohm mapping of permafrost; in Geophysical Applications of Surface Wave Impedance Measurements, L.S. Collett and O.G. Jensen (eds.); Geological Survey of Canada, Paper 81-15, Report V, p. 19-33.

Smith, H.W., Provazek, L.D. and Bostick, F.X.Jr.
1961: Directional properties and phase relations of the magnetotelluric fields at Austin Texas, Journal Geophys. Res. 66, 3, p. 870 - 880

Tyraskis, P.
1979: Multichannel auto-regressive data modelling, M.Sc. thesis, McGill University, Montreal .

Van Ngoc, P.
1976: Magneto-telluric reconnaissance survey in the Lillooet Valley, British Columbia, Rept. by the Mineral Exploration Research Institute (IREM/MERI), Montreal, to Earth Physics Branch, Energy Mines and Resources Canada, EPB open file 77-20.

Wait, J.R.
1962: Electromagnetic Waves in Stratified Media, International Series in Electromagnetic Waves, Vol. 3, Pergamon, Toronto, 372 pp.

VIII

INSTRUMENTATION FOR DIRECT MEASUREMENT OF PHASE OF AUDIO-FREQUENCY MAGNETOTELLURICS

E. Nichols and W.M. Telford
Laboratory in Applied Geophysics, McGill University

Nichols, E. and Telford, W.M., Instrumentation for the direct measurement of phase of audio-frequency magnetotellurics; in Geophysical Applications of Surface Wave Impedance Measurements, L.S. Collett and O.G. Jensen editors; Geological Survey of Canada, Paper 81-15, p. 95-102, 1981.

Abstract

The erratic nature of the magneto-telluric source field makes it difficult to measure directly the relative phase between the electric and magnetic fields, compared to conventional artificial source electromagnetic methods, since there is no control over source intensity, duration, azimuth or energy spectrum. An instrumentation scheme for acquiring and processing these signals to measure the phase and amplitude ratio is presented. The most critical aspect of the signal treatment is the frequency selection by a two-stage staggered band-pass filter. The signal is demodulated by means of either a reference phase-locked loop or an analog multiplication method. Source fluctuations are minimized by a signal integrity monitor and time-averaging through integration. Field testing of the prototype instrument is presently underway.

Resume

Dans le cas de la méthode magnéto-tellurique, la mesure directe de la différence de phase entre les champs électromagnétiques et magnétiques est plus difficile que dans celui des méthodes électromagnétiques conventionnelles à source synthétique à cause de la nature aléatoire des champs magnéto-telluriques. En effet, on ne dispose d'aucune contrôle sur les paramètres de la source tels que son intensité, sa durée, son azimuth ou -son spectre d'énergie. On présente ici un prototype d'instrument qui permet l'acquisition et le traitement de ces signaux pour en extraire la différence de phase ainsi que le rapport d'amplitude. L'étape la plus critique du traitement de signal et la sélection de fréquence qui est réalisée par un filtre passe bande à deux étages à pôle alterne. La démodulation du signal est produite par deux modules indépendants: soit par une maille à verrouillage de phase synchronisée sur l'un des signaux, soit par une multiplication analogique des signaux. On minimise l'effet des fluctuations de la source par un moniteur de l'intégrite des signaux et par une moyenne des mesures dans le temps par l'intermédiare de circuits intégrateurs. On procède actuellement aux essais sur le terrain du prototype décrit.

INTRODUCTION

The project of designing portable field instrumentation to make direct measurements of the relative phase as well as the amplitude of magnetotelluric (MT) signals was initiated following the demonstration of reasonably reliable phase measurements, in the low audio frequency range, of MT tape records (Mathur and Telford, 1981-VII). Smith et al. (1961) had previously obtained very stable results of the same type at a frequency of 0.056 Hz.

Phase detection has been implemented by two methods, one with phase-locked loop circuitry providing a reference signal for cosynchronous demodulation, the other by decoding the phase information via analog multiplication.

MT Source Characteristics and Detection

The propagation and attenuation of natural EM fields has been described elsewhere in this volume (Crossley, 1981-I) Detection and recording of these fields require some consideration of the source characteristics as well as the linear convolutions involved in the sequence, shown in Figure 1, between it and the measured response. Since the intention in the present work is to employ signals in the approximate range 1-15 kHz, the source energy is primarily due to electrical storms; these are known as spherics.

A lightning discharge consists of an initial cloud to ground leader strike generating frequencies at 20 kHz and higher, followed by a return ground to cloud strike up the ionized channel. Peak currents of 160 kA have been detected during the return strike which characteristically produces frequency components below 20 kHz (Doborzynski, 1974). Thus the signal energy is produced in irregular bursts, as illustrated in Figure 2.

There are several predominant frequencies (Schuman resonances) in the background spectrum, at 8, 14, 32 Hz, etc., as shown in Figures 3 and 5. The spherics also change frequency characteristics with distance from the source (Fig. 4). The MT power spectrum from 10^{-4} to 10^{6} Hz, with the frequencies chosen for this instrument, is displayed in Figure 5.

Although the energy is propagated practically vertically downwards in the earth because of the large contrast in conductivity between earth and air, resulting in

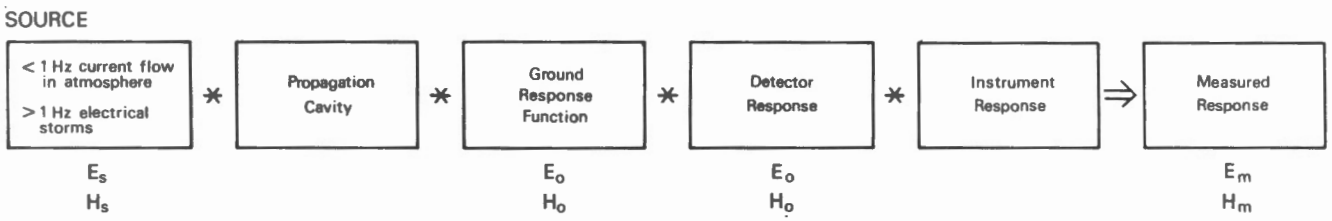

Figure 1. Response functions convolving the source EM energy to give measured response E_m *and* H_m.

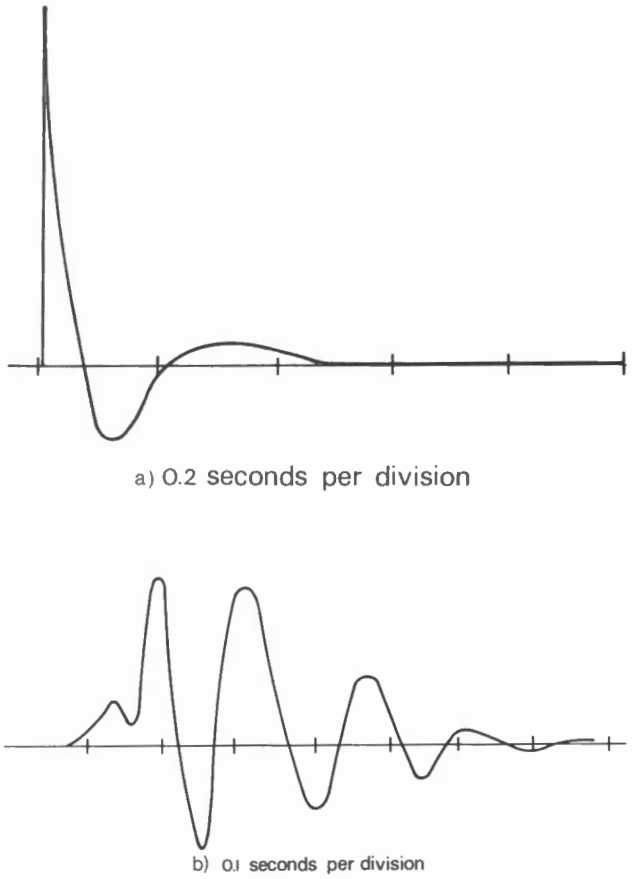

Figure 2. Electric fields generated by atmospheric electric activity (after Keller and Frischknecht, 1967). a) Electric field at a distance of 10 miles from a single stroke of lightning. b) Electric field at a distance of 100 miles from a single stroke of lightning.

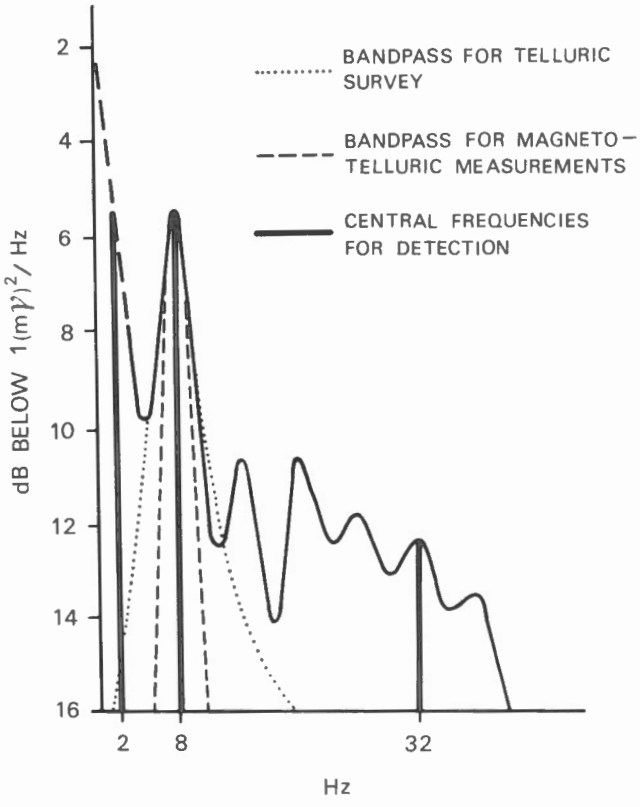

Figure 3. Power spectrum of sub-audio frequency natural magnetic field and band pass of telluric and magnetotelluric amplifiers.

a horizontally polarized plane wave, the changing azimuth of the remote source varies the direction of polarization. This produces erratic amplitude and phase instability if the ground impedance is anisotropic. However, if the impedance function can be considered two-dimensional, measurements of horizontal components parallel and normal to strike ($E_\perp$ and $H_{||}$, $E_{||}$ and $H_\perp$) will resolve this instability.

Thus an appropriate simultaneous measurement of horizontal E and horizontal orthogonal H fields allows determination of the complex earth impedance. The so-called complete ground response function (GRF) consists of a complex tensor of order 3. Where possible, however, this may be simplified to the two- or one-dimensional case. Measurement of the imaginary or phase component is more difficult and generally has been obtained from analysis of prerecorded data. To date only the amplitude or real part of the complex response has been read directly.

INSTRUMENTATION

A block diagram of the instrument under design is shown in Figure 6. The operation of each stage is discussed in the following, with emphasis on the phase sensitive circuits.

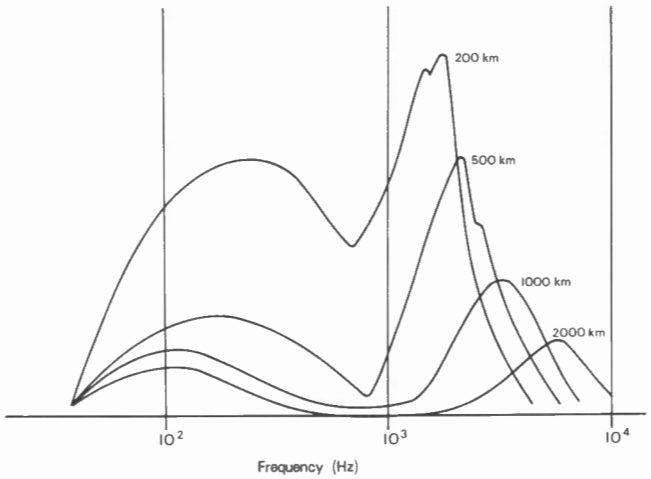

Figure 4. Effect of distance from lighting discharge on frequency and amplitude of electric fields.

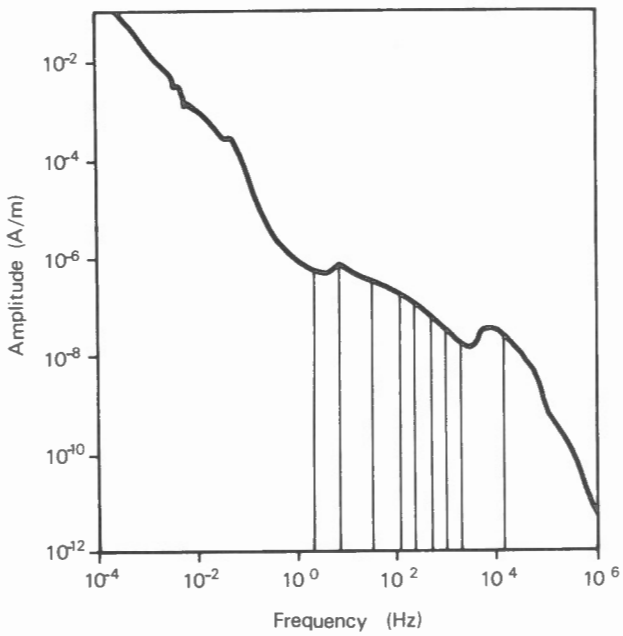

Figure 5. Natural EM field spectrum.

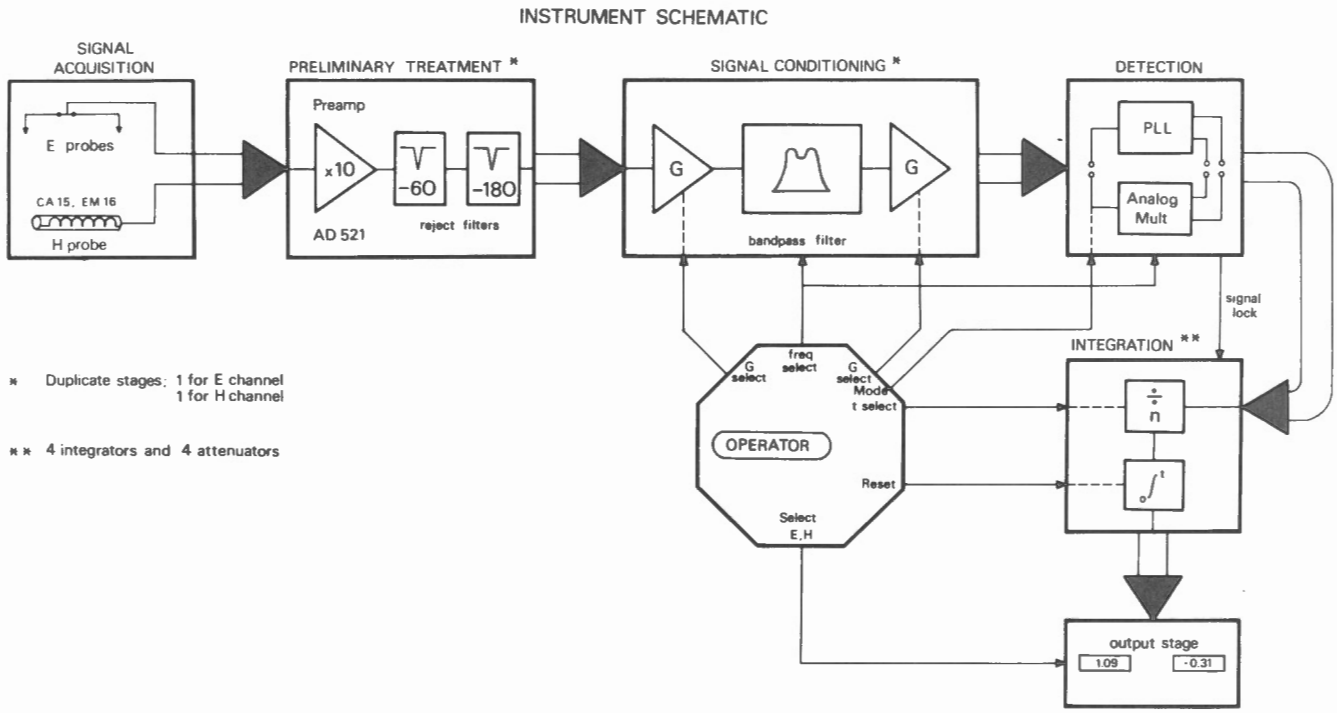

Figure 6. General instrument schematic.

Signal Acquisition

The operational range, spanning nearly five decades of frequency, poses a severe problem for the magnetic sensor in maintaining constant amplitude and phase response. The model CM15 sensor has a wide band low frequency ferrite core whose amplitude and phase characteristics are displayed in Figure 7. Selected frequencies in this range, marked on Figure 5, are 2, 8, 32, 128, 256, 512, 1024, 2048 Hz. (A standard EM16R sensor is used for the highest frequencies, in the VLF band.).

Detection of E-field signals is relatively simple, employing high performance instrumentation amplifiers such as the AD521 in the preamplifier section. The bandwidth of 300 kHz with gain of 10 provides stable frequency reception and the high input impedance (10^{10} Ω) produces insignificant loading of the E-field probes.

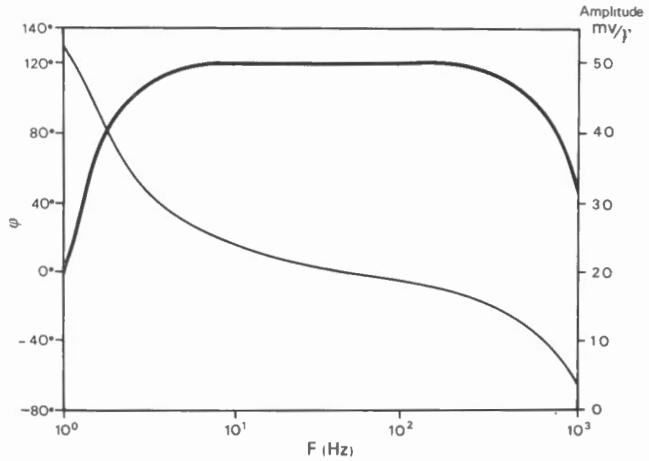

Figure 7. *Amplitude and phase characteristics for magnetic sensors, type CA15/A and CA15/B.*

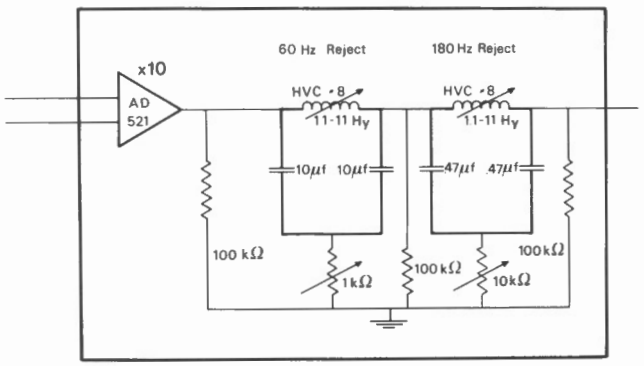

Figure 8a. *Preliminary signal treatment.*

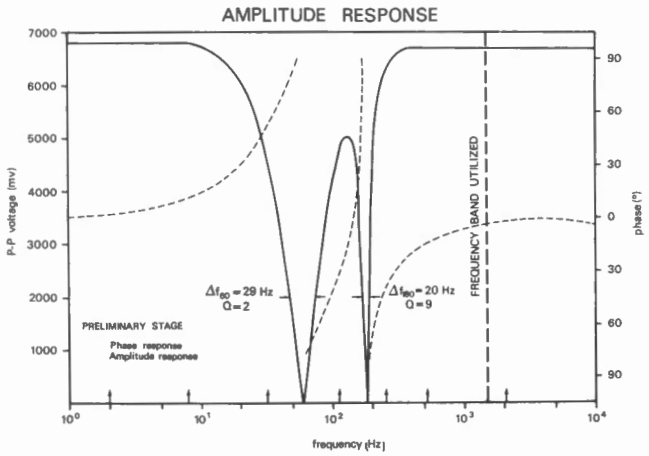

Figure 8b. *Amplitude and phase characteristics of Twin-T 60 and 180 Hz rejection filter.*

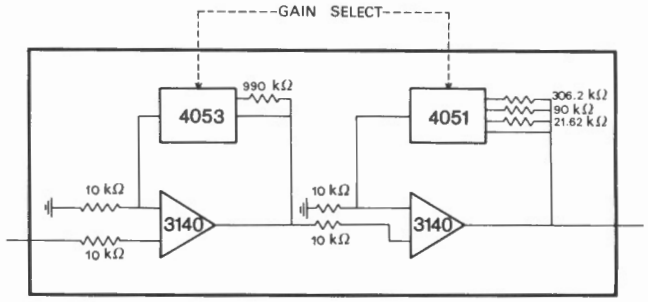

Figure 9. *Gain stage for single channel amplifier schematic.*

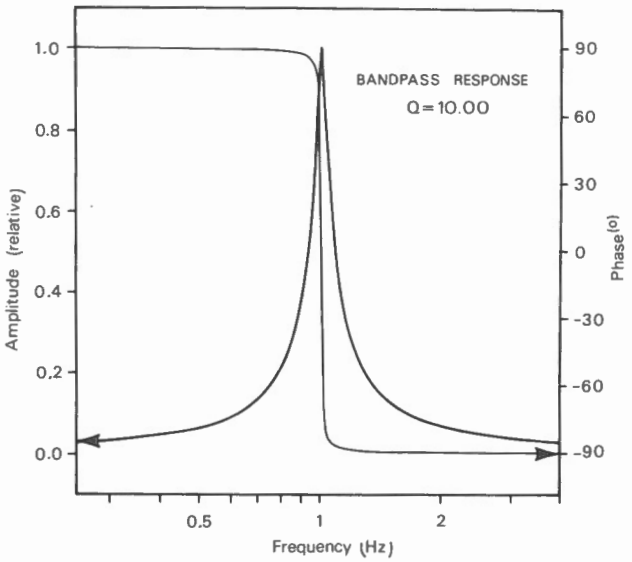

Figure 10. *Second order single pole band pass filter, amplitude and phase characteristics.*

Calibration of the AD521 revealed a maximum phase shift of 6°. This is identical for both E and H channels, however, so there is no relative phase change.

Preliminary Signal Treatment

The input E and H signals, after buffering in the AD521 preamplifier, operating in a true differential mode and obtaining a voltage gain of 10, pass through two cascaded Twin-T rejection filters (See Figure 8a.) to reduce 60 Hz and 180 Hz contamination. These filters provide a 46 db attenuation with amplitude and phase characteristics as in Figure 8b. As in the preamplifiers, the sections are made as identical as possible and with low Q to minimize relative drift.

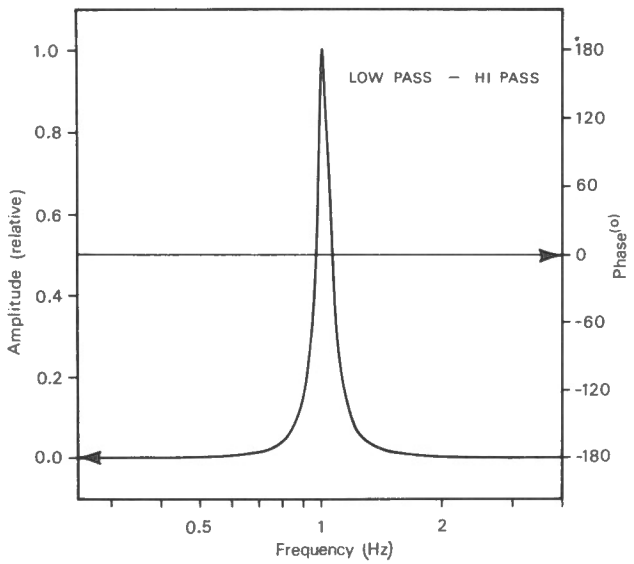

Figure 11a. *Second order cascaded low and high pass filter, amplitude and phase characteristics.*

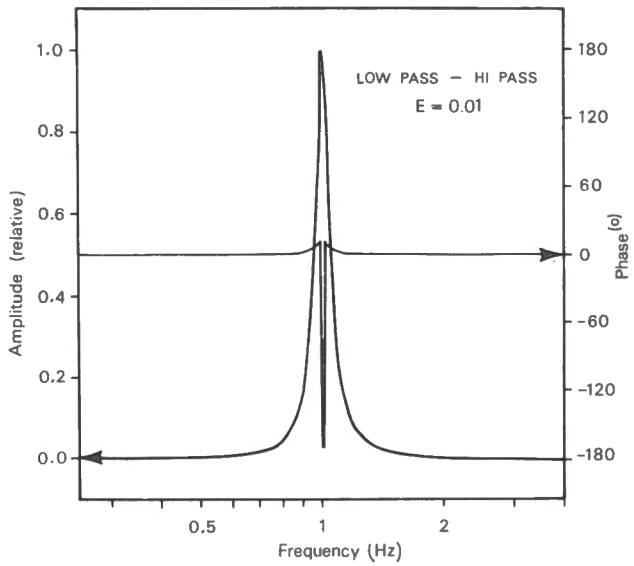

Figure 11b. *Effect of 1% drift between two channels on phase characteristic.*

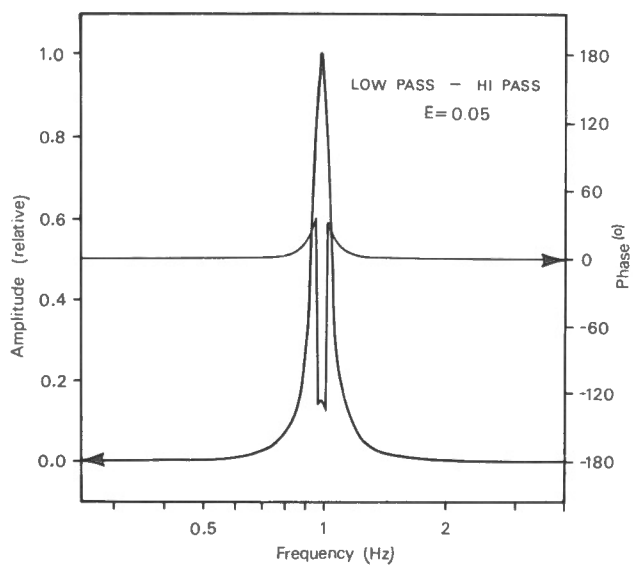

Figure 11c. *Effect of 5% drift between two channels on phase characteristic.*

Signal Conditioning

Signal amplification and frequency selection is carried out in this section. Two identical gain stages, one preceeding and the other following the band-pass filter, are provided for each channel to amplify the signals to a suitable level for detection. A schematic for one of these is shown in Figure 9. Analog multiplexers, mounted directly on board to minimize radiated noise, provide gain selection from 1 to 3162 ($1000\sqrt{10}$) in steps of $\sqrt{10}$.

Design of a stable filter is closely related to the inherent problem of large phase shift vs. good frequency discrimination. Four methods of analog filtering were studied: 1) second order single pole band-pass filter (BP), 2) cascaded low- and high-pass (LP and HP), 3) fourth order two pole BP, 4) cosynchronous demodulation and reconstruction technique.

Since a value of Q = 10 was desired for the filter, the simulated response was easily modelled for the first three cases. Figure 10, showing the response for filter 1, clearly illustrates the difficulty in maintaining phase stability near the centre frequency where phase gradient is practically vertical. A drift of 1% between channels produces a phase error of 63°, rendering the phase measurement meaningless.

The filter shown in Figure 11a, produced by cascading together second order LP and HP filters with equal cut-off frequencies and damping, yields an ideal response with zero phase shift. However, a perturbation of 1% between LP and HP cut-offs in the two channels produces a sharp discontinuity of 180° in phase at the center frequency, as can be seen in Figure 11b. The unstable region widens considerably with the offset, illustrated for 5% in Figure 11c.

Two pole fourth order BP filters are commonly used to give higher stopband attenuation. Instead of selecting equivalent filter sections to give maximum peaked response, the center frequencies of the two sections are staggered by a factor A and 1/A from the desired frequency, producing a wider passband and altering the phase response significantly. Figures 12a, b, c illustrate the effect of increasing the separation A. The price one pays for increasing the flat phase response region, however, is in higher insertion loss and loss of the flat passband gain, as is evident in these diagrams. For initial instrument tests a value A = 0.15 was chosen as a compromise in using this filter.

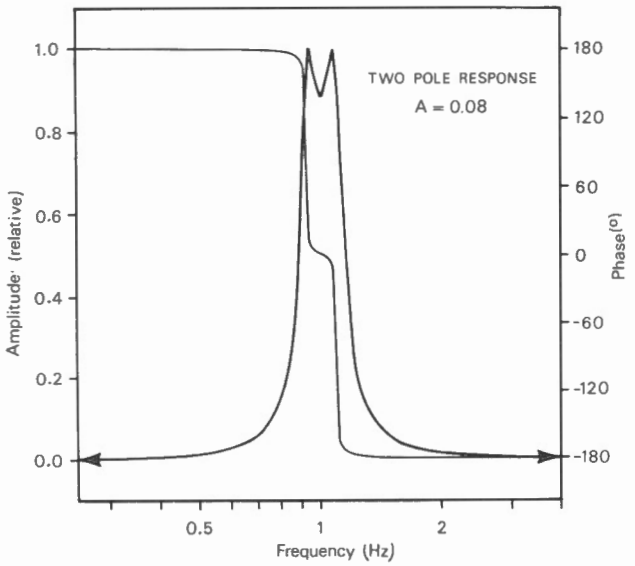

Figure 12a. *Fourth order two pole band pass filter, amplitude and phase characteristics, A = 0.08.*

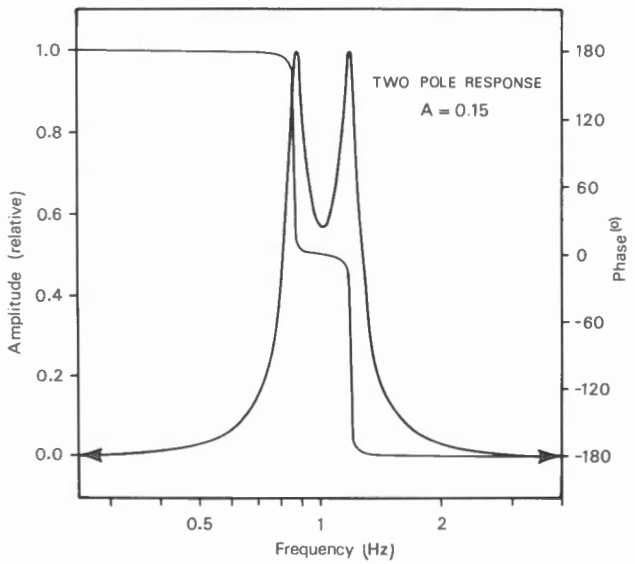

Figure 12b. *Fourth order two pole band pass filter, amplitude and phase characteristics, A = 0.15.*

Better phase stability between channels is possible with the pseudo-digital sampling and reconstruction scheme displayed in the block diagram of Figure 13. Simultaneous sampling of the E and H channels, using a clock of appropriate frequency, demodulates their signals into in-phase and quadrature components which are then low-pass filtered to remove the difference frequencies. Each channel signal is then recombined using an analog multiplexer driven by the same clock. A second low-pass filter is required to remove harmonics introduced in the switching. Since this filter would alias any odd harmonic of the sampling frequency a front end anti-aliasing filter is also necessary. However, this system requires more components than the first three and is further complicated by the fact that the low-pass filters must be different for each frequency selected.

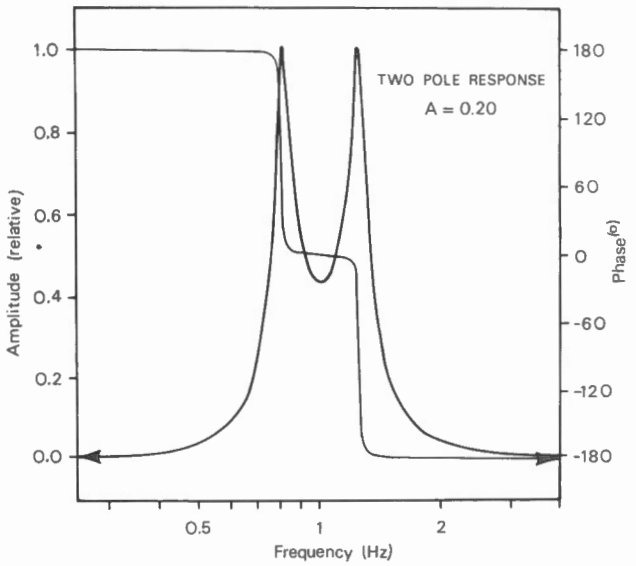

Figure 12c. *Fourth order two pole band pass filter, amplitude and phase characteristics, A = 0.20.*

As mentioned above, filter system 3 was chosen for the first instrument tests on the basis of lower power consumption and fewer components required.

Signal Measurement Stage

From a noisy input signal a relatively clean version is obtained with which amplitude and phase determinations may be carried out. Two measuring techniques are developed in the current model. The first involves synchronous demodulation employing a phase-locked loop (PLL) to provide the clock reference. The other is an analog multiplication scheme.

Phase-Locked Loop Detection

The core of this section, the PLL shown schematically in Figure 14a, is a closed loop feedback system which utilizes the filtered output from a phase sensitive detector to modulate the input of a voltage-controlled oscillator (VCO). The critical component in the feedback loop is the filtering, which will determine the transient response, lock acquisition time, locking range and acquisition range.

For example, in order to achieve a fast lock acquisition one would use a low-pass filter (gain R_2/R_1, time constant R_2C; See Figure 14b.) with adequate gain and suitably low time constant, depending on frequency. When lock acquisition switch S_1 is closed, the filter becomes an integrator with time constant R_1C. The advantage of an integrator is that the phase difference between the signal and the reference will be integrated to zero, thus locking the reference signal in phase with the input signal. The in-phase component is monitored by a comparator to provide a lock detection control signal which in turn monitors signal integrity.

The VCO output drives a CMOS 4020-14 bit binary counter which selects the desired frequency; this is divided by 2, using a CMOS 4027 dual JK Flipflop, to produce the

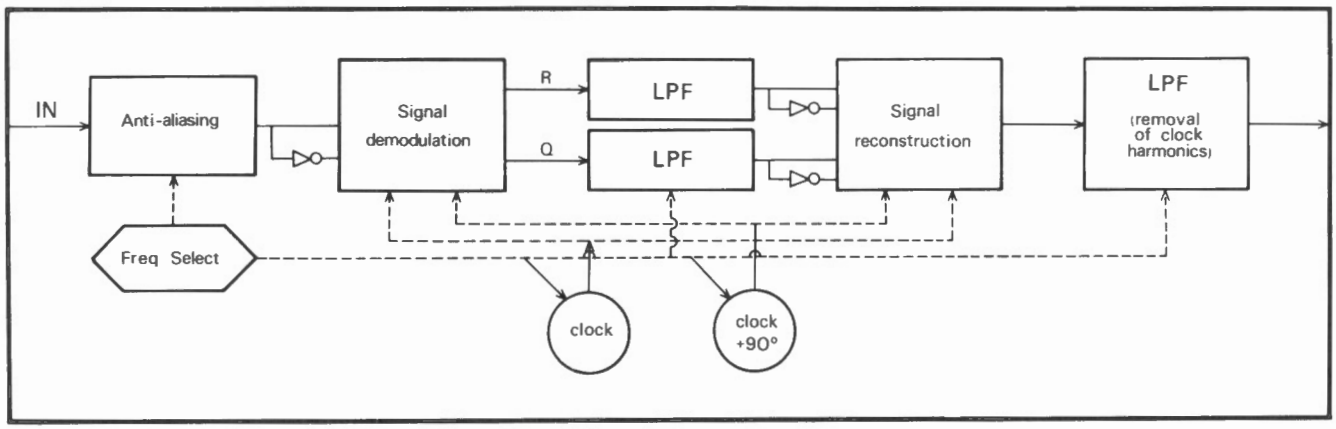

Figure 13. Block diagram for pseudo-digital sampling and reconstruction circuit.

reference in-phase and quadrature clock signals. These in turn drive the analog multiplexers to demodulate the E and H input signals into their in-phase and quadrature components (See Figure 14a.). Either E or H may be used as the PLL input signal as shown in Figure 14a.

Five outputs, E_R, E_φ, H_R, H_φ and lock detect, are sent to the integrator stage so that phase may be calculated from the relation

$$\varphi = \tan^{-1}(E_\varphi/E_R) - \tan^{-1}(H_\varphi/H_R)$$

Analog Multiplication Scheme

Phase information may be extracted from the E and H signals by two multiplications and simple trigonometric relations. If the E and H fields for a particular frequency are given by

$$E = E_o \sin \omega t \qquad H = H_o \sin(\omega t - \varphi)$$

then we have

$$\frac{E_o \sin \omega t \,.\, H_o \cos(\omega t - \varphi)}{E_o \sin \omega t \,.\, H_o \sin(\omega t - \varphi)} = \frac{\sin \varphi + \sin(2\omega t - \varphi)}{\cos \varphi - \cos(2\omega t - \varphi)}$$

Components involving $2\omega t - \varphi$ may be eliminated either by low-pass filtering or integrating the result and we are left with

$$\sin \varphi / \cos \varphi = \tan \varphi$$

Thus the phase information is retrieved by forming the arctangent of the quotient of the two time-averaged products. Since sine and cosine functions differ by 90° phase, a circuit shown in Figure 15 produces the two products for time averaging. Amplitude information is obtained by rectifying the E and H signals for integration. An integrity check is provided by requiring a minimum level of the rectified signals. Finally, the four signals plus the integrity monitor are applied to the integration stage.

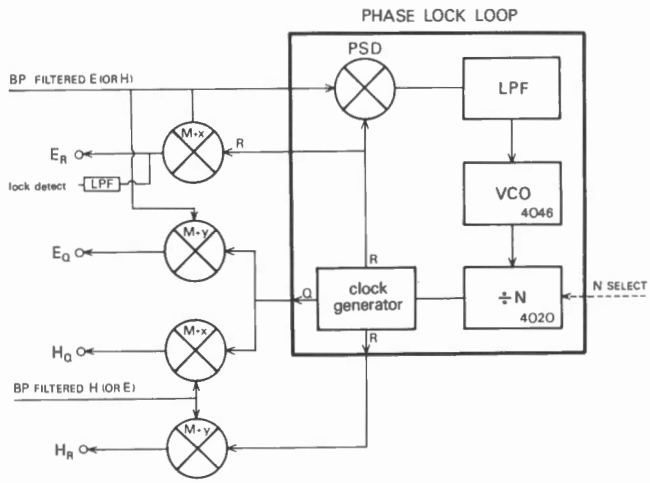

Figure 14a. Phase-locked loop detection method schematic.

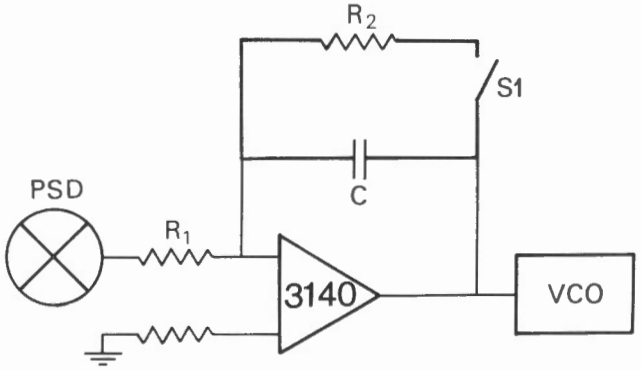

Figure 14b. Low pass filter for phase-locked loop schematic.

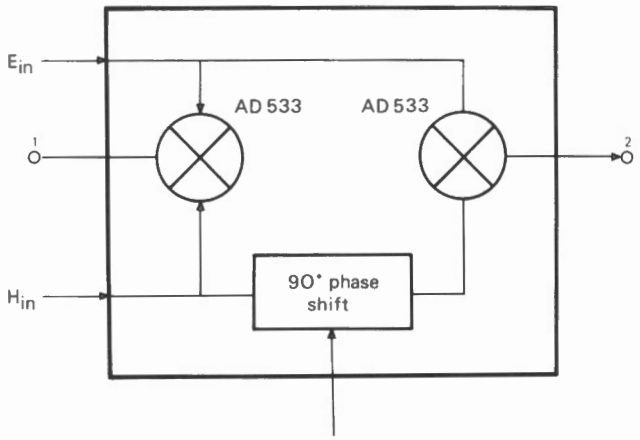

Figure 15. Phase detection by analog multiplier schematic.

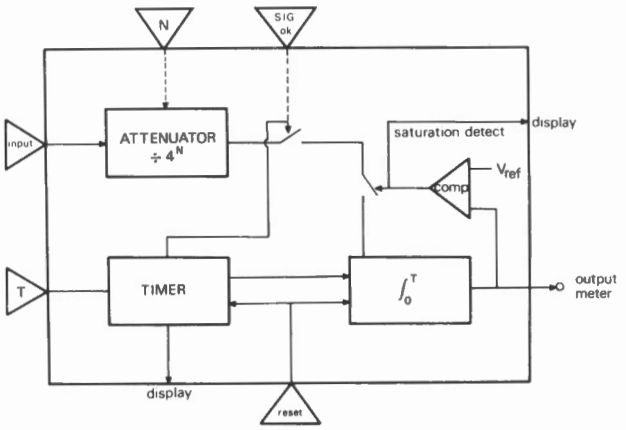

Figure 16. Single integrator stage showing logic control signals schematic.

Integration Stage

Whichever signal measurement technique is used (Multiplier or PLL board), four identical integrators average the four input signals, but only while the proper integrity check permits or until one or more integrators approach saturation. A timer allows variable integration times between 3 seconds and 16 minutes; it is controlled to shut off during loss of valid signal periods. Integrator outputs are displayed on two $3\frac{1}{2}$-digit liquid crystal Datel panel meters. When using the PLL, one meter displays in-phase E field (E_I) while the other is quadrature E field (E_Q); on throwing a two position toggle switch they indicate H_I and H_Q respectively. If the multiplication circuit is being used, the corresponding displays are $EH \cos\varphi$, $EH \sin\varphi$ and $|E|$, $|H|$ respectively. In both cases it is then possible to calculate ρ_a and φ. Figure 16 is a schematic of a single integration stage. Calibration of the four channel gains and time constants permits average accuracy of 0.4%.

FURTHER WORK

Final harness wiring and installation of frequency selection switches is currently under way. A numerical simulation testing both the PLL synchronous demodulation and multiplication techniques with MT sounding data tapes is presently being carried out to compare with results from the Maximum Entropy Method (MEM) of spectral analysis (Mathur and Telford, 1981-VII) and conventional Fourier analysis of the same data. It is hoped that field trials of the instrument in selected areas may be possible within a few months.

ACKNOWLEDGEMENTS

The research which this article summarizes was supported by the EMR Canada through Research Agreements 77-4-79 and 256-4-80.

REFERENCES

Crossley, D.J.
1981: The theory of EM surface-wave impedance measurements; in Geophysical Applications of Surface Wave Impedance Measurements, L.S. Collett and O.G. Jensen (eds.); Geological Survey of Canada, Paper 81-15, Report V, p. 1-17.

Doborzynski, Z.B.
1974: Prospecting with multi-frequency tellurics, M.Sc. thesis, McGill University, Montreal.

Mathur, R.K. and Telford, W.M.
1981: Magnetotelluric phase measurements; in Geophysical Applications of Surface Wave Impedance Measurements, L.S. Collett and O.G. Jensen (eds.), Geological Survey of Canada, Paper 81-15, Report V, p 87-93.

Smith, H.W., Provazek, L.D. and Bostick, F.X. Jr.
1961: Directional properties and phase relations of the magnetotelluric fields at Austin, Texas, Journal Geophys. Res. 66, 3, p. 870-880.

AUTHOR INDEX